Solvent-Engineered Tin(II) Oxide for Applications in Energy Storage Devices

A report submitted to the University of Dublin, Trinity College

For the degree of

Doctor of Philosophy in Chemistry

By

Seán Ryan

Supervisor: Prof. Valeria Nicolosi

June 2023

Trinity College Dublin

Declaration

I declare that this thesis has not been submitted as an exercise for a degree at this or any other university and it is entirely my own work.

I agree to deposit this thesis in the University's open access institutional repository or allow the Library to do so on my behalf, subject to Irish Copyright Legislation and Trinity College Library conditions of use and acknowledgement.

I consent to the examiner retaining a copy of the thesis beyond the examining period, should they so wish (EU GDPR May 2018).

Seán Ryan

Abstract

With the global economy finally accepting of the harm caused by fossil fuels to the planet as a whole and the reality that they are a finite resource, ambitious plans are being made to transition to carbon-neutral economies in the following decades. To allow for a seamless transition and allow the energy-abundant life we are all familiar with to continue, improvements must be made to the current electrodes used in electrochemical energy storage devices to improve performance. One renewable technology does not fit all, and research must be driven towards diversifying the technologies we rely on for energy storage.

In this present work, solvent-engineered Tin(II) Oxide (SnO) is synthesised for energy storage applications, in which the morphology of the SnO may be tuned through a simple change of reflux solvent. SnO lithium-ion battery electrodes are manufactured using simple and scalable techniques. Using an iterative approach, the optimized morphology, mass fraction, type of conductive additive and electrolyte are selected. A maximum capacity of 980 mAh g^{-1} was obtained at 0.1 C using the optimised heat treated Tuball-single walled carbon nanotube (SWCNT) nanoflower SnO composite, whilst an initial coulombic efficiency (ICE) of 80% was recorded in addition to maintaining a capacity of 815 mAh g^{-1} after 300 cycles at 0.5 C. Furthermore as a proof of concept, a full-cell was assembled using a lithium nickel manganese cobalt oxide cathode with the cathode shown to be the limiting factor.

It was found that the same electrode optimised performance in sodium-ion batteries as had been the case for the lithium counterpart. The electrode underwent an activation period with the sodium alloying reaction over several cycles, with the increase in capacity attributed to an electrochemical milling effect. The optimized composite had a maximum capacity of 574 mAh g^{-1} at 0.05 C, whilst in terms of cycling stability it displayed a capacity of 500 mAh g^{-1} after 60 cycles, which dropped to 405 and 261 mAh g^{-1} after 80 and 120 cycles respectively. Issues remained however around the ICE of the composite (51%) and the CE during cycling which remained under 99%.

SnO and Tuball inks were formed and printed as supercapacitor electrodes. Although the presence of SnO did not increase the capacitance through pseudocapacitance, it had the

effect of inhibiting the functionalization and the subsequent degradation of the SWCNTs in the presence of sulphate-based electrolytes. It was shown that the mechanism for shielding the SWCNTs involves a pseudo-reversible reaction between the sulphate ions and SnO, which leads to the co-existence of both SnO and Sn_3O_4 after cycling in devices as shown by x-ray diffraction and x-ray photoelectron spectroscopy. A 10% mass fraction of SnO was the optimum addition; still enabling shielding whilst also maximising the SWCNT mass fraction which is responsible for the electrode's capacitance. The electrode obtained a capacitance of 102 F g^{-1} at 2 A g^{-1} and a capacity retention in excess of 95% after 30,000 cycles at 10 A g^{-1}. An asymmetric device was assembled with MXene with a voltage window of 1.8 V, obtaining an energy density of 24.39 Wh kg^{-1} at 1 A g^{-1} and a capacity retention of 90% after 7,500 cycles.

In summary, this Thesis demonstrates the versatility of solvent-engineered SnO in combination with SWCNTs towards a range of renewable energy storage applications. The approaches taken are cost-effective, scalable and environmentally friendly. A composite material has been developed that optimises performance in both lithium/sodium-ion batteries, whilst employing the same constituent materials a wide voltage supercapacitor electrode is developed.

Acknowledgements

Firstly, I would like to thank Prof. Valeria Nicolosi for allowing me to join her research group to carry out my research in addition to constantly supporting my work and directing it. In addition to this I would like to thank her for always putting the welfare of her staff first and foremost and constantly solving all issues and problems we may face. I have always left meetings with a renewed interest and energy for my work, and she possesses an amazing skill of encouraging all her students even when results don't turn out as envisioned. It has been a pleasure to be able to call her my mentor for the past four years.

I would like to thank all the Nicolosi group for being so kind and helpful to me throughout my time there. I would like to particularly thank Sergio Pinilla for mentoring me on a day to day basis and giving up his time to help me with my project and answer the numerous questions I put to him. I am also thankful to Michelle P. Browne, who helped me gain a better understanding of material science and electrochemistry and also took the time to help me when I asked. I also thank João Coelho for mentoring me on all things concerning batteries and electrochemistry at the beginning of my PhD, Dahnan Spurling for lending me his expertise with supercapacitors, Lorcan McKeon for carrying out printing work for me and advising me on how best to fabricate devices and Sonia Jaśkaniec for mentoring me on the synthesis of my material. I would like to thank Lucia Hughes for assisting me with XRD and being a friend I could moan to when I needed a good moan. I would like to thank Dermot Daly, Megan Canavan and Clive Downing from the AML in Trinity College Dublin for teaching me how to operate the SEM/FIB and always lending a hand when called upon. I would like to thank Christopher Hobbs and Oskar Ronan, both formally of the Nicolosi group for carrying out TEM characterisation for me. I thank Danielle Douglas-Henry, Ainur Zhussupbekova, Lucy Prendeville and Sebastien Vaesen for their assistance with experimental techniques needed for this PhD fellowship. I thank Carol McCaffrey and Jesus Barco Montero for their assistance with all things concerning admin, supplies and funding. I also thank Trinity College Dublin and in particular the School of Chemistry for supporting me during this structured PhD.

I am very grateful for the continued support I receive from the Irish Research Council and thank them for awarding me a Government of Ireland Postgraduate Scholarship (GOIPG/2019/2428) without which I would not be able to carry out my work.

Finally (and most importantly), I would like to thank my family and friends for all their support, particularly my parents Michael and Anne for their unwavering support of me throughout my studies.

Table of Contents

Declaration ..... **i**

Abstract ..... **ii**

Acknowledgements ..... **iv**

Publications ..... **x**

Communications ..... **xi**

Abbreviations ..... **xii**

1. Introduction and Motivation **1**

2. Theory and Background **3**

2.1 Lithium-Ion Battery: Historical Development **3**

2.2 Electrochemistry of lithium-ion batteries **3**

2.3 Lithium-Ion Battery Anode Materials **5**

Lithium metal anodes 6

Carbon-based anodes 6

Metal Oxides 7

SnO properties 8

SnO as an anode material 9

2.4 Solid Electrolyte Interphase **10**

2.5 Electrolyte **11**

2.6 Nanomaterials **12**

2.7 Cathode Materials **13**

Transition Metal Oxides 13

2.8 Carbon Nanotubes for batteries **14**

P3-SWCNTs 16

Tuball 16

2.9 Sodium-Ion Batteries **16**

2.10 Sodium-Ion Battery Anode Materials **18**

SnO as an anode material for NIBs 19

Electrolyte for NIBs 20

2.11 Supercapacitors **20**

Pseudocapacitance 22

SnO as a supercapacitor material....24
Carbon Nanotubes for Supercapacitors....25

2.12 References....26

3. Experimental Techniques....33

3.1 Electrochemical Testing....33

Cyclic Voltammetry....33
Galvanostatic Charge-Discharge....33
Electrochemical Impedance Spectroscopy....34

3.2 Electron Microscopy....36

Scanning Electron Microscopy....37
Transmission Electron Microscopy....38
Energy Dispersive X-ray Spectroscopy....39

3.3 X-Ray Diffraction....40

3.4 X-Ray Photoelectron Spectroscopy....41

3.5 Infrared and Raman Spectroscopy....42

3.6 Nitrogen adsorption and BET analysis....44

3.7 References....46

4. Synthesis and Characterisation of Tin(II) Oxide....48

4.1 Wet Chemistry Synthesis of Tin(II) Oxide....48

Solvent Engineered Tin(II) Oxide Synthesis....49
Solvent Effect on Morphology....50

4.2 SnO Characterisation....52

TEM Characterization of SnO produced in methanol:water....52
Nitrogen Adsorption and BET analysis of synthesised SnO....54

4.3 Conclusions....55

4.4 Experimental....57

Synthesis of SnO....57

4.5 References....58

5. Tin(II) Oxide as a Lithium-Ion Battery Anode....60

5.1 Comparison Between Synthesised and Purchased SnO....60

5.2 Incorporation of Single-Walled Carbon Nanotubes in Anode....62

Optimisation of SWCNT Mass Loading....64

5.3 Investigation into the Effect of Morphology 67
Rate Performance and Cyclability 68
Impedance and Diffusion 71
5.4 Electrochemistry of Optimised Morphology 74
5.5 Alternative SWCNTs for Improved Cycling 77
Effect on Cycling 79
5.6 Differential Capacity Analysis and Electrolyte Investigation 81
Optimised Half-Cell Performance and Comparison to Other Works 84
5.7 Post-Mortem Analysis 88
5.8 Full-Cell Fabrication 90
5.9 Conclusion 92
5.10 Experimental 93
Preparation of SWCNTs dispersions 93
Preparation of SnO/Carbon Black slurry electrodes 93
Preparation of SnO/P3-SWCNTs film electrodes 93
Preparation of SnO/Tuball-SWCNTs electrodes 93
Heat Treatment of Tuball Electrodes 94
Freeze-Drying Electrodes 94
Electrochemical Cell Construction 94
Electrochemical Analysis 95
5.11 References 96
6. Tin(II) Oxide as a Sodium Ion-Battery Anode 100
6.1 Optimisation of SWCNT Mass Loading 101
6.2 Investigation into the Effect of Morphology 103
Rate Performance and Cyclability 103
Impedance and Diffusion 106
6.3 Electrochemistry of Optimised Morphology 108
6.4 Tuball SWCNTs for Improved Performance 111
Effect on Cycling 113
6.5 Differential Capacity Analysis and Alternate Electrolyte 115
Diglyme Electrolyte 117
Optimised Half-Cell Performance and Comparison to Other Works 118
6.6 Post-mortem Analysis 121

6.7 Conclusion **123**

6.8 Experimental **125**

Preparation of Electrodes 125

Electrochemical Cell Construction 125

Electrochemical Analysis 125

6.9 References **126**

7.Single-Walled Carbon Nanotubes/Tin(II) Oxide as a Supercapacitor Material **128**

7.1 Materials Characterisation **129**

Raman Spectroscopy 129

FTIR and XRD 130

7.2 XPS **131**

7.3 Electron Microscopy **133**

7.4 Mechanism of Electrochemical Anodic Oxidation of SWCNTs **135**

7.5 Electrochemical Analysis **136**

SWCNT/SnO Electrode 139

7.6 Full-Cell Asymmetric Device **141**

7.7 SnO as a Supercapacitor Material **143**

7.8 Conclusion **145**

7.9 Experimental **146**

Printing of SWCNT and SWCNT/SnO Electrodes 146

Printing of MXene electrodes 146

Electrochemical Analysis 146

7.10 References **148**

8. Conclusions and Future Work **151**

Appendix A **154**

Appendix B **155**

Appendix C **159**

Appendix D **164**

Appendix E **166**

Publications

Seán Ryan, Michelle P. Browne, Ainur Zhussupbekova, Dahnan Spurling, Lorcan McKeown, Danielle Douglas-Henry, Lucy Prendeville, Sebastien Vaesen, Wolfgang Schmitt, Igor Shvets and Valeria Nicolosi. "Single walled carbon nanotube functionalisation in printed supercapacitor devices and shielding effect of Tin(II) Oxide." *Electrochimica Acta* **448**, 142168 (2023).

Sergio Pinilla, **Seán Ryan**, Lorcan McKeon, Meiying Lian, Sebastien Vaesen, Ahin Roy, Wolfgang Schmitt, Jonathan N. Coleman and Valeria Nicolosi. "Additive Manufacturing of Li-ion Batteries: A Comparative Study between Electrode Fabrication Processes." *Advandced Energy Materials* **13**, 2203747 (2023).

Oskar Ronan, Ahin Roy, **Seán Ryan**, Lucia Hughes, Clive Downing, Lewys Jones and Valeria Nicolosi. "Templated Synthesis of SiO2 Nanotubes for Lithium-Ion Battery Applications: An In Situ (Scanning) Transmission Electron Microscopy Study." *ACS Omega* **8**, 925–933 (2023).

Sonia Jaśkaniec, Seán R. Kavanagh, João Coelho, **Seán Ryan**, Christopher Hobbs, Aron Walsh, David O. Scanlon & Valeria Nicolosi. "Solvent engineered synthesis of layered SnO for high-performance anodes." *npj 2D Materials and Applications* **5**, 27 (2021).

Seán Ryan, Sonia Jaśkaniec, Lucia Hughes, Valeria Nicolosi. "Solvent enginnered SnO/SWCNT composites for high performance lithium/sodium-ion batteries." Under Preparation (2023), *Work basis for Chapter 5 and 6.*

Communications

Seán Ryan, João Coelho, Sonia Jaśkaniec, Valeria Nicolosi. "Development of Lithium/Sodium-Ion Battery Electrodes Based on Solvent Engineered Tin(II) Oxide Nanomaterials." The Centre for Doctoral Training Workshop on Energy Storage and Applications, (23rd – 27th May 2022),Trinity College Dublin, Ireland. (Oral)

Seán Ryan, João Coelho, Sonia Jaśkaniec, Valeria Nicolosi. "Novel Materials for Future Renewable Battery Technology." Chemistry Careers in Energy and Sustainability, Science Week, Trinity College Dublin, Ireland (11th Nov 2021). (Oral)

Seán Ryan, João Coelho, Sonia Jaśkaniec, Valeria Nicolosi. "Development of Lithium/Sodium-Ion Battery Electrodes Based on Solvent Engineered Tin(II) Oxide Nanomaterials." Electrochemical Society 243rd Meeting (28th May – 2nd June 2023), Boston, USA. (Poster)

Seán Ryan, João Coelho, Sonia Jaśkaniec, Valeria Nicolosi. "Development of Lithium/Sodium-Ion Battery Electrodes Based on Solvent Engineered Tin(II) Oxide Nanomaterials." Materials Research Society Spring Meeting (8th – 13th May 2022), Honolulu, USA. (Poster)

Seán Ryan, João Coelho, Sonia Jaśkaniec, Valeria Nicolosi. "Development of Ultra-Thin Lithium-Ion Battery Electrodes Based on Solvent Engineered Tin(II) Oxide Nanomaterials." International Society of Electrochemistry & Royal Society of Chemistry Electrochemistry Group Irish Regional Early Career Meeting (27th May 2021), Online. (Poster). Awarded Poster Prize (2nd Place).

Abbreviations

CE	Coulombic Efficiency
CMC	Carboxymethyl cellulose
CNTs	Carbon Nanotubes
CV	Cyclic Voltammetry
DEC	Diethyl Carbonate
EC	Ethylene carbonate
EDL	Electric double layer
EDLC	Electric double layer capacitance
EDX	Energy dispersive x-ray spectroscopy
EIS	Electrochemical Impedance Spectroscopy
EMC	Ethyl methyl carbonate
EVs	Electric Vehicles
FD	Freeze dried
FEC	Fluoroethylene carbonate
FIB	Focused Ion Beam Milling
GCD	Galvanostatic charge-discharge
HOMO	Highest Occupied Molecular Orbital
HT	Heat treated
ICE	Initial Coulombic Efficiency
LIB	Lithium Ion Battery
LUMO	Lowest Unoccupied Molecular Orbital
MO	Metal Oxide
MWCNTS	Multi Walled Carbon Nanotubes
NIB	Sodium Ion Battery
NMC	Lithium nickel manganese cobalt oxide
NMP	N-Methyl-2-Pyrrolidone
P3	P3 SWCNTs
PVDF	Polyvinylidene Fluoride
SA	Sigma Aldrich
SC	Supercapacitor
SEI	Solid Electrolyte Interphase
SEM	Scanning Electron Microscope

SnO	Tin(II) Oxide
SnO(70% MeOH)	SnO synthesised in 70% methanol, 30% water
SnO(EtOH)	SnO synthesised in ethanol
SnO(H_2O)	SnO synthesised in water
SnO(Hex)	SnO synthesised in hexanol
SWCNTs	Single Walled Carbon Nanotubes
TEM	Transmission electron microscopy
TMO	Transition Metal Oxide
Tu	Tuball SWCNTs
XRD	X-Ray powder Diffraction

1. Introduction and Motivation

In recent years with the energy demands of the earth's population exponentially increasing, new and innovative energy storage devices must be developed. Climate change and the inevitable extinction of fossil fuel supplies have given rise to a surge in the hybrid and electric vehicle market along with huge increases in renewable energy infrastructure. The desire to move away from fossil fuels has never been greater, but societies will never fully commit to the clean energy revolution unless the new technologies at a minimum match the old (oil, coal, natural gas) if not exceed them. The current sanctions imposed on Russia in 2022/2023 for their invasion of Ukraine and the subsequent weaponisation of Russian gas have clearly shown how our overdependence on fossil fuels for everyday life is not sustainable for worldwide geopolitical stability in addition to the climate crisis. Hence, we as a global society must move away from fossil fuel-driven energy technologies to renewable-based driven energy technologies which include energy storage.

To allow electric vehicles to travel further, or for intermittent renewable energy sources such as solar or wind energy to be stored, improvements must be made to the electrochemical energy storage technology and in particular the electrode materials which are the key factor in the capacity of these devices. On this matter, both small and large-scale energy storage devices must move at the same pace; it is redundant to perfect a car that runs off only electricity if the source of the electricity is not renewable. Another factor that greatly influences the implementation of renewable storage technologies is cost. This is a global energy crisis we are facing and as such the costs must be manageable for both the poor and rich to truly help tackle our ever-growing carbon footprint. To do this energy storage technologies based on abundant and globally available resources must move to the forefront of research.

The research carried out during this PhD fellowship aims to find solutions to the problems stated above. Lithium-ion battery, sodium-ion battery and supercapacitor materials based on Tin(II) Oxide are developed with an emphasis placed on scalable production methods and inexpensive materials. Through tailoring the synthesis parameters, optimised morphologies for energy storage are explored and utilised in conjunction with carbon nanotubes to form composite materials that can be fabricated into electrodes in a number

of ways; through slurry casting, vacuum filtration and extrusion printing. These different methodologies of forming the electrode have different advantages, such as scalability for slurry casting and filtration whilst printing allows for quick prototyping and easy tailoring of electrode designs. Advanced techniques such as XRD, SEM and TEM will be used to characterise and analyse the materials and composites formed while a range of electrochemical methods will be used to fully assess the storage performance of fabricated devices. The overall aim of this PhD fellowship is to develop a composite material that fits all technologies based on Tin(II) Oxide with the incorporation of carbon nanotubes, which can be cost effective, high in energy capacity and rate performance.

The energy and climate crisis faced by the global population is the crucial problem that our generation will face and it must be tackled by scientific research today. This has been made ever more relevant by the awarding of the Nobel Prize in 2019 for the development of the lithium-ion battery. It is hoped that this project will aid in this task and provide insights that will aid in a comprehensive solution.

2. Theory and Background

2.1 Lithium-Ion Battery: Historical Development

The lithium-ion battery (LIB) became a household name in 1991 when Sony Corporation Japan[1] developed upon previous work done by Asahi Kasei Corporation[2] to produce the first commercially available rechargeable LIBs. From the periodic table, it becomes apparent why battery technology has been driven towards lithium (Li). It is the most electropositive (-3.04 V versus standard hydrogen electrode) and lightest metal known (ρ = 0.53 g cm^{-3}) and thus facilitates high energy density storage systems.[3,4] Furthermore, the small atomic radius of Li-ions offers a high diffusion coefficient when used as a charge carrier (~ 10^{-7} – 10^{-6} cm^2 s^{-1} in graphite)[5] allowing for higher power demands.[6] In the 1970s the first primary cells based upon Li had been assembled, whilst in the same period it had been shown that inorganic compounds could reversibly react with alkali metals. In 1972, Exxon commercially developed M. Stanley-Whittingham's work on rechargeable lithium metal batteries using TiS_2 as the cathode, Li-metal as the anode and a Li-perchlorate electrolyte.[3] Dendritic growth of the Li-metal led to explosion hazards, and a Li-Al alloy was utilised instead with poorer cyclability.

To combat the safety issues with Li in its metallic form, the focus was turned to so called "rocking-chair" batteries which had been demonstrated by Lazarri *et al.*[7] In 1980 John B. Goodenough made a seminal discovery, developing a cathode material that is still used today of $LiCoO_2$.[8] Akira Yoshino paired this cathode with a hard carbon anode in 1987. This paved the way for Sony Corporation in 1991 to release the C/$LiCoO_2$ rechargeable LIB, which is still the basis for the commercial technology which is used today with graphite having replaced hard carbon thanks to electrolyte adjustments. Goodenough, Stanley-Whittingham and Yoshino were jointly awarded the Nobel Prize in Chemistry in 2019 for the development of LIBs.

2.2 Electrochemistry of lithium-ion batteries

A basic battery contains one or many identical cells with each cell storing electrical power as chemical energy in two electrodes which are separated by an electrolyte.[9] The LIB rechargeable batteries of today consist of two electrodes, an anode and a cathode which are immersed in an electrolyte and separated by a polymer membrane as shown in Figure

2.1. The anode and the cathode must be capable of Li^+ ion insertion/de-insertion or alloying/de-alloying, whilst the electrolyte is a Li-salt containing a mixture of liquid organic solvents to ensure the rapid transfer of Li^+ ions within the cell.[10] The separator acts as an electronic insulator but as an ionic conductor and prevents direct electronic contact between the two electrodes which would result in a shorted cell.

In reference to electrochemical cells, the anode is taken as the negative electrode whilst the cathode is taken as the positive electrode during the charging process regardless that the roles of each reverse depending on whether the cell is charging/discharging. During charging of the LIB, reduction takes place at the anode as it accommodates electrons from the cathode which flow through the external circuit of the battery. The Li^+ ions migrate through the electrolyte from the cathode to the anode to balance the charge and this is a process known as intercalation/alloying. During the discharge process, the anode is oxidised and the Li^+ ions diffuse out of the active anode material to the cathode to again restore charge balance (see Figure 2.1). For testing purposes, a half-cell may also be assembled in which the anode is replaced by lithium metal as reference, and the working electrode is placed in the position of the cathode allowing electrochemical tests to be carried out in which an excess of lithium is available.

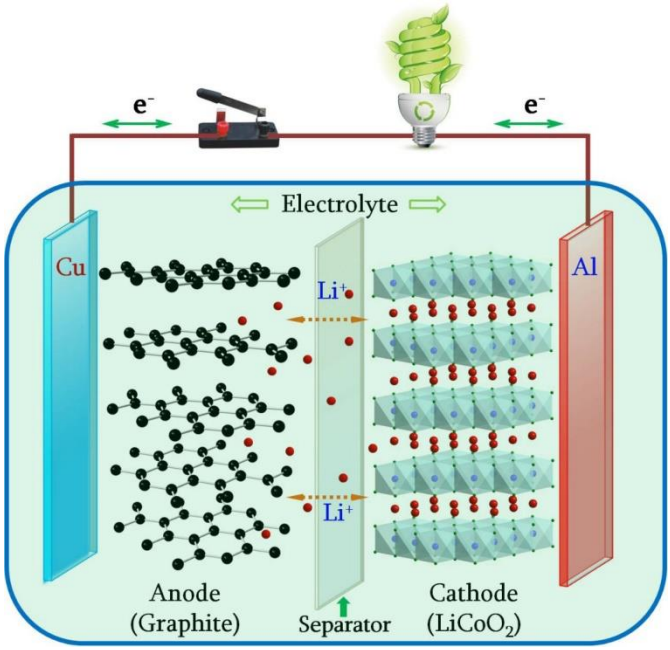

Figure 2.1: Schematic of the configuration of common rechargeable LIB with the intercalation/de-intercalation mechanism. This mechanism is the same when replacing the Li-ion with the Na-ion in sodium ion batteries. Reproduced and adapted with permission from Ref[11].

The choice of electrodes depends upon their electrochemical potential values as well as their positions relative to the HOMO(highest occupied molecular orbital)-LUMO(lowest unoccupied molecular orbital) energy gap of the electrolyte.[12] The electrochemical potential of the anode must be lower in energy than the LUMO of the electrolyte to prevent the reduction of the electrolyte. On the other hand, the electrochemical potential of the cathode should be greater than the energy of the HOMO to inhibit the oxidation of the electrolyte. During the first charge-discharge process an irreversible loss in capacity occurs due to the formation of the SEI (solid electrolyte interphase) layer which occurs due to the reaction between the electrolyte and electrode material which is necessary to prevent solvent intercalation and guarantees freedom of movement for the Li^+ ions,[12,13] and this is expanded upon in Section 2.4. The electrochemical mechanism present in today's batteries is known as a "rocking–chair" cell as both the anode and cathode are hosts for the reversible insertion/removal of the working ion into/from the electrolyte.[14] In the conventional first-generation LIB depicted in Figure 2.1, graphite is used as the anode whilst layered $LiCoO_2$ is the cathode material, producing the following reactions:[12,15]

$$\text{Cathode: } LiCoO_2 \leftrightarrow Li_{1-x}CoO_2 + xLi^+ + xe^- \tag{2.1}$$

$$\text{Anode: } 6C(graphite) + xLi^+ + xe^- \leftrightarrow xLiC_6 \tag{2.2}$$

2.3 Lithium-Ion Battery Anode Materials

Currently, the most commonly used anode materials[16] are those based on carbon (as referred to previously with graphite). For an active material to be considered a suitable candidate for LIBs, it should display reversible capacity, good ionic and electrical conductivity, long cycle life, high rate of lithium diffusion into the active material and low-cost/eco-compatibility.[17] The battery behaviour is not only dependent on the inherent properties of the material (physical/chemical) but also is highly dependent on the crystallinity/amorphous structure of the anode material as well as the shape, size and component state.[13] It follows thus that the architectural arrangement/structural design of the material is of equal if not greater importance than the material composition itself. As discussed, LIB technology was initially developed with a lithium-metal anode.

Lithium metal anodes

Li-metal is the ideal candidate for the anode material of a LIB, with a theoretical capacity of 3860 mA h g^{-1} (the method to calculate the theoretical capacity of a material is demonstrated in Section 3.1), a low density of 0.543 g cm^{-3} and the lowest negative electrochemical potential (-3.040 V vs standard hydrogen electrode).[18] With a theoretical capacity roughly 10 times greater than graphite, one may ask why Li-metal anodes have not yet been commercialised. There are two main barriers to the use of Li-metal; 1) the growth of Li dendrites during repeated charge/discharge processes and 2) the low coulombic efficiency (CE) (ratio of charge put in to charge released) associated with these processes. Dendrite formation presents a safety hazard within the LIB due to internal short circuiting, whilst the low CE leads to short cycle life.[19] With the same motivations that are the foundation of this PhD fellowship, a renewed interest has been expressed in Li-metal as an anode material due to the limitations of the carbon anode. Extensive studies have taken place on the Li-dendrite formation, with the focus being improving the stability of the SEI layer on the Li surface by adjustments to the electrolyte. Qian *et al.*[18] reported electrolytes composed of ether solvents and lithium bis(flurosulfonyl)imide salt enabling a CE of 99.1% without dendrite formation. However, the high concentration of electrolyte needed in this study (4 M) and the ever-rising cost of lithium question the feasibility of this method to be commercialised, whilst 99.1% efficiency is still problematic when cells are meant to function for many cycles. This study also doesn't answer the infinite volume issue associated with Li-metal where through subsequent cycles all the Li is stripped from the anode and intercalated into the cathode.[20] Recent work by the group of Ying Shirley Meng from the University of Chicago has highlighted how the porosity of the Li surface plays an important role in minimising this corrosion of the Li anode. [21]

Carbon-based anodes

Graphite anodes were the breakthrough in realising the lithium-ion "rocking chair" battery and gave rise to the commercial development of the LIB in 1991.[14] Graphite displays many favourable features for LIB, such as excellent electronic conductivity, a layered structure for Li-ion intercalation, good cyclability, low working potential and low cost. In the graphite structure, the carbon atoms arrange themselves into 6-membered sp^2 hybridized rings forming 2-dimensional sheets known as graphene. These sheets stack on

top of each other in an ABAB (i.e. hexagonal close packed (hcp)) stacking arrangement, bonded by Van der Waals forces to form the bulk material known as graphite. This layered structural arrangement allows the Li-ions to diffuse into the graphite, according to Equation 2.2. However, graphite allows the intercalation of only one Li-ion with six carbon-atoms resulting in the formation of LiC_6 with a maximum reversible capacity of 372 mAh g^{-1}.[17,22–24] Also the low potential at which lithium intercalation occurs in graphite increases the risk of lithium plating and dendrite formation which is detrimental to performance and safety.[25–27] Thus, there is a focus to develop anode materials which exceed the capacity of graphite.

Metal Oxides

To overcome the relatively low theoretical capacity of graphite and other intercalation anodes, alloy anodes have been proposed due to their high specific capacity and safety characteristics.[28,29] The general alloying mechanism is shown below:

$$xLi^+ + M + xe^- \leftrightarrow Li_xM \tag{2.3}$$

The most promising alloy materials have so far proven to be tin (Sn), silicon (Si), germanium (Ge), arsenic (As) and lead (Pb). When one considers natural abundance and toxicity, Sn and Si prove to be the most attractive options for future development.

The main challenge however for the implementation of alloy anodes is their large volumetric change during lithium insertion/extraction which often leads to poor cycling performance and the destruction of the active material. Metallic Sn was considered as a candidate for LIBs anodes due to its theoretical capacity of 994 mAh g^{-1}.[30] However, it was not a feasible material, due to the huge volume expansion of 360% caused by the Li-Sn alloying process.[31] Metal oxides (MOs) were proposed in an attempt to reduce the detrimental effects of the large volume change associated with alloy anodes. During the initial lithiation of the active material, an inactive-matrix composite of lithium oxide (Li_2O) is formed which plays a role of accommodating the volumetric expansion of the active component during subsequent charge/discharge cycles.[32] Li_2O is deemed inactive as it is electrically insulating, whilst also presenting an ionic conductivity of 10^{-12} S/cm allowing Li-ion movement at room temperature.[33] In addition to buffering the large

volumetric expansion, it also provides an ion conducting matrix ensuring the full potential of the active material is realised.[34] This conversion reaction is reversible in some (Co, Ni, Fe, Cu) transition metal oxides (TMOs) in which the transition metal does not alloy with lithium, instead creating a metallic network which enables good electrical conductivity allowing for the reversible reformation of Li_2O.[35,36] Thus, it was elected to investigate tin(II) oxide (SnO) as a potential anode material for LIBs as it is a MO material that is not widely studied as a LIB anode.

SnO properties

SnO is a *p*-type semiconductor (band gap 2.5 – 3 eV) which exists in the stable blue-black form ("*α-tin (II) oxide*").[37] This stable blue-black form of SnO assumes a layered tetragonal structure (litharge) with a P4/*nmm* space group (Figure 2.2) containing asymmetric four coordinate Sn sites and is the only example of a regular square-pyramidal tin(II) coordination.[38] It is found in nature as the mineral romarchite. Computational studies carried out by Aron Walsh and Graeme W. Watson of the School of Chemistry, Trinity College Dublin strengthened the understanding of the asymmetric structure using density functional theory. Their research[39] revealed that the asymmetric structure was not due to a lone pair of electrons ascribed to the $5s^2$ of Sn as had long been accepted,[38,40] but rather the coupling of the unfilled Sn (5p) with the antibonding combination arising from interaction the of Sn (5s) and O (2p). The resulting layered structure has a sizeable interlayer spacing (c = 4.85 Å) which is attractive for the alloying mechanism available in ion-batteries as it provides faster diffusion channels as well as moderating the volume changes associated with charge storage.[41] SnO is much less studied and utilised as a material due to its quick oxidation to tin(IV) oxide which is an *n*-type semiconductor.

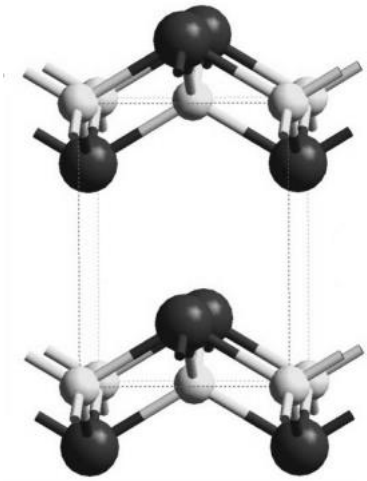

Figure 2.2: Layered structure of SnO with Sn atoms in dark grey colour and O atoms in light grey. Used with permission from Ref.[39].

SnO as an anode material

SnO is an outstandingly attractive LIB anode candidate due to its abundance, environmental benignity and high theoretical capacity.[42] As discussed, the adopted approach used is to prepare a composite structure of an active component in an inactive matrix, where the inactive matrix accommodates the volume expansion due to the lithiation process of the active component. Lithiation of SnO results in an inactive Li_2O phase with an active Sn phase (Equation 2.4).

$$SnO + 2Li^+ + 2e^- \rightarrow Sn + Li_2O \quad (2.4)$$

$$Sn + 4.4Li^+ + 4.4e^- \rightarrow Li_{4.4}Sn \quad (2.5)$$

This conversion reaction is considered irreversible and is attributed to the initial capacity loss after the initial formation cycles. The Li_2O accommodates the volume expansion of the alloying Li and Sn reaction, thus improving cyclability whilst still maintaining a relatively high theoretical capacity for the composite of 875 mAh g^{-1} with the full lithiation of Sn to form $Li_{22}Sn_5$ (Equation 2.5).[22,43] A drawback of this approach however is that the inactive host may operate as a diffusion barrier and limit electron transfer resulting in a lower than expected capacity.[28] Recent reports however have indicated through the reduction of the dimensions of the active material, the reversibility of the Li_2O reaction

may be enhanced.[22,44–46] If this capacity is considered, the total gravimetric capacity of the anode would rise to 1,273 mAh g^{-1}.

In relation to tin oxide compounds, tin(IV) oxide (SnO_2) is much more prevalent in the ion-battery research field[45,47–50] due to its thermodynamic stability.[36] However, the theoretical capacity of SnO_2 is 783 mAh g^{-1} leading to an increased interest to focus studies on the tin(II) state. SnO structures such as nanoflowers,[43] platelets,[51] nanobranches,[52] dendrites[53] and discs[54] have been synthesised to date with nanostructured morphologies being favoured with respect to usage in LIBs in order to obtain high-performance electrodes as discussed in Section 2.6. Compared with their fully crystalline counterparts, SnO nanocrystals offer shortened path lengths for electronic transport and higher electrode active specific areas, which can result in higher capacities and better charge/discharge rate capabilities.[43]

2.4 Solid Electrolyte Interphase

As was briefly touched upon in Section 2.2, the SEI is an integral part of the stability of a rechargeable ion-battery. The SEI layer is formed by precipitates from the reduced decomposition of solvents, salts, ions, and impurities all present in the electrolyte.[55] It mostly forms during the first charge due to the instability of the electrolyte at the operating potential of the anode, but formation will continuously occur until a complete SEI film is formed which in turn increases the electronic resistance on the anode which shifts the surface potential to within the stability window of the electrolyte. An optimized and stable SEI layer is expected to have negligible electrical conductivity to prevent continuous reduction of the electrolyte whilst having high ionic conductivity/permeability to allow for the operation of ion storage in the anode. Figure 2.3a shows the energetics of formation of the SEI. μ_A and μ_C are the electrochemical potentials of the anode and cathode respectively, while the stability window of the electrolyte (E_g) is the difference between the energy of the HOMO and LUMO. If μ_A is above the LUMO, then it will reduce the electrolyte and similarly if μ_C is below the HOMO it will oxidise the electrolyte (SEI effects on the cathode are not as severe as with the anode). The electrolytes widely used are composed of carbonates which have a reduction potential of roughly 1 V vs Li/Li^+ and are decomposed by an anode that operates below this threshold.[56,57] The alloying reactions of Sn with Li occur under 0.6 V vs Li/Li^+, thus SEI formation is inevitable with

a SnO anode.[22,58,59] SEI stability and formation are of key importance when dealing with alloy anodes such as SnO in which the huge volumetric change causes an unstable SEI to form which can become fractured upon repeated cycling and lead to further lithium consumption from the electrolyte which leads to capacity fade. Thus a dense and flexible SEI in which the molecular forces between it and the anode are strong[55] is a prerequisite for long battery lifetime and capacity retention. The SEI is mainly composed of inorganic reduction products such as LiF, Li_2O and Li_2CO_3 on the anode side for 2 - 10 nm,[60] and loosely packed organic/inorganic species such as lithium alkyl carbonate ($ROCO_2Li$) on the electrolyte side with a thickness in the range of 10 - 100 nm as shown in Figure 2.3b. It is of key importance that ion-batteries are produced under anhydrous conditions as even trace amounts of water in the cell can lead to the production of HF which readily dissolves the SEI.

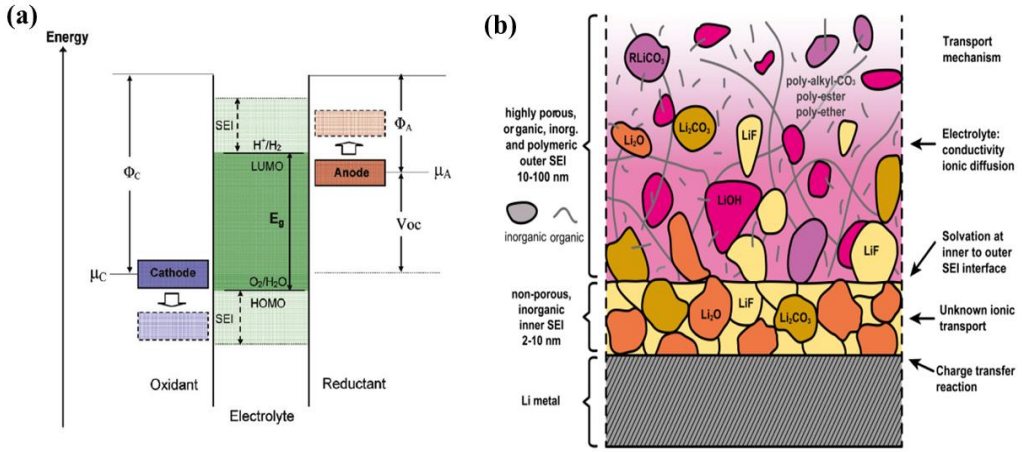

Figure 2.3: (a) Energetics of the formation of SEI layers on anode and cathode of ion-battery.[57] Φ_A and Φ_C are the anode and cathode work functions. *Eg* is the window of the electrolyte for thermodynamic stability. A μ_A > LUMO and/or a μ_C < HOMO requires kinetic stability by the formation of an SEI layer. Reprinted (adapted) with permission from {Goodenough, J. B.; Kim, Y. Chemistry of Materials 2010, 22, 587)}. Copyright {2010} American Chemical Society." (b) Schematic depiction of the composition of the SEI. Reprinted (adapted) with permission from Ref [60].

2.5 Electrolyte

The ability to conduct Li^+ ions is the main function of the electrolyte in the LIB.[10] The electrolyte is considered an inactive material, however, its effect on the chemical nature and the morphology of the SEI has a major influence on cyclability, power capability and safety performance of the battery. There are many choices for electrolyte such as ceramic solid electrolytes (e.g. sulfides),[61] polymeric electrolytes (e.g. poly(ethylene oxide)[57,61,62] and liquid aqueous electrolytes (lithium nitrate/sulphate)[62], however, the majority of electrolytes used in commercial LIBs, as well as scientific research, are liquid organic

solvent-based electrolytes.[57,62–64] This is composed of a Li salt such as $LiPF_6$ dissolved in an aprotic solvent such as ethylene carbonate (EC). This combination of $LiPF_6$ and EC was used in the initial graphite anode LIB as it formed a stable SEI and prevented the exfoliation of graphite that was caused by the previous electrolyte of propylene carbonate (PC).[65] It remains the electrolyte of choice today, with the only variation being the addition of alternative linear alkyl carbonates such as dimethyl carbonate (DMC), diethyl carbonate (DEC) or ethyl methyl carbonate (EMC).

2.6 Nanomaterials

As discussed, the commercial LIBs of today are limited with respect to their power output due to the diffusion rate of the lithium-ion into the intercalation host (graphite). An increase in the charge/discharge rate of more than one order of magnitude is required to meet the needs for future energy storage in EVs and renewable energy. The U.S Department of Energy has recognised this as a crucial target for battery development offering funding through its extreme fast charge (XFC) project with a goal to obtain a battery with a charge time of less than 10 minutes capable of storing at least 180 Wh kg^{-1}, with a capacity retention exceeding 80% over 500 cycles.[66]

Nanomaterials, often overhyped by exaggerated claims of ground-breaking properties have genuine potential in this case to meet and exceed expectations and have a significant impact on the LIBs of the future.[67] Their reduced dimensions significantly increase the rate of lithium-ion insertion/removal which overcomes the intrinsic diffusivity (D) of the Li-ion. This results in a decreased charge/discharge time as the characteristic time (t) of diffusion given as:

$$t = \frac{L^2}{D} \tag{2.6}$$

The time for intercalation decreases with the square of the particle size (L), highlighting the need to transition to the nanoscale for electrode materials. Other advantages obtainable at the nanoscale are higher surface areas permitting greater contact between the electrode and electrolyte resulting in increased lithium-ion flux across the interface. Nanomaterials also exhibit better accommodation of the strain caused by the volume expansion of intercalation/alloying, which in turn would increase the cyclability/battery life. It has been

reported that reducing the particle size to the nanometre range (<100 nm) can significantly improve the cycling performance of alloy anodes in numerous cases[22,28] with Yang *et al.* finding that reduction of SnSb powder from 3 μm to 300 nm increased the number of stable cycles from 3-70 cycles.[28,68]

Concerns remain however regarding the cost-effectiveness on a large industrial scale.[17] An additional drawback one must be aware of whilst transitioning to smaller dimensions and in turn, larger surface areas is the additional area which now must be covered in SEI, reducing the lithium inventory in the cell. Finally, due to the decreased density from their bulk counterpart, nanomaterials offer lower volumetric energy densities.[36] Thus, a happy medium should be found to obtain adequate power and energy densities by tailoring the morphology and dimensions of the selected material.

2.7 Cathode Materials

Due to the "rocking-chair" nature of the LIB where ions are shuttled between anode and cathode for each charge-discharge cycle, an intercalation cathode host is needed to support this mechanism. Cathodes may be manufactured from transition metal chalcogenides (TMCs), TMOs and polyanion compounds. Cathode materials are commonly TMOs which have layered, spinel or olivine crystal structures in which the metal cations display four- and/or sixfold coordination with oxygen anions in which Li ions may intercalate.[69] Currently, most intercalation cathode research is focused on TMOs and polyanion compounds due to their high operating voltage and the resulting higher energy storage capability.[70] $LiCoO_2$ remains the most popular cathode in LIB technology today.

Transition Metal Oxides

$LiCoO_2$ (LCO) was developed by John Goodenough and was the first and most successful commercialised cathode which was used in the initial SONY LIB. The Co and Li are located in octahedral sites in alternating layers of the material and form a hexagonal symmetry (Figure 2.4). LCO exhibited a high theoretical capacity of 274 mAh g^{-1}, a high volumetric capacity of 1363 mAh cm^{-3} whilst also maintaining good cycling performance.[70] Research however is focused on reducing the LIB markets reliance on the LCO cathode due to the high costs of Co and the unsafe/unethical mining practices which

accompany it. The Lithium Nickel Manganese Cobalt Oxide (NMC) cathode is another commercially available cathode which is widely used in the market. Its popularity has grown due to its similar theoretical specific capacity of 280 mAh g^{-1} with LCO and similar operating voltage while cheaper to produce as the Co content is reduced ($LiNi_{0.33}Co_{0.33}Mn_{0.33}O_2$).[71] NMC performance is attributed to the combination of Nickel (known for high specific capacity but poor stability) and Manganese (which forms a spinel structure achieving low internal resistance but offers low specific capacity), with each individual elements weaknesses with respect to battery performance masked by the other.

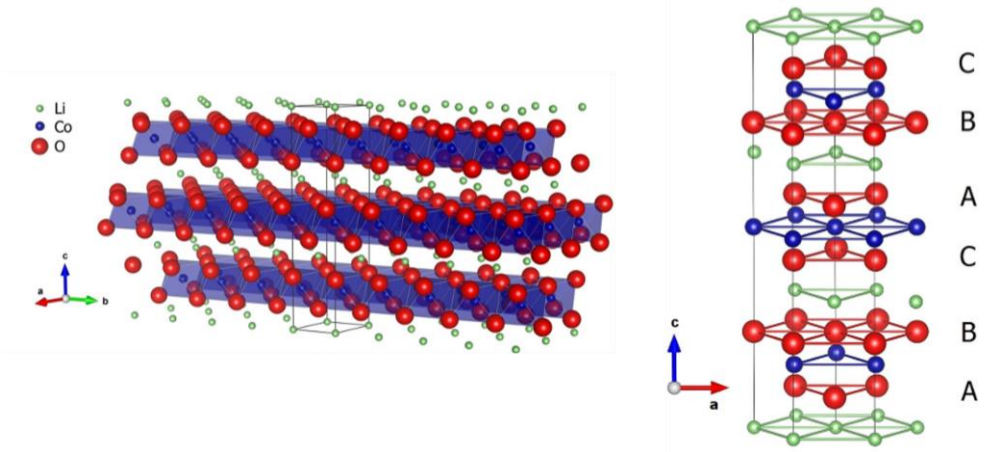

Figure 2.4: Layered crystalline structure of $LiCoO_2$ along with stacking arrangement of layers (ABCABC). Adapted with permission from Ref.[72].

2.8 Carbon Nanotubes for batteries

Carbon Nanotubes (CNTs) are polymeric cylindrical structures consisting of layers of graphene with open/closed ends.[73] They are a relatively new polymer, discovered by Sumio Iijima in 1991 in the soot produced in the arc-discharge of fullerenes.[73,74] Single-walled CNTs (SWCNTs) consist of a single graphene sheet wrapped into a cylindrical tube whilst multi-walled CNTs (MWCNTs) comprise an array of SWCNTs that are concentrically nested like rings of a tree trunk.[75] SWCNTs may be either metallic or semiconducting depending upon the orientation about which the graphene sheet is rolled.[75] This orientation is denoted by two integers (*n*,*m*) that combine with two basis vectors (a_1, a_2) to form the chiral vector, *C* as shown in Figure 2.5a. The nanotube is said to have an armchair configuration if $n = m$ (Figure 2.5d), a zig-zag configuration if $n = 0$ or $m = 0$ (Figure 2.5b), and a chiral configuration for any other n / m combination (Figure 2.5c).[76] All armchair SWCNTs are metallic, zig-zag SWCNTs are only metallic when *n*

or *m* is a multiple of 3, whilst all other SWCNTs are semiconductors with the band gap dependent upon the difference between *n* and *m*.[77]

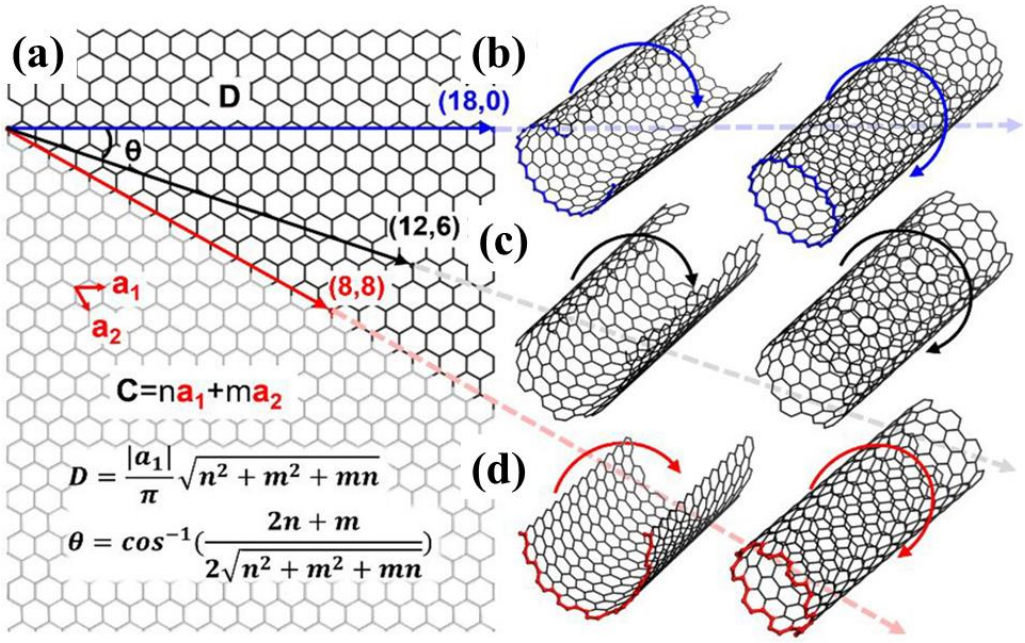

Figure 2.5: (a) Chirality of SWCNTs with basis vectors a_1 and a_2, along with the chiral angle θ and tube diameter D as functions of the chiral indexes (n, m). (b) Zig-zag configuration SWCNT. (c) Chiral SWCNT. (d) Armchair SWCNT. Reprinted (adapted) with permission from Ref.[76]. Copyright {2021} American Chemical Society.

Although not suited for battery applications, the incorporation of CNTs as a conductive additive at a lower weight loading than conventional carbon additives (carbon black/graphite) presents a more effective strategy to establish an effective electrical percolation network.[78] SWCNTs have excellent electrical properties, with a carrier mobility of ~10,000 $cm^2\ V^{-1}\ s^{-1}$, a room temperature conductivity in excess of 5×10^5 S m^{-1} and the capability to carry an electrical current density of $\sim 4 \times 10^9$ A cm^{-2}.[79] The high ratio of the SWCNTs length to diameter allows for lower weight doping fractions to achieve the same percolation threshold as other additives. SWCNTs also display exceptional mechanical properties which in addition to the electrochemical benefits provide improved stability during charge-discharge cycles in the active material and prevent cracking. SWCNTs have a Young's modulus[80] of 0.64 TPa and a tensile strength of ~37 GPa which it is hypothesised will act as reinforcement in the SnO to prevent cracking and disintegration of the electrode. The effectiveness of SWCNTs at maintaining structure integrity has been demonstrated with V_2O_5 cathodes, with a 5% mass loading also resulting in an excellent rate capability.[81] Due to the nature of the π-orbital overlap in chiral SWCNTs, electron conduction can occur via ballistic transport which in turn

improves battery performance at higher C-rates.[75,78,82] SWCNTs further improve battery performance by removing the need to incorporate a polymer binder in the slurry/film composite material which reduces capacity whilst also failing at higher temperatures, and the removal of the need for the inactive copper foil which decreases the usable capacity.

CNTs may be produced by 3 methods; 1) electric arc-discharge of graphite rods; 2) laser ablation of carbon and 3) chemical vapour deposition. Commercially produced SWCNTs will be utilised within this project, sourced from two manufacturers: Carbon Solutions Incorporated (CSI) and OCSiAl.

P3-SWCNTs

P3-SWCNTs from CSI are synthesised by the electric arc discharge method and purified with nitric acid. This method produces a ratio of semiconducting to metallic SWCNTs of 2 to 1, with a bundle length of ~1 μm and a bundle diameter of ~5 nm. P3-SWCNTs have been functionalised with carboxylic groups, making the material dispersible in solvents and more compatible with further chemical processing such as composite applications.[83]

Tuball

Tuball SWCNTs are produced by OCSiAl, the largest manufacturer of SWCNTs on the market. In addition, these are also the cheapest SWCNTs on the market (€70/kg at the time of writing). Their synthesis is protected by patents and thus not available to disseminate here. With this best price-to-performance ratio, Tuball SWCNTs provide a feasible cost-effective product for the implementation of CNTs in commercial applications. Due to their cheaper cost and upscaled production, Tuball SWCNTs have metal impurities of $<15\%$, with a CNT content of $\geq 80\%$. The SWCNTs have a diameter of 1.6(4) nm and a length greater than 5 μm.[84]

2.9 Sodium-Ion Batteries

As one might expect sodium behaves very similarly to lithium, both being alkali metals with Na directly below Li in Group 1 of the Periodic table. As a consequence, understanding and development of Na-ion batteries (NIBs) were directly available from the decades of work gone into the development of LIBs. NIBs undergo intercalation charge storing mechanisms with all the detailed features outlined in Section 2.2 applicable

to NIBs. Furthermore, alloy-based electrodes may also be employed in NIBs, with the same advantages and disadvantages as experienced for LIBs: large gravimetric capacity accompanied by the trade-off of a large volumetric change which leads to the pulverization of the active material along with the severing of the electrical network within the material. The standard reduction potential of Na^+/Na is -2.71 V versus a standard hydrogen electrode which is 330 mV greater than that of the Li^+/Li couple.[85] An important difference one must note is the greater ionic radius of the Na^+ ion (1.02 Å) in comparison to that of Li^+(0.73 Å).[86] This larger radius thus exerts a greater strain on the volume and internal structure of the host during the intercalation process in comparison to a lithium counterpart, while also impeding the rate of Na^+ storage due to sluggish kinetics.[87]

The urge to move from LIB technology to NIB technology is driven by the abundance of sodium and its equal distribution throughout the globe. The vast difference in the abundance of lithium and sodium can be seen in Figure 2.6a. In addition, lithium resources are distributed unequally around the planet (mainly concentrated in South America as shown in Figure 2.6b). As the demand for these resources rises as LIB technology becomes more widespread in energy storage and vehicle applications the price of this valuable commodity will continue to increase as it has been consistently during the 21st century. A comprehensive lithium supply forecast by Greim *et al.*[88] shows that society will face lithium shortages within the next century unless major improvements are made in the recycling of material and developing alternative batteries i.e. NIBs. Lithium prices are at all-time highs in excess of $40,000 per ton at the time of writing.[89] In contrast to this outlook, sodium resources are distributed equally, are abundant (Na is the 5th most abundant element in the crust), are low cost and when one considers the levels of Na in the oceans it can be deemed infinite. Na metal was produced first via the '*Castner process*' which involves the electrolysis of molten sodium hydroxide and then refined via the '*Downs process*' which utilises sodium chloride instead.[90] These processes of course may derive their power consumption from renewable energy sources ensuring green sodium production.[91–93] A further benefit of sodium metal production is that it may react with water to produce hydrogen gas needed for fuel cell electric vehicles, eliminating the need to store dangerous hydrogen gas.[94] Furthermore the production of hydrogen from sodium leaves a waste product of sodium hydroxide which may be fed back into the initial reaction to recover sodium or bubbled through with air to trap CO_2 thus ensuring a closed clean energy cycle in all cases.[92]

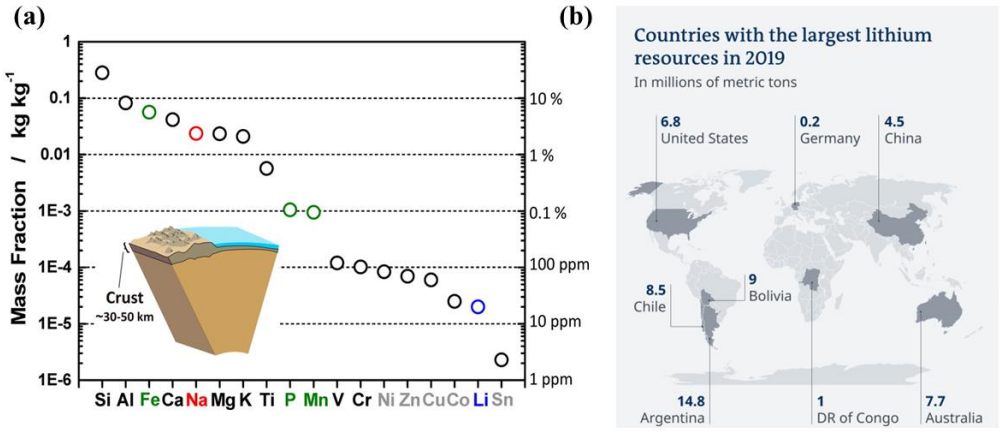

Figure 2.6: (a) Abundance of elements in the earth's crust. Reprinted and adapted with permission from Ref.[86]. Copyright 2014 American Chemical Society. (b) Countries with the largest lithium resources. Reprinted and adapted with permission from Ref.[95].

Development of NIBs is not aimed at replacing LIBs, but more so at reducing the reliance on Li. A particular area of interest for NIBs is large scale energy storage where cost and cycle-life are more critical factors than energy density and this is where NIB technology can thrive.[96,97] With plans from the EU to prohibit the sales of petrol/diesel vehicles by 2035 and the UK by 2030, this will unavoidably lead to an increased demand for LIB technology which is the most widespread in electric vehicles. This demand has been forecasted to lead to shortages as mentioned unless NIBs have been optimised to reduce the need for LIBs in large scale renewable energy storage, so LIBs may be focused on more energy density requiring technology. In battery technology, the emphasis must be placed on simultaneously developing and optimising multiple battery types, be it LIB/NIB or even calcium/potassium ion batteries so that there are different technologies to meet different demands.

2.10 Sodium-Ion Battery Anode Materials

Sodium metal provides the highest theoretical capacity of (1166 mAh g^{-1}) of potential anodes for NIBs, however, safety concerns prevent this setup from being commercialised. The low melting point of sodium metal (98° C), the dendrite formation on discharge cycles leading to internal shorting and the reactivity of metallic sodium with organic solvents used in electrolytes all pose unreasonable safety hazards.[98] Unfortunately, a rare dissimilarity between NIBs and LIBs is the use of graphite as an anode material. As discussed, the use of graphite as a negative electrode in LIBs was a seminal discovery allowing the technology to be rapidly commercialised. Graphite, however, is less

electrochemically active with Na, with the electrochemical insertion resulting in the formation of NaC_{64} with a low capacity of 35 mAh g^{-1}.[99,100] This large drop-off between the intercalation of lithium and sodium was initially thought to be due to the larger size of the sodium atom, however quantum mechanical methods by Herold *et al.*[101], Wang *et al.*[102] and Yoon *et al.*[103] have revealed that the low uptake of sodium in graphite is due to the thermodynamics of the competition between the first ionization energy of sodium and the enthalpy of ion-substrate bonding. The anode material of choice for NIBs is hard carbons. Hard carbons are prepared by high temperature carbonization of solid phase organic and polymer precursors,[85] resulting in a complex microstructure of graphene-like parallel layers embedded in a microporous amorphous phase. The Na-ions first insert between parallel graphene sheets (interplane distance must be greater than 3.7 Å)[104] whilst later occupying the pores of the amorphous structure. Hard carbon offers a capacity of 300 mAh g^{-1}, however much of the capacity occurs at low potentials which again leads to a safety risk due to metallic sodium plating.[105,106]

SnO as an anode material for NIBs

SnO is attractive for NIBs for the same reason it is attractive for LIBs; high theoretical capacity, layered structure, environmentally safe and abundant. The nature of the alloying reaction results in a huge volumetric change (in excess of 420%),[107,108] however through nanostructuring of the active component, the formation of a sodium oxide buffer matrix and the implementation of carbon nanotubes for structural and electrical enhancements it is hoped this change may be mitigated. Sn has a theoretical capacity of 847 mAh g^{-1} when alloying with sodium as in Equation 2.7 to form $Na_{3.75}Sn$ (the complete alloy formed is $Na_{15}Sn_4$).[107] When one accounts for the further capacity available through the conversion reaction to form sodium oxide (Equation 2.8) the total theoretical capacity rises to a figure of 1,144 mAh g^{-1} for the initial cycle, although the sodium oxide formation is considered irreversible after.[41,109,110] The theoretical reversible capacity thus is 746 mAh g^{-1} when one considers that the sodium oxide formation is not fully reversible.

$$Sn + 3.75Na^+ + 3.75e^- \rightarrow Na_{3.75}Sn \quad (2.7)$$

$$SnO + 2Na^+ + 2e^- \rightarrow Na_2O + Sn \quad (2.8)$$

Electrolyte for NIBs

Considerations regarding electrolytes are the same as discussed previously in Section 2.5 with the majority of NIBs using sodium salts such as $NaClO_4$ or $NaPF_6$ dissolved in carbonated organic solvents like EC, DMC or DEC.[111] However, due to the higher redox potential of Na, the reduction of carbonate-based electrolytes result in an SEI of different compositions and thus different performances.[112,113] Electrolytes using 'glymes' ([R-$(OCH_2CH_2)_n$-OR]) as solvents have been recently explored in NIBs to improve SEI engineering. Seh *et al.* studied the plating and stripping of Na and showed that combining 1M $NaPF_6$ with diglyme resulted in high reversibility which was related to the formation of a stable SEI.[114]

2.11 Supercapacitors

In terms of specific energy/power, supercapacitors (also known as electrochemical capacitors) bridge the gap between fuel-cells/batteries (which have large energy densities but low power densities) to conventional capacitors as shown in the Ragone plot in Figure 2.7a.[115] It is this combination of relatively high energy and power densities that has sparked so much interest in these devices. With the ever increasing implementation of intermittent, renewable energy conversion systems like wind turbines and solar panels, energy storage devices now must accommodate temporal fluctuations that range from seconds to hours.[116] This demand for both high power and high energy storage is one of the most prominent priorities of energy research today with improvements still needed in current supercapacitor technology to meet this ever-growing demand.

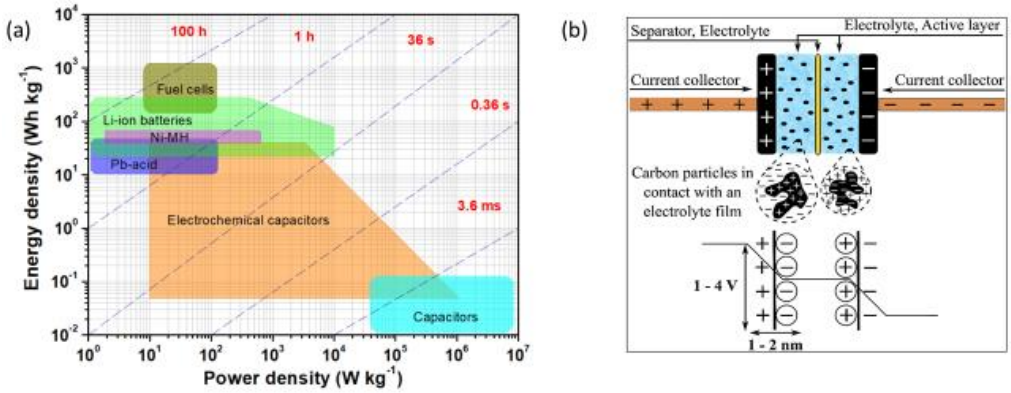

Figure 2.7: (a) Ragone Plot of different types of electrochemical energy storage devices and (b) Scheme of an electric double layer capacitor with the voltage drop at the electrode/electrolyte interface. Adapted from Ref.[115].

Supercapacitors (SC) store energy through the formation of an electrical double-layer (EDL) also known as a Helmholtz layer (Figure 2.7b) formed at the solid:electrolyte interface and through pseudocapacitance. A Helmholtz layer occurs after a voltage is applied to a SC and subsequently, the positive/negative ions accumulate at the electrodes of opposite polarity. One layer of charge remains in the surface structure of the electrode whilst the other consisting of ions of the opposite charge remains in the solution separated by a monolayer of solvent molecules. These solvent molecules separate the oppositely charged ions, and the charge/discharge process is equivalent to the dielectric behaviour of conventional capacitors as there is no faradaic reaction occurring during the energy storage process.[117] The capacitance (C_{dl}) is thus equivalent to that for conventional capacitors, and thus benefits from materials with large surface areas (A), whilst one must remember that the distance (d) is the average thickness of the double layer ($d = 1 – 2$ nm, depending on concentration, temperature and nature of electrolyte).[115] This is known as the Helmholtz-Perrin (HP) model as shown in Equation 2.9 where ε_r is the local relative permittivity of the double-layer and ε_0 is the electric vacuum permittivity. Further advancements have been made to the theoretical understanding of the electrical double layer with the Guoy-Chapman (GC) model which accounts for a diffuse layer that is affected by thermal energy according to the Maxwell-Boltzmann distribution, the Stern model which combines the HP and GC models in series (Appendix A, Equation A.4, A.5), and the Bockris/Devantham/Mullen (BDM) model which accounts for the dipolar properties of water. It must be noted however that in the case of supercapacitors, in which concentrated electrolytes are used (e.g., 0.1 M ≥) the capacitance is dictated by the HP layer.[115,118]

$$C_{dl} = \frac{\varepsilon_r \varepsilon_0 A}{d} \tag{2.9}$$

The total energy (E) stored in a capacitor may be calculated using Equation 2.10 where V refers to the voltage window of the capacitor.

$$E = \frac{CV^2}{2} \tag{2.10}$$

Pseudocapacitance

Pseudocapacitance occurs when energy is stored through fast and reversible faradic reactions at the electrode surface. Some ions may pervade the double layer and come in direct contact with the electrode material. When this occurs three types of pseudocapacitance may occur:

1. Underpotential Deposition: This occurs when hydrogen/metal ions in solution form an adsorbed monolayer on the electrode at a potential that is above their standard reduction potential.[119] Examples are:

$$Au + xPb^{2+} + 2xe^{-} \rightarrow Au.xPb_{ads} \quad (2.11)$$

$$Pt + xH^{+} + xe^{-} \rightarrow Pt.xH_{ads} \quad (2.12)$$

2. Redox Pseudocapacitance: The ion is adsorbed on the surface and a reversible redox reaction takes place, with no chemical reaction taking place. This is present in TMO-based SCs, a classic example of this being the oxidation-reduction of the Ru(III)/Ru(IV) redox couple present in hydrated RuO_2.

3. Intercalation Pseudocapacitance: Similar to the case described for LIBs, the ion intercalates in the layers of the redox-active electrode material without any changes to the structure of the electrode. This occurs when Li^+ intercalates in Nb_2O_5 SCs.

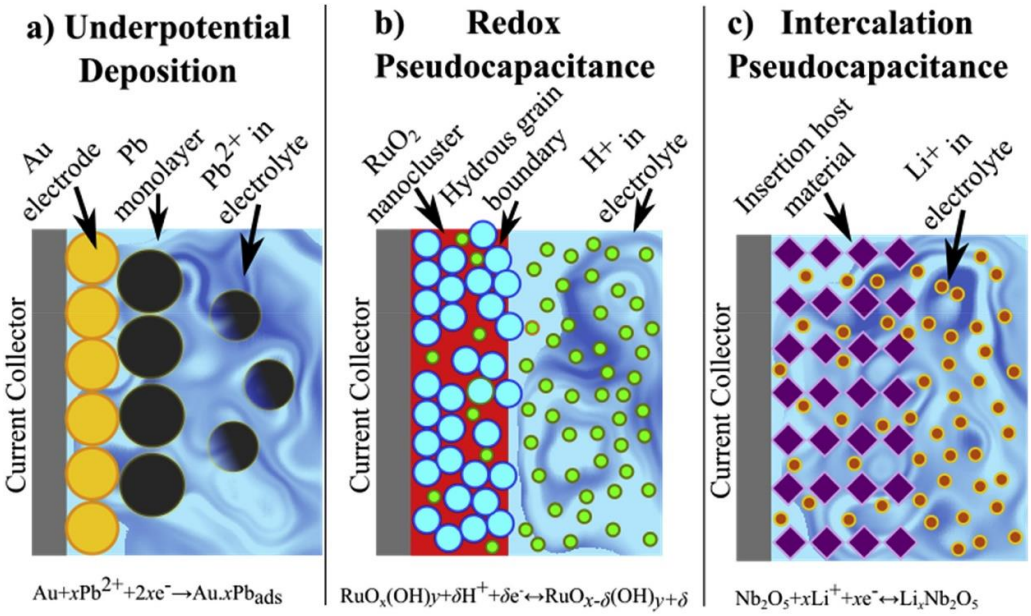

Figure 2.8: The three fundamental processes of pseudocapacitive behaviour: (a) Underpotential Deposition, (b) Redox Pseudocapacitance and (c) Intercalation Pseudocapacitance. Reprinted and adapted with permission from Ref.[115].

Although these three processes are inherently different, they all display similar electrochemical signals due to the relationship between potential and the extent of charge that occurs as a result of adsorption processes at the electrode/electrolyte interface,[120] that is a logarithmic relationship between the electrode potential and the extent of charge/discharge.[121] This is described mathematically with a modified version of the Nernst Equation (Equation 2.13 and Table 2.1) where E is the potential, E^0 is the standard potential of the redox couple, R is the gas constant, T is the temperature, n is the number of electrons, F is the Faraday constant and X is the extent of the surface coverage of the electrode surface by the potential determining ionic species.[119,121]

$$E = E^0 - \frac{RT}{nF} ln\left(\frac{X}{1-X}\right) \tag{2.13}$$

Pseudocapacitive Mechanism	Nernst-like Equation	X meaning in Equation 2.13
Underpotential	$E = E^0 - \frac{RT}{nF} ln\left(\frac{\theta}{1-\theta}\right)$	X = θ (fractional surface coverage)
Redox	$E = E^0 - \frac{RT}{nF} ln\left(\frac{[Ox]}{[Red]}\right)$	X = [Red][Ox] = 1 – [Red]
Intercalation	$E = E^0 - \frac{RT}{nF} ln\left(\frac{X}{1-X}\right)$	X = Occupancy of lattice sites of the layered structure

Table 2.1: Charge storage mechanisms that give rise to Nernst -like equation.

From Equation 2.13, an equation for pseudocapacitance (C_Φ; $F\ g^{-1}$) may be defined in terms of X as which was developed by Conway (derivation in Appendix A, Equation.A.1-A.3).[116,120,121]

$$C_\Phi = \frac{qF}{mRT} X(1-X) \tag{2.14}$$

As the plot of *E vs. X* is not entirely linear as in a capacitor, the capacitance is not always constant and so it is termed pseudocapacitance.[119]

SnO as a supercapacitor material

TMOs/MOs are ideal candidates for SC materials, and the discovery of pseudocapacitance occurred during investigations of RuO_2 which remains the premier supercapacitor material of choice today, although its astronomical cost (€17,050 per kg at the time of writing,[122] up from €9,600 in 2021[123]) and environmental toxicity make finding alternative TMOs a pressing matter. SnO and SnO_2 are heralded as potential supercapacitor materials due to their low cost, non-toxicity,[124,125] high thermal stability in air, and high power delivery ability[126] with the drawback being the poor electrical conductivity within the SnO_x matrix and the sluggish mass transport of electrolyte ions.[127] However, it may be questioned if SnO_x is an appropriate material for SC devices, or if the results published are reporting battery-type features/results for SC devices. To date, limited work has been carried out on SnO[128,129] with the majority of work focusing on SnO_2 and it is hoped the work carried out in this project through tuning morphologies and

optimising conductive additives such as CNTs will bring about a definite answer as to whether it is appropriate to use SnO in SC devices and the processes at play.

Carbon Nanotubes for Supercapacitors

Although not suited alone for battery applications as discussed in Section 2.6, CNTs are regarded as an extremely promising SC material. In addition to their high conductivity and mechanical stability, the large specific and highly accessible surface area obtainable with CNTs and in particular SWCNTs make them especially well-suited to charge storage via EDL capacitance (EDLC). Pseudocapacitance is also present in SWCNTs owing to the -O and -OH functional groups attached to the terminals of the tubes,[130] whilst further functionalisation of the SWCNTs although leading to an increase in their specific capacitance is detrimental to their conductivity and cycling stability.[131]

2.12 References

1. Yoshio, M., Brodd, R. J. & Kozawa, A. *Lithium-ion batteries: Science and technologies. Lithium-Ion Batteries: Science and Technologies* (Springer New York LLC, 2009). doi:10.1007/978-0-387-34445-4.
2. Blomgren, G. E. The Development and Future of Lithium Ion Batteries. *J. Electrochem. Soc.* **164(1)**, A5019–A5025 (2017).
3. Whittingham, M. S. Electrical energy storage and intercalation chemistry. *Science.* **192**, 1226 (1976).
4. Tarascon, J.-M. Is lithium the new gold? *Nat. Chem.* **2**, 510 (2010).
5. Persson, K. *et al.* Lithium Diffusion in Graphitic Carbon. *J. Phys. Chem. Lett.* **1**, 1176–1180 (2010).
6. Li, M., Lu, J., Chen, Z. & Amine, K. 30 Years of Lithium-Ion Batteries. *Adv. Mater.* **30**, 1800561 (2018).
7. Lazzari, M. A Cyclable Lithium Organic Electrolyte Cell Based on Two Intercalation Electrodes. *J. Electrochem. Soc.* **127**, 773–774 (1980).
8. Mizushima, K., Jones, P. C., Wiseman, P. J. & Goodenough, J. B. LixCoO2 (0. *Mater. Res. Bull.* **15**, 783–789 (1980).
9. Goodenough, J. B. How we made the Li-ion rechargeable battery. *Nat. Electron.* **1**, 204 (2018).
10. Kasnatscheew, J., Wagner, R., Winter, M. & Cekic-Laskovic, I. Interfaces and Materials in Lithium Ion Batteries: Challenges for Theoretical Electrochemistry. *Top. Curr. Chem.* **376**, 16 (2018).
11. Liu, C., Neale, Z. G. & Cao, G. Understanding electrochemical potentials of cathode materials in rechargeable batteries. *Mater. Today* **19(2)**, 109–123 (2016).
12. Roy, P. & Srivastava, S. K. Nanostructured anode materials for lithium ion batteries. *J. Mater. Chem. A* (2015) doi:10.1039/C4TA04980B.
13. Qi, W. *et al.* Nanostructured anode materials for lithium-ion batteries: principle, recent progress and future perspectives. *J. Mater. Chem. A* **5**, 19521–19540 (2017).
14. Wakihara, M. & Yamamoto, O. *Lithium ion batteries : fundamentals and performance*. (Kodansha, 1998).
15. Takami, T. *Functional Cobalt Oxides: Fundamentals, Properties and Applications.* (Pan Stanford, 2014).
16. Mekonnen, Y., Sundararajan, A. & Sarwat, A. I. A review of cathode and anode materials for lithium-ion batteries. in *SoutheastCon 2016* 1–6 (2016). doi:10.1109/SECON.2016.7506639.
17. Goriparti, S. *et al.* Review on recent progress of nanostructured anode materials for Li-ion batteries. *J. Power Sources* **257**, 421–433 (2014).
18. Qian, J. *et al.* High rate and stable cycling of lithium metal anode. *Nat. Commun.* **6**, 6362 (2015).
19. Xu, W. *et al.* Lithium metal anodes for rechargeable batteries. *Energy Environ. Sci.* **7**, 513–537 (2014).
20. Wang, L. *et al.* Engineering of lithium-metal anodes towards a safe and stable battery. *Energy Storage Mater.* **14**, 22–48 (2018).
21. Lu, B. *et al.* Suppressing Chemical Corrosions of Lithium Metal Anodes. *Adv. Energy Mater.* **12**, 2202012 (2022).
22. Shin, J. H. & Song, J. Y. Electrochemical properties of Sn-decorated SnO nanobranches as an anode of Li-ion battery. *Nano Converg.* **3(1)**, 9 (2016).

23. Asenbauer, J. *et al.* The success story of graphite as a lithium-ion anode material – fundamentals, remaining challenges, and recent developments including silicon (oxide) composites. *Sustain. Energy Fuels* **4**, 5387–5416 (2020).
24. Zhang, H., Yang, Y., Ren, D., Wang, L. & He, X. Graphite as anode materials: Fundamental mechanism, recent progress and advances. *Energy Storage Mater.* **36**, 147–170 (2021).
25. Wang, H. *et al.* Underpotential lithium plating on graphite anodes caused by temperature heterogeneity. *Proc. Natl. Acad. Sci.* **117**, 29453–29461 (2020).
26. Hu, D. *et al.* Research Progress of Lithium Plating on Graphite Anode in Lithium-Ion Batteries. *Chinese J. Chem.* **39**, 165–173 (2021).
27. Ho, A. S. *et al.* 3D Detection of Lithiation and Lithium Plating in Graphite Anodes during Fast Charging. *ACS Nano* **15**, 10480–10487 (2021).
28. Zhang, W.-J. A review of the electrochemical performance of alloy anodes for lithium-ion batteries. *J. Power Sources* **196**, 13–24 (2011).
29. Winter, M., Besenhard, J. O., Spahr, M. E. & Novák, P. Insertion Electrode Materials for Rechargeable Lithium Batteries. *Adv. Mater.* **10**, 725–763 (1998).
30. Park, J., Eom, J. & Kwon, H. Charge–discharge characteristics of a layered-structure electroplated Cu/Sn anode for Li-ion batteries. *Electrochim. Acta* **55**, 1825–1828 (2010).
31. Tamura, N., Ohshita, R., Fujimoto, M., Kamino, M. & Fujitani, S. Advanced Structures in Electrodeposited Tin Base Negative Electrodes for Lithium Secondary Batteries. *J. Electrochem. Soc.* **150**, A679–A683 (2003).
32. Winter, M. & Besenhard, J. O. Electrochemical lithiation of tin and tin-based intermetallics and composites. *Electrochim. Acta* **45**, 31–50 (1999).
33. Lorger, S., Usiskin, R. & Maier, J. Transport and Charge Carrier Chemistry in Lithium Oxide. *J. Electrochem. Soc.* **166**, A2215 (2019).
34. Fang, S., Bresser, D. & Passerini, S. Transition Metal Oxide Anodes for Electrochemical Energy Storage in Lithium- and Sodium-Ion Batteries. *Adv. Energy Mater.* **10**, 1902485 (2020).
35. Bresser, D., Passerini, S. & Scrosati, B. Leveraging valuable synergies by combining alloying and conversion for lithium-ion anodes †. *Energy Environ. Sci* **9**, 3348 (2016).
36. Zhang, H., Hasa, I. & Passerini, S. Beyond Insertion for Na-Ion Batteries: Nanostructured Alloying and Conversion Anode Materials. *Adv. Energy Mater.* **8**, 1702582 (2018).
37. Wiberg, N., Holleman, A. F. & Wiberg, E. *Holleman-Wiberg's Inorganic Chemistry*. (Elsevier Science, 2001).
38. Pannetier, J. & Denes, G. Tin(II) oxide: structure refinement and thermal expansion. *Acta Crystallogr. Sect. B* **36**, 2763–2765 (2018).
39. Walsh, A. & Watson, G. W. Electronic structures of rocksalt, litharge, and herzenbergite SnO by density functional theory. *Phys. Rev. B* **70**, 235114 (2004).
40. Lefebvre, I., Szymanski, M. A., Olivier-Fourcade, J. & Jumas, J. C. Electronic structure of tin monochalcogenides from SnO to SnTe. *Phys. Rev. B* **58**, 1896–1906 (1998).
41. Zhang, F., Zhu, J., Zhang, D., Schwingenschlögl, U. & Alshareef, H. N. Two-Dimensional SnO Anodes with a Tunable Number of Atomic Layers for Sodium Ion Batteries. *Nano Lett.* **17**, 1302–1311 (2017).
42. Cao, K., Jin, T., Yang, L. & Jiao, L. Recent progress in conversion reaction metal oxide anodes for Li-ion batteries. *Mater. Chem. Front.* **1**, 2213–2242 (2017).

43. Iqbal, M. Z. *et al.* Structural and electrochemical properties of SnO nanoflowers as an anode material for lithium ion batteries. *Scr. Mater.* **67**, 665–668 (2012).
44. Cheng, Y. *et al.* Adjusting the Chemical Bonding of SnO2@CNT Composite for Enhanced Conversion Reaction Kinetics. *Small* **13**, 1700656 (2017).
45. Wang, B. *et al.* Folding Graphene Film Yields High Areal Energy Storage in Lithium-Ion Batteries. *ACS Nano* **12**, 1739–1746 (2018).
46. Hu, R. *et al.* Dramatically enhanced reversibility of Li2O in SnO2-based electrodes: the effect of nanostructure on high initial reversible capacity. *Energy Environ. Sci.* **9**, 595–603 (2016).
47. Weeks, J. A. *et al.* Facile Synthesis of a Tin Oxide-Carbon Composite Lithium-Ion Battery Anode with High Capacity Retention. *ACS Appl. Energy Mater.* **2**, 7244–7255 (2019).
48. Mohamedi, M. *et al.* Amorphous tin oxide films: preparation and characterization as an anode active material for lithium ion batteries. *Electrochim. Acta* **46**, 1161–1168 (2001).
49. Zoller, F., Böhm, D., Bein, T. & Fattakhova-Rohlfing, D. Tin Oxide Based Nanomaterials and Their Application as Anodes in Lithium-Ion Batteries and Beyond. *ChemSusChem* **12**, 4140–4159 (2019).
50. Zhang, Q. *et al.* Graphene-based carbon coated tin oxide as a lithium ion battery anode material with high performance. *J. Mater. Chem. A* **5**, 19136–19142 (2017).
51. Krishnakumar, T., Pinna, N., Kumari, K. P., Perumal, K. & Jayaprakash, R. Microwave-assisted synthesis and characterization of tin oxide nanoparticles. *Mater. Lett.* **62**, 3437–3440 (2008).
52. Shin, J. H., Song, J. Y., Kim, Y. H. & Park, H. M. Low temperature and self-catalytic growth of tetragonal SnO nanobranch. *Mater. Lett.* **64**, 1120–1122 (2010).
53. Orlandi, M. O., Leite, E. R., Aguiar, R., Bettini, J. & Longo, E. Growth of SnO Nanobelts and Dendrites by a Self-Catalytic VLS Process. *J. Phys. Chem. B* **110**, 6621–6625 (2006).
54. Han, Z. *et al.* Solvothermal preparation and morphological evolution of stannous oxide powders. *Mater. Lett.* **48**, 99–103 (2001).
55. An, S. J. *et al.* The state of understanding of the lithium-ion-battery graphite solid electrolyte interphase (SEI) and its relationship to formation cycling. *Carbon N. Y.* **105**, 52–76 (2016).
56. Zhang, X., Kostecki, R., Richardson, T. J., Pugh, J. K. & Ross, P. N. Electrochemical and Infrared Studies of the Reduction of Organic Carbonates. *J. Electrochem. Soc.* **148**, A1341 (2001).
57. Goodenough, J. B. & Kim, Y. Challenges for Rechargeable Li Batteries. *Chem. Mater.* **22**, 587–603 (2010).
58. Courtney, I. A. & Dahn, J. R. Key Factors Controlling the Reversibility of the Reaction of Lithium with SnO 2 and Sn 2 BPO 6 Glass ELECTROCHEMICAL SCIENCE AND TECHNOLOGY Key Factors Controlling the Reversibility of the Reaction of Lithium with SnO 2 and Sn 2 BPO 6 Glass. *J. Electrochem. Soc* **144**, 2943 (1997).
59. Courtney, I. A. & Dahn, J. R. Electrochemical and In Situ X-Ray Diffraction Studies of the Reaction of Lithium with Tin Oxide Composites. *J. Electrochem. Soc* **144**, 2045 (1997).
60. Hess, M. Non-linearity of the solid-electrolyte-interphase overpotential. *Electrochim. Acta* **244**, 69–76 (2017).

61. Fergus, J. W. Ceramic and polymeric solid electrolytes for lithium-ion batteries. *J. Power Sources* **195**, 4554–4569 (2010).
62. Li, Q., Chen, J., Fan, L., Kong, X. & Lu, Y. Progress in electrolytes for rechargeable Li-based batteries and beyond. *Green Energy Environ.* **1**, 18–42 (2016).
63. Xu, K. Electrolytes and Interphases in Li-Ion Batteries and Beyond. *Chem. Rev.* **114**, 11503–11618 (2014).
64. Kalhoff, J., Eshetu, G. G., Bresser, D. & Passerini, S. Safer Electrolytes for Lithium-Ion Batteries: State of the Art and Perspectives. *ChemSusChem* **8**, 2154–2175 (2015).
65. Fong, R., von Sacken, U. & Dahn, J. R. Studies of Lithium Intercalation into Carbons Using Nonaqueous Electrochemical Cells. *J. Electrochem. Soc.* **137**, 2009–2013 (1990).
66. Chen, K.-H. *et al.* Enabling 6C Fast Charging of Li-Ion Batteries with Graphite/Hard Carbon Hybrid Anodes. *Adv. Energy Mater.* **11**, 2003336 (2021).
67. Bruce, P. G., Scrosati, B. & Tarascon, J.-M. Nanomaterials for Rechargeable Lithium Batteries. *Angew. Chemie Int. Ed.* **47**, 2930–2946 (2008).
68. Yang, J., Takeda, Y., Imanishi, N., Xie, J. Y. & Yamamoto, O. Intermetallic SnSbx compounds for lithium insertion hosts. *Solid State Ionics* **133**, 189–194 (2000).
69. Liu, C., Neale, Z. G. & Cao, G. Understanding electrochemical potentials of cathode materials in rechargeable batteries. *Mater. Today* **19**, 109–123 (2016).
70. Nitta, N., Wu, F., Lee, J. T. & Yushin, G. Li-ion battery materials: present and future. *Mater. Today* **18**, 252–264 (2015).
71. Usubelli, C. *et al.* Understanding the Overlithiation Properties of LiNi0.6Mn0.2Co0.2O2 Using Electrochemistry and Depth-Resolved X-ray Absorption Spectroscopy. *J. Electrochem. Soc.* **167**, 80514 (2020).
72. Freitas, B. G. A., Siqueira, J. M., Costa, L. M. da, Ferreira, G. B. & Resende, J. A. L. C. Synthesis and Characterization of $LiCoO_2$ from Different Precursors by Sol-Gel Method. *Journal of the Brazilian Chemical Society* vol. 28 (2017).
73. Iijima, S. Helical microtubules of graphitic carbon. *Nature* **354**, 56 (1991).
74. Iijima, S. Carbon nanotubes: past, present, and future. *Phys. B Condens. Matter* **323**, 1–5 (2002).
75. Baughman, R. H., Zakhidov, A. A. & de Heer, W. A. Carbon Nanotubes--the Route Toward Applications. *Science.* **297**, 787–792 (2002).
76. Qiu, L. & Ding, F. Understanding Single-Walled Carbon Nanotube Growth for Chirality Controllable Synthesis. *Accounts Mater. Res.* **2**, 828–841 (2021).
77. Saito, R., Dresselhaus, G. & Dresselhaus, M. S. *Physical Properties of Carbon Nanotubes*. (PUBLISHED BY IMPERIAL COLLEGE PRESS AND DISTRIBUTED BY WORLD SCIENTIFIC PUBLISHING CO., 1998). doi:doi:10.1142/p080.
78. Landi, B. J., Ganter, M. J., Cress, C. D., DiLeo, R. A. & Raffaelle, R. P. Carbon nanotubes for lithium ion batteries. *Energy Environ. Sci.* **2**, 549–712 (2009).
79. Hong, S. & Myung, S. Nanotube electronics: A flexible approach to mobility. *Nat. Nanotechnol.* **2**, 207–208 (2007).
80. De Volder, M. F. L., Tawfick, S. H., Baughman, R. H. & Hart, A. J. Carbon Nanotubes: Present and Future Commercial Applications. *Science.* **339**, 535 LP – 539 (2013).
81. Zhang, C. (John) *et al.* Liquid exfoliation of interlayer spacing-tunable 2D vanadium oxide nanosheets: High capacity and rate handling Li-ion battery

cathodes. *Nano Energy* **39**, 151–161 (2017).
82. DiLeo, R. A. *et al.* Enhanced Capacity and Rate Capability of Carbon Nanotube Based Anodes with Titanium Contacts for Lithium Ion Batteries. *ACS Nano* **4**, 6121–6131 (2010).
83. P3-SWNT | Carbon Solutions, Inc. https://www.carbonsolution.com/products/p3-swnt.
84. TUBALL™ Single Wall Carbon Nanotubes — iNanoComm. http://inanocomm.org/tuball/.
85. Chayambuka, K., Mulder, G., Danilov, D. L. & Notten, P. H. L. Sodium-Ion Battery Materials and Electrochemical Properties Reviewed. *Adv. Energy Mater.* **8**, 1800079 (2018).
86. Yabuuchi, N., Kubota, K., Dahbi, M. & Komaba, S. Research Development on Sodium-Ion Batteries. *Chem. Rev.* **114**, 11636–11682 (2014).
87. Hwang, J.-Y., Myung, S.-T. & Sun, Y.-K. Sodium-ion batteries: present and future. *Chem. Soc. Rev.* **46**, 3529–3614 (2017).
88. Greim, P., Solomon, A. A. & Breyer, C. Assessment of lithium criticality in the global energy transition and addressing policy gaps in transportation. *Nat. Commun.* **11**, 4570 (2020).
89. Morris, J. Rising Lithium Prices Could Stop The EV Revolution – Or Could They? *Frobes* https://www.forbes.com/sites/jamesmorris/2022/04/16/rising-lithium-prices-could-stop-the-ev-revolution--or-could-they/?sh=7a8ae86f7125 (2022).
90. Takeda, O., Uda, T. & Okabe, T. H. Chapter 2.9 - Rare Earth, Titanium Group Metals, and Reactive Metals Production. in (ed. Seetharaman, S. B. T.-T. on P. M.) 995–1069 (Elsevier, 2014). doi:https://doi.org/10.1016/B978-0-08-096988-6.00019-5.
91. Stern, A. G. Scalable, Self-Contained Sodium Metal Production Plant for a Hydrogen Fuel Clean Energy Cycle. in (eds. Nikolic, A. B. & Janda, Z. S.) Ch. 8 (IntechOpen, 2017). doi:10.5772/67597.
92. Baumann, M., Barelli, L. & Passerini, S. The Potential Role of Reactive Metals for a Clean Energy Transition. *Adv. Energy Mater.* **10**, 2001002 (2020).
93. Murahara, M., Sato, Y. & Okawara, T. Salt as Alternative Energy Material to Fossil Fuel <potential use of sodium metal for hydrogen generation> *MRS Proc.* **1492**, 189–194 (2013).
94. Stern, A. G. Design of an efficient, high purity hydrogen generation apparatus and method for a sustainable, closed clean energy cycle. *Int. J. Hydrogen Energy* **40**, 9885–9906 (2015).
95. U.S. Geological Survey. *Mineral Commodity Summaries 2019. Mineral Commodity Summaries* http://pubs.er.usgs.gov/publication/70202434 (2019) doi:10.3133/70202434.
96. Yong-Sheng Hu. Development of Sodium-Ion Batteries for Grid-Scale Energy Storage. *ECS Meet. Abstr.* (2016) doi:10.1149/ma2016-03/1/71.
97. Jana, A., Paul, R. & Roy, A. K. Chapter 2 - Architectural design and promises of carbon materials for energy conversion and storage: in laboratory and industry. in *Micro and Nano Technologies* (eds. Paul, R., Etacheri, V., Wang, Y. & Lin, C.-T. B. T.-C. B. N. for A. T. and E. E. S. and C.) 25–61 (Elsevier, 2019). doi:https://doi.org/10.1016/B978-0-12-814083-3.00002-0.
98. Slater, M. D., Kim, D., Lee, E. & Johnson, C. S. Sodium-Ion Batteries. *Adv. Funct. Mater.* **23**, 947–958 (2013).
99. Stevens, D. A. & Dahn, J. R. The Mechanisms of Lithium and Sodium Insertion

in Carbon Materials. *J. Electrochem. Soc.* **148**, A803–A811 (2001).
100. Ge, P. & Fouletier, M. Electrochemical intercalation of sodium in graphite. *Solid State Ionics* **28**–**30**, 1172–1175 (1988).
101. Hérold, A., Maréché, J.-F. & Lelaurain, M. A short Overview on the Binary and some New Ternary Sodium GICs. *Mol. Cryst. Liq. Cryst. Sci. Technol. Sect. A. Mol. Cryst. Liq. Cryst.* **310**, 43–49 (1998).
102. Wang, Z., Selbach, S. M. & Grande, T. Van der Waals density functional study of the energetics of alkali metal intercalation in graphite. *RSC Adv.* **4**, 4069–4079 (2014).
103. Yoon, G., Kim, H., Park, I. & Kang, K. Conditions for Reversible Na Intercalation in Graphite: Theoretical Studies on the Interplay Among Guest Ions, Solvent, and Graphite Host. *Adv. Energy Mater.* **7**, 1601519 (2017).
104. Cao, Y. *et al.* Sodium Ion Insertion in Hollow Carbon Nanowires for Battery Applications. *Nano Lett.* **12**, 3783–3787 (2012).
105. Li, Z. *et al.* High Capacity of Hard Carbon Anode in Na-Ion Batteries Unlocked by POx Doping. *ACS Energy Lett.* **1**, 395–401 (2016).
106. Nayak, P. K., Yang, L., Brehm, W. & Adelhelm, P. From Lithium-Ion to Sodium-Ion Batteries: Advantages, Challenges, and Surprises. *Angew. Chemie Int. Ed.* **57**, 102–120 (2018).
107. Li, Z., Ding, J. & Mitlin, D. Tin and Tin Compounds for Sodium Ion Battery Anodes: Phase Transformations and Performance. *Acc. Chem. Res.* **48**, 1657–1665 (2015).
108. Zhang, Y. *et al.* Ultrafine tin oxide on reduced graphene oxide as high-performance anode for sodium-ion batteries. *Electrochim. Acta* **151**, 8–15 (2015).
109. Lu, Y. C. *et al.* Electrochemical properties of tin oxide anodes for sodium-ion batteries. *J. Power Sources* **284**, 297–295 (2015).
110. Dixon, D., Ávila, M., Ehrenberg, H. & Bhaskar, A. Difference in Electrochemical Mechanism of SnO2 Conversion in Lithium-Ion and Sodium-Ion Batteries: Combined in Operando and Ex Situ XAS Investigations. *ACS Omega* **4**, 9731–9738 (2019).
111. Bommier, C. & Ji, X. Electrolytes, SEI Formation, and Binders: A Review of Nonelectrode Factors for Sodium-Ion Battery Anodes. *Small* **14**, 1703576 (2018).
112. Dugas, R., Zhang, B., Rozier, P. & Tarascon, J. M. Optimization of Na-Ion Battery Systems Based on Polyanionic or Layered Positive Electrodes and Carbon Anodes. *J. Electrochem. Soc.* **163**, A867 (2016).
113. Iermakova, D. I., Dugas, R., Palacín, M. R. & Ponrouch, A. On the Comparative Stability of Li and Na Metal Anode Interfaces in Conventional Alkyl Carbonate Electrolytes. *J. Electrochem. Soc.* **162**, A7060 (2015).
114. Seh, Z. W., Sun, J., Sun, Y. & Cui, Y. A Highly Reversible Room-Temperature Sodium Metal Anode. *ACS Cent. Sci.* **1**, 449–455 (2015).
115. Da Silva, L. M. *et al.* Reviewing the fundamentals of supercapacitors and the difficulties involving the analysis of the electrochemical findings obtained for porous electrode materials. *Energy Storage Mater.* **27**, 555–590 (2020).
116. Fleischmann, S. *et al.* Pseudocapacitance: From Fundamental Understanding to High Power Energy Storage Materials. *Chemical Reviews* (2020) doi:10.1021/acs.chemrev.0c00170.
117. Mohd Abdah, M. A. A., Azman, N. H. N., Kulandaivalu, S. & Sulaiman, Y. Review of the use of transition-metal-oxide and conducting polymer-based

fibres for high-performance supercapacitors. *Materials and Design* vol. 186 108199 (2020).
118. Brett, C. M. A. & Brett, A. M. O. *Electrochemistry: Principles, Methods, and Applications*. (Oxford University Press, 1993).
119. Augustyn, V., Simon, P. & Dunn, B. Pseudocapacitive oxide materials for high-rate electrochemical energy storage. *Energy Environ. Sci.* **7**, 1597–1614 (2014).
120. B. Conway. *Electrochemical Supercapacitors: Scientific Fundamentals and Technological ... - B. E. Conway - Google Books*. *kluwar academic/plenum: New York* (1999).
121. Liu, J. *et al.* Review Advanced Energy Storage Devices: Basic Principles, Analytical Methods, and Rational Materials Design. *Adv. Sci.* **5**, 1700322 (2018).
122. Ruthenium price | Umicore Precious Metals Management | Umicore. https://pmm.umicore.com/en/prices/ruthenium/.
123. Ruthenium | Precious Metals Management. https://pmm.umicore.com/en/prices/ruthenium.
124. Ng, A. M. C. *et al.* Metal oxide nanoparticles with low toxicity. *J. Photochem. Photobiol. B Biol.* **151**, 17–24 (2015).
125. Johnson, W. *et al.* Safety Assessment of Tin(IV) Oxide as Used in Cosmetics. *Int. J. Toxicol.* **33**, 40S-46S (2014).
126. Wang, Q., Tian, Y., Guan, S., Peng, Z. & Fu, X. Alloying Enhanced Supercapacitor Performance Based on Oxygen-Deficient Tin Oxide Nanorod Array Electrodes. *ACS Appl. Energy Mater.* **3**, 11333–11342 (2020).
127. Li, Z. J., Chang, T. X., Yun, G. Q. & Jia, Y. Coating single walled carbon nanotube with SnO2 and its electrochemical properties. *Powder Technol.* **224**, 306–310 (2012).
128. Murugan, A. *et al.* Structural and charge density distribution studies on Tin Oxide nanoparticles for Supercapacitor application. *J. Energy Storage* **28**, 101194 (2020).
129. Li, Y. *et al.* In situ template synthesis of SnO nanoparticles on nickel foam with high electrochemical performance. *J. Sol-Gel Sci. Technol.* **86**, 423–430 (2018).
130. Pan, H., Li, J., Yuan, • & Feng, P. Carbon Nanotubes for Supercapacitor. doi:10.1007/s11671-009-9508-2.
131. Xiao, X. *et al.* Freestanding functionalized carbon nanotube-based electrode for solid-state asymmetric supercapacitors. *Nano Energy* **6**, 1–9 (2014).

3. Experimental Techniques

3.1 Electrochemical Testing

Electrochemical testing was performed using a Bio-Logic VMP 300 and a Bio-Logic BCS-800 battery cycler.

Cyclic Voltammetry

Cyclic Voltammetry (CV) is a powerful potentiostatic electrochemical technique[1] used to probe the oxidation and reduction processes of molecular species and solid electrodes or the charging/discharging mechanisms of electrodes for LIBs/NIBs/SCs. A CV is performed by cycling the potential of a working electrode and measuring the resulting current. The potential of this working electrode is measured against a reference electrode which remains constant throughout, or in the case of two electrode measurements such as in LIBs the reference is with respect to the counter electrode. A graph of current as a function of potential is obtained, with the peaks providing information on the oxidation/reduction processes within the cell whilst also displaying the reversibility/irreversibility of the cell. The peaks occurring during these measurements represent phase transformations and/or redox reactions within the electrodes. Through the variation of the potential scan rate, insights are gained into the diffusion processes and electron kinetics within the material.[1,2] Specifics of CV parameters are stated in Chapters 5, 6 and 7.

Galvanostatic Charge-Discharge

Galvanostatic charge-discharge (GCD) cycling provides insights into the capacity of a battery/supercapacitor material, whilst also testing the materials lifetime through repetitive cycling. A constant current is applied to the material and the corresponding voltage is recorded. A predetermined max voltage is set, at which point the charging process will cease and the discharge will commence. This predetermined voltage may be obtained from the CV of the material and would coincide with the flat plateaus at either end of the CV in which the redox reactions have fully completed in a battery, or the stability window of the electrolyte for a SC. The current may be set according to a certain *C-rate* or in mA g^{-1}. A *C-rate* is a common parameter used in battery testing, with the time taken for a charge or a discharge to occur being equivalent to 1/*C-rate* in hours. So

for instance a 0.5 *C-rate* means a charge will take 2 hours, whilst a 20 *C-rate* means a charge will take 3 minutes. The current needed to obtain a specific *C-rate* is determined by the theoretical capacity of the material. The theoretical capacity ($Q_{theoretical}$) of a material may be worked out once the number of electrons (n) involved in the charging/discharging of the material is known. Using Faraday's constant (F), we may calculate the electrical capacity of the material in terms of moles and this may be converted to Ah g^{-1} via division with the molecular weight of the material (MW) and a time conversion as shown in Equation 3.1.

$$Q_{theoretical} = \frac{nF}{3600 \times MW} \tag{3.1}$$

For instance, the full lithiation of tin oxide results in the alloy $Li_{22}Sn_5$ and the formation of Li_2O. Thus using Equation 3.1, the theoretical capacity of SnO may be reported as 875 mAh g^{-1} (which is the most common way as the lithium oxide formation is deemed irreversible), or 1,313 mAh g^{-1} if the lithium oxide is considered. Specifics of GCD parameters are stated in Chapters 5, 6 and 7.

Electrochemical Impedance Spectroscopy

Electrochemical impedance spectroscopy (EIS) is a powerful technique to understand the electron transfer properties of electrochemical systems. An ideal resistor follows Ohm's Law (Equation 3.2), defining the resistance (R) as the ratio between voltage (V) and current (I).

$$R = \frac{V}{I} \tag{3.2}$$

An ideal resistor has several properties which make it an unsuitable choice for modelling real-world circuit elements such as it should follow Ohm's Law at all voltages/currents, the resistance value is independent of frequency and the alternating current and voltage signals through the resistor are always in phase with each other.[3] Real-world circuit elements display much more complex behaviours and thus a more general circuit parameter of impedance (Z) is used. As before with resistance, impedance is a measure of the ability of a circuit to resist the flow of current, the only difference being it is not

limited by the properties described previously. It may provide information on factors such as electrolyte resistance, interfacial charge transfer resistance and diffusion processes to name but a few.[4]

EIS is measured by applying a sinusoidal AC potential to the cell under study and measuring the resulting current through the cell. The response current is an AC current signal and may be analysed as a sum of sinusoidal functions (Fourier series). The excitation signal (Equation 3.3) has the following form when expressed as a function of time, where E_t is the potential at time t, E_0 is the amplitude of the signal and ω is the angular frequency.

$$E_t = E_0 \sin(\omega t) \tag{3.3}$$

In a linear system, the response current, I_t, is shifted in phase (φ) and has a different amplitude of I_0.

$$I_t = I_0 \sin(\omega t + \varphi) \tag{3.4}$$

A similar expression to Ohm's law allows one to calculate the impedance, expressed in terms of a magnitude, Z_0 and φ.

$$Z = \frac{E_t}{I_t} = Z_0 \frac{\sin(\omega t)}{\sin(\omega t + \varphi)} \tag{3.5}$$

By utilising Euler's relationship, the impedance may be expressed as a complex number (note j is used to represent the complex number i as not to cause confusion with the symbol for current).

$$\exp(j\varphi) = \cos(\varphi) + j\sin(\varphi) \tag{3.6}$$

Thus the potential and current may be written as:

$$E_t = E_0 \exp(j\omega t) \quad , \quad I_t = I_0 \exp(j\omega t - \varphi) \tag{3.7}$$

The impedance is given as the following complex number:

$$Z = \frac{E}{I} = Z_0 \exp(j\varphi) = Z_0 (\cos\varphi + j\sin\varphi) \quad (3.8)$$

The frequency of the AC signal is varied and the overall impedance is recorded as a function of frequency, allowing processes occurring on different timescales to be separated, identified and analysed. The impedance is represented as a complex number Z, which can be broken down into a real ($Z_{Rel} = R$, where R is resistance) and an imaginary part also called reactance, which has capacitive and/or inductive contributions ($Z_{Cap} = 1/\omega C$, $Z_{Ind} = \omega L$; where C is capacitance, L is inductance and ω is angular frequency). EIS spectra are usually presented in either Bode or Nyquist plots (Figure 3.1 A and B). For the Bode plot, the log of impedance and log of phase-shift is plotted as a function of the log of frequency. The advantage of this plot is that the frequency dependence is clearly visible. When Z_{Rel} (Re (Z)) is plotted on the x-axis, and Z_{Im} (Im (Z)) is plotted on the y-axis, a Nyquist plot is formed which may be fitted with equivalent circuits to probe the properties of the system under question. The Nyquist plot is more popular in electrochemistry as impedance models have been well established to fit the Nyquist representation. Specifics of EIS parameters are stated in Chapters 5, 6 and 7.

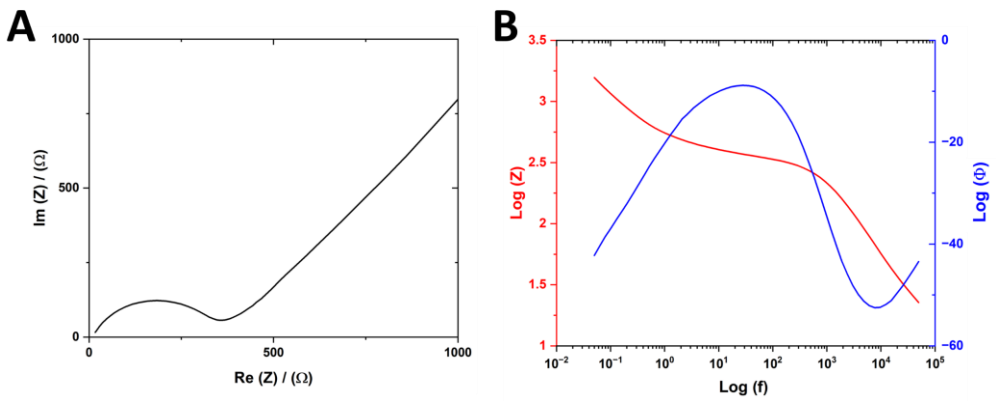

Figure 3.1: (A) Example of a Nyquist plot. (B) Example of a Bode plot, impedance shown in red whilst phase is plotted in blue.

3.2 Electron Microscopy

The resolution of an optical microscope (δ) is given by the Rayleigh criterion (Equation 3.9);[5] where λ is the wavelength of the radiation, μ the refractive index of the viewing medium, and β the semi-angle of collection of the magnifying lens.

$$\delta = \frac{0.61\lambda}{\mu \sin \beta} \tag{3.9}$$

Thus for visible light, with a wavelength of 550 nm (that of green light in the middle of the visible spectrum), the resolution is 330 nm. Thus for analysis on the nanoscale, an alternate system to visible-light microscopes is needed. From de Broglie's equation (Equation 3.10), and ignoring relativistic effects, it is shown that the wavelength of electron (λ) is inversely proportional to the voltage (V) accelerating it; where h is Planck's constant, m_o is the rest mass of the electron and e is the electron charge.

$$\lambda = \frac{h}{\sqrt{(2m_0 eV}} = \frac{1.22 \times 10^{-9}}{\sqrt{V}} \tag{3.10}$$

For a 100 kV beam therefore, the wavelength will be ~ 4 pm which is smaller than the diameter of an atom. In reality, due to imperfections in the lens, TEM technology can resolve details approximately 100 times larger than this (~0.5 – 1 Å), and SEM technology does not approach these beam energies.

Scanning Electron Microscopy

Scanning electron microscopy (SEM) operates by generating a high-energy electron beam using a field emission gun, which is focused on the sample using electromagnetic lenses through an ultra-high vacuum (Figure 3.2a). From the interaction between the electron beam and the sample, a number of different responses may be measured and used to provide topographic information. Secondary electrons are generated, occurring from the inelastic scattering (>50 eV) of electrons from the sample due to the excitation from the incoming beam and are accelerated back through the column to the detector. These low-energy electrons originate within nanometres of the sample's surface and are important for the examination of surface morphology (Figure 3.3a). Back-scattered electrons are also generated and caused by the elastic scattering of the electron beam (Figure 3.3a). These interactions occur deeper within the sample and provide information regarding the materials' composition.[6]

SEM was carried out using the Zeiss ULTRA plus Gemini SEM microscope in high vacuum mode with an acceleration voltage of 5 kV, a working distance of 6 mm and a 30 µm aperture located in the Advanced Microscopy Laboratory (AML) of TCD. Images were recorded using the SE2 and InLens detector. For the following work the morphology and surface analysis of the sample of the material is important and thus a beam voltage of 5 kV is used to generate electrons from the surface of the sample whilst not damaging the material.

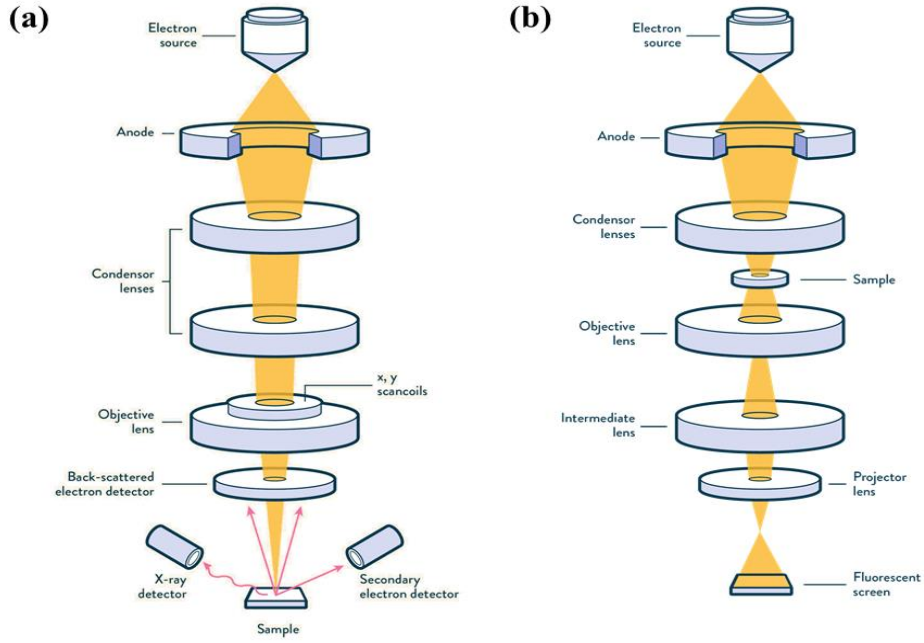

Figure 3.2: Schematic of (a) SEM and (b) TEM. Adapted and reproduced with permission from Technology Networks, Ref[7].

Transmission Electron Microscopy

Transmission electron microscopy (TEM) is another form of electron microscopy in which a high-voltage electron beam passes through a sufficiently thin sample (< 100 nm, transparent to electrons) creating a magnified image on a fluorescent screen below (Figure 3.2b). The beam interacts with the atomic nucleus and surrounding electron clouds of the sample, with the electrons scattered to form the corresponding TEM image and a diffraction pattern. The electrons may be scattered elastically or inelastically and a number of other signals such as secondary electrons and x-rays may be generated which can be detected by additional detectors. The TEM image may be formed either from the direct beam (known as Bright Field imaging) or from the diffracted beam (known as Dark Field imaging). Diffraction patterns are formed by the interaction of the electron beam with the sample and satisfy Bragg's law (Equation 3.11),[8] which allows one to work out

crystallographic information such as lattice parameters, crystal orientation and defects;[5,9] where n is the diffraction order, d is the atomic plane spacing and θ_B is the Bragg angle.

$$n\lambda = 2dsin\theta_B \tag{3.11}$$

The resolution available from a TEM is much greater than that of an SEM due to the higher beam voltage which is not feasible in samples used for SEM as it would destroy the thicker material. TEM was performed using a FEI Titan 80-300 Thermo Fisher Scientific, fitted with a Schottky field emission gun. The operating voltage was set to 300 kV and images were recorded using a Gatan UltraScan CCD camera.

Energy Dispersive X-ray Spectroscopy

Energy dispersive x-ray spectroscopy (EDX) works in conjunction with both TEM and SEM to produce chemical information about the sample complementing the morphological and structural data. When the electron beam hits the inner shell (K-shell) of an atom, core electrons are ejected leaving behind a positively charged hole. This hole attracts the negatively charged electrons from the outer shells (L- and M-shell) of the atom, which release a characteristic x-ray of the transition as they relax in energy which can be used to identify the elements present (Figure 3.3b). The size of the transition is described by α and β, with a relaxation from M to L or L to K described as Lα or Kα whilst a transition from M to K is described as Kβ. The emitted x-rays are then collected using a silicon drift detector, which measures the signal and a spectrum is plotted in which the chemical species present may be identified. In addition to the characteristic x-ray, another form of x-ray is produced when the incoming electron is slowed down via interaction with the nucleus of the atoms of the sample. This is known as *Bremsstrahlung* or 'breaking radiation' and gives rise to an exponentially decaying background signal in the EDX spectrum on which the characteristic x-ray peaks are superimposed.[5]

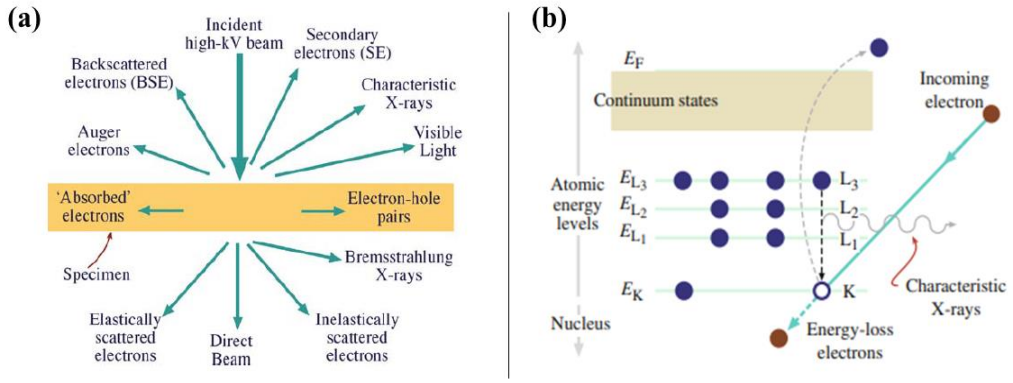

Figure 3.3: (a) Diagram showing various types of electron scattering and X-ray emission from a sample in SEM/TEM. (b) Diagram showing a core electron ejection and the subsequent relaxation of an outer electron along with the production of a characteristic x-ray. (Image adapted and reproduced with permission from Ref[5]).

For SEM, EDX was carried out using a 20 mm^2 Oxford Inca EDX detector and analysed using the Oxford Inca software. For TEM, EDX was carried out using a Bruker XFlash 6-30 EDS detector. Elemental mapping regions were imaged in Scanning Transmission Electron Microscopy (STEM) mode with an angle annular dark-field (HAADF) detector. EDX spectrum analysis was done using Bruker Esprit 2.0.

3.3 X-Ray Diffraction

X-Ray powder diffraction (XRD) is used for the phase identification of a crystalline material and can provide information on unit cell dimensions. The apparatus operates by generating x-rays in a cathode tube by heating a filament to produce electrons which are then focused on a metal target which in turn produce x-rays characteristic of the material. These x-rays are filtered and focused on the sample, and the resulting intensity of the reflected x-rays is measured as the source and detector are rotated. Peak intensity occurs when the geometry of the x-rays satisfies Bragg's Law (Equation 3.11), allowing constructive interference to occur.[10] From the resulting XRD spectrum, the Miller indices (*hkl*) of the material may be defined if the material is crystalline and the *d*-spacing may be calculated allowing for the identification of a compound. Additionally, the XRD pattern gives information on the crystallinity of the material, and one may use peak broadening to estimate the crystallite size via the Scherrer Equation.[11] In the present work powder XRD is used, which utilises the random orientation of crystal grains within the sample which ensures all crystallographic planes will be captured with no sample rotation necessary.

XRD was measured using a Bruker Advance Powder X-ray and a Panalytical X'Pert Pro diffractometer equipped with a Cu-Kα emission source (λ = 1.5406 Å) in the Bragg-Brentano configuration.

3.4 X-Ray Photoelectron Spectroscopy

X-ray photoelectron spectroscopy (XPS) is a surface-sensitive analytical technique in which x-rays are focused upon a sample under study and the kinetic energy of the resulting emitted electrons is measured. XPS is based on the photoelectric effect which Albert Einstein formally described and was awarded the Nobel prize for in 1921.[12] Kai Siegbahn developed XPS (initially referred to as electron spectroscopy for chemical analysis) in the 1950s and 1960s and received the Nobel prize for this work in 1981.[13] When soft x-rays (~6 keV) irradiate a sample, a core electron is ejected and emitted as a photoelectron which is analysed by a detector.[14] The energy of this emitted electron (*KE*) may be used to calculate the binding energy (*BE*) of the electron once the energy of the x-ray (*hv*) and the work function of the spectrometer (Φ_{spec}) is known, as shown in Equation 3.12.

$$BE = hv - KE - \Phi_{spec} \tag{3.12}$$

This concept may be seen graphically in Figure 3.4. XPS has the ability to determine the chemical environment (nearest neighbours, oxidation state) of the atoms present in a sample. For example, if an atom is bound to a highly electronegative atom, the binding energy of the emitted electron will be greater than if it was in a pure covalent bond. Similarly, if an atom is in a higher oxidation state, it will exhibit a positive charge and thus exert a greater hold on the core electrons leading to an increased binding energy. The XPS spectrum plots the counts per second against the binding energy and this can be compared to standard tables to allow for the elemental characterisation of the surface. XPS is a surface-sensitive technique (~10 nm) and must be performed under ultra-high vacuum environments (~10^{-9} mbar) to ensure a clean surface for analysis.[14] X-rays are generated using an Al source with a monochromator to ensure only Kα x-rays are passed through and remove Bremsstrahlung radiation.

XPS spectra were recorded using an Omicron MultiProbe XPS instrument. High-resolution spectra were obtained at a 50 eV pass energy with a monochromatic Al Kα (XM 1000, 1486.6 eV) source. Samples were attached to stainless steel sample holder by copper tape and degassed in the load lock and preparation chamber prior to the measurement. Obtained spectra were analysed in the CasaXPS software with Gaussian-Lorentzian shape fitting and Shirley background.

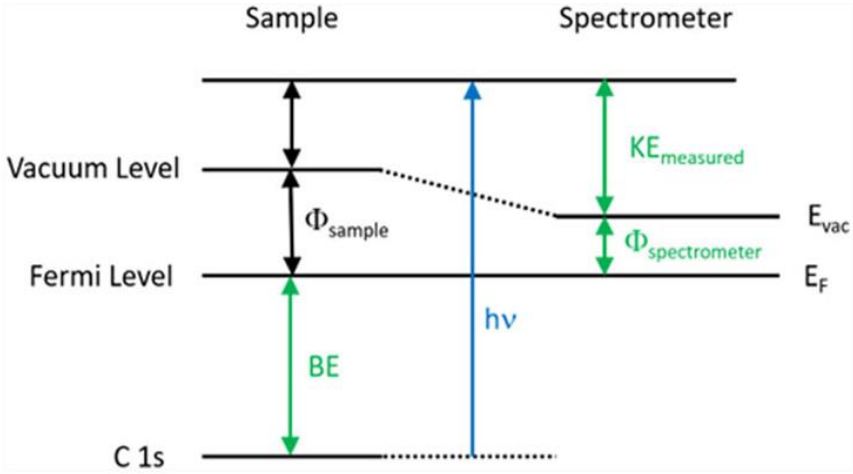

Figure 3.4: Energy level diagram illustrating schematically the basic XPS equation, with x-ray source energy (*hν*), the binding energy of the electron (*BE*), the measured kinetic energy of the electron (*KE*), and the work function of the spectrometer (*Φspec*). (Image reproduced with permission from Ref.[14])

3.5 Infrared and Raman Spectroscopy

Infrared spectroscopy (IR) utilises infrared light to probe the vibrations/rotations of the bonds within a compound and thus allow for the identification of the chemical structure present. The energy at which a peak occurs in the absorption/transmittance spectrum corresponds to the frequency of the vibration/rotation of a part of the molecule as the electric field of the radiation interacts with it.[15] For a molecule to be IR active it must have a net change in the dipole moment as it vibrates/rotates. A molecule containing N atoms has 3N degrees of freedom of which 3 are rotational, 3 are translational and the remainder are fundamental vibrations. Therefore there are 3N – 6 fundamental vibrations (this is 3N – 5 for linear molecules as there are only 2 rotational degrees of freedom). The frequency of the fundamental modes of vibration (ν) of the molecule is given by comparing the bond to a harmonic oscillator with a force constant k and reduced mass μ, as shown below in Equation 3.13. This quantity is more commonly expressed in terms of wavenumber ($\tilde{\nu}$).

$$\nu = \frac{1}{2\pi}\sqrt{\frac{k}{\mu}} \qquad \tilde{\nu} = \frac{1}{2\pi c}\sqrt{\frac{k}{\mu}} \tag{3.13}$$

Fourier transform infrared spectroscopy (FTIR) differs from conventional IR spectroscopy by how the sample is probed with light. In conventional IR monochromatic light sequentially irradiates the sample in the IR spectrum range whereas in FTIR the sample is irradiated with many frequencies of IR light all at once. FTIR utilises a Michelson Interferometer to create an interferogram of the IR source which is transmitted through the sample. By performing a Fourier transform on the output, the time domain signal may then be transformed to the frequency domain for analysis. Attenuated Total Reflectance (ATR) is used in parallel to FTIR due to the ease of sample preparation. In ATR, a crystal with a high refractive index is used to cause the incoming light to undergo total internal reflection.[15] During this reflection a small amount of light leaks into and is absorbed by the sample, which is sandwiched in contact with the crystal and allows for a spectrum to be recorded. FTIR spectra were recorded on a PerkinElmer Spectrum 100 equipped with a universal total reflectance (Diamond/KRS-5 sandwich assembly) sampling accessory. The spectra were recorded from 4000 to 350 cm^{-1}.

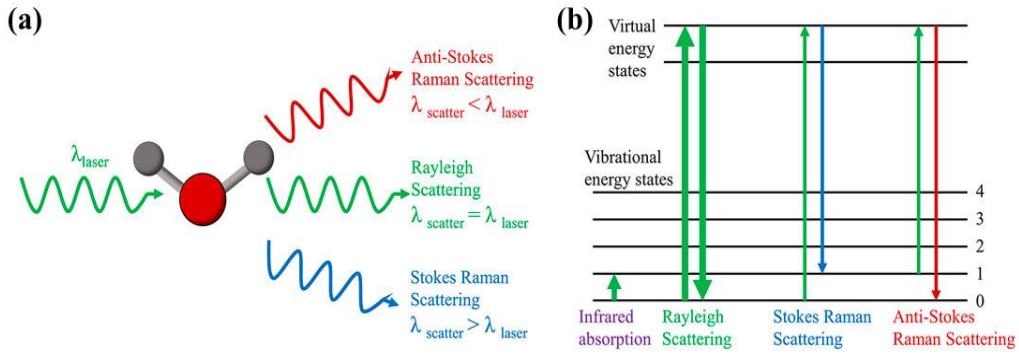

Figure 3.5: Raman Scattering. (a) Diagram of the interaction of light with a molecule and the scattering events possible. (b) Energy level diagram of Rayleigh, Stokes Raman and Anti-Stokes Raman Scattering and Infrared absorption. Adapted and reproduced with permission from Ref.[17].

Raman Spectroscopy is based on the Raman effect which was first identified by Chandrasekhara Venkata Raman in 1928 and which he also received the Nobel Prize in Physics for in 1930.[16] When light interacts with a molecule, the majority of the photons are elastically scattered at the same frequency which is known as Rayleigh scattering, however, about 1 in 10 million photons are scattered at a different frequency and this inelastic process is known as Raman scattering. The inelastically scattered photon can be

shifted to a higher energy (shorter wavelength) which is known as Anti-Stokes scattering or to a lower energy (longer wavelength) known as Stokes scattering (Figure 3.5).[17] For Raman measurements we focus on the Stokes scattering for analysis as for Anti-Stokes scattering the molecules have to be vibrationally active prior to measurement.[18] Although similar to FTIR in that it is a form of vibrational spectroscopy, Raman scattering relies on the change in the polarizability of a molecule. A temporary induced dipole moment (p) across the molecule is caused due to the molecular polarizability (α), where the polarizability is the deformability of the electron cloud about the molecule by an external electric field (E) from the source radiation,[19] as shown in Equation 3.14.

$$p = \alpha E \tag{3.14}$$

Raman and FTIR are normally used complimentary to one another as FTIR is normally more sensitive to specific polar functional groups such as -OH groups whilst Raman is sensitive to the molecular framework of a molecule such as the carbon framework in SWCNTs. Raman measurements were performed using a Horiba Raman system (LabRAM ARAMIS HORIBA Jobin Yvon) with integrated LabSpec 5 software. The objective lens was 100x (0.90 NA) and the laser wavelength was 524 nm. Spectra were recorded by defining a 10 µm x 10 µm area with a step size of 5 µm with an integration time of 2 s used for each scan.

3.6 Nitrogen adsorption and BET analysis

Physical gas adsorption (physisorption) on a solid/porous surface may be used to calculate the specific surface area using Brunauer-Emmett-Teller (BET) theory. The adsorption of gases onto a surface may happen either through chemisorption; whereby chemical bonds are formed between the surface and the adsorbate with an activation energy required or by physisorption; whereby the adhesion of the adsorbate molecules to the surface is the result of the same intermolecular forces for the imperfection of real gases and condensation vapours (attractive dispersion forces).[20] Physical adsorption may be recognised by its reversibility and the fact that the quantity of gas adsorbed at a given pressure increases with decreasing temperature.[21] Nitrogen (at boiling point of 77K) is typically used for adsorption measurements, in which the volume of gas adsorbed is measured as a function of the partial pressure. The BET equation is a generalization of

Langmuir's theory for monolayer adsorption,[22] and is presented in Equation 3.15; where V is the specific volume of gas adsorbed at relative pressure P/P_o, V_m is the specific monolayer capacity and c is termed the BET constant and is exponentially related to the energy of the monolayer adsorption.[20]

$$\frac{P/P_0}{V[1-P/P_0]} = \frac{1}{V_m c} + \frac{c-1}{c}\frac{P/P_0}{V_m} \tag{3.15}$$

Through linearisation of the adsorption isotherm obtained, which is in the form of $1/V$ *vs* P/P_0 using Equation 3.15, one may obtain the values of V_m and c from the graph as:

$$V_m = \frac{1}{Slope + Intercept} \quad , \quad c = 1 + \frac{Slope}{Intercept} \tag{3.16}$$

Once V_m is known, the specific surface area (S_{BET}) of the adsorbent (sample) of mass m may be calculated using Equation 3.17, where N_a is Avogadro's number, σ is the molecular cross-sectional area of the adsorbate molecule (for N_2 it is 0.162 nm^2) and M_v is the molar volume of the adsorbent:

$$S_{BET} = \frac{V_m N_a \sigma}{M_v m} \tag{3.17}$$

The BET plot is limited to ranges for P/P_0 of ~ 0.05 – 0.30 depending on the shape of the isotherm.[20,21]

Nitrogen adsorption at 77K was measured using a Quantachrome Autosorb-IQ. Prior to the measurements, each sample (+/- 200 mg) has been activated overnight at 150 °C under secondary vacuum. In a typical experiment, adsorption curves have been measured in the range of 0.0001 – 0.99 P/P_0, and desorption curves in the range of 0.99 – 0.3 P/P_0. To determine the pore volume, the Gurvich rule was used at 0.95 P/P_0.[20] This method assumes that the pressure is high enough so the nitrogen in the pores is actually in a bulk liquid state. Limiting the value at 0.95 is also used to avoid considering macropores and inter-particle voids.

3.7 References

1. Elgrishi, N. *et al.* A Practical Beginner's Guide to Cyclic Voltammetry. *J. Chem. Educ.* **95**, 197–206 (2018).
2. Gharbi, O., Tran, M. T. T., Tribollet, B., Turmine, M. & Vivier, V. Revisiting cyclic voltammetry and electrochemical impedance spectroscopy analysis for capacitance measurements. *Electrochim. Acta* **343**, 136109 (2020).
3. Basics of EIS: Electrochemical Research-Impedance Gamry Instruments. https://www.gamry.com/application-notes/EIS/basics-of-electrochemical-impedance-spectroscopy/.
4. Aguedo, J., Lorencova, L., Barath, M., Farkas, P. & Tkac, J. Electrochemical Impedance Spectroscopy on 2D Nanomaterial MXene Modified Interfaces: Application as a Characterization and Transducing Tool. *Chemosensors* vol. 8 (2020).
5. Williams, D. B. & Carter, C. B. *Transmission Electron Microscopy: A Textbook for Materials Science*. (Springer, 2009). doi:10.1007/978-1-61779-415-5_23.
6. Goldstein Joseph I. *et al. Scanning Electron Microscopy and X-ray Microanalysis*. *Scanning Electron Microscopy and Xray Microanalysis* (2003). doi:10.1007/978-1-4615-0215-9.
7. Gleichmann, N. SEM vs TEM | Technology Networks. *Technology Networks* https://www.technologynetworks.com/analysis/articles/sem-vs-tem-331262 (2020).
8. Bragg, W. L. & Bragg, W. H. The structure of some crystals as indicated by their diffraction of X-rays. *Proc. R. Soc. London. Ser. A, Contain. Pap. a Math. Phys. Character* **89**, 248–277 (1913).
9. BRAGG, W. L. The Specular Reflection of X-rays. *Nature* **90**, 410 (1912).
10. Bunaciu, A. A., Udriştioiu, E. gabriela & Aboul-Enein, H. Y. X-Ray Diffraction: Instrumentation and Applications. *Crit. Rev. Anal. Chem.* **45**, 289–299 (2015).
11. Patterson, A. L. The Scherrer Formula for X-Ray Particle Size Determination. *Phys. Rev.* **56**, 978–982 (1939).
12. Einstein, A. Über einen die Erzeugung und Verwandlung des Lichtes betreffenden heuristischen Gesichtspunkt. *Ann. Phys.* **322**, 132–148 (1905).
13. Nordling, C., Sokolowski, E. & Siegbahn, K. Precision Method for Obtaining Absolute Values of Atomic Binding Energies. *Phys. Rev.* **105**, 1676–1677 (1957).
14. Stevie, F. A. & Donley, C. L. Introduction to x-ray photoelectron spectroscopy. *J. Vac. Sci. Technol. A* **38**, 63204 (2020).
15. Stuart, B. Infrared Spectroscopy. in *Kirk-Othmer Encyclopedia of Chemical Technology* (2005). doi:https://doi.org/10.1002/0471238961.0914061810151405.a01.pub2.
16. RAMAN, C. V & KRISHNAN, K. S. A New Type of Secondary Radiation. *Nature* **121**, 501–502 (1928).
17. Liu, K., Zhao, Q., Li, B. & Zhao, X. Raman Spectroscopy: A Novel Technology for Gastric Cancer Diagnosis . *Frontiers in Bioengineering and Biotechnology* vol. 10 (2022).
18. Introduction to Raman Spectroscopy techniques- Oxford Instruments. https://andor.oxinst.com/learning/view/article/raman-spectroscopy.
19. Larkin, P. J. Chapter 2 - Basic Principles. in (ed. Larkin, P. J. B. T.-I. and R. S. (Second E.) 7–28 (Elsevier, 2018). doi:https://doi.org/10.1016/B978-0-12-804162-8.00002-1.

20. Thommes, M. *et al.* Physisorption of gases, with special reference to the evaluation of surface area and pore size distribution (IUPAC Technical Report). **87**, 1051–1069 (2015).
21. Dollimore, D., Spooner, P. & Turner, A. The bet method of analysis of gas adsorption data and its relevance to the calculation of surface areas. *Surf. Technol.* **4**, 121–160 (1976).
22. Brunauer, S., Emmett, P. H. & Teller, E. Adsorption of Gases in Multimolecular Layers. *J. Am. Chem. Soc.* **60**, 309–319 (1938).

4. Synthesis and Characterisation of Tin(II) Oxide

This Chapter will deal with the synthesis of SnO and the subsequent characterisation of the material. The synthesised SnO was used in Chapters 5,6 and 7.

4.1 Wet Chemistry Synthesis of Tin(II) Oxide

Synthesis of micro and nanomaterials can be subdivided into two categories; the top-down approach in which a larger piece of material is broken down into nano/micro-sized entities or the bottom-up approach in which atomic or molecular species are integrated to form nano/micro structures.[1] The top-down approach requires complex and energy-intensive setups to proceed, and even with these setups particles with surface defects and non-uniform shapes may be produced which limit their potential use.[1] The bottom-up approach however, is largely based on wet chemical synthesis which is relatively simple, cost-effective, scalable and able to achieve superior control over the nanostructure.[1,2] For these reasons the wet chemical synthesis of SnO was undertaken for this study.

To date, the majority of SnO syntheses require highly basic pH and/or hydrothermal conditions which can limit the scalability of the synthesis.[3–8] For example Uchiyama *et al.*[6] produced SnO nanoflowers in highly basic conditions (pH 13.0 – 13.3) using a concentrated SnF_2 precursor (0.5 M) in an autoclave. This complicated approach is not suited for industrial-scale production owing to the precise conditions, especially the pH-range and the size limitations of the autoclave. Sun *et al.*[5] similarly utilised a hydrothermal synthesis, which was limited by the size of the autoclave. From the literature, the oxide particle's nucleation and crystal growth produced by the hydroxide decomposition reaction seems to be highly dependent on solvent polarity and the coordinated ligands.[9–11] This is likely a result of the control over the hydrolysis of the intermediate reaction.[12] It was decided to utilise a simple hydroxide decomposition reaction for the production of SnO and investigate the role of the solvent used on the morphology of the end product. The synthesis also avoided the use of hydrothermal conditions in the interest of cost and scalability.[13,14] Instead a simple reflux reaction at ambient pressure/atmosphere was undertaken. Through tailoring the morphology of the end product through the synthesis, it was envisioned that the SnO could be optimised toward energy storage applications whilst also avoiding the costly top down approach to produce nanoscale materials.

Solvent Engineered Tin(II) Oxide Synthesis

Layered SnO particles were produced in a two-step reaction process as detailed in the experimental section. In the first step, a white precipitate of tin oxide-hydroxide ($Sn_6O_4(OH)_4$) was obtained as confirmed by XRD analysis (JCPDS no. 46-1486) (Figure 4.1B), which appeared as small nanoparticles with no defined structure from the SEM analysis (Figure 4.1A) consistent with previous work using similar precursors carried out by Kitabayashi *et al.*[15]

$$6SnCl_2 + 12NH_4OH \rightarrow Sn_6O_4(OH)_4 + 12NH_4Cl + 4H_2O \quad (4.1)$$

$$Sn_6(OH)_4 \cdot nH_2O \xrightarrow{EtOH} 6SnO + (n+1)H_2O$$

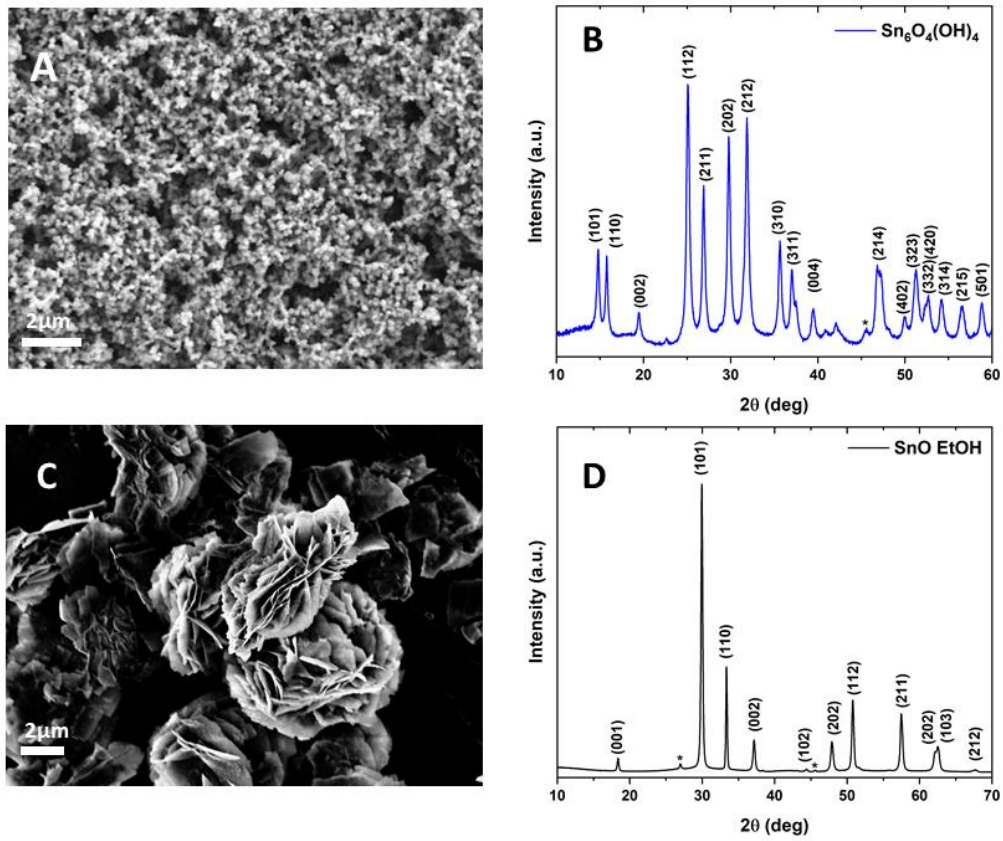

Figure 4.1: (A) SEM image of $Sn_6O_4(OH)_4$ and (B) corresponding XRD pattern. (C) SEM image of SnO produced in ethanol and (D) corresponding XRD pattern. The asterisk indicates an equipment peak.

In the second step, the thermal decomposition of the tin-oxide hydroxide occurred in the presence of an alcohol, water, or an alcohol:water mixture under reflux (shown with ethanol in Equation 4.1, please note there is no risk of oxidation to SnO_2 as the

temperatures used are well below those needed to induce this transformation which occurs at 500º C). Refer to Section 4.4 for the exact parameters used. The presence of pure SnO was confirmed by XRD (Romarchite phase SnO, JCPDS 06-0395) (Figure 4.1D) and an example of the crystalline structure available through this synthesis is shown in Figure 4.1C.

Solvent Effect on Morphology

The hydroxide-to-oxide transformation was observed only when the solvent was boiling. For ethanol (boiling point 78 ºC), SnO nanoflowers were produced (Figure 4.2A). Nanoflower morphologies of SnO have been reported previously using highly basic conditions (current work was neutral) and/or hydrothermal conditions at temperatures exceeding solvent boiling points (current work was at atmospheric pressure).[4,5,7] To demonstrate the scalability for potential industrial applications, we expanded the synthesis to a 1-L flask (10-fold increase in reactants) with the SEM images confirming no changes in the SnO product (Appendix B, Figure B.1A). Additional alcohols of methanol, 1-propanol, 1-butanol, 1-hexanol and water were investigated to see the effect on the SnO morphology by changing the properties of the solvent used for reflux (boiling point, chain length, polarity).

SnO particles produced in 1-hexanol have perforated thick-squares (Figure 4.2C) and were significantly thicker in comparison to ethanol and other shorter chained alcohols tested (1-propanol, 1-butanol) (Appendix B, Figure B.1B and C). Similarly thick squares with a high degree of crystallinity were produced when water was used as the solvent (Figure 4.2D), with no perforation visible from the SEM images. The formation of these thick structures in water is most likely a result of the higher surface tension, density and dipole moment of water in comparison to shorter alcohols. SnO was also produced using an optimum 70:30 ratio of methanol:water, which produced thin-square platelet structures (Figure 4.2B). The hydroxide-to-oxide formation was not observed for pure methanol, most likely owing to its low boiling point (65 ºC), so water addition was incorporated. However, just a 10% water addition was sufficient to induce the hydroxide-to-oxide formation with increments of 20% tested (Appendix B, Figure B.2). As the water content was increased, SnO particles became larger and thicker as the polarity of the system was increased.

A comprehensive report on this work regarding solvent effects on the morphology of SnO was co-authored by myself along with Jaśkaniec *et al.*[12] Within this work, it was found that the solvent-morphology relationship is very complex with polarity and reaction temperature key factors. Particular solvents (70:30 methanol:water, ethanol) adsorb selectively on specific crystal planes directing the crystal growth in certain directions, which results in the thin platelet-like morphologies observed. Samples produced in longer carbon-chain alcohols are much bulkier, as a result of the higher surface tension for these solvents in comparison to shorter chained-alcohols. Computational work using density functional theory (DFT) was carried out by Seán Kavanagh relating the surface shapes obtained to the Gibbs-Wulff theorem which states that the shape of a crystalline material is given by the polyhedron that minimizes the overall surface shape. The predicted structures agreed well with the SnO produced in water, 1-butanol and 1-hexanol; whilst the in vacuo equilibrium shape predicted deviates from those produced in shorter chained alcohols demonstrating the complex relationship solvent properties have on nanoparticle morphology.

For the scope of this PhD fellowship into energy storage applications, four suitable morphologies were selected from this study; SnO produced in ethanol (nanoflowers), 1-hexanol (perforated thick squares), 70:30 methanol:water (platelets) and water (thick squares) as shown in Figure 4.2. These morphologies were selected as they encompass the unique dimensions/features of SnO obtainable through the solvent-engineered synthesis utilised. Thus, these morphologies would allow an insight into the effect of SnO morphology on energy storage applications in LIBs, NIBs and SCs.

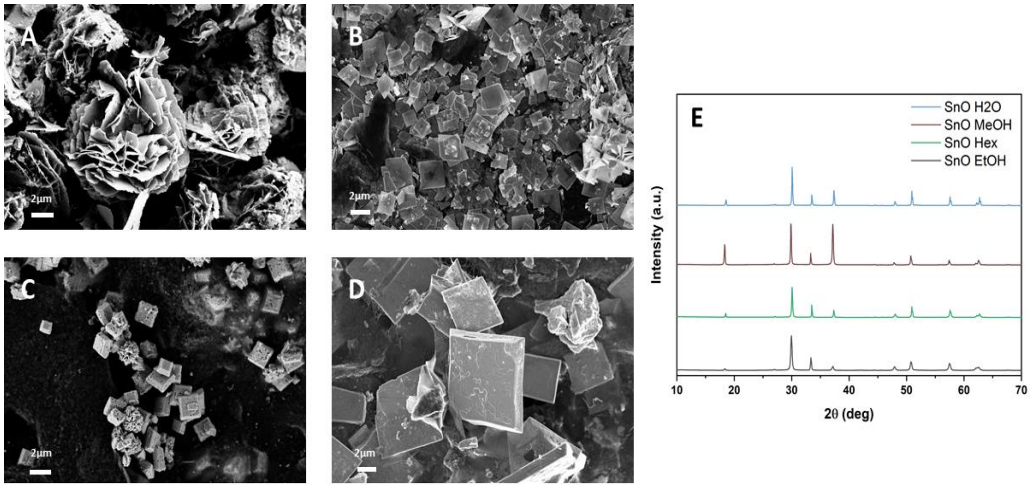

Figure 4.2: SEM images of SnO produced in (A) ethanol, (B) 70:30 methanol:water, (C) 1-hexanol, (D) water and the corresponding XRD patterns (E).

4.2 SnO Characterisation

The XRD data presented in Figures 4.1D and 4.2E confirm that the synthesised material was indeed SnO with a tetragonal crystal structure with space group P4/*nmm* (No. 129).[16] This is known as the romarchite structure of SnO with lattice parameters $a = b = 3.802$ Å, $c = 4.836$ Å and $\alpha = \beta = \gamma = 90^{o}$.[4] No other diffraction peaks inconsistent with the proposed structure were observed suggesting that all the samples produced were of high purity. SEM and XRD were also carried out on commercially produced SnO from Sigma Aldrich (SA) which displayed an identical crystal structure, although a much larger crystallite size when compared to the synthesised product (Appendix B, Figure B.3). The XRD spectra of the SnO produced in 70:30 methanol:water displays greater peak intensities for the peaks at 18º ({001}) and 37º ({002}). This indicates a preferential orientation of the crystallites within the platelets along these crystal directions, which often occurs when these crystal planes align with the Miller index of the particle surface.[6,17–19]

TEM Characterization of SnO produced in methanol:water

TEM characterization was carried out on the sample produced in 70:30 methanol:water due to its thin 2D nature, consequently being more suitable than the other samples towards TEM. TEM analysis (Figure 4.3A) confirmed that the material consists of single square platelets with a side length of ~3 μm (particle size distribution histogram – Appendix B, Figure B.4A). The size distribution of the perforated squares (side length ~1.8 μm) , and thick-squares (side length ~8.7 μm) are also included in Appendix B, Figure B.4B/C (nanoflower not included as it is composed of irregular platelets forming irregular shapes).

The selected area diffraction pattern (SAED) in Figure 4.3B demonstrated high crystallinity, also confirming the presence of tetragonal crystal symmetry, with the indexed pattern's spacing in agreement with that obtained from XRD (Appendix B, Figure B.5 and Table B.1). High-resolution TEM (HRTEM) of the sample perpendicular to the (001) plane provides additional evidence of the high quality of the sample produced. The TEM micrograph (Figure 4.3A) revealed that primarily formed platelets serve as nucleation centres for further crystal growth, with this statement being additionally supported by the electron energy thickness map in Figure 4.3C, where regions of higher intensity clearly indicate crystal formation on top of existing formed structures. This is interesting when one considers the similarities between the platelets and the nanoflower structures produced in ethanol.

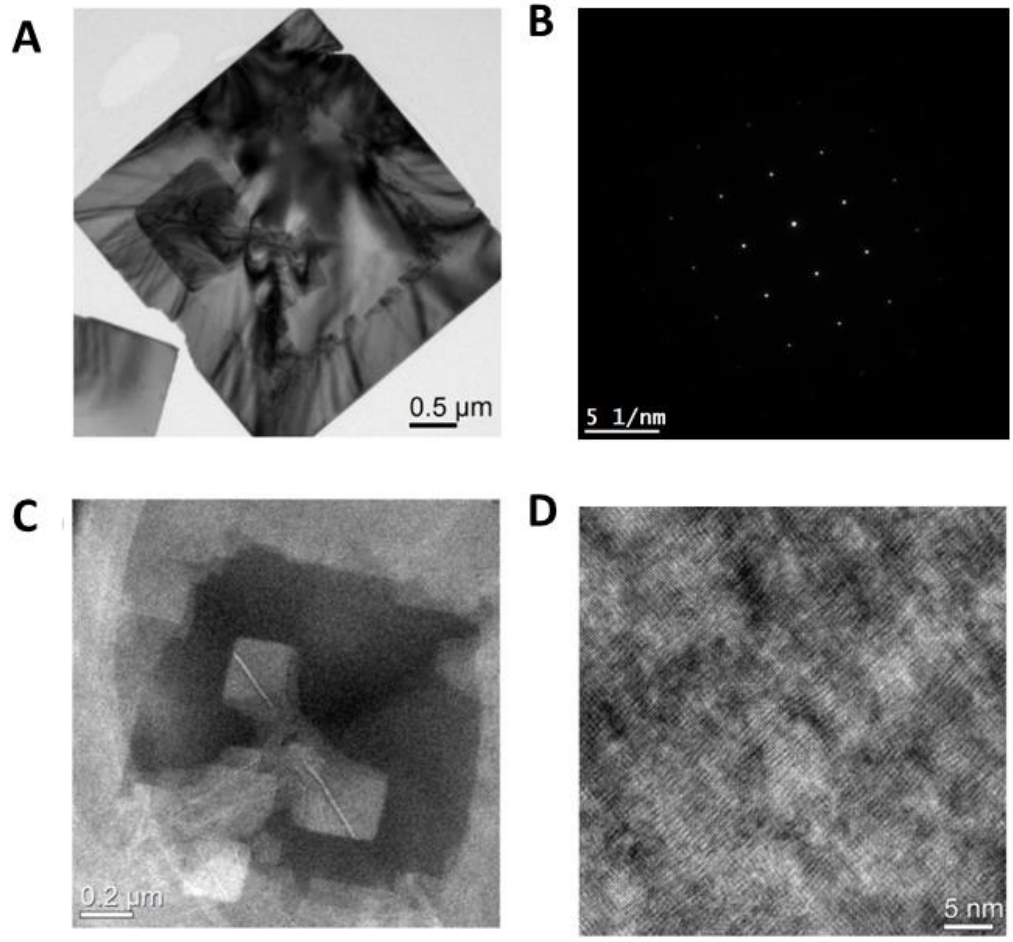

Figure 4.3: (A) TEM micrograph of SnO platelet produced in 70:30 methanol:water, (B) corresponding selected area diffraction pattern, (C) energy electron loss thickness map of SnO platelet and (D) HRTMEM micrograph of SnO platelet. TEM was performed by Dr Christopher Hobbs and Dr Oskar Ronan.

The exact growth mechanism of the nanoflowers is not known as of yet, with M.Z Iqbal *et al*[4,20] hypothesising that square sheets initially form, transforming into square-based

pyramids as a result of increasing the reaction time which subsequently divides into stepped pyramids and skeletal structures which forms the basis for the nanoflowers (Appendix B, Figure B.6). The results obtained in this current study provides additional evidence for this supposed mechanism.

Nitrogen Adsorption and BET analysis of synthesised SnO

Nitrogen adsorption at 77 K of the synthesised SnO and commercially produced SnO by SA was carried out to determine the specific surface area of the materials. The adsorption isotherms and corresponding specific BET surface areas and specific pore volumes are presented in Figure 4.4 and Table 4.1 (Appendix B, Figure B.7). The isotherms confirm the porosity of all samples present. The BET surface areas for all synthesised samples were larger than that of the commercially produced SnO by SA, with all samples being at least 400% larger in specific area except for the sample produced in 1-hexanol which was only 25% larger, with the pore volumes following a similar trend. The nanoflower morphology produced in ethanol had the largest specific area of 31.66 m^2 g^{-1} and pore volume of 0.06116 cm^3 g^{-1}.

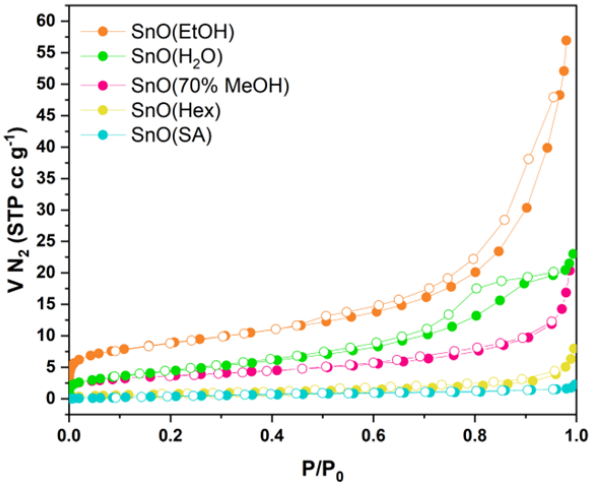

Sample	BET surface (m^2 g^{-1})	Pore Volume (cm^3 g^{-1})
Ethanol	31.66	0.06166
Water	16.62	0.03037
70% Methanol	12.98	0.01834
1-Hexanol	3.051	0.005966
Sigma Aldrich	2.406	0.002287

Figure 4.4: N_2 adsorption isotherms of SnO synthesised in various solvents; measurements were carried out by Dr Sebastien Vaesen.

Table 4.1: Corresponding specific pore volume and specific BET area.

All materials display isotherm behaviours consistent with macroporous materials (pore size >50 nm) made of plate-like particles (Type II + H3 hysteresis) except SnO produced in water which displays a Type IVa isotherm revealing the presence of mesopores (>2 nm; <50 nm), the hysteresis indicating a pore size wider than 4 nm. This sample also

presents a small steep increase around P/P_0 = 1, which could be attributed to nitrogen condensation in the interparticle voids.[21–23] Interestingly, the thick-squares produced in H_2O are slightly larger in surface area than the thin platelets produced with 70% methanol, which is contrary to what one would expect from examining the SEM images (Figure 4.2). This would indicate that the space in between the individual layers composing the thick-squares is accessible to the N_2 molecule (Figure 4.5). The nanoflower SnO combines the thin platelet morphology with interlayer separation which is the reason for it possessing the greatest BET surface area, whilst the perforated thick squares produced in hexanol has the lowest BET surface area of the synthesised materials due to its bulky structure with no layer separation apparent from SEM (Figure 4.2).

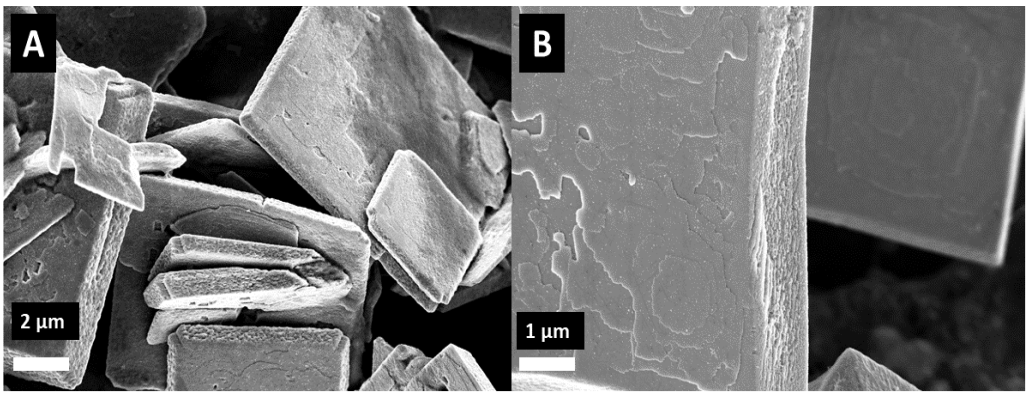

Figure 4.5: (A) and (B) SnO produced in H_2O showing individual layers composing thicker squares.

4.3 Conclusions

The wet chemical synthesis of SnO was investigated, with the influence of the solvent used during reflux having a major influence on the morphology obtained. The methodology used allows for a facile two-step synthesis of tuneable morphologies of SnO at ambient pressure and atmosphere, which was also demonstrated to be scalable. Various high quality morphologies of SnO were synthesised, without requiring the use of hydrothermal conditions or a highly basic pH. Through our investigation, we established that more polar solvents produced bulkier morphologies, as a result of the higher surface tension, density and dipole moment in comparison to shorter chain alcohols. Samples produced in longer carbon-chain alcohols are much bulkier, as a result of the higher surface tension for these solvents in comparison to shorter chain alcohols. Most probably, particular solvents (70:30 methanol:water, ethanol) adsorb selectively on specific crystal planes directing the crystal growth in certain directions, which results in the thin platelet-like morphology, whilst the longer chained solvents such as 1-hexanol with additional

London dispersion forces present would attract more solvent molecules inhibiting preferential growth. In addition, DFT calculations linked the shapes obtained for certain solvents (1-butanol, 1-hexanol, water) with those predicted with the thermodynamically favoured crystal shape in vacuo (Gibbs-Wulff construction). The in-vacuo equilibrium shape predicted deviates from those produced in shorter chain alcohols demonstrating the complex relationship between solvent properties and nanoparticle morphology.

Four unique morphologies were selected for further investigations into energy storage; nanoflowers, platelets, perforated thick squares and thick squares. These morphologies were selected as they encompassed all the unique structural features that could be obtained through the solvent-engineered synthesis, and thus we could investigate the effects of these unique morphologies on energy storage applications. The TEM carried out on the platelets demonstrated the high crystallinity and quality of the synthesised material. N_2 adsorption coupled with BET analysis demonstrated the higher surface areas obtainable through the synthesis used compared to purchasing via a commercial producer, whilst also demonstrating the difference in surface areas obtainable through the synthetic approach developed. The SnO structures developed in this Chapter are investigated as LIB anodes (Chapter 5), NIB anodes (Chapter 6) and SC electrodes (Chapter 7).

4.4 Experimental

Synthesis of SnO

$SnCl_2$ (7.584 g, 0.04 mol, anhydrous, 98%, Alfa Aesar) was dissolved in ice-cold distilled water (400 ml) and placed on a magnetic stirring plate. NH_4OH (12.8 ml, 0.08 mol, 25%, Merck) was added dropwise and left to stir for 1 hour. The solution was transferred to centrifuge tubes and separated in the centrifuge (Heraeus Multifuge x1 Centrifuge) at 5000 rpm for 5 minutes. The $Sn(OH)_2$ precipitates were washed with distilled water (twice) and ethanol (once) before being re-dispersed in ethanol in a 100 ml round-bottom flask and heated at 120 °C for 24 hours under reflux. The product was again separated via centrifuge, repeating the wash procedure as above. The final product was kept in ethanol solution and dried as needed, to minimise the risk of oxidation to SnO_2. This method was the template for all morphologies of SnO produced, only substituting the ethanol for other solvents.

4.5 References

1. Nikam, A. V, Prasad, B. L. V & Kulkarni, A. A. Wet chemical synthesis of metal oxide nanoparticles: a review. *CrystEngComm* **20**, 5091–5107 (2018).
2. Tan, C. & Zhang, H. Wet-chemical synthesis and applications of non-layer structured two-dimensional nanomaterials. *Nat. Commun.* **6**, 7873 (2015).
3. Zhang, F., Zhu, J., Zhang, D., Schwingenschlögl, U. & Alshareef, H. N. Two-Dimensional SnO Anodes with a Tunable Number of Atomic Layers for Sodium Ion Batteries. *Nano Lett.* **17**, 1302–1311 (2017).
4. Iqbal, M. Z. *et al.* Structural and electrochemical properties of SnO nanoflowers as an anode material for lithium ion batteries. *Scr. Mater.* **67**, 665–668 (2012).
5. Sun, Y.-H., Dong, P.-P., Lang, X. & Nan, J.-M. A novel rose flower-like SnO hierarchical structure synthesized by a hydrothermal method in an ethanol/water system. *Chinese Chem. Lett.* **25**, 915–918 (2014).
6. Uchiyama, H., Ohgi, H. & Imai, H. Selective Preparation of SnO2 and SnO Crystals with Controlled Morphologies in an Aqueous Solution System. *Cryst. Growth Des.* **6**, 2186–2190 (2006).
7. Ávila, H. A. & Rodríguez-Páez, J. E. Solvent effects in the synthesis process of tin oxide. *J. Non. Cryst. Solids* **355**, 885–890 (2009).
8. Huda, A., Handoko, C. T., Bustan, M. D., Yudono, B. & Gulo, F. New route in the synthesis of Tin(II) oxide micro-sheets and its thermal transformation. *Mater. Lett.* **211**, 293–295 (2018).
9. Ning, J. *et al.* Syntheses, Characterizations, and Applications in Lithium Ion Batteries of Hierarchical SnO Nanocrystals. *J. Phys. Chem. C* **113**, 14140–14144 (2009).
10. Ejaz, A. & Jeon, S. The insight study of SnO pico size particles in an ethanol-water system followed by its biosensing application. *Biosens. Bioelectron.* **117**, 129–137 (2018).
11. Ungula, J. & Dejene, B. F. Effect of solvent medium on the structural, morphological and optical properties of ZnO nanoparticles synthesized by the sol–gel method. *Phys. B Condens. Matter* **480**, 26–30 (2016).
12. Jaśkaniec, S. *et al.* Solvent engineered synthesis of layered SnO for high-performance anodes. *npj 2D Mater. Appl.* **5**, 27 (2021).
13. Asim, N. *et al.* Research and Development Aspects on Chemical Preparation Techniques of Photoanodes for Dye Sensitized Solar Cells. *Int. J. Photoenergy* **2014**, 518156 (2014).
14. Abid, N. *et al.* Synthesis of nanomaterials using various top-down and bottom-up approaches, influencing factors, advantages, and disadvantages: A review. *Adv. Colloid Interface Sci.* **300**, 102597 (2022).
15. Kitabayashi, S. & Koga, N. Thermal Decomposition of Tin(II) Oxyhydroxide and Subsequent Oxidation in Air: Kinetic Deconvolution of Overlapping Heterogeneous Processes. *J. Phys. Chem. C* **119**, 16188–16199 (2015).
16. Pannetier, J. & Denes, G. Tin(II) oxide: structure refinement and thermal expansion. *Acta Crystallogr. Sect. B* **36**, 2763–2765 (1980).
17. Singh, M. *et al.* Soft exfoliation of 2D SnO with size-dependent optical properties. *2D Mater.* **4**, 25110 (2017).
18. Liang, L., Sun, Y., Lei, F., Gao, S. & Xie, Y. Free-floating ultrathin tin monoxide sheets for solar-driven photoelectrochemical water splitting. *J. Mater. Chem. A* **2**, 10647–10653 (2014).
19. Okamura, K., Nasr, B., Brand, R. A. & Hahn, H. Solution-processed oxide

semiconductor SnO in p-channel thin-film transistors. *J. Mater. Chem.* **22**, 4607–4610 (2012).
20. Iqbal, M. Z. *et al.* Facile synthesis of self-assembled SnO nano-square sheets and hydrogen absorption characteristics. *Mater. Res. Bull.* **47**, 3902–3907 (2012).
21. Thommes, M. *et al.* Physisorption of gases, with special reference to the evaluation of surface area and pore size distribution (IUPAC Technical Report). **87**, 1051–1069 (2015).
22. Thommes, M. & Cychosz, K. A. Physical adsorption characterization of nanoporous materials: progress and challenges. *Adsorption* **20**, 233–250 (2014).
23. Alothman, Z. A. A Review: Fundamental Aspects of Silicate Mesoporous Materials. *Materials* vol. 5 2874–2902 (2012).

5. Tin(II) Oxide as a Lithium-Ion Battery Anode

This Chapter will discuss the investigation into the use of solvent-engineered SnO as an anode in LIBs. As discussed in Chapter 2, the motivation for this investigation is due to the enhanced gravimetric capacity available through the use of SnO, whilst also the enhanced stability due to the presence of an oxide matrix for the reversible alloying reaction.

To date, the majority of the research carried out on SnO_x compounds in LIBs have focused upon SnO_2 due to its thermodynamic stability, however, it presents a lower gravimetric capacity and a much larger contribution to the amount of inactive lithium present in the battery due to the doubling of the oxygen content present. Recent work of note carried out on SnO_2 has been done by Hu *et al.*[1] in which a reversible capacity of ~800 mAh g^{-1} was achieved for over 200 cycles, however, in this particular study, thin films prepared via high-vacuum magnetron sputtering were used which suggest issues with scalability and processing for commercial applications. *Li et al.*[2] developed porous SnO_2 hollow microspheres with a capacity fade over the first 100 cycles to 504 mAh g^{-1}, similar to the previous quoted work however the scalability remains a question as the synthesis required the use of hydrothermal reactors, which are volume limited. Investigations have also been carried out into the suitability of Sn_3O_4 as a LIB anode material with work carried out by Chen *et al.*[3] revealing a high initial charge in excess of 1,000 mAh g^{-1}, however the cycling stability of this work is of concern with a gradual decrease over the first 50 cycles from 1,200 to 500 mAh g^{-1}. As stated, to date the work carried out on SnO has been limited; Iqbal *et al.*[4] synthesised SnO nanoflowers with a capacity fade to 200 mAh g^{-1} after 25 cycles whilst Shin *et al.*[5] synthesised Sn-decorated SnO nanobranches, with a capacity retention of 502 mAh g^{-1} after 50 cycles, with no conductive carbon source or binder needed. Thus, due to the high theoretical capacity, potential for stable cycling and the limited previous work on the material, SnO was chosen to be investigated as a potential anode for LIBs.

5.1 Comparison Between Synthesised and Purchased SnO

Initial studies focused on the justification of synthesising the SnO using the solvent-engineered wet chemical synthesis developed in Chapter 4. Prior to investigating the

various morphologies obtainable through this synthesis developed, it was thought that it be prudent to first verify that tailoring the morphology and transitioning the dimensions of the material to the nanoscale would be beneficial for battery performance. To do this, synthesised material was compared to commercially purchased SnO from SA. Traditional slurry casting electrodes were formed by combining both the SnO synthesised in ethanol (SnO(EtOH)) and the SA product respectively with a binder and a conductive carbon source as is traditionally done in the field of batteries and is outlined in the experimental section of this Chapter.

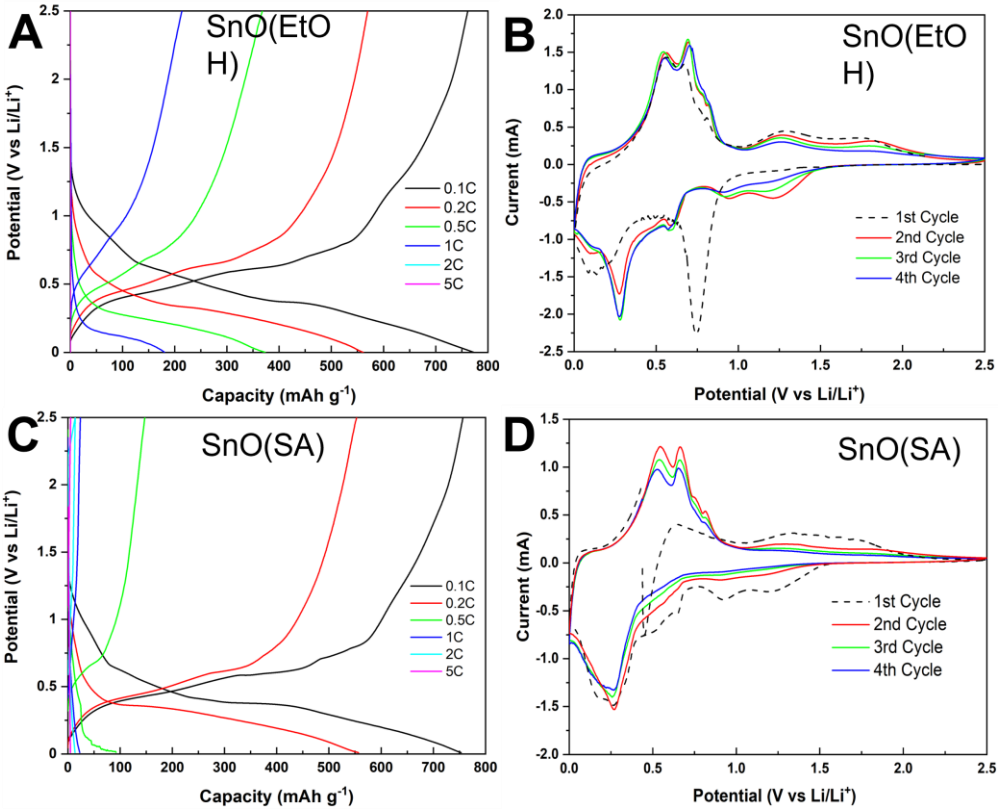

Figure 5.1: (A) GCD curves for the SnO(EtOH) electrode at various *C-rates*. (B) CV profile for the SnO(EtOH) at 0.1 mV s^{-1} scan rate. (C) GCD curves for the SA SnO electrode at various *C-rates*. (D) CV profile for the SA SnO at 0.1 mV s^{-1}.

The synthesised nanoflower morphology (SnO(EtOH)) displayed a superior energy storage performance with a capacity of 780 mAh g^{-1} compared to 750 mAh g^{-1} for that of the SA product at 0.1 C from 0.001 – 2.5 V vs Li^+/Li (Figure 5.1). Note that the listed capacities for this dissertation are for the total mass of the electrode unless otherwise stated (as opposed to active mass as it is felt this metric is a truer reflection of the obtainable capacity for the potential real-world device based on the composite and this PhD fellowship is driven towards manufacturing real-world devices). The most striking

difference however occurs when one looks at the anode performance upon increasing the charge/discharge rate. The synthesised SnO retains a capacity of 180 mAh g^{-1} at 1 C, whilst the SA SnO has essentially failed by 0.5 C (retaining less than 100 mAh g^{-1}). Upon investigation of the CV profiles of each anode (Figure 5.1B and D), differences again become apparent which may be explained with reference to the size and morphology of the materials. Both CVs display highly reversible behaviour excluding the initial cycle (a more detailed discussion on the characteristics of the CV will be provided in subsequent sections). Both the anodic and cathodic peaks are much sharper and more defined in the synthesised product than the SA SnO. The smooth and broad reaction peaks of the SA SnO suggest that the bulkier commercial material acted as a barrier to the Li_xSn alloying/dealloying reaction, consistent with previous work by Shin *et al.*[5] The synthesised nanoflower morphology with free volume provides the Li^+ ions with a shorter diffusion path and facilitates the alloying/de-alloying reactions, while in contrast, the dense SA structure acts as a diffusion barrier. Therefore, for higher rate capabilities, the synthesis must be driven towards highly porous nanocrystalline structures.[6]

5.2 Incorporation of Single-Walled Carbon Nanotubes in Anode

SnO(EtOH)/P3-SWCNT composite electrodes with varying mass fractions of P3-SWCNT were prepared and tested in LIB coin cells to identify at what P3-SWCNT mass fraction battery performance would be optimised. The SnO/P3-SWCNT composite electrodes were prepared using vacuum filtration whereby the composite was collected on a polyolefin separator film (same as used in the LIB coin-cell). All electrodes formed were of areal loading 1 mg cm^{-2}. SEM analysis confirmed that the P3-SWCNTs were mixed well within the SnO and dispersed evenly throughout. From Figure 5.2, one may see the P3-SWCNTs appearing as a thin 'web-like' structure encompassing the SnO particles. With increasing mass fractions of CNTs the coverage increases to fully encompass the nanoflowers as in Figure 5.2G. The P3-SWCNTs can be seen to cover the sample and in doing so provide a conductive carbon network which binds the sample together, which in turn removes the need for carbon black/polyvinylidene fluoride (PVDF) binder to be required to make the electrode as done previously with the slurry casting method.

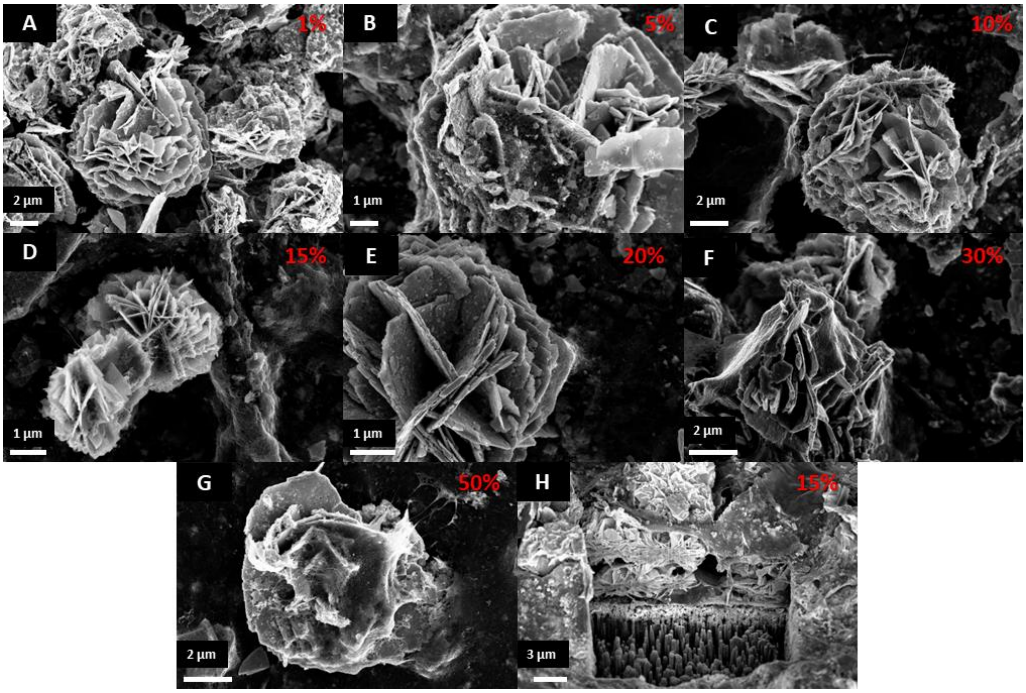

Figure 5.2: (A-G) SEM images of SnO/SWCNT composites. (H) FIB cross-section of SnO/SWNT composite.

Using focused ion-beam milling (FIB) to form a cross-section, the distribution of the SWCNTs within the electrode was further investigated for the 15% composite. From the SEM image of the cross-section formed (Figure 5.2H) it is seen that the SWCNTs form segregated networks within the electrode. These networks occur for particulate matrices with particle sizes which are larger than the nanotube length (microscale).[7] The excluded volume associated with the microparticles drives the formation of these segregated networks, where the SWCNTs form networked 2-D membranes which wrap and interconnect the active material.[7,8] If the active material present is nanoscale in all dimensions, the nanotubes will not form these networks and instead a homogeneous distribution will form throughout. The advantage of segregated networks is improved conductivity and the potential to fabricate thicker electrodes with higher robustness.[7,9]

By removing the need for the inactive copper foil, the energy density of the device is increased in addition to an increase in the depth of discharge and the ability to maintain a near-zero volt state of charge.[10] For example, in a slurry cast electrode of 12 mm diameter, roughly 10 mg of the mass is due to the copper base. For the same size electrode on a polyolefin separator, the weight drops to 1.5 mg or for free-standing electrodes which is obtainable with SWCNTs it drops to nil. Thus the effective gravimetric capacity is

maximised by transitioning away from the copper current collector, in addition to the costs saved by its removal.

Optimisation of SWCNT Mass Loading

The electrochemical performance of the SnO/P3-SWCNT composites with different P3-SWCNTs mass fractions (1 – 50%) was analysed using GCD measurements. As the P3-SWCNT% increases initially, more conductive networks are established resulting in a better rate capability and higher capacities as seen in Figure 5.3. The maximum specific capacity for the material was reached at a mass fraction of 15% P3-SWCNTs with a specific capacity of 897 mAh g^{-1} at 1 C (Figure 5.3). The far superior performance obtainable using SWCNTs is clearly indicated by this result, as using the same material in an electrode formed using the traditional slurry method as done in Section 5.1, the obtainable capacity at 1 C was less than 200 mAh g^{-1}. At this stage, a wider conductive network can connect more particles in the system, enabling more efficient transport of the stored charge to and from the current collector and therefore the capacity is maximised.[11] Additionally the impedance of the electrode gets reduced, and the overpotentials experienced with increased rates reduce in magnitude, allowing for more charge storage. At this point, higher concentrations of P3-SWCNTs no longer improve the composite capacity[12] but rather act to reduce capacity as the mass of active material is replaced with the P3-SWCNT network which is not suitable as an anode material(see the capacity of pure SWCNT electrode in Appendix Figure C.1).

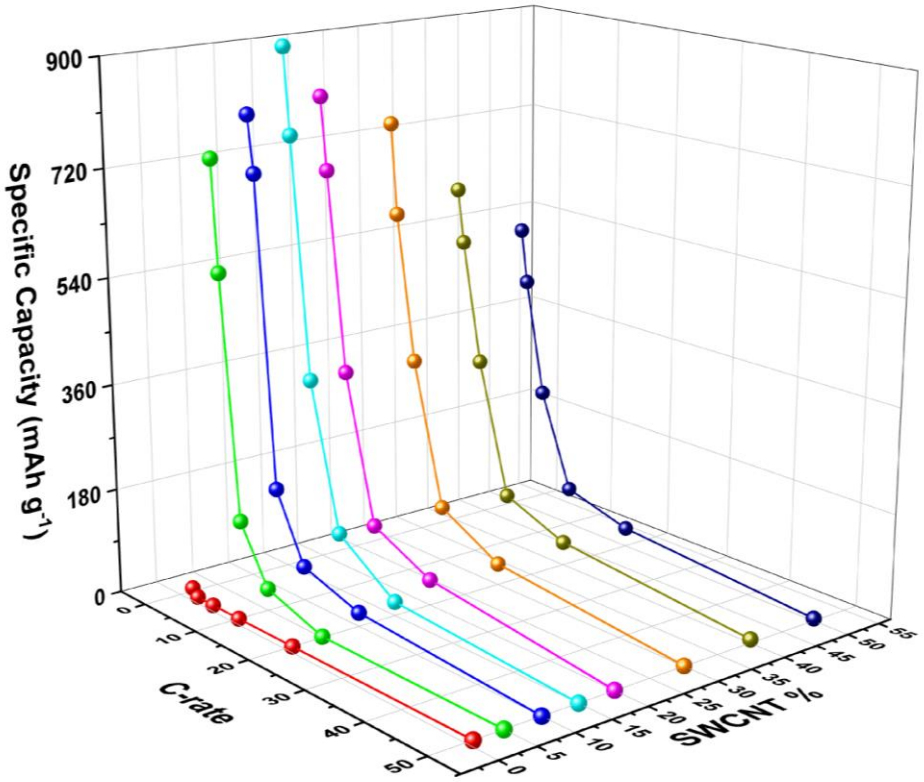

Figure 5.3: SnO/SWCNTs composite discharge capacities (5th cycle) as a function of carbon nanotubes mass fraction at different *C-rates*; *C-rates* on the x-axis, SWCNT% on the y-axis and specific capacity on the z-axis.

Using the GCD data obtained, a further investigation was carried out into the role of the SWCNT% on the battery performance using the semi-empirical model developed by Tian *et al.* (Equation 5.1) which links the capacity obtained by GCD curves to the physical parameters of the electrodes.[13] The semi-empirical model was developed from work carried out on rate-limited supercapacitors.[14,15]

$$\frac{Q}{M} = Q_M \left[1-(R\tau)^n\left(1- e^{-(R\tau)^{-n}}\right)\right] \tag{5.1}$$

Here Q/M is the measured rate-dependent specific capacity, Q_M is the low-rate specific capacity whilst τ is the characteristic time associated with the charge/discharge. τ is a measure of the minimum amount of time required to fully charge the device and the point at which the capacity starts to exponentially decay with rate, and is thus the critical factor in determining the rate performance.[13] The exponent n describes the decay behaviour in capacity at a high rate and indicates the rate-limiting mechanism of the cell. Its values are

generally comprised between 0.5 and 1, which corresponds to diffusive and resistive limitations respectively. *R* is the rate and is defined in Equation 5.2, where *I/M* is the specific current density and $(Q/M)_E$ represents the experimental measured specific capacity (at a given current). Note how this rate differs from the *C-rate*, which is defined in terms of theoretical capacity whereas *R* in this case has the advantage of relating directly to the experimental charge/discharge time of the cell by *1/R*.[13]

$$R = \frac{I/M}{(Q/M)_E} \tag{5.2}$$

A simulation of Equation 5.1 is shown in Figure 5.4A displaying the effect of the parameters discussed. It is worth mentioning that the GCD data for each sample is not always present in the same location as the experiment was initially launched in *C-rate* and then transformed using Equation 5.2. Using this model, the rate-dependent capacities can be fitted and the values of Q_M, τ and n can be extracted (note the log of Equation 5.2 was used for fitting/plotting the experimental data).

From the fitting of the GCD data, it is seen that the results obtained from the rate equation agree with those that were concluded from the initial observation of the data (Table 5.1). A mass fraction of 15% SWCNT gives the lowest value for τ (meaning it has the highest *R*-value before it begins decaying to the high-rate regime), and the largest Q_M. The value of n indicates it has a combination of both electrical and diffusion limitations in the high-rate regime. The drop in τ and subsequent saturation/increase after 15% mass fraction of SWCNTs is consistent with the literature study carried out using Equation 5.1 by Tian *et al.*[13] As the mass fraction of conductive additive is increased, so too does the conductivity of the electrode, thus allowing for more of the active mass to be utilised for charge storage whilst enabling faster charge/discharge rates. Above a saturation point (15% SWCNT in this case) more conductive additive is no longer advantageous as it is in excess and thus the gravimetric capacity will suffer, with the gravimetric capacity of SWCNTs alone being negligible (Appendix C, Figure C.1). From the results obtained, it was concluded that a mass fraction of 15% P3-SWCNT optimised the performance of the SnO(EtOH) electrode and it was elected to perform a study into the effects of the morphology using this mass loading. (Note that the 1% mass fraction SnO/P3-SWCNT electrode is omitted from the analysis as it failed to produce a working anode).

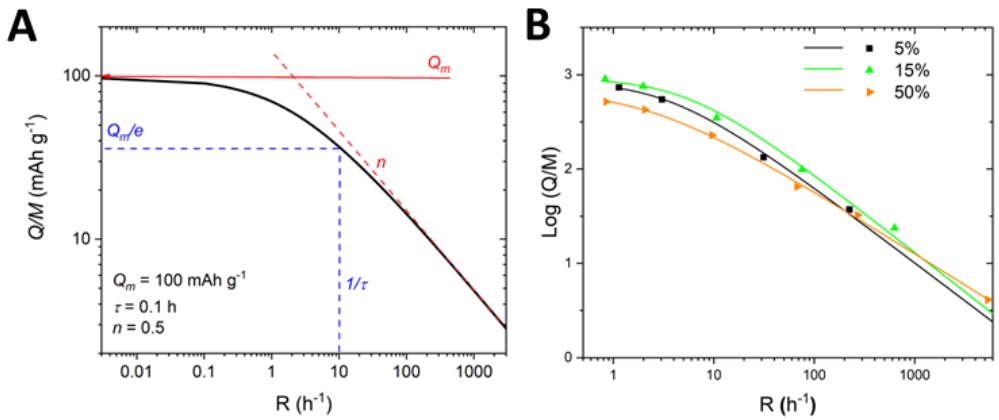

SWCNT %	Q_m (mAh g^{-1})	τ (h)	n
5	873	0.105	0.81
10	875	0.075	0.83
15	936	0.072	0.84
20	898	0.078	0.77
30	808	0.079	0.78
40	810	0.12	0.66
50	682	0.135	0.66

Figure 5.4: (A) Specific capacity plotted versus Rate Equation using the parameters indicated in the graph and displaying the effect of these parameters. (B) Selection of GCD experimental data fitted using Equation 5.1, see full dataset in Appendix Figure C.2.

Table 5.1: Parameters Q_M, τ and n for each mass fraction of SWCNT after fitting GCD data using Equation 5.1.

5.3 Investigation into the Effect of Morphology

As the SWCNT % had now been optimised, the focus of the study turned to investigating the effects of the various morphologies synthesised on the energy storage capabilities of a LIB anode. As discussed in the previous chapter, four unique morphologies were synthesised using 4 different solvents. Ethanol which produced SnO nanoflowers (Figure 5.5A), 70:30 methanol:water (70% methanol) which produced thin-square shaped platelets (Figure 5.5D), 1-hexanol which produced perforated thick-squares (Figure 5.5C) and water which produced squares (Figure 5.5D). All active materials were combined with a 15% mass fraction of SWCNTs and electrodes were formed via vacuum filtration, with SEM images displaying a homogenous distribution of SWCNTs around active material in the formed electrodes (Figure 5.5).

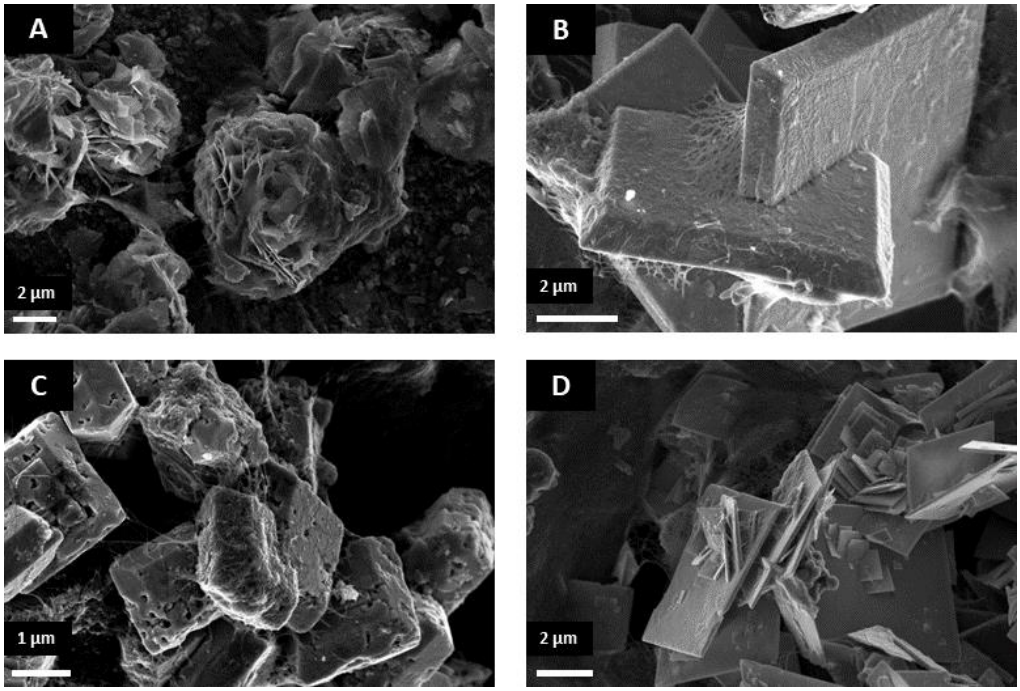

Figure 5.5: LIB electrodes formed using P3-SWCNT and SnO produced in (A) ethanol, (B) water, (C) 1-hexanol and (D) 70% methanol.

Rate Performance and Cyclability

These electrodes were used to manufacture half-cell LIBs with Li-foil as the counter electrode, and the specific capacities of the various morphologies were analysed using GCD testing at various *C-rates* as displayed in Figure 5.6A. The tested SnO of the various morphologies produced high-capacity anodes in all cases, with initial capacities (note that the initial formation cycle is not included in this plot as this would include the irreversible capacity owing to the SEI/Li_2O formation) in excess of 900 mAh g^{-1} for all SnO/P3 composites except that formed with SnO(H_2O) which still displayed a large initial capacity of 835 mAh g^{-1}. Capacities in excess of the expected theoretical capacity in this case suggest that the morphologies produced allow for the conversion reaction to be partially reversible at least for the initial cycles (this is further elaborated on in Section 5.4). One may observe the impact of particle morphology from the rate performance plot at various *C-rates* in Figure 5.6A. The thinner, platelet-like morphologies of SnO formed in ethanol and 70% methanol produced the highest initial capacities at low *C-rates*, with initial discharges of 960 mAh g^{-1} and 985 mAh g^{-1}. The reduced thicknesses and significantly increased surface area of the platelet-like structures permit greater contact between electrode and electrolyte resulting in higher Li^+ flux across the interface and thus a greater charge capacity.[1,16,17] The bulkier morphology of the perforated thick-square

produced in 1-hexanol produces an anode which performs significantly lower in terms of initial capacity to its thin counterparts, with a capacity of 900 mAh g^{-1} and this result again may be rationalised by the morphology and reduced surface area (see Chapter 4, Figure 4.4 and Table 4.1 for BET surface areas).

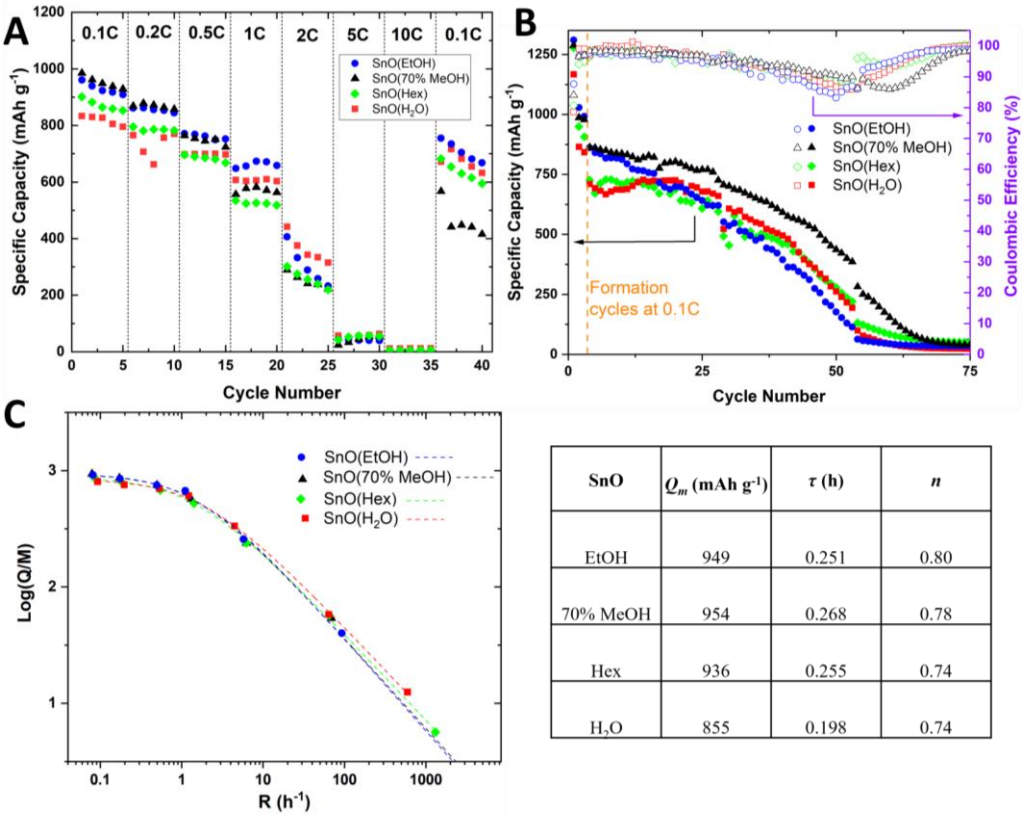

SnO	Q_m (mAh g^{-1})	τ (h)	n
EtOH	949	0.251	0.80
70% MeOH	954	0.268	0.78
Hex	936	0.255	0.74
H_2O	855	0.198	0.74

Figure 5.6: (A) Rate capability of tested morphologies of synthesised SnO with 15% mass fraction SWCNTs at various *C-rates*. (B) Cycling performance of the SnO morphologies at 0.5 C. (C) Experimental GCD data fitted using Equation 5.1 for SnO morphologies.

Table 5.2: Parameters for Equation 5.1 obtained via the fitting of experimental GCD data in Figure 5.6C.

The outlier in the data at first glance is the sample produced in water as it does not follow the trend displayed between the BET surface area and charge storage capacity (it has the second largest BET surface area of 16.62 m^2 g^{-1}). It is thought this discrepancy may occur for two reasons: (1) The area accessible to the N_2 molecule is not the same as that of the solvated Li^+ ion in the electrolyte, the effective size of the N_2 molecule is roughly 3 Å,[18] whilst the size of the solvated Li^+ ion is in excess of 3 Å for the EC/DMC electrolyte employed.[19–22] In Chapter 4, the average side length of the standard shapes were measured (SnO(70% MeOH) ~ 3 μm, SnO(Hex) ~ 1.8 μm, SnO(H_2O) ~ 8.7 μm). As the SnO is not conducting the larger size of the SnO(H_2O) particles would make them more resistive, limiting energy storage performance. (2) The highly structured and crystalline

morphology present in this sample is limiting the materials' performance. It is known that highly crystalline materials perform poorer in comparison to more structurally disordered counterparts with defects present, as is the case with studies done on Si and Sn.[23,24] These reasons would account for the enhanced performance available through the '*perforated*' thick-squares produced in 1-heaxnol, with the perforation leading to enhance Li-diffusion consistent with previous reports,[25] whilst the less accessible active sites of the thick-squares produced in water lead to poorer electrochemical performance in comparison.

Upon re-cycling the material at 0.1 C (Figure 5.6A), the enhanced stability of the nanoflower morphology is displayed by its capacity retention of 79% of its initial value whilst the platelet morphology only retains 60%. Herein, capacity retention is defined as the ratio of the charge storage capacity at a given cycle to the value measured during the initial cycle. The contacted points between the individual platelets in the nanoflowers may provide additional paths for the electron flow perpendicular to the plane, and this may account for the enhanced stability over multiple cycles.[26]

The cycling stability of all four morphologies was tested using GCD at a rate of 0.5 C with initial formation cycles at 0.1 C to aid stable SEI formation (Figure 5.6B). The cycling stability of all composites is unstable, with a sharp decline in performance between the 25th and 50th cycle for all composites which coincides with worrying CEs below 90%. For a functioning battery, a CE in excess of 99% is required, otherwise the fall in capacity upon each subsequent cycle is detrimental to long term use. However, there are some features from this data that are promising. In the region where cycling is stable, capacities higher than 600 mAh g^{-1} are obtainable for all composites and this figure is certainly impressive at such a quick rate. Compared to other work on SnO, Shin *et al*.[5] achieved similar cycling capacities but at a rate of 0.1 C whilst utilising a much more complicated process whereby Sn nanoparticles were grown on SnO nanobranches via vapour transport method. The initial coulombic efficiency (ICE) of the SnO samples produced was 87% (EtOH), 84% (70% MeOH), 80% (1-hexanol) and 78% (H_2O). A major issue for SnO, and all TMOs/MOs is that they suffer from low ICE limiting their use in real-world full-cells as the lithium consumption caused during the initial cycle limits/negates the excellent gravimetric capacity for additional cycles. This occurs since the supply of Li^+ in a full-cell comes from the cathode, and any Li^+ loss will greatly decrease the energy density of the full-cell. Commercial anodes such as lithium titanate

and graphite have ICEs > 90%.[27,28] The ICEs of all produced samples are thus very promising and their performance is better than most of their SnO_2 counterparts with reviews carried out on the subject by Li *et al.*[29] and Lan *et al.*[28] revealing the vast majority of tested materials fail to exceed an ICE of 65%. Cycling data was also obtained from cycling to only 1 V vs Li/Li^+, as this has been reported to enhance the stability[5,30] whilst the trade-off is a loss of gravimetric capacity. A more gradual loss in capacity was observed, however, the initial capacities of all composites were under 600 mAh g^{-1} and as the capacity was still continually dropping on each subsequent cycle the issue of cycling remains unsolved (Appendix C, Figure C.3).

Furthermore, the composites were fitted (Figure 5.6C) using Equation 5.1 as done previously, with the tabulated constants shown in Table 5.2. Excluding the sample produced in H_2O, all τ and n values calculated were quite consistent, with the sample produced in ethanol having the lowest τ value of 0.251, meaning it will be able to obtain a marginally higher rate before being subject to the high-rate regime. Interestingly the sample produced in H_2O has an even lower τ value of 0.198, owing to the fact its initial capacities were lower and it had the highest capacity obtainable at 2 C.

Impedance and Diffusion

EIS was carried out on each of the morphologies in the un-lithiated state after the initial formation cycles to probe the electrochemical behaviours of the respective composites, with the EIS spectra (Figure 5.7A) being fit using the equivalent circuit model shown in Figure 5.7B, using the Z-fit software package from BioLogic. In this model R_s is the series or ohmic resistance, R_{surf} and CPE_{surf} refer to the surface resistance and constant phase element (CPE) related to the SEI layer. A CPE is used in the place of a capacitor in these models as the inhomogeneities in the surface of metal oxides result in nonideal capacitances in the double-layer formed at the SEI.[31] R_{CT} and CPE_{CT} are attributed to the charge-transfer resistance and related double-layer capacitance. Z_W is known as the Warburg impedance and describes the solid state Li-ion diffusion within the electrode and the associated resistance,[17,32] whilst CPE_W is the associated capacitance arising from this process. The resistance results of the fitting of the equivalent circuit to the Nyquist plot of the experimental data are tabulated in Table 5.2. Focusing on R_{surf} and R_{CT}, it is seen that the SnO(EtOH) has both the lowest SEI resistance and lowest charge transfer resistance

when compared to the other samples (excluding $SnO(H_2O)$), with values of 68.3 Ω and 10.9 Ω, respectively. The $SnO(H_2O)$ displays a unique spectrum when compared to the other morphologies which is dominated by the charge-transfer semi-circle, with a value of 52.9 Ω obtained from the fitting, whilst it does however display the lowest value obtained for the R_{surf} parameter. This leads one to conclude that owing to the highly crystalline structure, a thin SEI is formed on the accessible surface area whilst the limiting factor for the material is the charge transfer within this structure as it is unable to intercalate Li-ions within to allow alloying to occur relative to the other morphologies. From the impedance measurements, it can be concluded that the SnO(EtOH) is the optimal morphology.

CV measurements at different scan rates (Figure 5.7C) were used to probe the apparent Li^+ ion diffusion coefficients for the various morphologies using the Randles-Sevchik Equation at 298 K as shown below (Equation 5.3),[33,34] where i_p is the peak current, n_e is the number of electrons (4.4 in this case as used the peaks corresponding to $Li_{4.4}Sn$) at the chosen peak, A is the active surface area of the electrode (1.13 cm^2) , C is the concentration of Li ions in the electrolyte (1 x 10^{-3} mol cm^{-3}) , D_{Li} is the apparent Li diffusion coefficients, and v is the scan rate. It is referred to as an apparent diffusion coefficient as the contact area we use is smaller than the real contact area experienced by the electrolyte in the cell.[35]

$$i_p = \pm (2.69 \times 10^5) n_e^{3/2} A C D^{1/2} v^{1/2} \qquad (5.3)$$

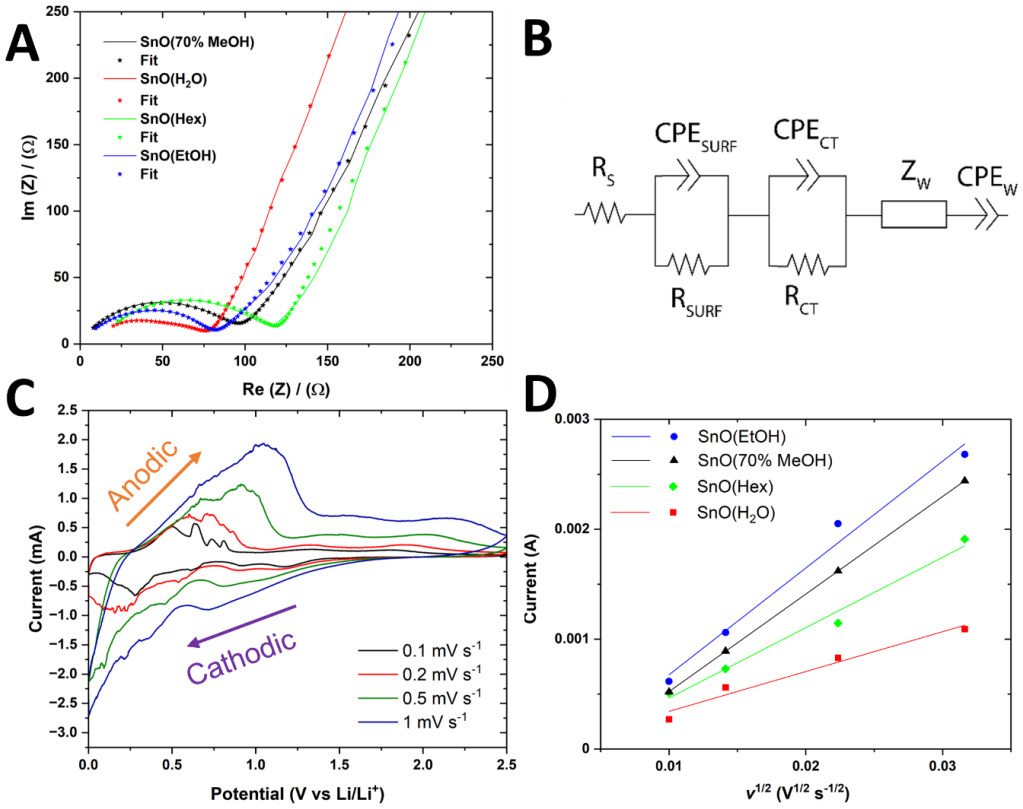

SnO	R_S (Ω)	R_{SURF} (Ω)	R_{CT} (Ω)	D_{anodic} ($\cdot 10^{-9}$ cm^2 s^{-1})
EtOH	4.5	68.3	10.9	1.19
70% MeOH	17.9	95.1	25.1	1.01
Hexanol	62.5	102.2	26.1	0.520
H_2O	4.4	21.3	52.9	0.167

Figure 5.7: (A) EIS spectra for the synthesised SnO morphologies and the Z-fit approximation using the equivalent circuit (Note *Rs* is subtracted to allow for easier visual comparison). (B) The equivalent circuit used to fit the EIS spectra. (C) CV profile of SnO(Hex) at various scan rates. (D) Anodic peak current as a function of the square root of scan rate.

Table 5.3: Equivalent circuit parameters calculated using Z-fit of the EIS spectra and the anodic diffusion coefficients calculated using the Randles-Sevchik equation.

By plotting i_p as a function of $v^{1/2}$ (Figure 5.7D), one may use the slope of the linear fit to obtain the D_{Li} of the material, as was done and tabulated in Table 5.3. Due to the overpotential experienced with increasing scan rate, the progression of the final cathodic peak (final alloying peak) was unable to be tracked so only the anodic diffusion coefficient was evaluated. From Table 5.3, it is seen that the SnO(EtOH) has the greatest D_{Li} for the anodic processes, with a value of 1.19 x 10^{-9} cm^2 s^{-1}. This value is larger than the reported SnO_2 apparent diffusion coefficients which vary between 10^{-13} and 10^{-10} cm^2 s^{-1},[36–39] whilst Lv *et al.*[40] recorded an anodic value of 1.90 x 10^{-9} cm^2 s^{-1} using Tin(II) Oxide

Carbodiimide ($Sn_2O(CN_2)$) which was synthesised using a hydrothermal reaction with expensive precursors. The increase of an order of magnitude in the value of D_{Li} for Tin(II) Oxide over Tin(IV) Oxide demonstrates the diffusion barrier caused by the Li_2O.[28] This again highlights the cost advantages one may obtain through the use of the developed wet-chemical synthesis reported here. The sample produced in water was the most diffusion limited for the anodic process, again displaying the limitations of this highly crystalline morphology for use as a LIB anode.[28] It is well known that through nanostructuring of the material, the diffusion kinetics of the Li ion into the active material may be enhanced and this is certainly the case for the SnO(EtOH) morphology here.[2,3,28,41–43]

As the SnO(EtOH) anode has displayed the optimal performance in reference to all the morphologies tested using GCD, EIS and CV measurements, it was chosen to just focus on this morphology for further optimisation.

5.4 Electrochemistry of Optimised Morphology

From the voltammogram presented in Figure 5.8A, the characteristic conversion and alloying reactions of SnO(EtOH) may be investigated. During the initial cathodic sweep, the large cathodic peak at 0.85 V, corresponds to the initial SEI formation and the initial conversion reaction of SnO to metallic Sn,[2,5,38,44,45] imbedding the metallic Sn particles in the Li_2O matrix according to Equation 2.4. This metallic Sn is further lithiated at the reductive peaks at 0.6, 0.3 and 0.15 V corresponding to the formation of various Li_xSn alloys until full lithiation occurs with $Li_{22}Sn_5$.[26,42,44,45] The peaks at 0.55, 0.68, 0.78 and 0.8 V in the anodic sweep correspond to the delithiation of Li_xSn alloys.[2,5,26,30,45,46] Upon further oxidation, a broad peak is reported at 1.25 V which corresponds to the start of the conversion reaction with the formation of Sn and Li_2SnO_3, which is completed at 1.82 V with the partial reformation of SnO.[5,26,42,47,48] On subsequent cathodic sweeps the reformation of Sn and Li_2SnO_3 can be seen at 1.25 V, with the formation of Sn and LiO_2 occurring at 0.95 V in these cathodic sweeps. The formation of Li_2SnO_3 has only recently been elucidated by Ferraresi *et al.*[47] with the use of XPS to monitor the exact species at this point, with a general ambiguity in the field prior; just acknowledgment of the conversion and not the exact steps.[2,49] The CV curves display exceptional reversible characteristics for all cycles excluding the initial, highlighting the different charge storage

mechanism present in the initial and subsequent cycles. (CVs of all composites displayed similar characteristics, see Appendix C, Figure C.4). Thus, the morphologies present display some reversible conversion reaction allowing for the reformation of SnO, contrary to general consensus throughout the field that this reaction is irreversible,[45,50] however recently it has been acknowledged that this reaction is partially reversible depending on the structure of the electrode.[5,26,28,41]

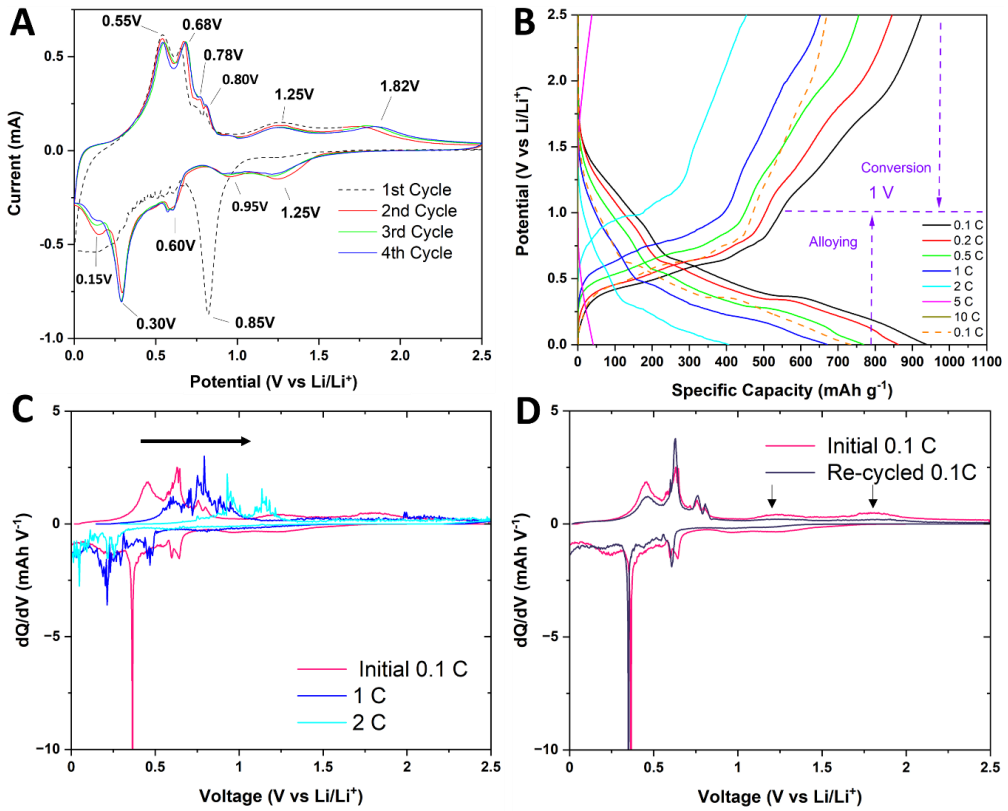

Figure 5.8: (A) CV of SnO(EtOH) electrode at 0.1 mV $s^{-1}$and (B) GCD profile of SnO(EtOH) electrode at various rates, with low rate alloying and conversion cut-offs marked. (C) *dQ/dV* analysis of GCD data at 0.1, 1 and 2 C displaying the overpotential present with increased rates. (D) *dQ/dV* analysis of initial 0.1 C and re-cycled 0.1 C, with arrows indicating a decrease in the intensity of the conversion reaction.

Upon examination of the GCD curve, the contributions from the alloying and conversion reaction may be separated by utilising the information gathered from the analysis of the CV profile and differential capacity analysis (*dQ/dV*) of the GCD profile. The appearance of the *dQ/dV* plot appears similar to that of a CV plot, with the peaks representing plateaus in the voltage profile of the GCD curves which correspond to phase transitions in the active material,[51] thus allowing one to track the onset of the alloying/conversion reactions with respect to rate. It may also be used to elucidate failure mechanisms in batteries as will be discussed in Section 5.6. The conversion reaction happens above 1 V up to 0.5 C, with the alloying reaction occurring below (at faster rates an overpotential is observed

shifting the onset of the conversion to higher potentials as shown in Figure 5.8C and Appendix C, Table C.1). Two distinct slopes can be seen from the GCD curves at low rates during the charging of the electrode, beginning at ~1.25 V (corresponding to the beginning of the conversion reaction) and ~0.6 V (corresponding to the alloying reaction), consistent with similar peaks observed in the *dQ/dV* profile (Figure 5.8D). The GCD curves display constant slopes in place of constant voltage plateaus due to the nanostructuring of the material (compared to SA GCD curve in Figure 5.1C).[50]

Interestingly, from the analysis of the GCD curves it is calculated that 60% of the discharge capacity is obtained from the alloying reaction whilst the remaining 40% is obtained from the conversion, which is consistent for rates up to 1 C. Upon re-cycling at 0.1 C, the alloying reaction accounts for 70% of the capacity, indicating that the conversion reaction is not completely reversible for the material at this point. This point is reinforced when examining Figure 5.8D, where there is a drop in the intensity of the conversion reaction (marked by arrows) whilst the alloying peaks remain constant. Upon analysis of the GCD curves of the other morphologies (see Appendix C, Figure C.4 and Table C.1), similar trends are observed, with the thin platelet-like morphology of SnO(70% MeOH) displaying a capacity of 60% from alloying which increases to 76% upon re-cycling at 0.1 C, whilst the bulkier morphologies of SnO(Hex) and SnO(H_2O) have alloying charge capacities of 63% (increasing to 68%) and 68% (increasing to 72%). Fascinatingly, these ratios allow one to see the rates at which both the alloying and conversion reactions may take place together and the rate at which this synergy falls apart. For all composites the alloying charge percentage increases at 1 C, except for the SnO(70% MeOH) which may be a consequence of the reduced dimensions of the thin platelet allowing the conversion reaction to proceed at faster rates. The conversion reaction between Sn and Li_2O is difficult and diffusion-limited, thus rate plays a key factor as shown.[50] Reports indicate on SnO_2 through nanostructuring, the Sn/LiO_2 interface may be maximised, allowing the maximisation of the conversion reaction,[28,52,53] whilst the use of CNTs provides short pathways for the Li^+ transfer leading to a high reaction reversibility which is the case here.[28,50,54] In the present work we have achieved the conversion reaction with the largest sized particles to date,[2,5,26,40,50] which is advantageous for further use in the full-cell configuration as it minimises the amount of Li loss to SEI formation.

5.5 Alternative SWCNTs for Improved Cycling

The focus of the study now turned to optimising the one parameter which was limiting and, in some respects, the most important parameter when one considers LIB technology, cycle life. OCSiAl are the most cost-effective and largest supplier of SWCNTs on the market, thanks to their CVD flow synthesis which they have patented and named the resulting product Tuball (Tu) SWCNTs.[55] They have the advantage of being water dispersible (with a polymer surfactant), allowing them to form compatible inks with active materials for more complicated fabrication processes such as 3D printing whilst also enabling post-processing of the electrode with techniques such as freeze-drying (FD). For a more complete discussion on the impact of electrode preparation and the effects of additive manufacturing on electrode performance, see the paper by Pinilla *et al.*[56] which I co-authored in parallel with the study into SnO. The difference between the morphologies of the P3 and Tu-SWCNTs is apparent upon examination of the SEM image in Figure 5.9B, where at a 15% mass fraction the Tu product encapsulate the active material in a '*carpet-like*' structure of SWCNTs as opposed to the finely distributed '*web-like*' structures observed for the P3 product. It was hypothesised that this encapsulation of the SnO by the tensile strong Tu-SWCNTs would assist in improving the cyclability by containing the volume expansion the active material is subjected to upon repeated charging/discharging. Through this apparent enhanced coverage, even with the fracturing/breaking of active material, the SWCNT '*carpet*' should ensure electrical connection remains in the electrode.

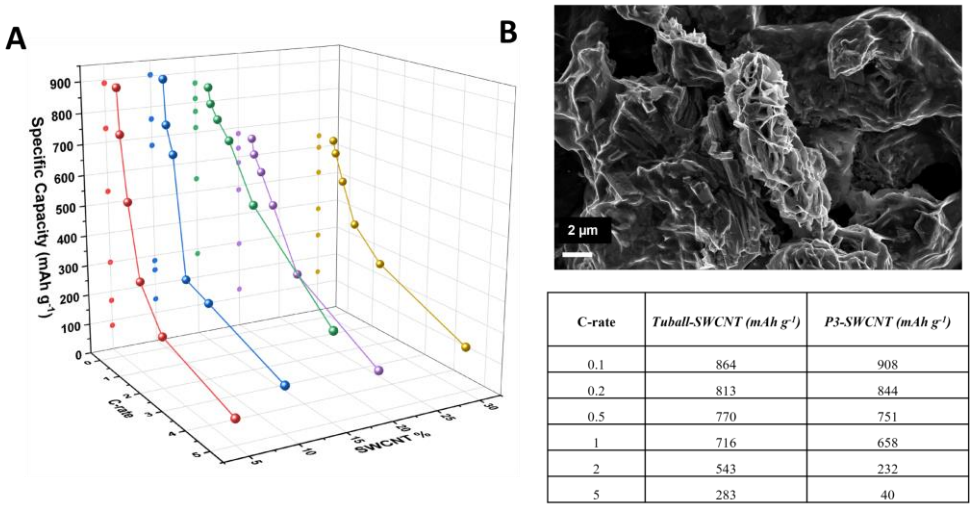

C-rate	*Tuball-SWCNT (mAh g⁻¹)*	*P3-SWCNT (mAh g⁻¹)*
0.1	864	908
0.2	813	844
0.5	770	751
1	716	658
2	543	232
5	283	40

Figure 5.9: (A) SnO/Tu-SWCNT composite discharge capacities at various *C-rates* as a function of SWCNT %. (B) SEM image of the composite of SnO with 15% mass fraction Tu-SWCNTs.

Table 5.4: Comparison of SnO with 15% mass fraction of Tu-SWCNTs vs SnO with 15% mass fraction of P3-SWCNTs in terms of capacity.

As was done previously, a SWCNT mass loading study was initially carried out to ensure the optimum mass fraction was chosen in regard to capacity and rate performance (Figure 5.9A). Note all samples were heated under vacuum (400 ºC) with a small Ar air flow to remove the polymeric binder of carboxymethyl cellulose (CMC) used to disperse the SWCNTs in H_2O. The removal of the CMC was confirmed via thermogravimetric analysis at approximately 300 ºC (Appendix C, Figure C.5), which was consistent with previous reports.[57] (Note the SnO was not oxidised to SnO_2 as this occurs at temperatures in excess of 500 ºC,[58,59] and this data is shown in Chapter 7, Figure 7.3B). This was done to maximise the gravimetric capacity by removing the inactive polymer, whilst also maximising the rate capability as battery binders are known to act as diffusion barriers.[60]

Although not possessing the greatest initial capacity at 0.1 C, a mass fraction of 15% Tu-SWCNTs optimised the performance of the composite. Both the 5% and 10% composite have marginally higher initial capacities at 0.1 C (889 and 903 mAh g^{-1} respectively) than the 15% composite (864 mAh g^{-1}), however as the rate is increased the decrease in capacity is much less severe with the 15% composite, with impressive capacities recorded of 813, 770, 716 and 543 mAh g^{-1} at 0.2, 0.5, 1 and 2 C respectively. Furthermore, it also displayed a useable capacity at 5 C (roughly 5 A g^{-1}) of 284 mAh g^{-1}, which was the first tested composite to work at this rate. This result is quite remarkable when one considers this corresponds to a charge/discharge time of 12 minutes. This is greater than the capacity obtainable for graphite at this quick rate.[61,62] The improved rate performance relative to the P3-SWCNTs can be seen in Table 5.4.

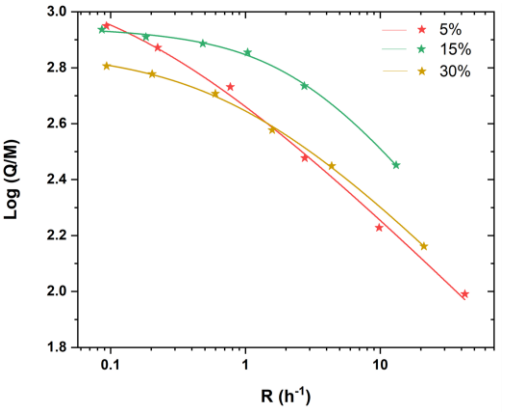

SWCNT %	Q_m (mAh g^{-1})	τ (h)	n
5	1385	1.35	0.48
10	1222	0.66	0.48
15	883	0.10	0.68
20	731	0.15	0.64
30	745	0.22	0.52

Figure 5.10: Selection of GCD experimental data for SnO/Tu-SWCNT composites fitted using Equation 5.1, see full dataset in Appendix C, Figure C.6.

Table 5.5: Parameters Q_M, τ and n for each mass fraction of Tu-SWCNT after fitting GCD data using Equation 5.1.

Using Equation 5.1, the parameters Q_M, τ and n for each mass fraction of Tu-SWCNT could be extracted after fitting the experimental GCD data to allow for comparison (Figure 5.10 and Table 5.5). From the extracted parameters, we can see that the 15% mass fraction has the lowest value of τ (0.1 h), consistent with that observed from the GCD data and displaying the excellent rate capability of this composite. The value of Q_M (883 mAh g^{-1}) agrees closely with the experimental value and the n value of 0.68 suggests both electrical and diffusion limitations in the high-rate region. The values obtained for the 5% mass fraction however displays the limitations of the equation. The value of Q_M exceeds that of the theoretical total capacity of the composite (1313 mAh g^{-1} if one considers the SnO conversion reaction fully reversible). Thus, one should be vigilant of understanding the underlying chemical limitations of the system, and aware that for low mass fractions of conductive additive where the decay capacity starts with small rates, the fitting will overestimate the low rate limit as there are not enough data points to provide for an accurate assessment. This limitation for the equation is again seen with the n values below 0.5, which as reported occurs due to fitting errors associated with datasets showing small capacity falloffs at higher rates.[13] Due to the excellent rate capability and stability, a 15% mass fraction of Tu-SWCNTs was deemed to optimise the performance of the anode.

Effect on Cycling

As previously stated, as the Tu-SWCNTs are water dispersible with the addition of CMC, it allows for additional post-processing treatments. Recalling the main factor in investigating the use of Tu-SWCNTs was to increase the cycling stability of the composite, 3 alterations of the SnO/Tu composite were investigated (heat treated, untreated, freeze-dried) and compared to the performance of the optimised SnO/P3 composite. It was elected to investigate the effect of CMC as previous reports have demonstrated that it can have a positive effect on cycle life whilst being much more environmentally friendly than the PVDF/N-methyl-2-pyrrolidone (NMP) standard binder combination used in the battery field,[63,64] with work carried out on Si, in particular, demonstrating its effectiveness at prolonging cycle life.[65] FD works by quickly freezing a material with trapped moisture and subsequently dropping the surrounding pressure causing sublimation from the solid to the gas phase. FD is a simple and effective approach to prevent agglomeration and improve the specific surface area of the anode.[66] The micropores created by this process would also provide adequate space for the Li-Sn

alloying reactions to take place whilst maintaining an electrical connection throughout.[67] It was envisioned that this porous structure should provide increased rate capability by fully maximising the active material present.

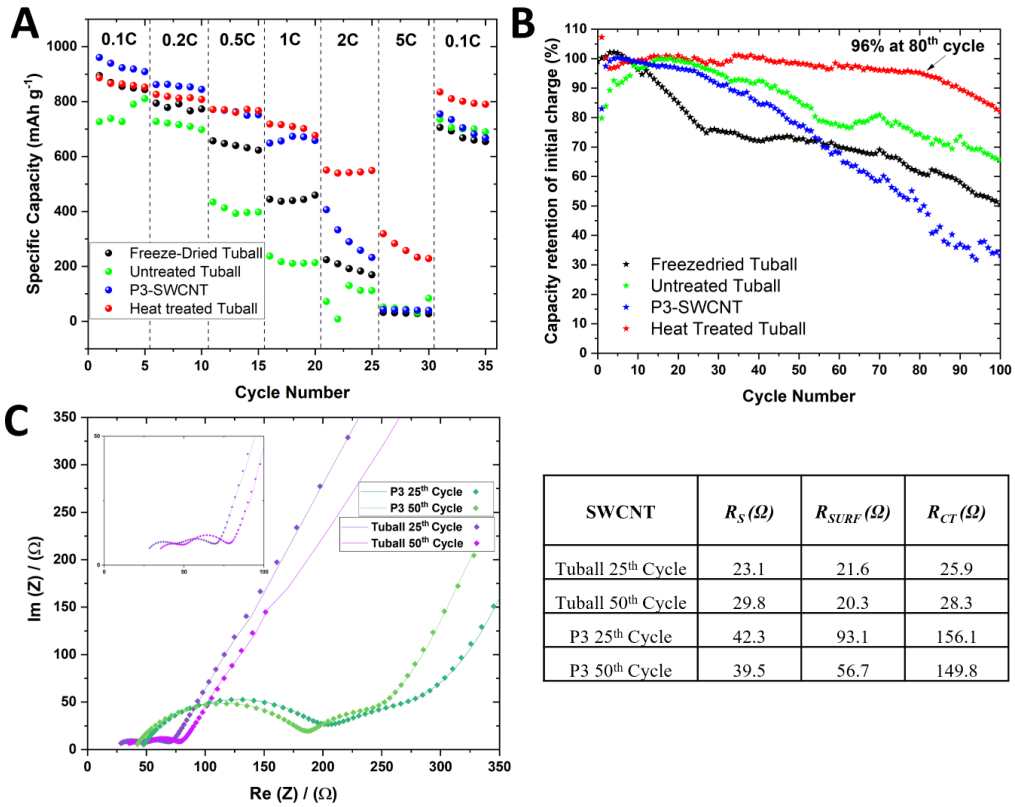

SWCNT	R_S (Ω)	R_{SURF} (Ω)	R_{CT} (Ω)
Tuball 25th Cycle	23.1	21.6	25.9
Tuball 50th Cycle	29.8	20.3	28.3
P3 25th Cycle	42.3	93.1	156.1
P3 50th Cycle	39.5	56.7	149.8

Figure 5.11: (A) Rate capability of SnO composites with Tu-SWCNT(various treatments) and P3-SWCNT. (B) Cycling performance of composites at 0.5 C from 0.005 – 1 V. (C) EIS spectra (line) and Z-fit (symbol) of SnO composite with Tu/P3-SWCNTs after 25/50 cycles (zoomed in inset of Tuball EIS in the high-frequency region).

Table 5.6: Values obtained for the Equivalent circuit used to model the EIS spectra.

From Figure 5.11A, it is apparent that the heat-treated (HT) SnO/Tu composite displays the best rate capability of all the tested composites, surpassing the performance of the P3 at 0.5 C, whilst demonstrating impressive capacities at 2 C (550 mAh g^{-1}) and 5 C (318 mAh g^{-1} initially). Although not possessing the greatest capacity at 0.1 C (886 mAh g^{-1}), upon re-cycling at this rate it maintains 94% of the initial obtained capacity, an impressive figure and significant improvement on the P3 composite (78%). The FD sample displayed improved rate capability to that of the untreated sample, however, its performance throughout was less than that of the P3 and HT Tu.

As cycling stability was the hidden gem left to uncover for this investigation into solvent-engineered SnO, all composites were tested in Figure 5.11B, electing to test under 1 V vs

Li/Li^+, primarily to focus on achieving a stable capacity in the alloying region before progressing to the conversion reaction (as the phrase goes, "*you must learn to walk before you can run"*). The HT Tu electrode performs the best again, retaining 96% of its initial capacity at the 80th cycle before a gradual loss in capacity is recorded. The electrode where the CMC was left unaltered displays the next best performance, whilst the P3 and FD electrodes display a constant fall in capacity throughout. Though improvements have been made through the use of HT Tu electrodes relative to the study carried out on the P3-SWCNTs, cyclability still remained a driving force in the investigation at this stage (electric vehicle batteries end of life occurs at 70 – 80% initial capacity[68]). Furthermore, EIS analysis carried out after the 25th/50th cycles clearly display the differences in the R_{surf} and R_{CT} of the HT Tuball and P3 electrodes (Figure 5.11C and Table 5.6). One does not need to utilise the Z-fit software as the magnitude of the size of the semi-circles shows how upon cycling, the P3 composite is much more resistive. The HT Tu electrode displays excellent stability in the R_{surf} and R_{CT} values while it is cycling stably, with only minor changes in these values simulated using the Z-fit of the equivalent circuit. It is believed that the HT-Tuball's performance is superior due to the enhanced coverage obtained relative to the P3-product, agreeing with the initial hypothesis. The FD treatment did not enhance the performance however, most likely owing to a loss of contact of active material in the much more porous network formed. This may be seen by the SEM images and the FIB cross-section of the FD electrode, displaying pockets of isolated SnO within the porous SWCNT distribution (Figure 5.12).

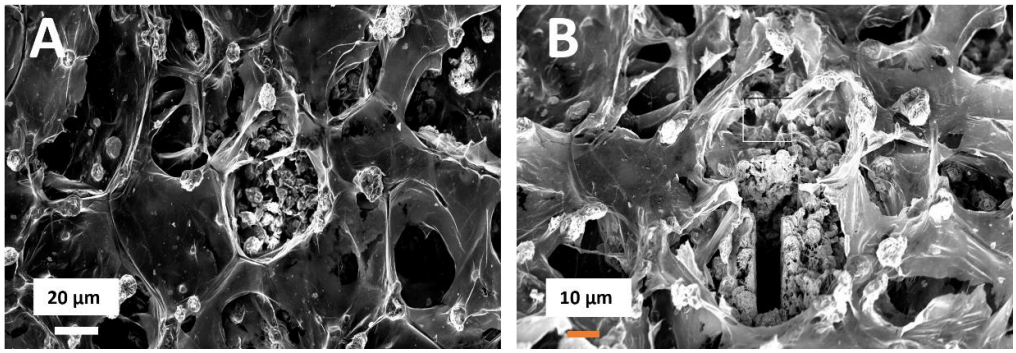

Figure 5.12: (A) SEM image of FD-Tu electrode and (B) SEM image of FIB cross-section of the same electrode.

5.6 Differential Capacity Analysis and Electrolyte Investigation

To ascertain the exact cause of the decrease in capacity recorded for all SnO electrodes to date, differential capacity analysis (*dQ/dV*) was undertaken. *dQ/dV* analysis is reported to

be an effective method to indicate the failure mechanism at play within a battery and it is a powerful form of data analysis that can be applied to GCD data to allow the features to be seen/interpreted more easily.[69,70] Through the analysis of how these features (peaks and plateaus) behave with respect to cycle number the cause for capacity fade in the electrode may be deduced. As stated previously, the appearance of the *dQ/dV* plot appears similar to that of a CV plot, with the peaks representing plateaus in the voltage profile of the GCD curves which correspond to phase transitions in the active material.[51]

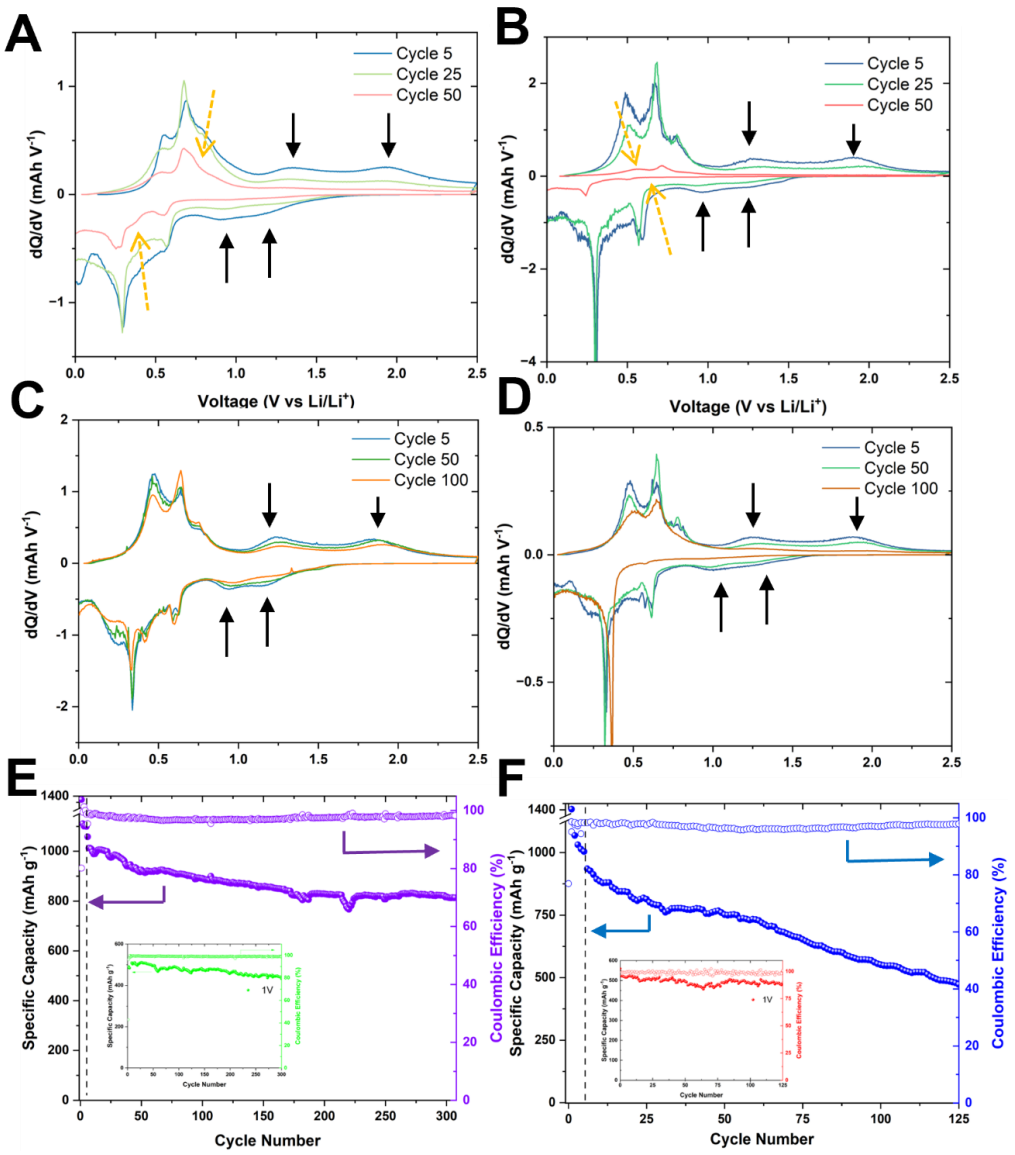

Figure 5.13: Differential capacity analysis of SnO with (A) 15% HT Tu-SWCNTs, (B) 15% P3-SWCNTs, (C) 15% HT Tu-SWCNTs with 10% FEC added to the cell electrolyte and (D) 15% P3-SWCNTs with 10% FEC added . (E) Cycling stability of SnO with 15% HT Tu-SWCNTs with 10% FEC addition with data obtained with voltage cut-off of 2.5 V in purple and 1 V inset in green. (F) Cycling stability of SnO with 15% P3-SWCNTs with 10% FEC addition with data obtained with voltage cut-off of 2.5 V in blue and 1 V inset in red.

From Figure 5.13A and B, it is observed that as both the Tu and P3 composites are subjected to an increasing number of cycles, there is a significant change observed in the *dQ/dV* plots. The initial curves appear consistent with the CV curves for the material as expected, with distinctive alloying/de-alloying peaks (under 1 V) and conversion peaks (above ~1 V). Between the 5th and 25th cycles, the most striking change occurs when one analyses the conversion peaks (indicated by black arrows). The decrease in height of these peaks indicates that the irreversibility of the conversion reaction is the cause for the initial fade in capacity, as the alloying peaks remain roughly equivalent at this stage (see Appendix C, Figure C.9 for normalised *dQ/dV* plot), consistent with work carried out on SnO_2.[47] Progressing through to the 50th cycle, it can be seen that in addition to a complete loss of the peaks from the conversion reaction, the alloying peaks have now also significantly decreased in size (indicated by yellow arrows). The degradation is far more severe in the P3 composite as expected from the cycling data. As the peaks shift to slightly different voltages, this represents a loss of lithium inventory in the cell and this is the cause for the unstable cycling witnessed.[51] Due to the huge volumetric change associated with the alloying, a cause for the loss of active material in the anode may be an unstable SEI. During subsequent alloying/de-alloying cycles, fracturing and breaking of the SEI would lead to a loss of Li-inventory (as the Sn contracts after delithiation, the SEI may peel off).[71,72] In addition, with each additional cycle continuous SEI build-up would lead to increased cell impedance, making the full-delithiation of the Sn problematic, again causing loss of Li-inventory.[73] This is consistent with the voltage shifts observed.[74] Similar failure mechanisms have been reported with Si and SiO.[74,75] To create a more stable SEI, fluoroethylene carbonate (FEC) was added to the electrolyte used to this point of LP30 (1 M $LiPF_6$ in EC:DMC, 1:1).

FEC is known to aid in the cycling stability of alloy-type anodes, with extensive work carried out on Si and Sn.[71,73,74,76,77] In the presence of FEC which degrades at a higher reduction potential than both EC and DMC, a denser, thinner and more uniform SEI is formed in contrast to interphases formed in FEC-free electrolytes which are more porous and permeable by electrolytes.[71,72,76] This SEI layer has been found to inhibit the emergence of large cracks and suppress further the decomposition of EC/DMC, leading to enhanced electrochemical performance and improved CE.[77] The SEI layer also remains stable upon discharging above 1.5 V in Sn anodes, with the particles held intact.[73] In Si anodes, FEC additive leads to the formation of insoluble crosslinked poly(ethylene

oxide)-based polymers which could better passivate the electrode and resist the volume expansion whilst the increased formation of LiF in the SEI results in a lower overall impedance, and it is assumed the same would occur for Sn.[71,72,76,78]

From Figure 5.13C and D, the vast improvement in the *dQ/dV* analysis can be seen at the 5th,50th and 100th cycle through the addition of 10% wt. FEC to the LP30 electrolyte with respect to the pure LP30 data (Figure 5.13A and B). For the Tu electrode, the *dQ/dV* plots remain unchanged over the first 100 cycles, demonstrating that the previous issues of the non-reversible conversion reaction and loss of Li-inventory in the cell have been solved. Furthermore, this improvement is reflected in the cycling stability of the material, with a capacity of 820 mAh g^{-1} recorded after over 300 cycles at a rate of 0.5 C (Figure 5.13E) and a capacity of 430 mAh g^{-1} at the same point at a 1 V cut-off. The CE remained in excess of 99% and the ICE of 80% was also satisfactory when one considers use in a full-cell. With regard to the P3 composite, the FEC again caused a dramatic improvement in the cycling stability, reflected through the *dQ/dV* plot (Figure 5.13D), where the conversion reaction is still stable after 50 cycles and the loss of Li-inventory is nowhere near as dramatic as without FEC. The cycling stability however is not as impressive as the Tu counterpart, with capacity fading to 480 mAh g^{-1} after 125 cycles, whilst with the 1 V cut-off the composite also recorded roughly 480 mAh g^{-1} at the same point, indicating that again the conversion reaction is the cause for the capacity fade. These results however are extremely promising, with the SnO HT Tu composite achieving stable cycling at a high rate with remarkable capacity.

Optimised Half-Cell Performance and Comparison to Other Works

As the cycling stability issue has been solved through the addition of FEC to the electrolyte, the final optimised composite electrode of HT SnO(EtOH) with 15% Tu-SWCNTs was investigated. The FEC has no detrimental effects on the rate performance of the electrode (Figure 5.14A), with a specific capacity of 980 mAh g^{-1} at 0.1 C, which is greater than the 886 mAh g^{-1} recorded without FEC present, again displaying the positive effect FEC has on the conversion reaction. The rate performance remains exceptional, with a usable and stable capacity obtainable at 5 C of ~320 mAh g^{-1}. Furthermore, a mass loading study was undertaken to demonstrate how the SnO/SWCNT inks allow for greater areal capacities to be recorded (Figure 5.14B). The trend is obvious

to see, with more mass, a larger areal capacity is obtained, with a second cycle specific capacity ranging from 0.85 to 2.82 mAh cm^{-2} for 1.6 to 6.9 mg cm^{-2} mass loadings. Upon re-cycling at 0.1 C, all loadings tested record capacities in excess of 95% of the last initial 0.1 C value. The commercial graphite anodes are expected to have areal capacities of 2.5 – 3.5 mAh cm^{-2} at a mass loading of 10 mg cm^{-2} and this simple study demonstrates the SnO/SWCNT composite may achieve this value with approximately 40% less mass.[79]

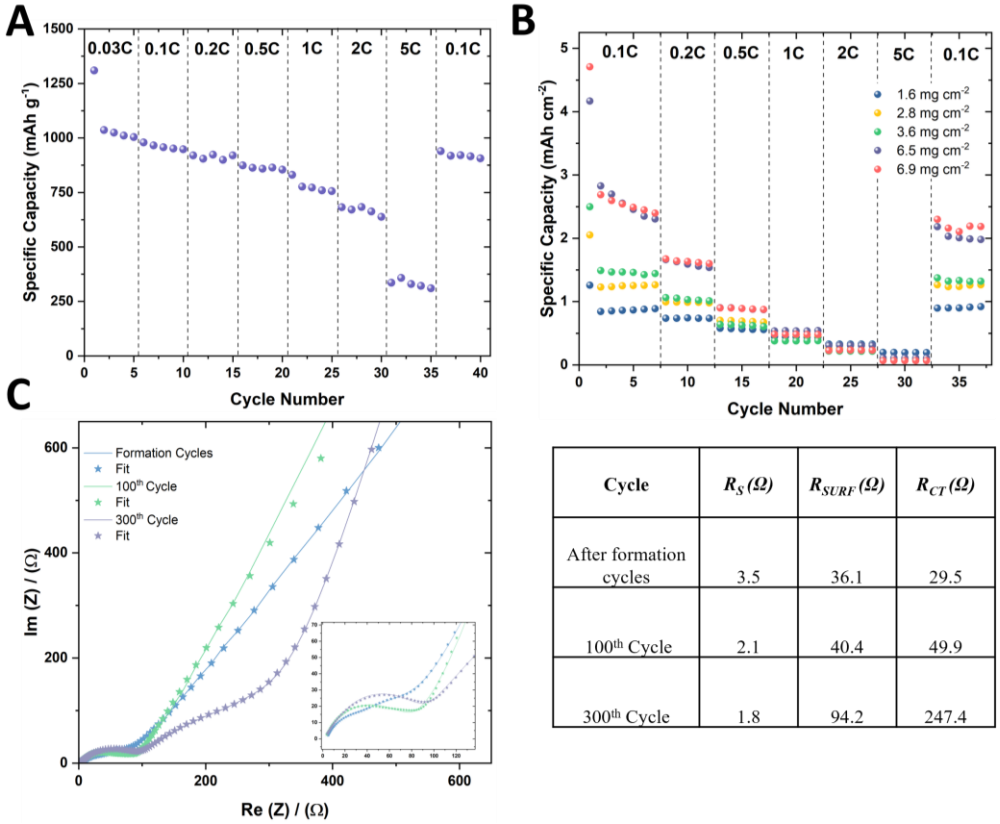

Cycle	R_S (Ω)	R_{SURF} (Ω)	R_{CT} (Ω)
After formation cycles	3.5	36.1	29.5
100th Cycle	2.1	40.4	49.9
300th Cycle	1.8	94.2	247.4

Figure 5.14: (A) Rate performance of optimised SnO/Tu electrode in half-cell configuration with LP30 and 10% FEC electrolyte. (B) Rate performance of several mass loadings of SnO/Tu electrode. (C) EIS spectra and subsequent Z-fit were carried out during cycling of the SnO/Tu electrode at 0.5 C, with zoomed inset of high-frequency region.

Table 5.7: Equivalent circuit parameters obtained through use of Z-fit of Figure 5.14C.

Furthermore, EIS was utilised to monitor the ongoing changes in resistance the electrode would experience, using Z-fit and the equivalent circuit shown in Figure 5.7B. Over the first 100 cycles, the FEC leads to a negligible change in the R_{surf} whilst the R_{CT} increase by 20.4 Ω, once again demonstrating the role of the FEC in forming a stable SEI. The EIS at the 300th cycle shows the R_{surf} has risen to 94.2 Ω, which is still an acceptable increase when one considers the fast rate and number of cycles and this is visibly seen in the inset in Figure 5.14C, where no major change is seen in the size of the semi-circle. The largest

increase occurs in the R_{CT} to 247.4 Ω, with this increase attributable to the stress and strain the active material has been subject to over 300 cycles.

There of course are areas for improvement regarding this study. The drop between the capacities on the first and second cycles as the mass loading increases is a cause for concern, with drops ranging from 32% for the lowest mass loading to 45% for the greatest mass loading. Furthermore, as the mass loading increases, the gravimetric capacity decreases. This is a common problem in energy storage owing to diffusion limitations of thicker electrodes. In both cases, it is hoped improvements may be made by utilising even slower formation cycles to ensure the full lithiation of the electrode occurs whilst also ensuring a stable SEI is formed throughout. It would also be interesting to explore FD again to explore if opening additional free space would relieve some of the diffusion limitations a thicker electrode will naturally experience.

The results of the optimised half-cell were compared to similar to work in the field in Table 5.8 on the next page.

Materials	Preparation methods	Initial Discharge (mAh g^{-1}), ICE (%)	Capacity Retention	Ref
SnO_2 nanoparticles	Hydrothermal	523 56	118 mAh g^{-1} after 50 cycles at 0.1 C	80
Sn-decorated SnO nanobranches	Vapor transport method	980 60	502 mAh g^{-1} after 50 cycles at 0.1 A g^{-1}	5
SnO_2 nanoparticles	Auto-combustion and calcination	2213 57	618 mAh g^{-1} after 40 cycles at 0.05 C	81
SnO_2 nanoparticles	Wet chemical and hydrothermal	1800 50	460 mAh g^{-1} after 30 cycles at 0.1 A g^{-1}	82
SnO_2 nanoparticles with graphene	Hydrothermal	1400 40	250 mAh g^{-1} after 200 cycles at 0.5 A g^{-1}	37
SnO_2 nanoparticles with graphene oxide	Ultrasonic method and calcination	932 N/A	492 mAh g^{-1} after 100 cycles at 0.2 C	83
Porous SnO_2 hollow microspheres	Hydrothermal	1600 50	504 mAh g^{-1} after 100 cycles at 0.2 A g^{-1}	2
SnO_2 nanoparticles bound to CNTs	Hydrothermal	1708 62.5	546 mAh g^{-1} after 100 cycles at 0.05 A g^{-1}	50
Sn_3O_4 with graphene	Hydrothermal	1727 65	631 mAh g^{-1} after 50 cycles at 0.06 A g^{-1}	3
SnO_x-C composite	Solid state pyrolysis	1350 67	450 mAh g^{-1} after 400 cycles at 0.5 C	84
Amorphous SnO_2 porous cages	Electrostatic spray deposition	1491 69	560 mAh g^{-1} after 100 cycles at 0.5 C	85
CNT-SnO_2 nanorods	Hydrothermal	1290 64	698 mAh g^{-1} after 40 cycles at 0.72 A g^{-1}	86
SnO with SWCNTs	Wet chemical	1310 (1540)* 80	815 (958)* mAh g^{-1} after 307 cycles at 0.5 C / 0.44 A g^{-1}	This work

Table 5.8: Electrochemical performances of previously reported SnO_x LIB electrodes. * Denotes active capacity of current work.

From Table 5.8, a direct comparison may be made between the work carried out in this study and similar work carried out previously in the field (note both total mass and active mass have been reported for this study, the majority of reports fail to mention how they calculate mass so it is assumed it was based off active mass as is more common throughout). In terms of initial capacity, notable work was carried out by Rai *et al.*[81] recording a value of 2213 mAh g^{-1} , however, this capacity is owing to the large surface area of the anode, which results in the less than satisfactory ICE of 57%. This demonstrates once more, the disadvantage of large surface areas in anodes due to the irreversible capacity loss. In terms of ICE, the work carried out by Yu *et al.*[85] achieves the next best value of 69% with respect to the current work. The morphology of the SnO_2 cages synthesised was on the microscale with average diameters of 5 μm, and this is most likely the reason for the high ICE. This work and the work by Chen *et al.*[86] achieved reasonable cycling results, however, the current work far exceeds the performance in both capacity and cycle life. The work presented in this fellowship provides the highest ICE, the highest capacity and stable cycles at a quick rate, whilst also utilising a simple and scalable synthesis.

5.7 Post-Mortem Analysis

To further understand the contribution of FEC to the anode, post-mortem SEM, EDX and XRD were carried out on the anodes after cycling, in the fully discharged state. From the SEM images, significant contrasts in the morphology of the used electrodes are observed. The electrode with no FEC additive in the cell displayed severe cracks upon inspection (Figure 5.15A), and none of the original nanoflower morphology is visible having been consumed by the growing SEI. In contrast, the electrode cycled with FEC additive displays a completely different morphology (Figure 5.15C), whereby the nanoflowers may still be made out but covered by an amorphous layer presumably composed of SEI and LiO_2. Taking cross-sections of both electrodes, EDX was used to probe how the composition of the electrode varied with FEC. With no FEC added (Figure 5.15B), we can see from the EDX analysis that C, O (both constituents in the SEI) and Sn are all present throughout the analysed section. As there is no stable SEI formed, the Sn, C and O are all spread throughout. With successive alloying reactions, more Sn becomes exposed to the electrolyte, forming additional SEI and consuming the Li inventory of the cell. In comparison, with FEC added (Figure 5.15D), both the C and O contributions are

limited to the topper section analysed whilst the Sn intensity is spread evenly throughout the bulk of the electrode with a noticeable drop approaching the upper surface. When FEC is present, a stable SEI is formed whereby the active material of Sn and SnO for the anode is shielded from successive reactions with the electrolyte, demonstrated by the drop in the Sn intensity towards the surface exposed to the electrolyte. It is also shown that the SEI is flexible, as the Sn which expands towards the surface is clearly covered by new SEI, whilst the Sn which expands towards the current collector remains as Sn, hence the segregation. This segregation was consistent over multiple electrodes (see Appendix C, Figure C.7).

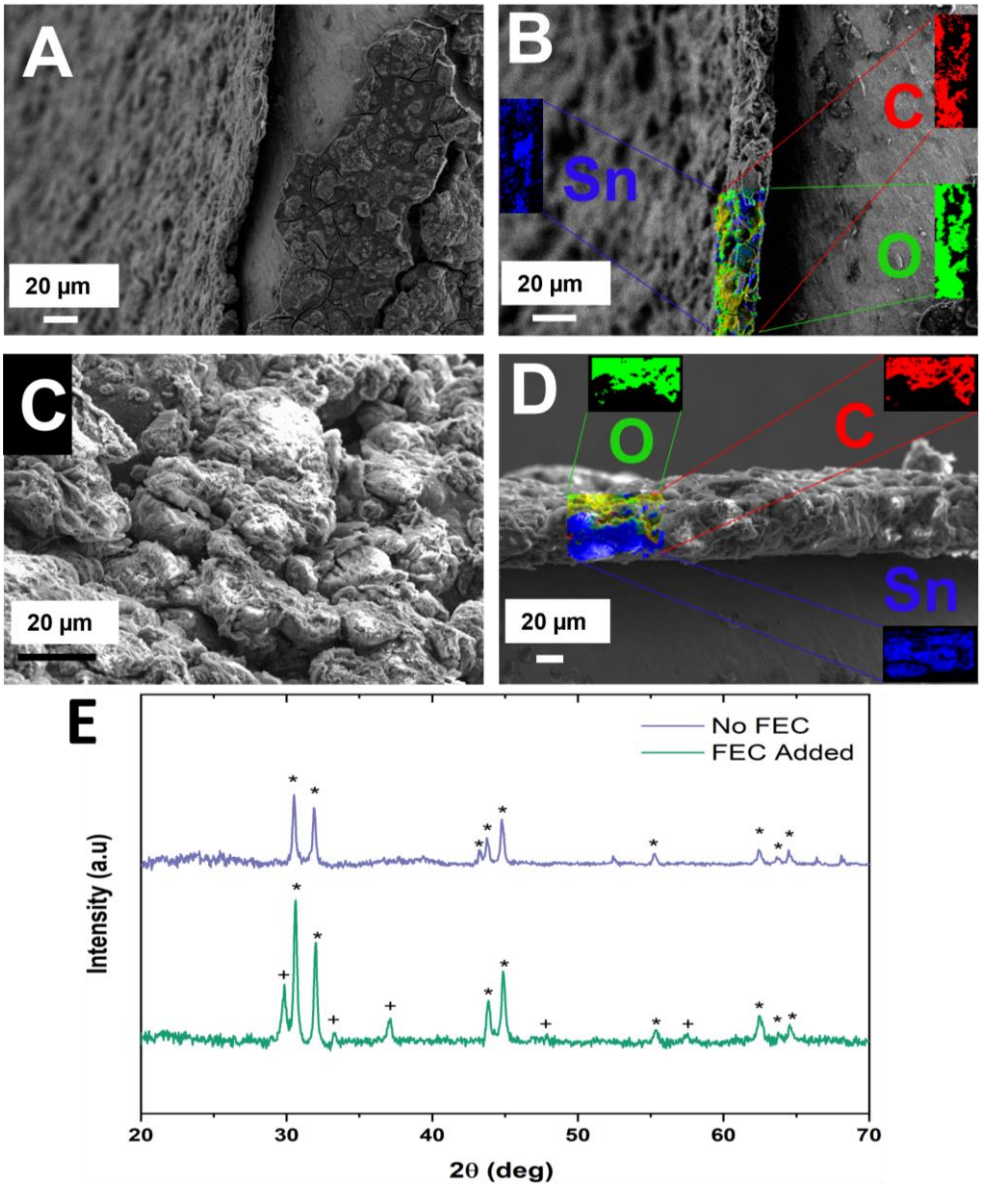

Figure 5.15: Post-mortem SEM image of (A) SnO/Tu-SWCNT electrode and (B) resulting EDX map of. (C) Post-mortem SEM image of (C) SnO/Tu-SWCNT electrode with 10% FEC present in the cell and (D) resulting EDX map. (E) Post-mortem XRD analysis of SnO/Tu-SWCNT electrodes with/without FEC.

Furthermore, from the XRD analysis carried out (Figure 5.15E), it is shown that with FEC, both SnO (PDF 01-072-1012, marked with a +) and Sn (PDF 03-065-0296, marked with a *****) are present in the discharged electrode (SEI and amorphous LiO_2 unable to be seen on XRD). With no FEC, only Sn is present in the discharged electrode, showing that the conversion reaction has failed (refer to the *dQ/dV* analysis in Figure 5.13B which shows this reaction has failed). Combining this result with the EDX, we can conclude that the O contribution for the electrode with no FEC is solely due to SEI and LiO_2, whilst in the electrode with FEC where the Sn and O contributions overlap, there clearly remains SnO.

5.8 Full-Cell Fabrication

As the optimised HT SnO Tu-SWCNT composite anode had now been established, as a proof of concept a full-cell was assembled to further demonstrate its readiness for real-world use. As a cathode, NMC 532 (Ni:Mn:Co = 5:3:2) was selected, combined with 0.5% mass fraction of Tu-SWCNTs, as this was found previously to optimise the performance of the cathode.[7] The SEM image of the cathode shows a uniform covering of SWCNTs over the active material of NMC (Figure 5.16A). The oxidation peak at 4.1 V in the CV of the NMC cathode and the reduction peak at 3.5 V (Figure 5.16B) corresponds to the Co^{3+}/Co^{4+} redox couple, whilst the lack of a redox peak at 3 V indicates that there is no Mn^{3+} in the material, which is the reason for the incorporation of Mn as it gets oxidised to Mn^{4+} during synthesis via the reduction of Ni^{3+} to Ni^{2+} which serves as a structural stabiliser.[87] The capacity of the NMC 532 cathode was ~160 mAh g^{-1} (see Appendix C, Figure C.8 for GCD data).

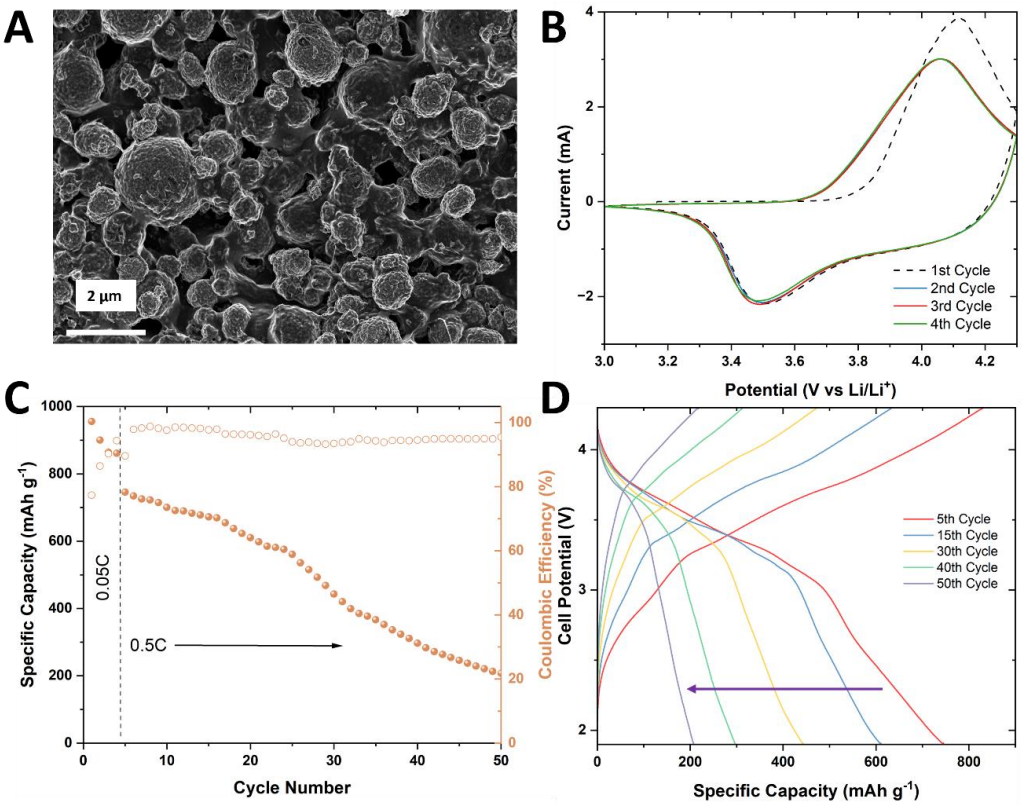

Figure 5.16: (A) SEM image of NMC cathode. (B) CV of NMC cathode at a scan rate of 0.1 mV s^{-1}. (C) Full cell GCD cycling data. (D) Full cell GCD charge/discharge curves at 0.5 C.

For full-cell fabrication, the *N/P* ratio (that is the ratio of the charge storage capacity of the negative to the positive) was set to ~1.1 to minimize the risk of Li-plating (balancing this with the first discharge capacity of the optimised cell, the cathode was ~8 times larger in mass).[88,89] The initial cycling data was promising, with the full-cell performance being equivalent to the half-cell at the initial slow *C-rate* (0.1 C), with a capacity of 955 mAh g^{-1} after the initial formation cycle (Figure 5.16C). However, upon increasing the cycling rate to 0.5 C, a steady drop in capacity and a CE of < 99% was recorded, with the capacity fading from 750 to 562 to 208 mAh g^{-1} between the 5th, 25th and 50th cycles. This fall in capacity is expressed in the GCD profile as well (Figure 5.16D). Through examination of the NMC cathode half-cell however, it is apparent that its cycling stability follows a similar trend, (see Appendix C, Figure C.8) with a capacity fade of 48% over the first 50 cycles. Therefore, it is the cathode engineering where improvements must be made. However this is still a very positive result, and where this study is left at the moment. The cell exhibits its full capacity at low rates, and through optimising the cathode to cycle stably, a stable full-cell can be developed with performance levels similar to that of the half-cell.

5.9 Conclusion

Using solvent-engineered SnO, high-performance LIB anodes were developed in terms of capacity, rate performance and cycling stability. The advantage of the solvent-engineered SnO was demonstrated as opposed to commercially purchased SnO from SA, and through the implementation and optimisation of P3-SWCNTs, the rate performance and specific capacity obtainable was greatly improved from the traditional slurry method, whilst also reducing the overall mass of the electrode and reducing the need for a copper current collector. The effect of morphology was investigated, with the nanoflower SnO produced in ethanol optimising the electrochemical energy storage of the material. Alternative SWCNTs manufactured by Tuball were utilised to improve the cyclability of the composite, whilst through the incorporation of 10% FEC to the electrolyte, stable and high-capacity cycling was observed. This improvement through the addition of FEC was attributable to the formation of a flexible SEI which could withstand the volumetric expansion during alloying, as was shown by post-mortem analysis of the electrodes with SEM and EDX, whilst also enabling the conversion reaction to be reversible as shown additionally by *dQ/dV* analysis. The optimised HT SnO(EtOH) with 15% Tu-SWCNTs has a capacity of 980 mAh g^{-1} at 0.1 C, an ICE of 80% and maintains a capacity of 815 mAh g^{-1} after 300 cycles at 0.5 C. Through analysis of similar work using the same materials, it is shown that this work is on a level of its own as it combines a cheap and scalable synthesis to form a high-performing anode with a high ICE, all factors which should optimise its potential commercialisation in the future. As a proof of concept, a full-cell LIB was developed with an NMC cathode. High initial capacity was recorded in the full-cell showing that the full performance of the anode is still obtainable in this configuration, whilst the cycling limitations of the cell were caused by the cathode.

Future work would look to further optimise the full-cell configuration by obtaining an optimised green cathode, exploring even more electrolyte additives such as vinylene carbonate and increasing the areal capacity of the anode. Furthermore, using the methods and iterative approach adopted, additional materials have been (investigated SiO_2)[90] and will be studied in the hope of producing more cost-effective, high-performance anodes.

5.10 Experimental

Preparation of SWCNTs dispersions

20 mg P3-SWCNT (CSI) was dissolved in 200 ml of propan-2-ol and dispersed using a tip-sonicator (Fisherbrand Ultrasonic Dismembrator) for 45 minutes with a 3.2 mm tip at an amplitude of 40%. The P3-SWCNTs solution was then placed in a sonic bath (FisherBrand 11207) for an hour at a frequency of 37 Hz. Tuball SWCNTs dispersions were used as purchased.

Preparation of SnO/Carbon Black slurry electrodes

SnO (200 mg) was placed in a mortar along with carbon black (42.8 g) and PVDF (42.8 g) and crushed until forming a fine grey powder with a mortar and pestle. The mortar was placed in a fume hood and NMP was added dropwise (1400 μl) whilst continually mixing. The mixture was placed on previously flattened Cu foil on a glass plate and spread using a doctor blade at 50 turns. The slurry was left to dry overnight and electrodes were cut using a 12 mm electrode puncher (El-Cell).

Preparation of SnO/P3-SWCNTs film electrodes

A 0.1% SnO dispersion was made using propan-2-ol as solvent. Various concentrations of SnO/P3-SWCNTs dispersions were made, in which the accurate percentage of each material was known. These dispersions were filtered using vacuum filtration (EMD Millipore™ 47 mm Glass Vacuum Filter) using the electrochemical cell separator as filter paper as shown in Figure 5.17A. Once fully dried, electrodes were cut using a 12mm electrode puncher as above.

Preparation of SnO/Tuball-SWCNTs electrodes

Using a 0.2% SWCNT, 0.4% CMC Tuball solution in water, SnO slurries of various mass fraction SWCNTs were prepared as done previously with the SnO/Carbon Black/PVDF slurry (Figure 5.17B), however with no need for the addition of PVDF or NMP as before. Alternatively they were prepared using the vacuum filtration method detailed for the SnO/P3-SWCNT composites.

Heat Treatment of Tuball Electrodes

Electrodes were placed in a tube furnace and heated under vacuum with an argon air flow at a ramp of 10 ºC/min with a 2 hr hold at 400 ºC to carbonise the CMC binder.

Freeze-Drying Electrodes

Wet SnO/Tuball slurries were first frozen in a freezer at −20 °C, and then the frozen samples were freeze-dried at 10 Pa and −50 °C (Labconco FreeZone 2.5 L Freeze Dry System).

Electrochemical Cell Construction

All electrochemical cells were constructed in an Argon-filled glove box (MBRAUN, Figure 5.17D). Within the cell casing, a wave spring and two spacers are placed initially on the coin cell base (negative end). For a half-cell, lithium foil is placed on top of the spacer, with the electrolyte LP30 [1 M LiFP6 in EC:DMC (50:50)] and a separator being placed next. The working electrode (anode/cathode) is placed on the other side of the separator (polyolefin membrane, Celgard 3501, 25 μm) and the cell lid is placed on, encasing the cell (as shown in Figure 5.17C). The cell is crimped using a hydraulic crimping machine (MSK-110). For a full-cell, the anode is placed on top of the spacers, followed by the electrolyte [1M $LiPF_6$ in EMC:FEC (95:5)] and a separator. The cathode is placed on top of the separator and the cell is encased and sealed as with the half-cell.

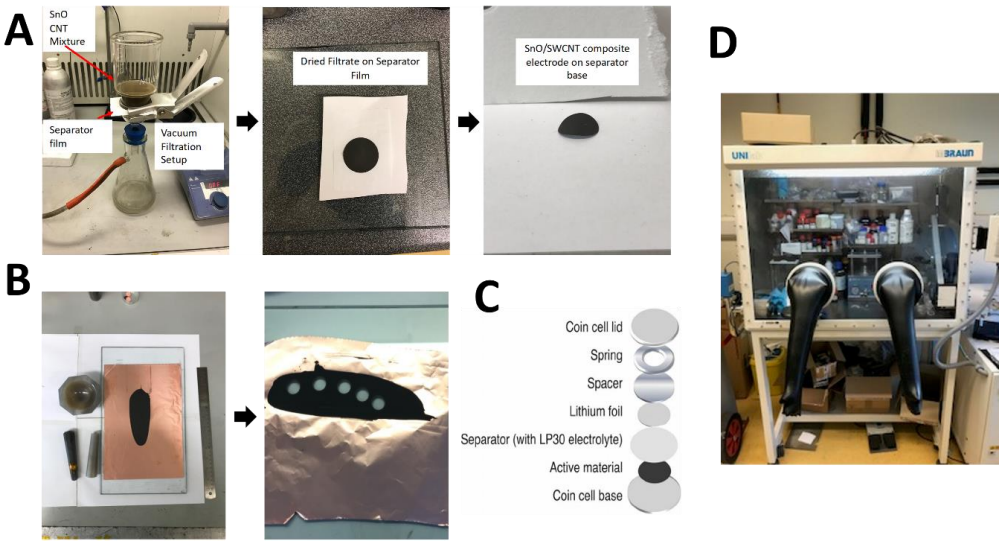

Figure 5.17: (A) Vacuum filtration setup used to form SnO/P3-SWCNT electrodes. (B) Mortar and pestle are used to mix active materials and carbon source for slurry cast electrodes and resulting punched electrodes. (C) Schematic of how a coin cell was assembled. (D) Glovebox used for all coin cells assembled.

Electrochemical Analysis

All electrochemical measurements were performed using either a Bio Logic VMP 300 or a Biologic BCS-805 and analysed using the EC-Lab software. For battery testing, CVs were run at various scan rates for 5 cycles in a voltage range of 0.001 – 2.5 V vs Li/Li^+ while GCD measurements were run at charge rates of 0.1, 0.2, 0.5, 1, 2, 5 and 10 C between 0.005 – 2.5 V vs Li/Li^+ for capacity testing/cycling and 0.005 – 1 V vs Li/Li^+ for additional cycling testing. For EIS measurements, the cell was fully discharged so it was in a fully de-lithiated state and left to rest for 1 hr before beginning the EIS testing. EIS was then recorded at an open circuit potential from 1 MHz to 50 mHz, and the resulting spectra obtained were analysed using the Z-fit software from EC-lab.

5.11 References

1 R. Hu, D. Chen, G. Waller, Y. Ouyang, Y. Chen, B. Zhao, B. Rainwater, C. Yang, M. Zhu and M. Liu, *Energy Environ. Sci.*, 2016, **9**, 595–603.

2 H. Li, Q. Su, J. Kang, M. Huang, M. Feng, H. Feng, P. Huang and G. Du, *Mater. Lett.*, 2018, **217**, 276–280.

3 X. Chen, Y. Huang, K. Zhang, X. Feng and C. Wei, *J. Alloys Compd.*, 2017, **690**, 765–770.

4 M. Z. Iqbal, F. Wang, H. Zhao, M. Y. Rafique, J. Wang and Q. Li, *Scr. Mater.*, 2012, **67**, 665–668.

5 J. H. Shin and J. Y. Song, *Nano Converg.*, 2016, **3(1)**, 9.

6 J. Haetge, P. Hartmann, K. Brezesinski, J. Janek and T. Brezesinski, *Chem. Mater.*, 2011, **23**, 4384–4393.

7 S.-H. Park, P. J. King, R. Tian, C. S. Boland, J. Coelho, C. (John) Zhang, P. McBean, N. McEvoy, M. P. Kremer, D. Daly, J. N. Coleman and V. Nicolosi, *Nat. Energy*, 2019, **4**, 560–567.

8 I. Jurewicz, P. Worajittiphon, A. A. K. King, P. J. Sellin, J. L. Keddie and A. B. Dalton, *J. Phys. Chem. B*, 2011, **115**, 6395–6400.

9 C. Gabbett, C. S. Boland, A. Harvey, V. Vega-Mayoral, R. J. Young and J. N. Coleman, *Chem. Mater.*, 2018, **30**, 5245–5255.

10 B. J. Landi, M. J. Ganter, C. D. Cress, R. A. DiLeo and R. P. Raffaelle, *Energy Environ. Sci.*, 2009, **2**, 549–712.

11 J. Coelho, A. Pokle, S.-H. Park, N. McEvoy, N. C. Berner, G. S. Duesberg and V. Nicolosi, *Sci. Rep.*, 2017, **7**, 7614.

12 T. M. Higgins, D. McAteer, J. C. M. Coelho, B. M. Sanchez, Z. Gholamvand, G. Moriarty, N. McEvoy, N. C. Berner, G. S. Duesberg, V. Nicolosi and J. N. Coleman, *ACS Nano*, 2014, **8**, 9567–9579.

13 R. Tian, S.-H. Park, P. J. King, G. Cunningham, J. Coelho, V. Nicolosi and J. N. Coleman, *Nat. Commun.*, 2019, **10**, 1933.

14 R. Cornut, D. Lepage and S. B. Schougaard, *Electrochim. Acta*, 2015, **162**, 271–274.

15 T. M. Higgins and J. N. Coleman, *ACS Appl. Mater. Interfaces*, 2015, **7**, 16495–16506.

16 C. Liu, Z. G. Neale and G. Cao, *Mater. Today*, 2016, **19**, 109–123.

17 Y. Wang, Z. X. Huang, Y. Shi, J. I. Wong, M. Ding and H. Y. Yang, *Sci. Rep.*, 2015, **5**, 9164.

18 F. Vallejos-Burgos, F.-X. Coudert and K. Kaneko, *Nat. Commun.*, 2018, **9**, 1812.

19 W. Cui, Y. Lansac, H. Lee, S.-T. Hong and Y. H. Jang, *Phys. Chem. Chem. Phys.*, 2016, **18**, 23607–23612.

20 M. Shakourian-Fard, G. Kamath and S. K. R. S. Sankaranarayanan, *ChemPhysChem*, 2016, **17**, 2916–2930.

21 Z. Li, L. Yuan, Z. Yi, Y. Sun, Y. Liu, Y. Jiang, Y. Shen, Y. Xin, Z. Zhang and Y. Huang, *Adv. Energy Mater.*, 2014, **4**, 1301473.

22 B. Ravikumar, M. Mynam and B. Rai, *J. Phys. Chem. C*, 2018, **122**, 8173–8181.

23 Q. Fan, P. J. Chupas and M. S. Whittingham, *Electrochem. Solid-State Lett.*, 2007, **10**, A274.

24 A. Ulvestad, A. H. Reksten, H. F. Andersen, P. A. Carvalho, I. J. T. Jensen, M. U. Nagell, J. P. Mæhlen, M. Kirkengen and A. Y. Koposov, *ChemElectroChem*, 2020, **7**, 4349–4353.

25 Z. Liu, X. Yuan, S. Zhang, J. Wang, Q. Huang, N. Yu, Y. Zhu, L. Fu, F. Wang,

Y. Chen and Y. Wu, *NPG Asia Mater.*, 2019, **11**, 12.
26 B. Wang, J. Ryu, S. Choi, G. Song, D. Hong, C. Hwang, X. Chen, B. Wang, W. Li, H.-K. Song, S. Park and R. S. Ruoff, *ACS Nano*, 2018, **12**, 1739–1746.
27 T.-F. Yi, L.-J. Jiang, J. Shu, C.-B. Yue, R.-S. Zhu and H.-B. Qiao, *J. Phys. Chem. Solids*, 2010, **71**, 1236–1242.
28 X. Lan, X. Xiong, J. Liu, B. Yuan, R. Hu and M. Zhu, *Small*, 2022, **18**, 2201110.
29 X. Li, X. Sun, X. Hu, F. Fan, S. Cai, C. Zheng and G. D. Stucky, *Nano Energy*, 2020, **77**, 105143.
30 I. A. Courtney and J. R. Dahn, *J. Electrochem. Soc*, 1997, **144**, 2045.
31 A. R. C. Bredar, A. L. Chown, A. R. Burton and B. H. Farnum, *ACS Appl. Energy Mater.*, 2020, **3**, 66–98.
32 D. Aurbach, *J. Power Sources*, 2000, **89**, 206–218.
33 N. Elgrishi, K. J. Rountree, B. D. McCarthy, E. S. Rountree, T. T. Eisenhart and J. L. Dempsey, *J. Chem. Educ.*, 2018, **95**, 197–206.
34 T. Kim, W. Choi, H.-C. Shin, J.-Y. Choi, J. M. Kim, M.-S. Park and W.-S. Yoon, *J. Electrochem. Sci. Technol*, 2020, **11**, 14–25.
35 N. Ding, J. Xu, Y. X. Yao, G. Wegner, X. Fang, C. H. Chen and I. Lieberwirth, *Solid State Ionics*, 2009, **180**, 222–225.
36 G. Ali, S. A. Patil, S. Mehboob, M. Ahmad, H. Y. Ha, H.-S. Kim and K. Y. Chung, *J. Power Sources*, 2019, **419**, 229–236.
37 J.-D. Xie, H.-Y. Li, B. Umesh, T.-C. Lee, J.-K. Chang and Y. A. Gandomi, *Electrochim. Acta*, 2018, **292**, 951–959.
38 B. Han, W. Zhang, D. Gao, C. Zhou, K. Xia, Q. Gao and J. Wu, *J. Power Sources*, 2020, **449**, 227564.
39 F. Zoller, S. Häringer, D. Böhm, H. Illner, M. Döblinger, Z. Sofer, M. Finsterbusch, T. Bein and D. Fattakhova-Rohlfing, *Adv. Funct. Mater.*, 2021, **31**, 2106373.
40 Z. Lv, W. Dong, B. Jia, S. Zhang, M. Xie, W. hao and F. Huang, *Chem. - A Eur. J.*, 2021, **27**, 2717–2723.
41 M. A. Kebede, *Curr. Opin. Electrochem.*, 2020, **21**, 182–187.
42 J. Ding, Z. Li, H. Wang, K. Cui, A. Kohandehghan, X. Tan, D. Karpuzov and D. Mitlin, *J. Mater. Chem. A*, 2015, **3**, 7100–7111.
43 F. Zoller, D. Böhm, T. Bein and D. Fattakhova-Rohlfing, *ChemSusChem*, 2019, **12**, 4140–4159.
44 X. Liu, Y. Han, J. Zeng, H. Yang, K. Zhou and D. Pan, *J. Mater. Sci. Mater. Electron.*, 2018, **29**, 5710–5717.
45 M. Mohamedi, S.-J. Lee, D. Takahashi, M. Nishizawa, T. Itoh and I. Uchida, *Electrochim. Acta*, 2001, **46**, 1161–1168.
46 I. A. Courtney and J. R. Dahn, *J. Electrochem. Soc*, 1997, **144**, 2943.
47 G. Ferraresi, C. Villevieille, I. Czekaj, M. Horisberger, P. Novák and M. El Kazzi, *ACS Appl. Mater. Interfaces*, 2018, **10**, 8712–8720.
48 M. Mirolo, X. Wu, C. A. F. Vaz, P. Novák and M. El Kazzi, *ACS Appl. Mater. Interfaces*, 2021, **13**, 2547–2557.
49 I. A. Courtney, R. A. Dunlap and J. R. Dahn, *Electrochim. Acta*, 1999, **45**, 51–58.
50 Y. Cheng, J. Huang, H. Qi, L. Cao, J. Yang, Q. Xi, X. Luo, K. Yanagisawa and J. Li, *Small*, 2017, **13**, 1700656.
51 A. Fly and R. Chen, *J. Energy Storage*, 2020, **29**, 101329.
52 R. Hu, H. Zhang, Z. Lu, J. Liu, M. Zeng, L. Yang, B. Yuan and M. Zhu, *Nano Energy*, 2018, **45**, 255–265.
53 B. Zhang, Y. Yu, Z. Huang, Y.-B. He, D. Jang, W.-S. Yoon, Y.-W. Mai, F. Kang

and J.-K. Kim, *Energy Environ. Sci.*, 2012, **5**, 9895–9902.
54 R. Lv, L. Zou, X. Gui, F. Kang, Y. Zhu, H. Zhu, J. Wei, J. Gu, K. Wang and D. Wu, *Chem. Commun.*, 2008, 2046–2048.
55 M. R. Predtechenskiy, A. A. Khasin, A. E. Bezrodny, O. F. Bobrenok, D. Y. Dubov, V. E. Muradyan, V. O. Saik and S. N. Smirnov, *Carbon Trends*, 2022, **8**, 100175.
56 S. Pinilla, S. Ryan, L. McKeon, M. Lian, S. Vaesen, A. Roy, W. Schmitt, J. N. Coleman and V. Nicolosi, *Adv. Energy Mater.*, 2023, **13**, 2203747.
57 D. de Britto and O. B. G. Assis, *Thermochim. Acta*, 2009, **494**, 115–122.
58 S. Kitabayashi and N. Koga, *J. Phys. Chem. C*, 2015, **119**, 16188–16199.
59 C. M. Campo, J. E. Rodríguez and A. E. Ramírez, *Heliyon*, 2016, **2**, e00112.
60 S.-L. Chou, J.-Z. Wang, H.-K. Liu and S.-X. Dou, *J. Phys. Chem. C*, 2011, **115**, 16220–16227.
61 Q. Cheng, Y. Okamoto, N. Tamura, M. Tsuji, S. Maruyama and Y. Matsuo, *Sci. Rep.*, 2017, **7**, 14782.
62 D. Jang, S. Suh, H. Yoon, J. Kim, H. Kim, J. Baek and H.-J. Kim, *Appl. Surf. Sci. Adv.*, 2021, **6**, 100168.
63 R. Wang, L. Feng, W. Yang, Y. Zhang, Y. Zhang, W. Bai, B. Liu, W. Zhang, Y. Chuan, Z. Zheng and H. Guan, *Nanoscale Res. Lett.*, 2017, **12**, 575.
64 L. Qiu, Z. Shao, D. Wang, F. Wang, W. Wang and J. Wang, *Cellulose*, 2014, **21**, 2789–2796.
65 D. Bresser, D. Buchholz, A. Moretti, A. Varzi and S. Passerini, *Energy Environ. Sci.*, 2018, **11**, 3096–3127.
66 C. Ma, J. Jiang, T. Xu, H. Ji, Y. Yang and G. Yang, *ChemElectroChem*, 2018, **5**, 2387–2394.
67 H. Xu, J. Chen, D. Wang, Z. Sun, P. Zhang, Y. Zhang and X. Guo, *Carbon N. Y.*, 2017, **124**, 565–575.
68 J. Liu, Q. Duan, K. Qi, Y. Liu, J. Sun, Z. Wang and Q. Wang, *J. Energy Storage*, 2022, **46**, 103910.
69 H. Kato, Y. Kobayashi and H. Miyashiro, *J. Power Sources*, 2018, **398**, 49–54.
70 H. M. Dahn, A. J. Smith, J. C. Burns, D. A. Stevens and J. R. Dahn, *J. Electrochem. Soc.*, 2012, **159**, A1405.
71 Y. Jin, N.-J. H. Kneusels, L. E. Marbella, E. Castillo-Martínez, P. C. M. M. Magusin, R. S. Weatherup, E. Jónsson, T. Liu, S. Paul and C. P. Grey, *J. Am. Chem. Soc.*, 2018, **140**, 9854–9867.
72 K. Xu, *Chem. Rev.*, 2014, **114**, 11503–11618.
73 S. Hong, M.-H. Choo, Y. H. Kwon, J. Y. Kim and S.-W. Song, *Adv. Mater. Interfaces*, 2016, **3**, 1600172.
74 C. C. Nguyen and B. L. Lucht, *J. Electrochem. Soc.*, 2014, **161**, A1933.
75 L. Zhang, Y. Qin, Y. Liu, Q. Liu, Y. Ren, A. N. Jansen and W. Lu, *J. Electrochem. Soc.*, 2018, **165**, A2102.
76 T. Jaumann, J. Balach, U. Langklotz, V. Sauchuk, M. Fritsch, A. Michaelis, V. Teltevskij, D. Mikhailova, S. Oswald, M. Klose, G. Stephani, R. Hauser, J. Eckert and L. Giebeler, *Energy Storage Mater.*, 2017, **6**, 26–35.
77 D. M. Seo, C. C. Nguyen, B. T. Young, D. R. Heskett, J. C. Woicik and B. L. Lucht, *J. Electrochem. Soc.*, 2015, **162**, A7091.
78 T. Hou, G. Yang, N. N. Rajput, J. Self, S.-W. Park, J. Nanda and K. A. Persson, *Nano Energy*, 2019, **64**, 103881.
79 J. Zhong, T. Wang, L. Wang, L. Peng, S. Fu, M. Zhang, J. Cao, X. Xu, J. Liang, H. Fei, X. Duan, B. Lu, Y. Wang, J. Zhu and X. Duan, *Nano-Micro Lett.*, 2022,

14, 50.
80 N. Wan, T. Zhao, S. Sun, Q. Wu and Y. Bai, *Electrochim. Acta*, 2014, **143**, 257–264.
81 A. K. Rai, L. T. Anh, J. Gim, V. Mathew and J. Kim, *Electrochim. Acta*, 2013, **109**, 461–467.
82 H. Song, X. Li, Y. Cui, D. Xiong, Y. Wang, J. Zeng, L. Dong, D. Li and X. Sun, *Int. J. Hydrogen Energy*, 2015, **40**, 14314–14321.
83 R. Liu, N. Zhang, X. Wang, C. Yang, H. Cheng and H. Zhao, *Front. Mater. Sci.*, 2019, **13**, 186–192.
84 J. A. Weeks, H.-H. Sun, H. S. Srinivasan, J. N. Burrow, J. V Guerrera, M. L. Meyerson, A. Dolocan, A. Heller and C. B. Mullins, *ACS Appl. Energy Mater.*, 2019, **2**, 7244–7255.
85 Y. Yu, C.-H. Chen and Y. Shi, *Adv. Mater.*, 2007, **19**, 993–997.
86 S. Chen, Y. Xin, Y. Zhou, F. Zhang, Y. Ma, H. Zhou and L. Qi, *J. Mater. Chem. A*, 2014, **2**, 15582–15589.
87 A. Manthiram, *Nat. Commun.*, 2020, **11**, 1550.
88 M. Luo, M.-T. F. Rodrigues, L. L. Shaw and D. P. Abraham, *ACS Appl. Energy Mater.*, 2022, **5**, 5513–5518.
89 Y. Abe and S. Kumagai, *J. Energy Storage*, 2018, **19**, 96–102.
90 O. Ronan, A. Roy, S. Ryan, L. Hughes, C. Downing, L. Jones and V. Nicolosi, *ACS Omega*, 2023, **8**, 925–933.

6. Tin(II) Oxide as a Sodium Ion-Battery Anode

As the performance of SnO together with SWCNTs had been optimised toward LIB technology, the focus of the study pivoted to focusing on sodium-ion chemistry. As discussed, SnO had the advantage of forming alloys with both lithium and sodium respectively and thus the opportunity arises for one composite material to fill the need for both technologies (*kill two birds with one stone*) whilst costs would be minimised through economies of scale.

Similar to the previous work with LIBs, the majority of the research in the field is focused on SnO_2. At this moment in time, Sn-based materials in NIBs do not perform as well as their LIB counterparts in any of the key indicators (capacity, rate, CE, cycling stability).[1] Recent work of note has been carried out by Zhang *et al.*[2] investigating ultrafine SnO_2 nanoparticles on reduced graphene oxide, with a maximum charge capacity of 324 mAh g^{-1} and stable cycling achieved for 80 cycles at 50 mA g^{-1}. Ding *et al.*[3] employed a SnO_2-carbon nanocomposite with a maximum capacity of 531 mAh g^{-1} and a capacity retention of 81% over 200 cycles. In terms of work with SnO, Lu *et al.*[4] utilised flower-like SnO to from NIB anodes, with a maximum capacity of 500 mAh g^{-1}. Zhang *et al.*[5] synthesised ultrathin SnO nanosheets on carbon cloth, with the thinnest sheets composed of 2 monolayers of SnO optimising results with a maximum capacity of 848 mAh g^{-1} and a reversible capacity of 665 mAh g^{-1} at 100 mA g^{-1}. However, the amount of inactive mass present due to the carbon cloth has not been considered either in terms of the results (they report in terms of the active mass of SnO) or in terms of practical sense; as having this much inactive material present for atomically thin materials completely counteracts the advantage one would gain from the small dimensions. Also, it must be stated again that all works quoted here utilise hydrothermal syntheses with scalability and cost issues.

As there still remains many obstacles in terms of a high-performance SnO anode, this motivated the work to investigate the material in a NIB cell and attempt to optimise the performance to exceed the current state-of-the-art work. The same methods and iterative process as used in the previous Chapter were implemented again for this study.

6.1 Optimisation of SWCNT Mass Loading

Initially, SnO formed using ethanol as the reflux solvent was combined with varying mass fractions of P3-SWCNT to establish at what mass loading Na-ion storage would be optimised. The electrodes were formed identically as had been for the investigation carried out into LIBs and so the SEM images in Figure 5.2 are still representative of the electrodes. As is shown in Figure 6.1, once again a mass fraction of 15% P3-SWCNTs optimises the energy storage capability for the composite. Striking differences however are realised when comparing the data for NIB electrodes (Figure 6.1) with the LIB electrodes (Figure 5.3). Firstly, the obtainable capacities are much lower for the electrode when subjected to sodium chemistry. The maximum capacity for the SnO(EtOH) with 15% P3-SWCNT in a LIB was 960 mAh g^{-1} whilst switching to Na the maximum capacity drops to 430 mAh g^{-1} (maximum theoretical capacity of the Na-Sn alloying is 746 mAh g^{-1}). Furthermore, the NIB electrode was more rate-limited at this stage. The GCD testing had to be halted at 1 C as rates above this were not able to sustain stable energy storage, whilst we can see even by 1 C, the capacity for the optimised composite has dropped to 48% (206 mAh g^{-1}) that of its maximum value. Contrast this with the LIB anode, where a capacity of 70% of the maximum was obtainable at 1 C (673 mAh g^{-1}). This drop off in performance as one transitions from Li to Na chemistry is common throughout the field, and is the main reason why NIBs which have been under investigation since the 1980's have to this point failed to be widely commercialised.[6–8] As stated, the reason for this drop-off is primarily a consequence of the larger ionic size of Na^+, and the sluggish kinetics associated with.[2,9,10] However these early results are not without promise, the capacity of hard carbon (300 mAh g^{-1}) has been exceeded in addition to also surpassing the capacity of several of the quoted results reported in the previous section (the capacity obtained is 506 mAh g^{-1} when converted to active mass for comparison).

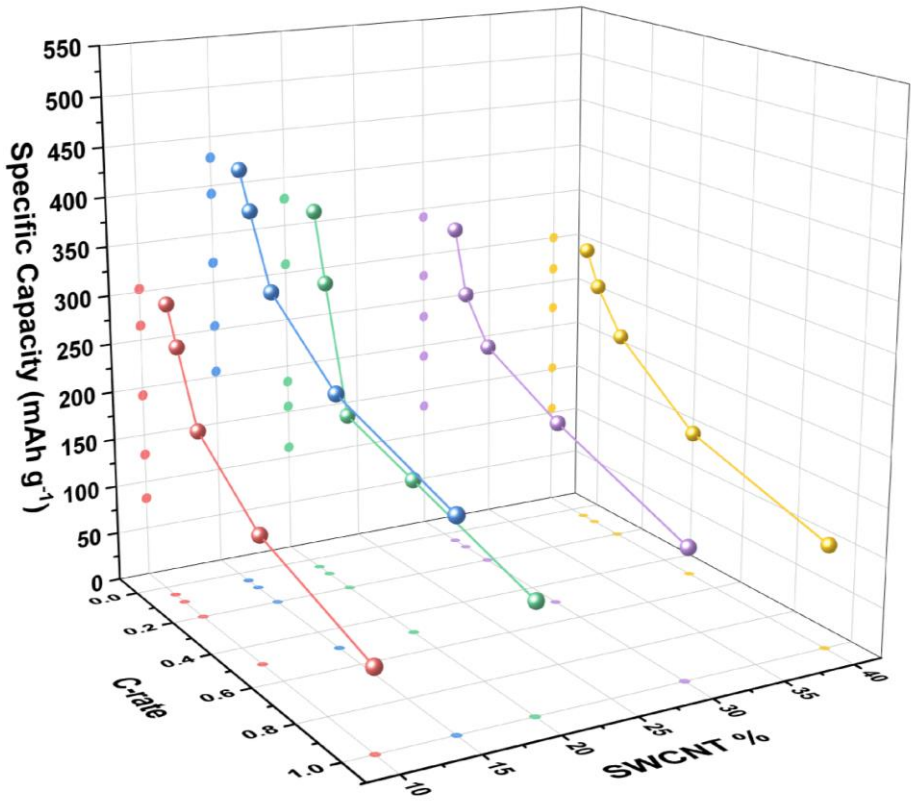

Figure 6.1: SnO/SWCNTs composite discharge capacities (5th cycle) as a function of P3-SWCNT mass fraction at different *C-rates*; *C-rates* on the x-axis, SWCNT% on the y-axis and specific capacity on the z-axis.

The rate equation (Equation 5.1) developed by Tian *et al.*[11] was again utilised to provide additional analysis of the GCD data and extract the parameters Q_m, τ and n with the results displayed in Table 6.1. In agreement with the GCD results in Figure 6.1, a mass fraction of 15% is calculated to obtain the greatest low rate capacity for the composite of 645 mAh g^{-1}. The τ value is seen to drop with every increase in SWCNT %, up to a value of 30% at which point saturation occurs and more conductive additive is no longer advantageous to the rate capability. However, even though the 30% composite obtains the lowest value for τ, and hence the greatest rate capability before it is subjected to the high-rate exponential decay, the initial capacity is inferior (66%) to that obtained at 15% SWCNT. The n values are all below 0.5 except for the 20% mass fraction, which as stated previously is a consequence of fitting errors associated with a small capacity drop-off at higher rates (all relative to initial capacities). Similar to the results for the composite as an electrode for LIBs, 15% P3-SWCNT optimises the performance in NIBs too, albeit without meeting the theoretical capacity of the material at this point. The study now turned to examining the effect of the SnO morphology on the NIBs performance.

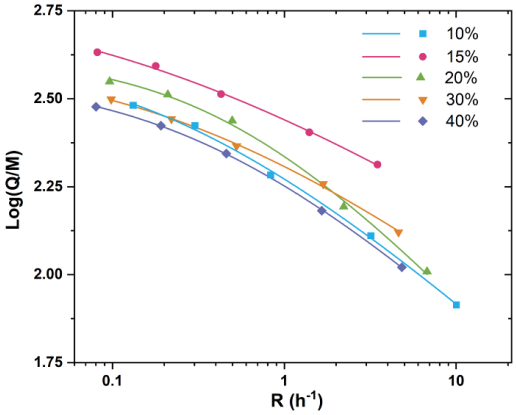

SWCNT %	Q_m (mAh g^{-1})	τ (h)	n
10	446	0.66	0.45
15	645	0.52	0.33
20	435	0.44	0.55
30	426	0.38	0.40
40	380	0.46	0.47

Figure 6.2: GCD experimental data fitted using Equation 5.1.

Table 6.1: Parameters Q_M, τ and n for each mass fraction of SWCNT after fitting GCD data using Equation 5.1.

6.2 Investigation into the Effect of Morphology

Four unique morphologies of SnO were investigated as a potential NIB anode combined with 15% mass fraction P3-SWCNTs. As a reminder, the morphologies were nanoflowers (SnO(EtOH)), thin-square platelets (SnO(70% MeOH)), perforated thick-squares (SnO(Hex)), and thick-squares (SnO(H_2O)). All morphologies tested produced functioning NIB anodes.

Rate Performance and Cyclability

The large drop off from the initial to subsequent cycle was due to the irreversible formation of sodium oxide and the SEI, which one may recall occurred for the lithium chemistry as well. Similar to the results obtained from the study on LIBs, the thin platelet-like morphologies of SnO produced in EtOH and MeOH obtain the best performance in terms of capacity at all rates tested. Again analogous to the results recorded for LIBs, the thicker morphologies produced in hexanol and water recorded lower capacities at all rates, with the thick square morphology produced in water producing the lowest capacities throughout. The results once again may be rationalised by the surface area of the unique SnO particles, with those with larger surface areas having larger energy storage capabilities due to the increased Na^+ flux across the interface. As was rationalised with the work on LIBs, the significantly poorer energy storage capabilities of the sample produced in water with reference to the other morphologies is a consequence of the highly structured and crystalline morphology. The limitations of the NIB compared to the LIB technology is also apparent from when one compares the overall results (Figure 6.3A) to

those for the LIB presented in Figure 5.6A, with in excess of a 50% drop in specific capacity recorded through use of the Na^+ ion. As discussed, this is a common theme across the field where materials are tested for both NIBs and LIBs, and is attributable to the larger atomic size of Na and its lower diffusion coefficient in Sn compared to Li (Gu *et al.* measured the diffusivity of Na to be 3% of Li at room temperature into Sn and corroborated this finding through in-situ TEM).[12,13]

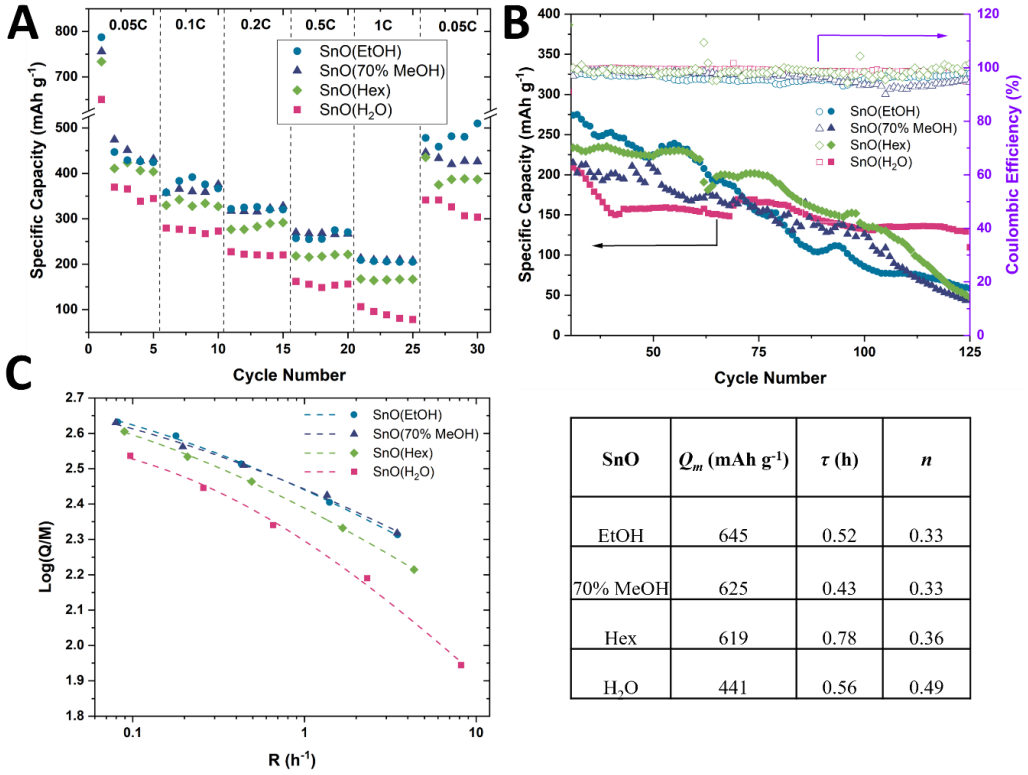

SnO	Q_m (mAh g^{-1})	τ (h)	n
EtOH	645	0.52	0.33
70% MeOH	625	0.43	0.33
Hex	619	0.78	0.36
H_2O	441	0.56	0.49

Figure 6.3: (A) Rate capability of tested morphologies of synthesised SnO with 15% mass fraction P3-SWCNTs at various *C-rates*. (B) Cycling performance of the SnO morphologies at 0.5 C after rate capability test. (C) Experimental GCD data fitted using Equation 5.1 for SnO morphologies.

Table 6.2: Parameters for Equation 5.1 obtained via the fitting of experimental GCD data in Figure 6.3C.

Interestingly, upon recycling at 0.05 C in Figure 6.3A, the capacity of the composites remained constant, with the nanoflower sample produced in ethanol increasing its capacity by 20%. This suggests an 'activation' period of several cycles is needed in which repeated sodiation/de-sodiation causes a rearrangement of the anode to allow more tin to participate in the alloying reaction. This is consistent with work carried out on other alloy/conversion materials and SnO_2.[14,15] It has well been established that a feature associated with SnO_x materials in NIBs is that the active Sn particles that form in the Na_2O matrix become electrically isolated due to the diffusion barrier of the matrix, shown by the existent of un-alloyed Sn after complete charging of the cell.[5,16–20] Biswal *et al.*[15]

suggested this 'activation' process occurs due to an electrochemical milling effect during charge/discharge cycles, leading to a decreasing size of Sn which allows the Na_2O conversion to become reversible owing to the increased surface area, similar to how the decreased size of Sn leads to greater LiO_2 reversibility for LIBs. Furthermore, in addition to increasing its capacity upon recycling at 0.05 C, the nanoflower morphology also obtains the greatest capacity at this stage, with the enhanced stability obtainable due to the contacted points between the flowers, as was the case in the LIB study.[21] After conducting the rate test, cycling stability testing was carried out on all 4 morphologies using GCD at a rate of 0.5 C (Figure 6.3B). The cycling stability of all composites is not stable at this stage, with a gradual loss in capacities being measured throughout and CEs below 99% recorded. By the 100th cycle the capacity of all morphologies has dropped to below 200 mAh g^{-1}.

This initial study into solvent engineered SnO for NIBs although by no means perfect, polished or finished, has presented some exciting features to encourage further work. The maximum capacity obtained (excluding the initial) of 510 mAh g^{-1} was for the nanoflower morphology, and this compares favourably to other work carried out on SnO_x composites. When this value is converted to active mass to allow for an adequate comparison with other works, a value of 600 mAh g^{-1} is obtained. This result compares favourably to other works carried out on SnO_2 by Lu *et al.*[4] (500 mAh g^{-1}), by Mao *et al.*[16] (227 mAh g^{-1}) and by Su *et al.*[19] (578 mAh g^{-1}). The ICE of the SnO samples were 47% (EtOH), 47% (70% MeOH), 51% (H_2O) and 45% (Hex). This value is considerably lower that the values recorded for their LIB counterparts (>78%) and is a result of the irreversible formation of the Na_2O matrix.

The rate equation (Equation 5.1) was utilised once more to predict Q_M and analyse the constant τ as shown in Figure 6.3C and Table 6.2. The SnO(EtOH) had the largest Q_M of 645 mAh g^{-1}, whilst the SnO(70% MeOH) had the lowest τ value of 0.43 h, once again displaying the advantages of the thin platelet-like morphologies in terms of capacity and rate capability. The values of n obtained from the high-rate regime are neglected and as discussed previously, are fitting errors due to small capacity fall-offs at higher rates.[11] Overall however, at this point and similar to the work on LIBs the morphological advantages of the thin platelet-like morphology is clearly evident.

Impedance and Diffusion

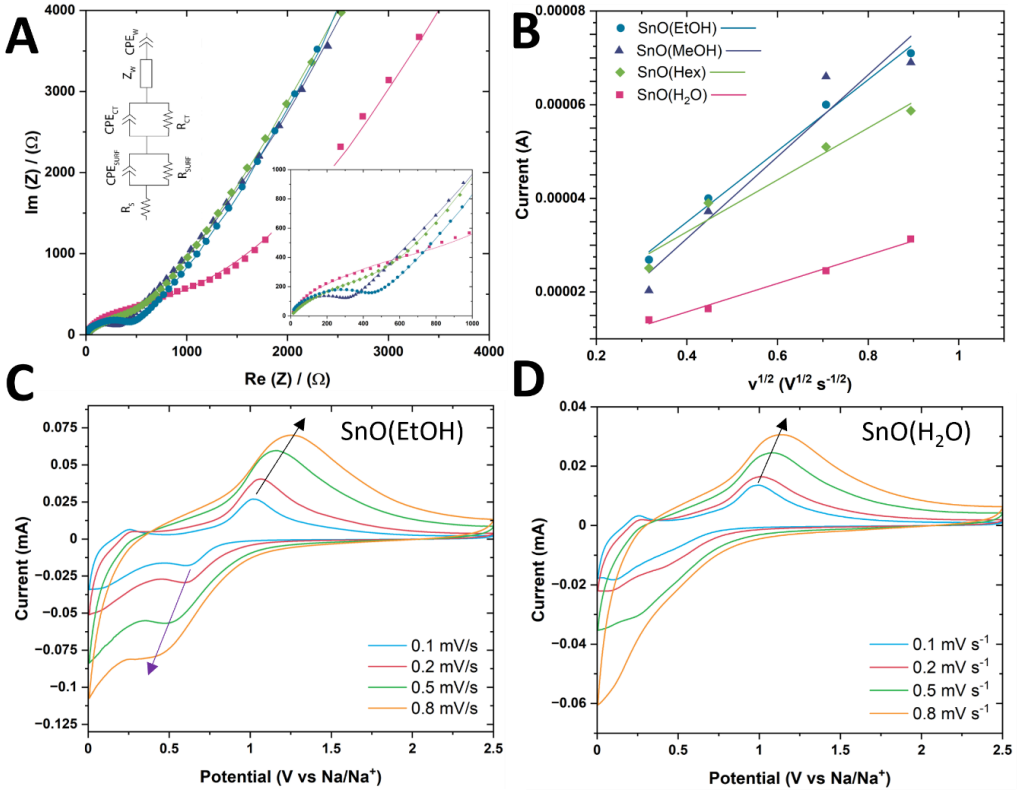

SnO	R_S (Ω)	R_{SURF} (Ω)	R_{CT} (Ω)	$D_{anodic} / n^3 (\cdot 10^{-12}$ cm^2 s^{-1})
EtOH	1	278.2	86.1	5.5
70% MeOH	4.2	259.7	87.8	7.3
Hexanol	1.2	344.5	398.3	2.5
H_2O	4.6	358	984.9	0.9

Figure 6.4: (A) EIS spectra (with zoomed inset on the high-frequency region) for the synthesised SnO morphologies and the Z-fit approximation using the equivalent circuit shown inset (please note the legend that applies to (B) also applies for (A)). (B) Anodic peak current as a function of the square root of scan rate. (C) CV profile of SnO(EtOH) at various scan rates. (D) CV profile of SnO(EtOH) at various scan rates.

Table 6.3: Equivalent circuit parameters calculated using Z-fit of the EIS spectra and the anodic diffusion coefficients calculated using the Randles-Sevchik equation.

EIS was used to probe the various resistances at play in the un-sodiated state of the anodes after the initial formation cycles, with the same equivalent circuit that was used in Chapter 5 being employed again. The resistance results obtained from using the Z-fit software on the Nyquist plots of the experimental data are tabulated below in Table 6.3. Focusing on the surface resistance (R_{surf}) and the charge transfer resistance (R_{CT}), it is seen that similar to the work on the materials in the LIB configuration, the thin platelet-like structures have the lowest associated resistances. For example, the thin platelets of SnO(70% MeOH)

have a R_{surf} of 259.7 Ω and a R_{CT} of 87.8 Ω, whilst the thick-squares of SnO(H_2O) have resistances of 358 Ω and 984.9 Ω respectively. The electrochemical limitations caused by the larger Na^+ ion is also evident when one compares the EIS results to those obtained in Chapter 5, Table 5.3 for the LIB counterpart. Taking the nanoflower sample of SnO(EtOH), from switching the ion to Na^+, the R_{surf} increases from 68.3 Ω to 278.2 Ω, whilst the R_{CT} increases from 10.9 Ω to 86.1 Ω.

As was done in Chapter 5, the Randles-Sevchik Equation (Equation 5.3) was utilised to probe the apparent Na^+ diffusion coefficients (D_{Na}) of the various morphologies. All constants were the same as used in Chapter 5 except for the active surface (A in Equation 5.3) which was 0.12 cm^2. CV measurements were recorded at various scan rates on the 4 morphologies of SnO, as shown in Figure 6.4C and D, with the slope of the linear fit of the anodic peak current versus the square root of scan rate being used to find D_{Na}. Due to the overpotential of the cathodic peak with increasing sweep rate, it was difficult to track the progression of the final alloying peak current, thus only the anodic D_{Na} is evaluated. Furthermore, as the anodic peak that was chosen to be evaluated is at ~1 V, it is a combination of the dealloying/conversion reaction.[3,5,12,16,18,19,22–24] Therefore the number of electrons was omitted from Randles-Sevchik calculation due to the ambiguity in the actual number of electrons associated with the peak, whilst also acknowledging that this equation is being used as a comparison between the 4 morphologies and thus the number of electrons remains a constant for all, without changing the result of the analysis.

From the results displayed in Table 6.3, it is shown that the thin-platelet morphology and nanoflower morphology of SnO have the largest diffusion coefficients of $7.3/n^3$ and $5.5/n^3$ x 10^{-12} cm^2 s^{-1} respectively. These values are similar in magnitude to that obtained by Han *et al.*[24] on encapsulated tin oxide nanoparticles in holey carbon nanotubes (5.78 x 10^{-13} cm^2 s^{-1}). Once again, the diffusion limitations of the Na^+ ion in relation to the Li^+ ion is shown when doing a direct comparison to the results tabulated in Table 5.3, with the Na^+ ion diffusing in the order of 10^3 times slower. Again, the thicker samples of the perforated thick square (Hex) and the thick square (H_2O) are the most diffusion limited morphologies, with the trend observed mirroring that which was measured for the LIB work. Once again, this emphasises the advantages obtained through nanostructuring dimensions in one's active material in terms of diffusion capabilities which in turn is intrinsically linked to the materials rate capability. Furthermore, the cathodic peak at 0.5

V vs Na/Na^+ in the CV of SnO(EtOH) (Figure 6.4C, marked by an arrow) is not visible in the CV of SnO(H_2O). This holds true when the SnO(70% MeOH) is compared with the SnO(Hex) in Appendix D, Figure D.1. This is a consequence of the diffusion limitations of the bulkier materials, with the peak being supressed/elongated due to an overpotential as opposed to the well-defined peaks of the platelet like structures.[25]

Both the nanoflower (EtOH) and thin-platelet (70% MeOH) had produced the best results to date in terms of capacity, rate performance, impedance and diffusion. Due to its slightly larger specific capacity and its better initial cycling performance, it was elected to continue the optimisation of a NIB anode with the nanoflower SnO(EtOH). Although the SnO(MeOH) platelet had a marginally greater diffusion coefficient, as well as marginally smaller τ from the rate equation, the differences were not significant enough to outweigh the crucial factors of capacity and cycling. Furthermore, the aim of this PhD fellowship was to develop a composite material that fits both LIB and NIB technology and choosing SnO(EtOH) has the added advantage of being the superior morphology for LIB technology also.

6.3 Electrochemistry of Optimised Morphology

Using the voltammogram presented in Figure 6.5A, the electrochemical processes at play during the sodiation/de-sodiation of the SnO(EtOH)/P3 anode may be elucidated. One may notice that compared to the CVs for the same material in the LIB configuration (Figure 5.8A), the redox peaks associated with alloying/conversion are much broader and washed out owing to the kinetic limitations of the Na^+ ion.[3] During the initial cathodic sweep, the subtle peak at 1 V corresponds to the formation of the SEI.[12,17,18,22] The peak beginning at 0.6 V is associated with the conversion reaction, liberating the Sn particles and the formation of the Na_2O matrix. This peak overlaps with the initial sodiation of the Sn which is centred at 0.2 V, to form the Na_xSn alloys, to the final terminal alloy of $Na_{15}Sn_4$.[13,15,26] In subsequent cycles, this large peak is separated into two peaks at 0.6 V and 0.1 V.[15] In the initial anodic sweep the peak at 0.25 V is associated with the initial de-sodiation of $Na_{15}Sn_4$, whilst the broad peak centred at 1 V but continuing to 1.75 V is a combination of the peaks associated with the final de-alloying of the Na_xSn and the subsequent reconversion of Sn to SnO.[5,12,15,18] The CV curves display exceptional

reversible characteristics for all cycles, except for the initial cycle, ensuring that the electrochemical reactions present are fully reversible at the initial stages.

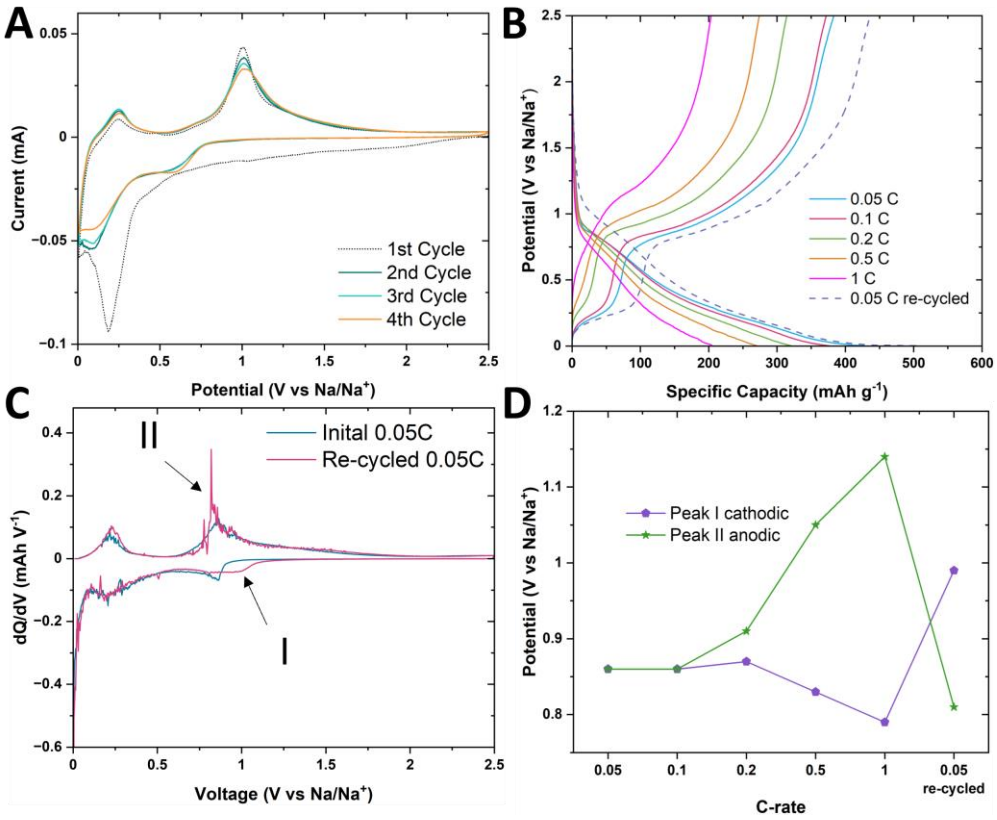

Figure 6.5: (A) CV of SnO(EtOH) electrode at 0.1 mV $s^{-1}$and (B) GCD profile of SnO(EtOH) electrode at various rates and re-cycled at 0.05 C. (C) *dQ/dV* analysis of GCD profile in (B). (D) Variation in anodic/cathodic peak voltage with C-rate.

Figure 6.5B shows the GCD profiles of the composite from 0.05 to 1 C, and the subsequent re-cycling at 0.05 C. The sloping curves and plateaus of the GCD profiles are consistent with the CV results. During sodiation (charging) of the anode at slow rates (< 0.2 C), we see two distinct slopping plateaus from roughly 0.9 to 0.5 V and from 0.5 to 0.05 V, coinciding with the two distinct peaks in the cathodic scan of the CV. For the de-sodiation (discharging) of the anode, two sloping plateaus are observed again coinciding with the two anodic peaks on the CV, from 0.15 to 0.3 V and from 0.75 to ~1.2 V. Recalling that the maximum theoretical capacity of SnO in a NIB is 1,144 mAh g^{-1} considering the oxide conversion reaction, and 746 mAh g^{-1} when only considering the alloying reaction, it is clear the SnO(EtOH)-P3 composite is short of these figures. During the initial discharge, a capacity of 787 mAh g^{-1} was recorded, which is 81% (when converted to active mass) that of the maximum for this cycle (without considering the irreversible capacity from SEI formation), demonstrating that the full potential capacity

of the anode is not utilised. This inability to reach the theoretical capacity of SnO_x in a NIB configuration is a common feature throughout the previous work carried out on the material, with the explanation deduced from numerous studies using XRD and XPS attributable to unreacted Sn when the anode is finished charging.[2–4,17,18,23] This unreacted Sn is most likely present due to the lower diffusivity of Na^+ in Sn and the denser Na_2O shell which blocks electronic and ionic transport into the inner region of Sn particles.[3,27] The activation process mentioned previously is also apparent in the GCD profile, with enhanced capacity obtained upon the re-cycling of the anode at 0.05 C. This may be deduced as alluded to previously to an electrochemical milling effect which decreases the Sn particle size, reducing the negative effects of the slow Na^+ diffusivity in the anode and allowing for increased alloying conversion reactions. This is apparent when one compares the 0.05 C to the re-cycled 0.05 C GCD profile at the discharge plateau from 0.15 to 0.3 V. This plateau is due to the first dealloying of the Na_xSn, and upon re-cycling 56% more capacity is obtainable owing to a greater amount of Sn being able to participate in the alloying reaction due to the reduced size from activation.

Differential capacity analysis (*dQ/dV*) was performed on the GCD profiles to monitor the onset of the initial cathodic reaction (peak I) and final anodic reaction (peak II) which correspond to the beginning/completion of the alloying/conversion in Figure 6.5C. Due to the overlapping of the alloying/conversion reactions, it is not possible to pinpoint an exact start/end of the conversion/alloying reaction.[3,9,16,28] As shown in Figure 6.5D, onset and completion of the charge/discharge process remain relatively stable up to 0.2 C, however above this point we see larger overpotentials take hold, so at 1 C a potential of 0.8 and 1.15 V is needed to begin/complete the reaction compared to 0.86 V for both anodic and cathodic processes at 0.05 C. The effect of the activation process is demonstrated here also, with the onset of the cathodic reaction increasing to 1 V whilst the completion of the anodic reaction falls to 0.8 V. This is further evidence for the electrochemical milling effect, with less of a driving force needed to initiate the reactions due to the decreased size of the active particles counteracting the low ionic and electrical conductivity of the Na_2O matrix.[15,16]

6.4 Tuball SWCNTs for Improved Performance

Similar to the research carried out on LIBs, the focus of the study into the composite for NIBs now shifted towards varying the source of SWCNTs. A noticeable difference however at this point in the NIB study compared to the LIB study was that the specific capacity of the composite remained an issue. Therefore, the incorporation of Tuball SWCNTs into the anode was not only hoped to stabilise the cycling life by creating a network that limits the active mass loss through maintaining together the "milled" material, but also enhance the electrical conductivity within the anode to reduce the overpotential experienced during cycling. As discussed in Chapter 5, the advantages of using Tuball SWCNTs are their superior price offering (€70/kg compared to the P3 cost of $280/g, which is an astronomical difference), whilst also being sold in a water dispersible form using a surfactant which allow for more complicated fabrication processes to be investigated. As is shown in Figure 6.6B, there is a stark difference observed via SEM in the coverage of the active material when comparing the SWCNTs. The P3 product presents finely distributed 'web-like' arrangements of SWCNTs which while still connecting the active material leave a lot of the surface area uncovered. This is juxtaposed to the Tuball product in Figure 6.6B, which covers all active material completely with a 'carpet-like' arrangement of SWCNTs, ensuring all active material is fully immersed in conductive carbon. It was hypothesised that this apparent more complete coverage of SWCNTs would enhance the conductivity of the electrode and counteract the electrical limitations experienced to date from the Na^+ ion. In addition to conductivity, it was envisaged that Tuball SWCNTs would have a similar effect as in the study on LIBs where it significantly enhanced the cycling performance of the anode.

The same methodology carried out previously towards analysing the SWCNTs was employed once more, beginning with a mass loading study to optimise the specific capacity and rate performance (Figure 6.6A). As has been done in Chapter 5, the surfactant of CMC was removed using thermal carbonisation at 400 ºC. This was carried out to maximise the specific capacity of the composite and enhance the rate capability by removing the inactive CMC which has been reported to act as a diffusion barrier.[29] As shown in Figure 6.6A, and as is a common theme throughout both studies into LIBs and NIBs, a 15% mass fraction of Tuball SWCNTs optimised the specific capacity. At 0.05 C, a capacity of 534 mAh g^{-1} was recorded, whilst at 1 C a capacity of 270 mAh g^{-1} was

maintained. It must be restated that optimized hard carbons obtain a capacity of 300 mAh g^{-1} at slower rates, so these initial results are promising.[7,30,31] The 20% composite although having a marginally larger capacity at 1 C (276 mAh g^{-1}) fails to exceed/match the performance of the 15% composite at all other rates, with the largest difference between capacities recorded at 0.05 C (473 mAh g^{-1}).

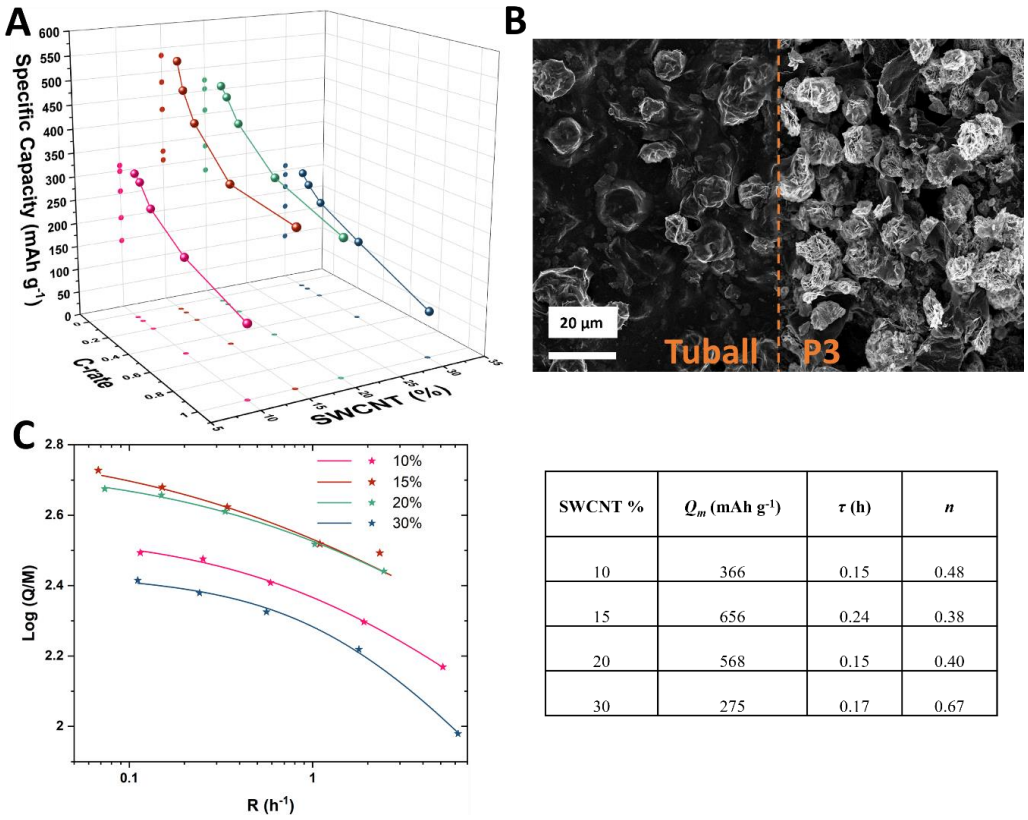

SWCNT %	Q_m (mAh g^{-1})	τ (h)	n
10	366	0.15	0.48
15	656	0.24	0.38
20	568	0.15	0.40
30	275	0.17	0.67

Figure 6.6: (A) SnO/Tu-SWCNT composite discharge capacities at various C-rates as a function of SWCNT %. (B) SEM image of SnO with 15% mass fraction Tuball and P3 SWCNTs to allow for comparison between the coverage afforded by each product. (C) GCD experimental data for SnO/Tu-SWCNT composites fitted using Equation 5.1.

Table 6.4: Parameters Q_M, τ and n for each mass fraction of Tu-SWCNT after fitting GCD data using Equation 5.1.

Using Equation.5.1, the parameters Q_M, τ and n for each mass fraction of Tu-SWCNT could be extracted after fitting the experimental GCD data to allow for further comparison. Consistent with the visual analysis of the GCD data, the 15% mass fraction presents the largest predicted Q_M of 656 mAh g^{-1}. It does however present the marginally largest predicted value of τ (0.24 h) when compared to the other mass fractions, but practically speaking the differences are not large enough to cause concern. As hypothesised, the τ values are much lower compared to those calculated for the P3-SWCNTs (Figure 6.2), suggesting that the Tuball-SWCNTs are more effective at

sodiation of the anode at increased rates for all mass-fractions. The values of *n* obtained from the high-rate regime are neglected and as discussed previously, are fitting errors due to small capacity fall-offs at higher rates.[11]

Effect on Cycling

Analogous to the investigation with the same material in LIBs, both heat-treated (HT) and FD anodes were investigated in NIBs. As the CMC had caused poorer rate capability/specific capacity with LIBs, it was not investigated in the NIB configuration due to the diffusion limitations already present. Even though the FD anodes did not add any benefit in LIBs, it was considered worthwhile to investigate this electrode processing method once more to see if the porous structure would respond differently with the Na^+ ion.

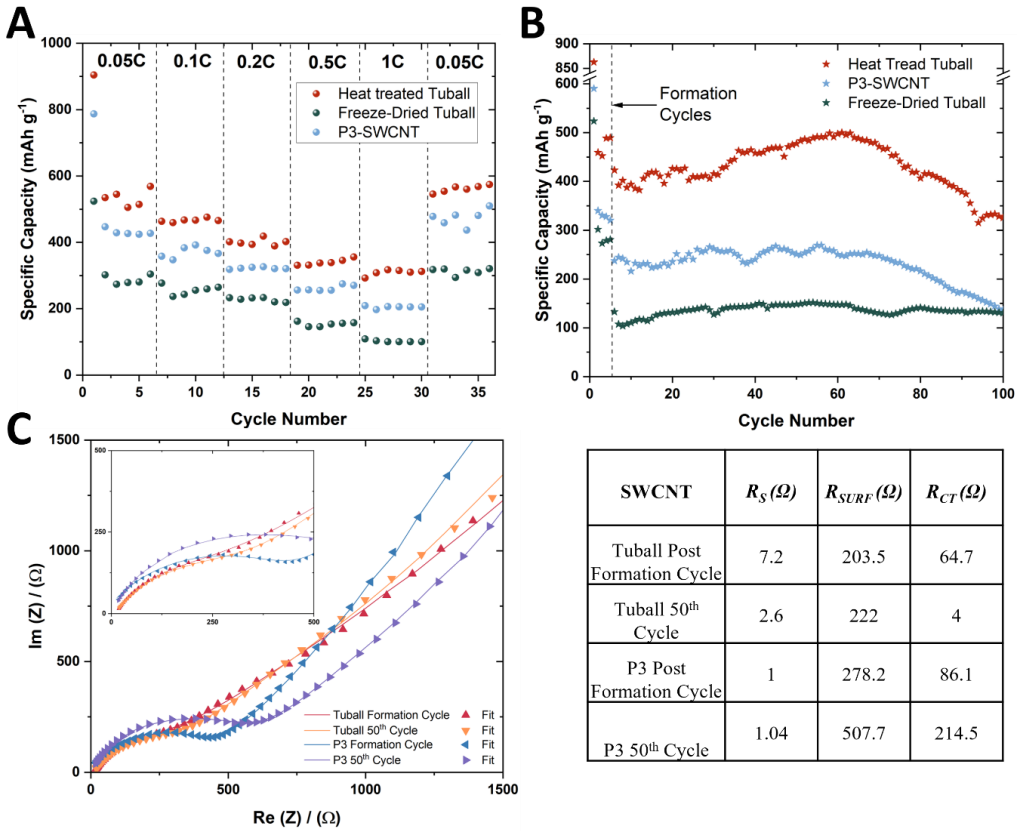

SWCNT	R_S (Ω)	R_{SURF} (Ω)	R_{CT} (Ω)
Tuball Post Formation Cycle	7.2	203.5	64.7
Tuball 50th Cycle	2.6	222	4
P3 Post Formation Cycle	1	278.2	86.1
P3 50th Cycle	1.04	507.7	214.5

Figure 6.7: (A) Rate capability of SnO composites with HT,FD Tuball SWCNT and P3-SWCNT. (B) Cycling performance of composites at 0.1 C from 0.005 – 2.5 V after initial formation cycles at 0.05 C. (C) EIS spectra of SnO composite with Tu/P3-SWCNTs after 25/50 cycles with zoomed inset of high-frequency region.

Table 6.5: Values obtained for the Equivalent circuit used to model the EIS spectra.

From Figure 6.7A, it is shown that the HT-Tuball composite has superior performance at all rates in comparison to the FD and P3 composite. It demonstrates the highest capacities up to this point in this investigation with specific capacities of 569, 476, 418, 355 and 311 mAh g^{-1} from 0.05 – 1 C. The activation process that had been observed previously with the P3 composites is also present here, with the capacity increasing marginally upon re-cycling at 0.05 C to 574 mAh g^{-1}. The FD sample had the lowest capacity at all rates, with the capacity only exceeding 300 mAh g^{-1} at 0.05 C and upon re-cycling/activation. Thus, the porous network formed using the FD acts to isolate active material, meaning less mass can take part in the sodiation process.

Cycling stability tests were carried out at 0.1 C in Figure 6.7B after initial formation cycles at 0.05 C to ensure a stable SEI was formed. The HT-Tuball composite once again had superior cycling performance compared to the FD and P3 counterparts. After the initial formation cycles, the capacity was roughly 400 mAh g^{-1}, climbing to a maximum capacity of 500 mAh g^{-1} at the 60th cycle, and then proceeding to gradually fall off to a capacity of 326 mAh g^{-1} after 100 cycles had been completed. The P3-SWCNT composite displayed the next best performance, however, its maximum stable cycling was at roughly 270 mAh g^{-1} between the 30th and 60th cycles before falling to 136 mAh g^{-1} by the 100th cycle. The FD samples' cycling stability was the lowest measured, with its maximum stable cycling at roughly 145 mAh g^{-1}. It did however display the smallest drop-off in capacity, falling to 130 mAh g^{-1}, however as the figure is so low it is unlikely this small drop-off is of any practical use.

Using EIS, the different resistance forces at play in the anode as it was subjected to GCD cycling testing were examined. From the Nyquist plot displayed in Figure 6.7C, and the subsequent Z-fit of this data, these resistive forces were decomposed and displayed in Table 6.5. For the HT-Tuball composite, we see the size of the semi-circle in the Nyquist plot decreases after 50 cycles, and this is reflected in the Z-fit approximation with the R_{CT} dropping from 64.7 to 4 Ω. This again elucidates the activation the anode experiences through subsequent cycles, with the active material getting electrochemically milled to smaller sizes and reducing the charge transfer resistance in the electrode. In stark contrast, the P3 composite with the fine 'web-like' SWCNTs, experiences an increase in the R_{CT} over 50 cycles, with the value climbing from 86.1 to 214.5 Ω. There is also a larger increase in the R_{surf} from 278.2 to 507.7 Ω, and this is visible through the increased size of

the semi-circle in the Nyquist plot. The HT-Tuball SWCNT composite is the better-performing material in terms of rate, cycling stability and in terms of conductivity when analysed using EIS, and thus it was decided to proceed with this investigation using it.

6.5 Differential Capacity Analysis and Alternate Electrolyte

In an effort to explain the cause for the capacity fade in the HT-Tuball SnO composite, *dQ/dV* analysis was applied once again to the GCD cycling data to monitor the changes in the plot as the number of cycles increased. The progression in the features of the *dQ/dV* analysis over the first 150 cycles is displayed in Figure 6.8A and B. It is shown that as the cycling progresses from the 5th to the 25th to the 50th cycle, the anodic peak centred roughly at 0.9 V associated with the final de-alloying and initial re-oxidation of the Sn is split into two distinct peaks (marked by arrows) associated with each process individually. Similar to the results obtained for the P3 composite in Figure 6.5C, the onset of the initial cathodic reaction shifts from 0.75 to 0.95 V over the initial 50 cycles. The initial dealloying peak (~0.2 V) increases in intensity over this range, as does the terminal alloying peak (< 0.1 V, Figure 6.8C); an indication of the activation process discussed previously which can be directly correlated to the capacity increase over the first 50 cycles in Figure 6.8D. All the above processes occur due to the activation process occurring in the anode due to the electrochemical milling effect discussed previously, leading to an increase in capacity and a reduction in the overpotentials needed for conversion/alloying.[15,32] Examining the progression in the *dQ/dV* profile over the remaining 100 cycles which coincide with a decrease in capacity, it is apparent the activation process has ceased and new features become apparent. The intensity of the final alloying and initial de-alloying peaks fall progressively between cycles 50 and 150 indicating that there is a drop-off in the amount of active Sn participating over this range. The final anodic reaction which had become more pronounced over the initial 50 cycles and associated with the re-conversion of Sn to SnO (indicated by the arrow in Figure 6.8A) becomes suppressed, whilst the final de-alloying peak shifts to higher voltages with cycling (marked by arrow in Figure 6.8B). This coincides with the suppression of the initial cathodic peak at 0.95 V, suggesting the conversion reaction becomes more difficult over this range.

Linking this to the cycling and CE data displayed in Figure 6.8D, a failure mechanism may be proposed. The CE fluctuates around 95%, even during the activation process, thus

even when the discharge capacity of the anode is increasing, it is still consuming 5% of the sodium inserted. This would most likely be attributable to the additional SEI produced due to the electrochemical milling of the Sn to form smaller particles. As the battery's capacity decreases, the alloying/de-alloying peaks shift towards increased voltages suggesting a conductivity loss, again a consequence of SEI and Na_2O build-up. Thus as activation proceeds, Sn is milled to smaller and smaller sizes, allowing for greater alloying capacity whilst also maintaining the conversion reaction. After 50 cycles, the conversion reaction becomes more and more difficult, due to the build-up of the SEI and leading to more and more inactive Na_2O. The alloying reactions still proceed but become electrically limited due to the diffusion barriers of the SEI/Na_2O and thus drop in capacity as the previous active material becomes electrically isolated/insulated. All the time sodium is being consumed by the anode in this charge/discharge process which proves problematic for the implementation of the material into a full cell, with CEs in excess of 99% required.

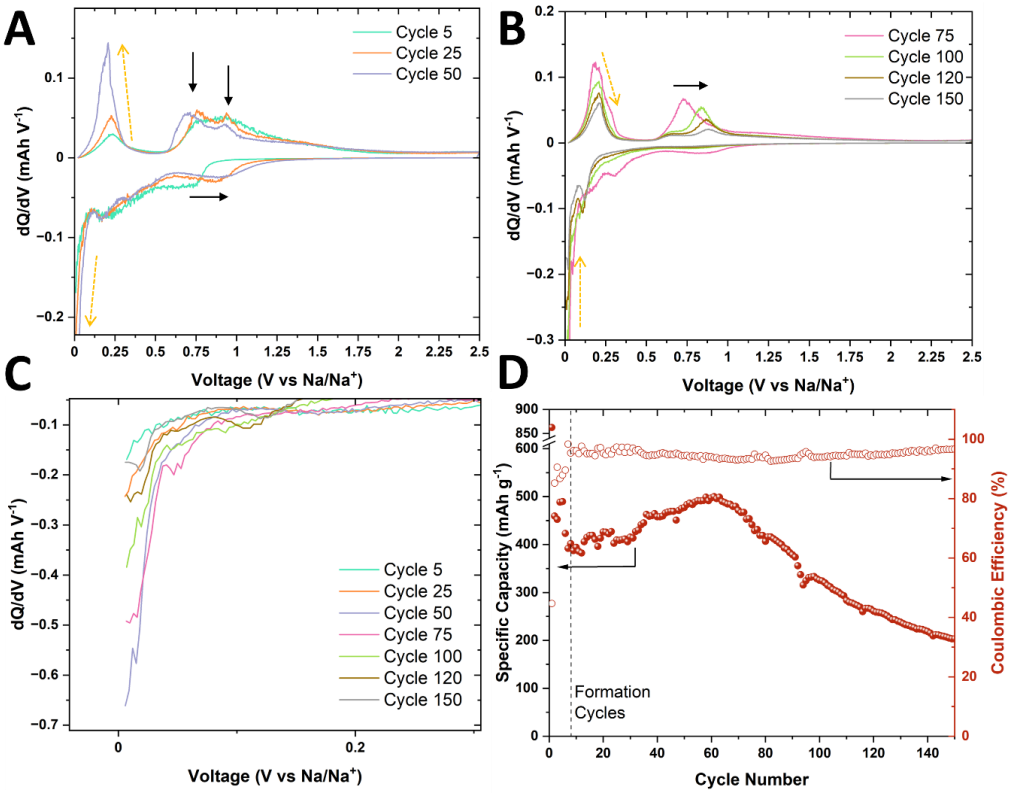

Figure 6.8: Differential capacity analysis of SnO with 15% HT Tuball SWCNTs; (A) over the initial 50 cycles, (B) over the final 100 cycles. (C) Zoomed dQ/dV plot of all cycles to display the final alloying peak below 0.2 V vs Na/Na^+.(D) Cycling stability of SnO with 15% HT Tuball SWCNTs for 150 cycles at 0.1 C with a voltage cut-off of 2.5 V vs Na/Na^+.

Diglyme Electrolyte

In an effort to stabilise the cycling and try to improve the CE, an alternate electrolyte was investigated (to date the electrolyte was 1M $NaPF_6$ in EC:DMC (1:1), 10% FEC). Recent work carried out on diethylene glycol dimethyl ether (diglyme) electrolytes with Sn anodes has proved promising. Zhang *et al.*[33] utilised 1M $NaPF_6$ diglyme electrolyte with a metal Sn anode, achieving 99% CE after the 5th cycle and cycling capacity retention of 88% after 100 cycles. The improvement in the stability of the electrode was attributed to the formation of a thin SEI which prevents the formation of insulating domains. Li *et al.*[34] found that diglyme-based electrolytes promote faster charge transfer at the SEI/electrode interface. Huang *et al.*[35] studied the properties of the SEI formed on the Sn anode in diglyme using cryogenic TEM, and demonstrated that the SEI is a rather thin polymeric film with superior elasticity and stability, which provides stability during the volume changes associated with sodiation. For these reasons, 1 M $NaPF_6$ in diglyme was investigated as a potential electrolyte.

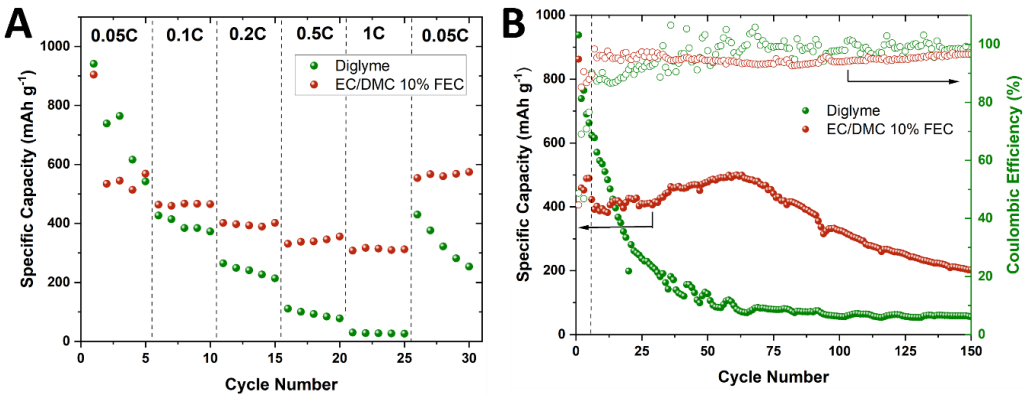

Figure 6.9: (A) Rate performance comparison of SnO with 15% HT Tuball SWCNTs with 1M NaPF6 in EC:DMC (1:1), 10% FEC and 1 M NaPF6 in diglyme. (B) Cycling comparison of the two electrolytes.

The initial specific capacities obtainable using the diglyme electrolyte are higher at 0.05 C in Figure 6.9A, with the first cycle producing a capacity of 972 mAh g^{-1}, dropping to 740 mAh g^{-1} subsequently. However, by the 5th cycle at 0.05 C, and as the testing progressed through the rates the original electrolyte proved to have the superior performance. Furthermore, the activation process which is observed in the original electrolyte is not observed using the diglyme-based electrolyte, with the capacities upon re-cycling at 0.05 C dropping from 430 to 254 mAh g^{-1}. Upon examination of the GCD cycling data at 0.1 C displayed in Figure 6.9B, a similar trend is observed, whereby the diglyme electrolyte starts off with greater initial capacity, but by the 14th cycle the EC/DMC-based electrolyte has surpassed its performance. The degradation in the

performance of the diglyme electrolyte is quite intense, with capacities below 100 mAh g^{-1} present just after the 50th cycle. Once again, no activation is present. Analysing the *dQ/dV* plot of the diglyme GCD cycling data over the first 20 cycles (Appendix D, Figure D.2), it appears that there is quite a rapid loss of active material participating in the anode, whilst similar to the failure mechanism in the EC/DMC electrolyte the conversion reaction ceases but at a much earlier cycle number (between 7-9 cycles). Although diglyme electrolytes have worked well in Sn metal anodes to date,[36] it appears they do not transition over to SnO anodes and work with the same effect.

Optimised Half-Cell Performance and Comparison to Other Works

Although improvements could still be made with regard to specific capacity and cycling stability, the final optimised electrode settled upon from this PhD fellowship for the NIB was SnO(EtOH) with 15% HT Tu-SWCNTs. Summarising the results obtained briefly, a maximum capacity of 574 mAh g^{-1} was measured after activation at 0.05 C, stable and increasing cycling capacity was recorded for the initial 85 cycles at 0.1 C, with a maximum capacity of 500 mAh g^{-1} on the 60th cycle dropping to 405 mAh g^{-1} by the 85th cycle. Furthermore, it must again be stressed that the results quoted are in terms of total mass, reflecting the true performance of the anode and not just the active material within. A gradual decline followed with the capacity falling to 203 mAh g^{-1} at the 150th cycle. Areas for concern remain primarily based on the low ICE and consistent CE below 99%, which are both major obstacles to overcome to progress the material to the commercialisation phase. As is displayed in Figure 6.10A, the initial charge-discharge obtains a low ICE of 51%, and although this value is an improvement on that measured with the P3-SWCNT (47%), it is still a major amount of irreversible sodium consumption.

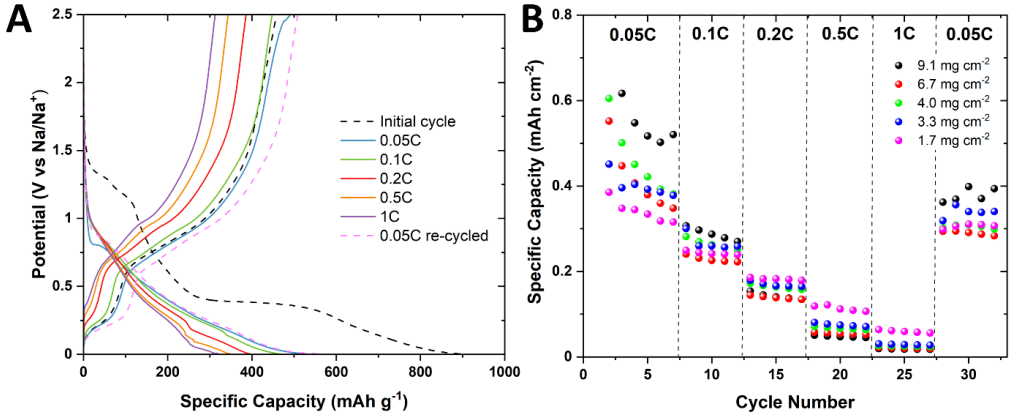

Figure 6.10: (A) GCD profiles at various rates of SnO(EtOH) with 15% HT Tu-SWCNTs. (B) Rate performance at several mass loadings of the optimised electrode.

Similar to the investigation into SnO with LIBs, a mass loading study was also carried out on the anode in the NIB configuration. Conversely to the LIB, there is no obvious trend in the NIB results displayed in Figure 6.10B. Initially, the larger mass loadings have slightly higher areal capacities, but not as much as would be expected considering the difference in the areal loadings. For example, a loading of 9.1 mg cm^{-2} has an areal capacity of 0.52 mAh cm^{-2} on the 7^{th} cycle at 0.05 C whilst an areal loading of 1.7 mg cm^{-2} produces an areal capacity of 0.32 mAh cm^{-2}. This again is further evidence of the diffusion barriers faced when using the Na^+ ion, with the same problems not encountered for the LIB counterparts. Upon re-cycling at 0.05 C, it is observed that only the lowest mass loading electrode of 1.7 mg cm^{-2} is able to maintain the original capacity at this rate, evidence that the activation process previously observed is not present in thicker electrodes. The drop between the first and second cycles is also quite striking when one analyses the initial cycle discharges shown in Appendix D, Figure D.3; with all second cycles being 37% or less than the initial cycle except for a mass loading of 9.1 mg cm^{-2} (however I suspect the initial cycle does not achieve full sodiation for the 9.1 mg cm^{-2} loading, thus the second cycle still has irreversible capacity in it as it sodiates fresh electrode). This is much lower than the optimised electrode at 1 mg cm^{-2} which has a value of 59% (from Figure 6.7A).

The results of the optimised half-cell anode were compared to similar work carried out in the field in Table 6.6.

Materials	Preparation methods	Initial Discharge (mAh g^{-1}), ICE (%)	Capacity Retention	Ref
SnO_2 nanoparticles	Wet chemical	907 15	N/A	37
SnO nanoflowers	Hydrothermal	720 61.5	530 mAh g^{-1} after 50 cycles at 0.05 C	4
SnO monolayers on carbon cloth	Hydrothermal	1072 79.1	665 mAh g^{-1} after 100 cycles at 0.1 C	5*
SnO_2 nanoparticles	Hydrothermal	728 9	92 mAh g^{-1} after 30 cycles at 0.1 C	27
SnO_2-carbon nanoparticles	Hydrothermal	946 48.5	372 mAh g^{-1} after 200 cycles at 0.5 0.1 C	3
SnO_2 nanoparticles within CNTs	Hydrothermal	768 50	234 mAh g^{-1} after 100 cycles at 0.1 C	24
SnO microspheres	Hydrothermal	958 48	310 mAh g^{-1} after 50 cycles at 0.1 C	19
Carbon-coated SnO_2 nanoparticles	Hydrothermal	1014 50.7	413 mAh g^{-1} after 200 cycles at 0.5 C	23
SnO with MWCNTs	Ball mill	471 48	72 mAh g^{-1} after 120 cycles at 0.1 A g^{-1}	16
SnO_2 nanoparticles with graphene	Hydrothermal	1079 36.4	343 mAh g^{-1} after 100 cycles at 0.1 C	18
SnO_2/graphene/CNT fibre	Hydrothermal/wet-spinning/freeze drying	1150 22	164 mAh g^{-1} after 100 cycles at 0.5 A g^{-1}	22
C-SnO_2 nanospheres	Hydrothermal	1298 27	251 mAh g^{-1} after 100 cycles at 0.1 A g^{-1}	12
SnO with SWCNTs	Wet chemical	1064 51	588 mAh g^{-1} at 60/ 307 mAh g^{-1} after 120 cycles at 0.1 C / 0.08 A g^{-1}	This work

Table 6.6: Electrochemical performances of previously reported SnO_x NIB electrodes.

In Table 6.6, the results obtained in this study have been converted to active mass to allow for accurate comparison to the other work (although it is personally felt to be more appropriate to report total mass). Upon comparison to the other reported results of similar work in the field, it can be seen that the work in this PhD fellowship certainly meets and for the most part exceeds similar work. The ICE of the composite is superior to all tabulated values except for the work carried out by Zhang *et al.*[5] (marked by an *) which was discussed at the start of this chapter; with reservations regarding the amount of inactive mass in this work that is not reported, whilst also considering that the benefits of having atomically thin materials in one's anode are outweighed by the inactive materials present to enable this morphology. In terms of cycling stability, the present work again exceeds for the most part the other reported results. Other works of note with excellent cycling stability were carried out by Kalubarme *et al.*[23] whereby an impressive stable cycling capacity of 413 mAh g^{-1} was recorded after 200 cycles at 0.5 C, whilst Ding *et al.*[3] utilised a nanostructured SnO_2-carbon composite which obtained a capacity of 372 mAh g^{-1} after 200 cycles at 0.1 C. Both these works however utilise carbon-coated nanoparticles in addition to adding additional carbon black to the anode for conductivity, which once again leads to a large amount of inactive material present in the anode. The NIB anode of SnO(EtOH) with Tuball SWCNT developed in the Chapter is scalable, cost-effective, requires very little post-processing and utilises the minimum amount of inactive conductive source as possible; with the obtained results although not fully optimised, an improvement on the majority of the work published in the field.

6.6 Post-mortem Analysis

Post-mortem analysis of the optimised half-cell configuration using 1M $NaPF_6$ in EC:DMC (1:1) with 10% FEC was carried out on the anode in the un-sodiated state. From the SEM image shown in Figure 6.11A and C, we can see that the morphology has completely transformed during the cycling. Originally in Figure 6.11C the nanoflowers were covered in SWCNTs, however after cycling in Figure 6.11A the nanoflowers seem to be submerged in what presumably is the Na_2O, with cracks appearing within this structure also. This is similar to the cracked post-mortem electrode present in the LIB study without FEC present. In this case, however, FEC is present but the failing mechanism is the same, overgrowth of the SEI and Na_2O which causes the battery to degrade. Using EDX, a cross-section of the electrode was examined to probe the

distribution of the elements (C, O, Na, Sn) within. What is visible from the EDX analysis is that there are pockets of metallic Sn within the discharged electrode, not in contact with any other elements. As is visible, the Sn is spread throughout whereas the C, O and Na have regions with no signal at all. This suggests that some of the lower than expected capacity may be due to isolated Sn which is unable to take part in the alloying/conversion reaction, agreeing with previous reports.[2–4,17,18,23] These isolated pockets of Sn as is shown are quite large, appearing on the microscale with the image displayed having a pocket roughly 10 μm in width. For the anode to be a completely reversible conversion/alloy anode the only Na present in the discharge state would be from the SEI, which is clearly not the case, again demonstrating that the Na_2O conversion is not fully reversible. Thus, from the SEM/EDX analysis, the lower capacity compared to the theoretical capacity and unstable cycling can be attributed to isolated pockets of inactive Sn, irreversible production of Na_2O and the diffusion barriers caused by the Na_2O and continued growth of the SEI.

XRD analysis was carried out on the cycled electrode in the discharged state, with the spectrum displayed in Figure 6.11D. It is shown that both Sn (marked by a *) and SnO (marked by a +) are present in the discharged electrode, agreeing with the EDX results. This suggests that the conversion reaction may still be taking place even when the capacity of the electrode is falling with cycling. This would mean that as the battery is failing, more and more active Sn becomes inactive, however, the Sn that remains electrically active and reversibly storing ions is still participating in the conversion reaction. $Na_4Sn_3O_8$ (marked by a ▲) is also present in the XRD, and this is most likely an intermediate in the Sn to SnO conversion which has not fully de-sodiated upon discharge.

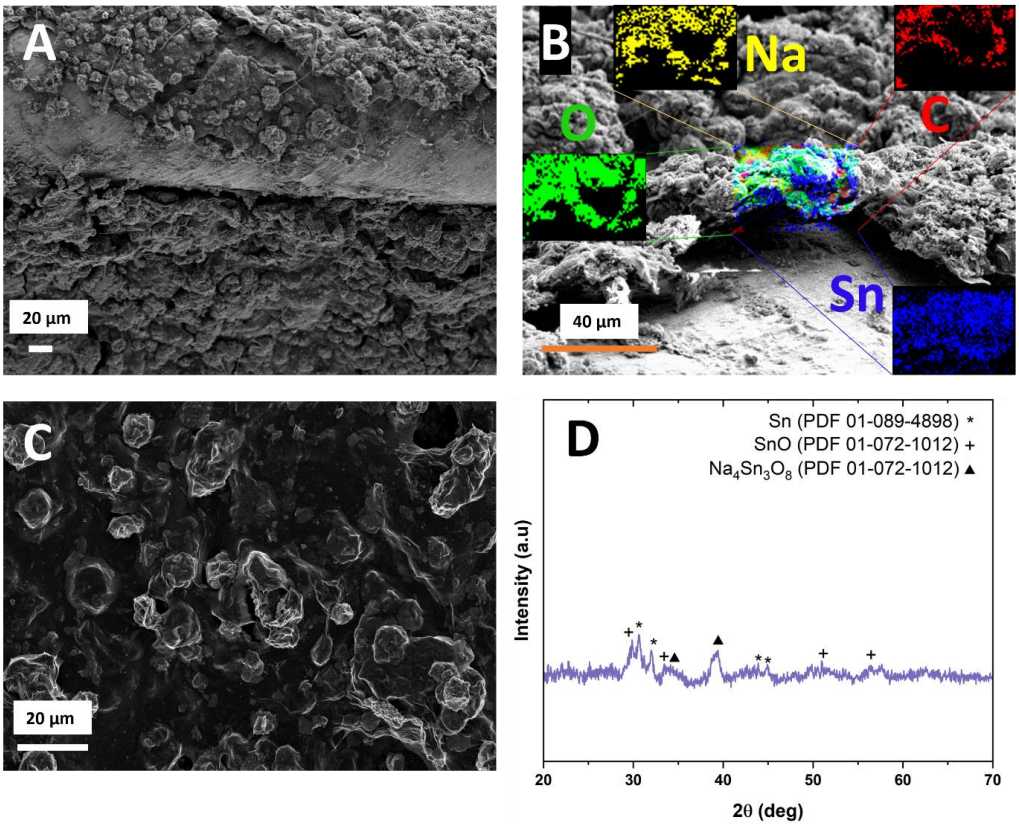

Figure 6.11: Post-mortem SEM image of (A) HT SnO/Tu-SWCNT electrode and (B) resulting EDX map. (C) SEM image of fresh HT SnO/Tu-SWCNT. (D) Post-mortem XRD analysis of HT SnO/Tu-SWCNT electrode.

6.7 Conclusion

Complimenting the research carried out in LIBs, solvent-engineered SnO along with SWCNT have been manufactured into high-capacity NIB anode materials. Using the same iterative approach adopted in Chapter 5, the nanoflower SnO produced in ethanol was selected as the optimal morphology. To improve specific capacity, rate capability and cyclability HT Tuball SWCNTs were used as a conductive additive source, with a 15% mass fraction optimising performance. It was observed that the SnO anode undergoes an activation process with capacity improvement over the initial 50 cycles, and this was attributed to the electrochemical milling effect whereby active material is progressively broken down to enable a greater surface area for sodiation to occur. The optimised composite had a maximum capacity of 574 mAh g^{-1} at 0.05 C after activation, whilst in terms of cycling it had a capacity of 500 mAh g^{-1} after 60 cycles, which dropped to 405 and 261 mAh g^{-1} after 80 and 120 cycles respectively. The ICE of the anode still needs improvement, with a value of 51% and the CE during cycling remains below 99% which is a cause for concern for the potential commercialisation of the anode. The diffusion

limitations of the Na^+ ion were also present throughout the work, with lower rates having to be utilised to combat this. Furthermore, as the areal loading of the electrode was increased, a similar areal capacity increase in charge storage was also not recorded, again a consequence of the slow diffusion of the Na^+ ion. The work, however, surpassed most previous work carried out on similar materials in the field and has plenty of promise for future research and development.

Future work would look to investigate more electrolytes, in particular, to try to enhance the ICE and CE and in doing so stabilise the cycling stability. It would also be informative to carry out in-situ TEM and operando XRD/Raman to monitor the progression of the sodiation/de-sodiation, to gain a more fundamental insight into the exact reactions taking place within the anode. The optimised anode obtained for the LIB from this PhD fellowship remarkably is the same as for the NIB, which is an exciting prospect for developing a scalable and cost effective composite that can be interchanged into either technology.

6.8 Experimental

Preparation of Electrodes

All electrodes were prepared the same as is outlined in Chapter 5, Section 5.10.

Electrochemical Cell Construction

All electrochemical cells were constructed in an Argon-filled glove box (MBRAUN). Within the cell casing, a wave spring and two spacers are placed initially on the coin cell base (negative end). For a half-cell sodium metal is placed on top of the spacer, with the electrolyte 1 M NaFP6 in EC:DMC (50:50) with 10% FEC and a glass separator being placed next. The working electrode (anode/cathode) is placed on the other side of the glass separator (Whatman, GF 10) and the cell lid is placed on, encasing the cell. The cell is crimped using a hydraulic crimping machine (MSK-110).

Electrochemical Analysis

All electrochemical measurements were performed using either a Bio Logic VMP 300 or a Biologic BCS-805 and analysed using the EC-Lab software. For battery testing, CVs were run at various scan rates for 5 cycles in a voltage range of 0.005 – 2.5 V vs Na/Na^+ while GCD measurements were run at charge rates of 0.05, 0.1, 0.2, 0.5 and 1 C between 0.005 – 2.5 V vs Na/Na^+ for capacity testing/cycling. For EIS measurements, the cell was fully discharged so it was in a fully de-sodiated state and left to rest for 1 hr before beginning the EIS testing. EIS was then recorded at an open circuit potential from 1 MHz to 50 mHz, and the resulting spectra obtained were analysed using the Z-fit software from EC-lab.

6.9 References

1 Z. Li, J. Ding and D. Mitlin, *Acc. Chem. Res.*, 2015, **48**, 1657–1665.
2 Y. Zhang, J. Xie, S. Zhang, P. Zhu, G. Cao and X. Zhao, *Electrochim. Acta*, 2015, **151**, 8–15.
3 J. Ding, Z. Li, H. Wang, K. Cui, A. Kohandehghan, X. Tan, D. Karpuzov and D. Mitlin, *J. Mater. Chem. A*, 2015, **3**, 7100–7111.
4 Y. C. Lu, C. Ma, J. Alvarado, T. Kidera, N. Dimov, Y. S. Meng and S. Okada, *J. Power Sources*, 2015, **284**, 297–295.
5 F. Zhang, J. Zhu, D. Zhang, U. Schwingenschlögl and H. N. Alshareef, *Nano Lett.*, 2017, **17**, 1302–1311.
6 D. Kundu, E. Talaie, V. Duffort and L. F. Nazar, *Angew. Chemie Int. Ed.*, 2015, **54**, 3431–3448.
7 P. K. Nayak, L. Yang, W. Brehm and P. Adelhelm, *Angew. Chemie Int. Ed.*, 2018, **57**, 102–120.
8 K. Chayambuka, G. Mulder, D. L. Danilov and P. H. L. Notten, *Adv. Energy Mater.*, 2018, **8**, 1800079.
9 Y. Xu, Y. Zhu, Y. Liu and C. Wang, *Adv. Energy Mater.*, 2013, **3**, 128–133.
10 J.-Y. Hwang, S.-T. Myung and Y.-K. Sun, *Chem. Soc. Rev.*, 2017, **46**, 3529–3614.
11 R. Tian, S.-H. Park, P. J. King, G. Cunningham, J. Coelho, V. Nicolosi and J. N. Coleman, *Nat. Commun.*, 2019, **10**, 1933.
12 X. Ao, J. Jiang, Y. Ruan, Z. Li, Y. Zhang, J. Sun and C. Wang, *J. Power Sources*, 2017, **359**, 340–348.
13 M. Gu, A. Kushima, Y. Shao, J.-G. Zhang, J. Liu, N. D. Browning, J. Li and C. Wang, *Nano Lett.*, 2013, **13**, 5203–5211.
14 B. Konkena, H. Kaur, R. Tian, C. Gabbett, M. McCrystall, D. V. Horvath, K. Synnatschke, A. Roy, R. Smith, V. Nicolosi, M. D. Scanlon and J. N. Coleman, *Small*, 2022, **18**, 2203918.
15 R. Biswal, D. Nayak, S. Janakiraman, N. V. P. Chaudhary, S. Ghosh and V. Adyam, *J. Solid State Electrochem.*, 2021, **25**, 561–573.
16 J. Mao, X. Fan, C. Luo and C. Wang, *ACS Appl. Mater. Interfaces*, 2016, **8**, 7147–7155.
17 W. Chen, K. Song, L. Mi, X. Feng, J. Zhang, S. Cui and C. Liu, *J. Mater. Chem. A*, 2017, **5**, 10027–10038.
18 J.-K. Meng, W.-W. Wang, Q.-C. Wang, M.-H. Cao, Z.-W. Fu, X.-J. Wu and Y.-N. Zhou, *Electrochim. Acta*, 2019, **303**, 32–39.
19 D. Su, X. Xie and G. Wang, *Chem. – A Eur. J.*, 2014, **20**, 3192–3197.
20 X. Wu, X. Lan, R. Hu, Y. Yao, Y. Yu and M. Zhu, *Adv. Mater.*, 2022, **34**, 2106895.
21 B. Wang, J. Ryu, S. Choi, G. Song, D. Hong, C. Hwang, X. Chen, B. Wang, W. Li, H.-K. Song, S. Park and R. S. Ruoff, *ACS Nano*, 2018, **12**, 1739–1746.
22 Y. Zhang, Z. Bi, Y. Liang, W. Zuo, G. Xu and M. Zhu, *Energy Storage Mater.*, 2022, **48**, 35–43.
23 R. S. Kalubarme, J.-Y. Lee and C.-J. Park, *ACS Appl. Mater. Interfaces*, 2015, **7**, 17226–17237.
24 B. Han, W. Zhang, D. Gao, C. Zhou, K. Xia, Q. Gao and J. Wu, *J. Power Sources*, 2020, **449**, 227564.
25 Z. Zhang, R. Wang, J. Zeng, K. Shi, C. Zhu, X. Yan, Z. Zhang, R. Wang, J. Zeng, K. Shi, C. Zhu and X. Yan, *Adv. Funct. Mater.*, 2021, **31**, 2106047.
26 J.-M. Liang, L.-J. Zhang, D.-G. XiLi and J. Kang, *Rare Met.*, 2020, **39**, 1005–

1018.
27 D. Dixon, M. Ávila, H. Ehrenberg and A. Bhaskar, *ACS Omega*, 2019, **4**, 9731–9738.
28 L. D. Ellis, T. D. Hatchard and M. N. Obrovac, *J. Electrochem. Soc.*, 2012, **159**, A1801–A1805.
29 S.-L. Chou, J.-Z. Wang, H.-K. Liu and S.-X. Dou, *J. Phys. Chem. C*, 2011, **115**, 16220–16227.
30 J. Zhao, L. Zhao, K. Chihara, S. Okada, J. Yamaki, S. Matsumoto, S. Kuze and K. Nakane, *J. Power Sources*, 2013, **244**, 752–757.
31 E. Irisarri, A. Ponrouch and M. R. Palacin, *J. Electrochem. Soc.*, 2015, **162**, A2476.
32 V. J. Ovejas and A. Cuadras, *Sci. Rep.*, 2019, **9**, 14875.
33 B. Zhang, G. Rousse, D. Foix, R. Dugas, D. A. D. Corte and J.-M. Tarascon, *Adv. Mater.*, 2016, **28**, 9824–9830.
34 K. Li, J. Zhang, D. Lin, D.-W. Wang, B. Li, W. Lv, S. Sun, Y.-B. He, F. Kang, Q.-H. Yang, L. Zhou and T.-Y. Zhang, *Nat. Commun.*, 2019, **10**, 725.
35 J. Huang, X. Guo, X. Du, X. Lin, J.-Q. Huang, H. Tan, Y. Zhu and B. Zhang, *Energy Environ. Sci.*, 2019, **12**, 1550–1557.
36 B. Qin, A. Schiele, Z. Jusys, A. Mariani, T. Diemant, X. Liu, T. Brezesinski, R. J. Behm, A. Varzi and S. Passerini, *ACS Appl. Mater. Interfaces*, 2020, **12**, 3697–3708.
37 D. Spada, S. Davino, A. Girella, C. Milanese and M. Bini, *J. Solid State Electrochem.*, 2021, **25**, 1401–1410.

7.Single-Walled Carbon Nanotubes/Tin(II) Oxide as a Supercapacitor Material

As discussed in Chapter 2, although not suited toward ion-battery technology, SWCNTs are an incredibly well suited material for use in SC devices. The large capacitances obtainable from SWCNTs are due to their highly accessible surface areas in which most of the charge is stored in the EDL. However, electrochemically active functionalities on the terminals of the tubes also lead to a pseudocapacitive charge storage mechanism.[1] Further additions of redox-active functional groups although leading to an increase in the specific capacitance, leads to a decrease in conductivity and cycling stability.[2]

The capacity obtainable in SC devices is also reliant on the electrolyte used and the size of the ion present. Sulphate-based electrolytes such as sulphuric acid (H_2SO_4) or potassium sulphate (K_2SO_4) are amongst the most widely used electrolytes in SC devices due to the large specific capacitances associated as a result of the small cationic radii.[3] In particular the H^+ ion (forms the hydronium ion in water) possesses the highest specific capacitance due to the small hydration sphere radius, a large ionic mobility and the highest molar ionic conductivity.[3] To maximise the energy storage capacity of the next generation of SCs, an increase in the workable voltage window of the device is an attractive solution, in addition to using an electrolyte which maximises capacity whilst maintaining the stability of the active material. As shown in Equation 2.10 in Chapter 2, the energy stored in an SC device is proportional to the voltage window squared.

The anodic functionalisation of SWCNTs was reported at the turn of the century by Sumanasekera *et al.*[4] with further studies expanding on the mechanisms at play carried out subsequently.[5,6] However, to my knowledge, no one to this point has presented an effective strategy to offset the anodic functionalisation of SWCNTs which in doing so expands the voltage window of a SWCNT-based supercapacitor device and maintains the integrity of the structure for enhanced cycling stability.

As discussed previously, TMOs are widely used as SC materials with RuO_2 as the premier material to date. The role of SnO_x to date is not yet fully understood in terms of a SC material, with previous work reliant on reduced graphene oxide[7–9] or nickel foam[10–12]

supports which makes it difficult to ascertain to what extent the SnO_x is contributing, and the electrochemical data provided is more indicative of battery-like energy storage rather than fast surface redox reactions. Due to its layered nature, one may assume that SnO would be suitable for intercalation pseudocapacitance, and it was an aim of this Chapter to investigate to what extent SnO could contribute to the capacitance of an SWCNT/SnO composite SC electrode. The following work in this chapter has been published as a journal article in Electrochimica Acta under the name "Single walled carbon nanotube functionalisation in printed supercapacitor devices and shielding effect of Tin(II) Oxide".[13]

7.1 Materials Characterisation

SWCNT/SnO composite electrodes were produced using extrusion printing as shown in Figure 7.1A/B and were tested as SC devices in a three-electrode wet electrochemical cell setup using CV and GCD measurements. The effect of the presence of SnO on the functionalisation of the SWCNTs was subsequently characterised, through a comparative study between pure SWCNT electrodes and electrodes formed with an addition of 10% mass fraction SnO.

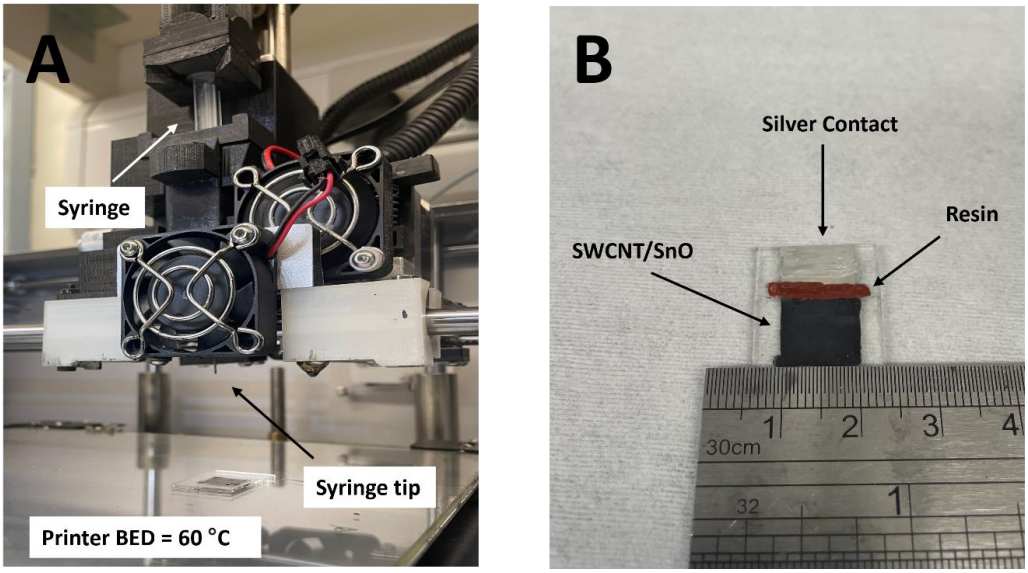

Figure 7.1: (A) Picture of Nano3DPrint extrusion printer used to fabricate SC devices. (B) Picture of an as-fabricated SC device with a silver contact and a protective resin layer.

Raman Spectroscopy

Raman spectroscopy is a powerful technique for probing the structure of graphitic materials and in particular SWCNTs. Five distinctive Raman bands from SWCNTs are

shown in Figure 7.2A/B: the radial breathing mode (RBM) at the low-frequency end (~ 100 – 200 cm^{-1}), the D-band (1329 cm^{-1}), the G-band (1577 cm^{-1}) which contains both the G^+ and G^- band, the M-band (1730 cm^{-1}) and the G' band (~2650 cm^{-1}).[14] When SWCNTs are functionalised, the hybridization of the carbon is changed from sp^2 to sp^3.[15] The D-band (A_{1g} symmetry) represents forbidden out-of-plane vibrations in a perfect graphite lattice and is a key indicator of deviations from the ideal structure,[16] whilst the G-band (E_{2g} symmetry) is due to in-plane vibrations and characteristic of sp^2 hybridized carbon; thus the ratio of the D/G band intensities (I_D/I_G) allows one to quantify disorder in the SWCNT structure and deviations from the perfect sp^2 network.[17,18] The I_D/I_G ratio for both the pristine and annealed SWCNT electrodes remain constant at 0.04 respectively, whilst for the SWCNT electrode subject to use in H_2SO_4 the ratio increases to 0.07 (Figure 7.2A). In comparison, all the SWCNT/SnO composite electrode's I_D/I_G ratios remain constant at 0.03 (Figure 7.2B), suggesting that electrochemical oxidation is being inhibited by the presence of SnO.

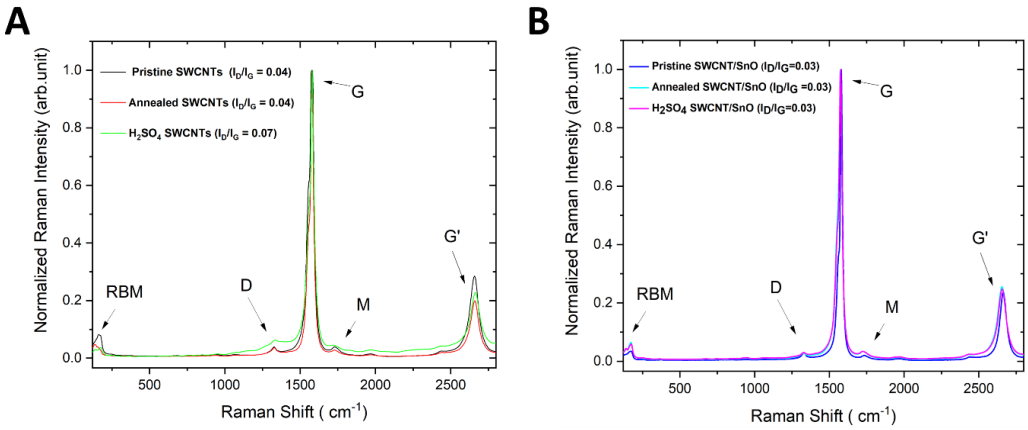

Figure 7.2: Raman spectroscopy for (A) pure SWCNT electrodes and (B) SWCNT/SnO electrodes.

FTIR and XRD

FTIR was carried out on 5 samples shown in Figure 7.3A (Pristine SWCNTs, Annealed SWCNTs, Annealed SWCNT/SnO composite, H_2SO_4 SWCNT/SnO composite, H_2SO_4 SWCNTs). The H_2SO_4 SWCNT sample displays a peak at 1720 cm^{-1} which is due to the stretching of the carbonyl group (C = O) and is unique to this spectrum.[19–21] The band at 1250 cm^{-1} is partly due to C – O stretching vibration and is further confirmation of the oxidative process.[19,22] In addition, the S = O symmetric (1150 cm^{-1}) and asymmetric vibrations (1300 cm^{-1}) lie in this region leading to the broad absorption band.[23] The long broad peak at 3350 cm^{-1} is due to the O – H stretch.[24] The peak at 890 cm^{-1} may be due to

S – OR bond, but lies in the fingerprint region so may be hard to distinguish.[25] C = C stretching at 1620 cm^{-1} is common to all samples, although more pronounced in the pure SWCNT samples as expected.[19,22] The peak at 1080 cm^{-1} is due to C – O and this occurs on the tails of the SWCNTs and is common to all samples.[21,26] Peaks at 2160 and 2000 cm^{-1} are seen in all samples and are consistent with overtones of the 6-ringed carbon of the graphene/graphite structure of SWCNTs.[27,28] The peaks on the two spectra obtained from the samples with SnO at 640, 600, 570 and 500 cm^{-1} are due to the Sn – O vibrations.[12,29–31]

The structures of the SWCNT/SnO composites were analysed using XRD pre- and post-mortem in SC devices in Figure 7.3B. The annealed SWCNT/SnO is consistent in structure with that of pure SnO (JCPDS 06-0395).[32] This confirmed that the thermal carbonisation of the CMC binder did not cause the SnO to oxidise to SnO_2, consistent with previous reports on the thermal stability of SnO.[33] Post-cycling, additional XRD peaks (*) are recorded consistent with Sn_3O_4 (JCPDS 16-0737).[30,34,35] Therefore, it is suggested that a hybrid structure exists where both SnO and Sn_3O_4 exist in tandem.

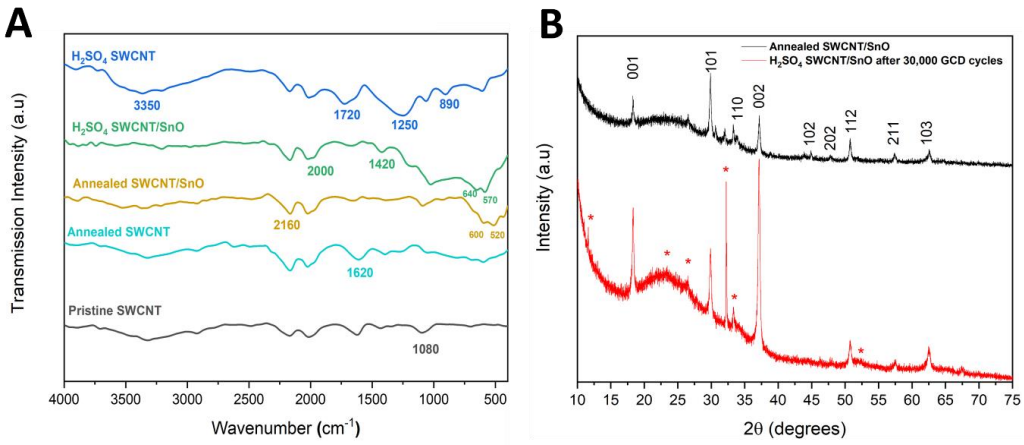

Figure 7.3: (A) FTIR of pristine SWCNT (grey), annealed SWCNT at 400 ºC (cyan), annealed SWCNT/SnO at 400 ºC (mustard), SWCNT/SnO post-mortem use in H_2SO_4 (green) and SWCNT post-mortem use in H_2SO_4 (blue). (B) XRD pattern of SnO/SWCNT pre/post-mortem use after 30,000 GCD cycles in H_2SO_4 (a y-offset has been applied on the relative intensities for display purposes).

7.2 XPS

X-Ray Photoelectron Spectroscopy (XPS) was utilised in this study to determine the changes (if any) to the SWCNTs after H_2SO_4 treatment when the SWCNTs were mixed with/without SnO. In order to compare the various samples, first the high-resolution C1s region was analysed, Figure 7.4A-D.

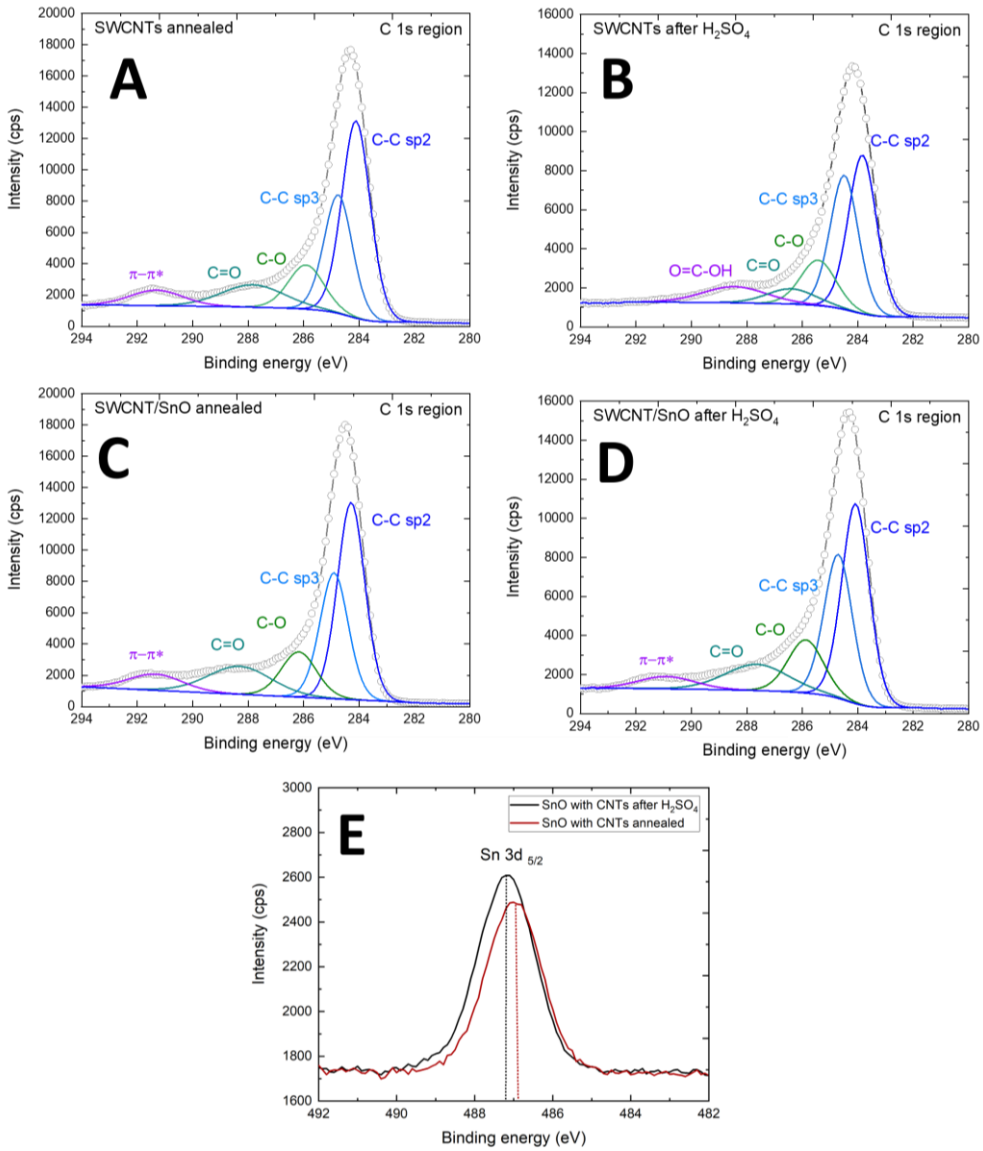

Figure 7.4: (A) XPS C1s core level for SWCNT annealed. (B) XPS C1s core level for SWCNT post use in SC device with 0.5M H_2SO_4. (C) XPS C1s core level for SWCNT/SnO annealed. (D) XPS C1s core level for SWCNT/SnO post use in SC device with 0.5M H_2SO_4. (E) XPS Sn $3d_{5/2}$ region of SWCNT/SnO post use in SC device with 0.5M H_2SO_4 and SWCNT/SnO annealed.

The C1s region of the SWCNT annealed sample was fitted with typical contributions of annealed SWCNTs i.e. presence of C – C sp^3 due to C – O and carbonyl contributions in the C – C sp^2 structure due to the annealing process, Figure 7.4A.[36,37] After H_2SO_4 treatment, the sample appeared to have further oxidised due to the decrease in the C – C sp^2 peak and the disappearance of the $\pi - \pi^*$ bonds which show a decrease in the graphitic carbon in the sample, Figure 7.4B. This agrees with the reported Raman results. Furthermore, the C – C sp^3 contribution increases, indicating the introduction of defects to the carbon structure, Table 7.1. These defects can be easily explained by the appearance of the carboxylic group contribution (O = C – OH) after H_2SO_4 treatment.

C1s Contribution	SWCNTs Annealed	SWCNTs post H_2SO_4	SWCNTs/SnO Annealed	SWCNTs/SnO post H_2SO_4
sp^2	43.8 % 284.1 eV	38.5 % 283.8 eV	40.9 % 284.2 eV	39.9 % 284 eV
sp^3	26.3 % 284.8 eV	32.5 % 284.5 eV	27 % 284.9 eV	29.5 % 284.7 eV
C – O	12.3% 285.9 eV	13.8 % 285.4 eV	12.1 % 286.2 eV	13.6 % 285.9 eV
C = O	11.2 % 287.8 eV	6.3 % 286.4 eV	13.4 % 288.3 eV	12 % 287.6 eV
C = O – OH	n/a	8.9 % 288.4 eV	n/a	n/a
$\pi - \pi^*$	6.4 % 293.1 eV	n/a	6.6 % 291.3 eV	5 % 290.9 eV

Table 7.1: XPS C1s contributions and corresponding binding energies for SWCNT and SnO/SWCNT electrodes.

Interestingly, for the SWCNT annealed sample with the SnO, the fitted contributions before and after H_2SO_4 treatment were not altered, Figure 7.4C/D. This result indicates that the SnO hinders the SWCNTs from oxidation during the H_2SO_4 process. Additionally, when comparing the pure SWCNT annealed sample, Figure 7.4A, to the SWCNT/SnO annealed sample, Figure 7.4C, it is evident that the SnO doesn't form bonds with the SWCNTs as the two samples exhibit near identical fits. However, from the high-resolution $Sn3d_{5/2}$ region, Figure 7.4E, the shift in the peak to a higher binding energy by 0.2 eV indicates that the original SnO is itself oxidised after the H_2SO_4 treatment in agreement with the XRD analysis. Hence, the SnO may block/shield the SWCNT from being oxidised as it itself interacts with the anions present, resulting in partial oxidation during cycling with H_2SO_4.

7.3 Electron Microscopy

SEM analysis was carried out to examine the morphology of the SWCNTs and SnO in both pre- and post-use in SC devices. There was no noticeable difference in morphology between the pure SWCNT SC devices pre/post use due to the limitations of the resolution of the SEM, Figure 7.5A and B. The morphology of the SnO however does exhibit differences once it has undergone use in SC devices. Pristine SnO has a relatively clear surface on the square platelet, Figure 7.5C and D. However, upon cycling this platelet becomes covered in nanoparticles, Figure 7.5E and F. Using the XRD analysis it may be assumed these nanoparticles consist of Sn_3O_4, and due to their reversible production, the

SWCNTs are shielded from undergoing any irreversible oxidation processes in the electrolyte.

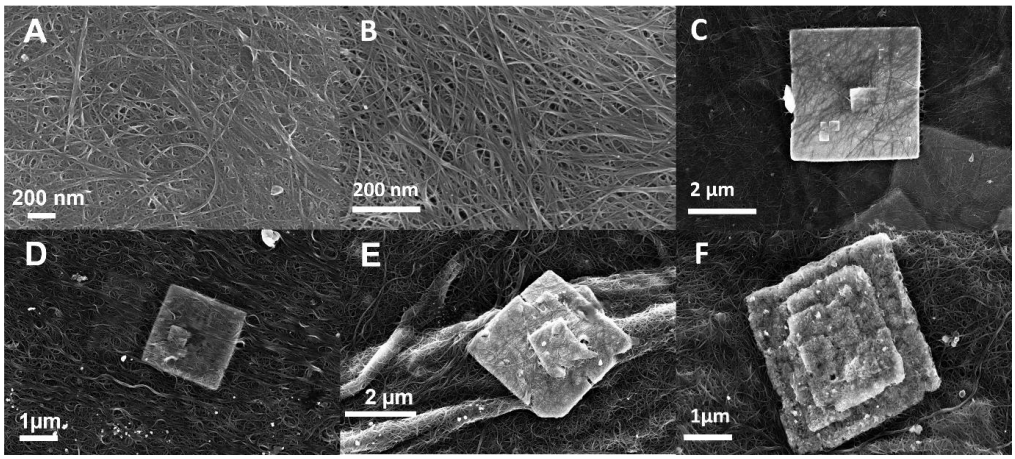

Figure 7.5: SEM images of (A) annealed SWCNTs, (B) SWCNTs post-use in 0.5M H_2SO_4, (C – D) annealed SWCNT/SnO, (E – F) SWCNTs/SnO post use in 0.5M H_2SO_4.

TEM was utilised to characterise the morphology of the tubes of the SWCNTs having undergone the various treatments (Figure 7.6). Both as received (Figure 7.6A) and annealed SWCNTs (Figure 7.6B) have a very similar appearance overall with subtle differences. The walls of the annealed SWCNT appear less clear and rough due to the carbonisation of CMC, whilst in addition, the tubes have a greater tendency to clump together. The tendency of annealed samples to clump together is due to the removal of the CMC which acts as a repellent between adjacent tubes, leading to favourable conditions for bundle formation.[37]

Pure SWCNTs analysed post-use in devices displayed further deterioration in the wall clarity (Figure 7.6C), agreeing with the suggestion of functionalisation and wall damage to the graphitic structure of pure SWCNTs. In addition, nanoparticles were distributed on the walls of the SWCNT matrices (Figure 7.6D), which were identified as sulphates originating from the electrolyte using EDX (Figure 7.6E and Appendix E, Figure E.1A) and consistent with the presence of sulphur in the XPS survey scan (Appendix E, Figure E.1C). SWCNTs from the composite with SnO similarly displayed clumped morphologies with small particles distributed throughout (Figure 7.6F and G) identified as SnO with trace amounts of sulphur using EDX and consistent with the XPS survey scan (Figure 7.6H, Appendix E, Figure E.1B and D).

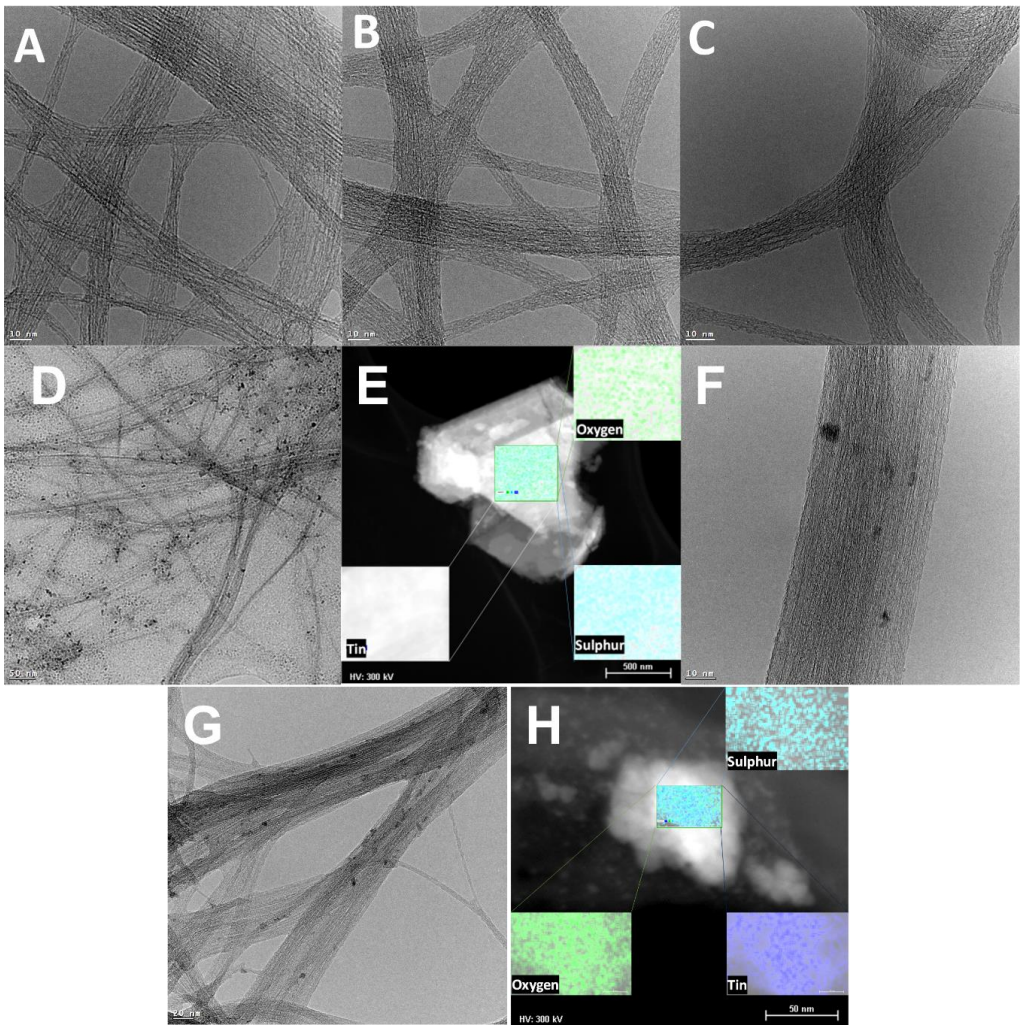

Figure 7.6: TEM images of (A) as received SWCNT material, (B) annealed SWCNT sample, (C) annealed SWCNT sample post use in supercapacitor device in H_2SO_4 (D) and particles dispersed throughout after use, (E) EDX map of particles dispersed on SWCNT post use in H_2SO_4, (F) annealed SWCNT/SnO sample post use in 0.5M H_2SO_4 (G) and associated particles throughout, (H) EDX map of particles dispersed on SWCNT/SnO tubes post use in H_2SO_4.

7.4 Mechanism of Electrochemical Anodic Oxidation of SWCNTs

The mechanism for the anodic oxidation and subsequent functionalisation of SWCNTs was first described by Sumanasekera *et al.*[4] Initial contact between H_2SO_4 and SWCNTs with no external potential applied leads to a spontaneous chemical reaction in which the SWCNT walls are decorated with H_2SO_4 molecules and HSO_4^- ions according to Equation 7.1. This spontaneous reaction is unique to SWCNTs and does not take place in graphite.[4,38,39] This leads the cell potential to climb to roughly 0.2 V vs Ag/AgCl reference.

$$SWCNT + (1+\upsilon)H_2SO_4 \rightarrow SWCNT^{+}HSO_4^{-} \cdot \upsilon H_2SO_4 + H^{+} + e^{-}(anode) \quad (7.1)$$

Upon the commencement of cyclic voltammetry/galvanostatic charging and increasing the potential from ~0.2 V to 0.5 V vs Ag/AgCl, 'overcharging' is observed in which the cell potential causes the neutral H_2SO_4 molecules in the interstitial channels of the tube bundles to be converted to HSO_4^-, and the hydrogen ion is formed at the anode and evolved/lost as hydrogen at the cathode as shown in Equation 7.2 and 7.3 (note voltages refer to those measured between working electrode (anode for functionalisation) and reference, counter (cathode during functionalisation) experiences oppositely polarised voltages).[4–6,39,40] This conversion of H_2SO_4 creates new holes in the SWCNT π-band which is consistent with the XPS (Figure 7.4B) and Raman (Figure 7.2A) results measured.

$$SWCNT^{+}HSO_4^- \cdot \upsilon H_2SO_4 \rightarrow SWCNT^{(1+\delta)+}(HSO_4^-)_{(1+\delta)} \cdot (\upsilon-\delta)H_2SO_4 + \delta e^- + \delta H^+ \ (anode) \quad (7.2)$$

$$\delta H^+ + \delta e^- \rightarrow \delta/2H_2 \ (cathode) \quad (7.3)$$

As the potential exceeds 0.5 V vs Ag/AgCl, 'overoxidation' occurs in which the presence of H_2O allows for the irreversible electrochemical formation of C – O bonds, leading to further functionalisation of the SWCNTs with a disordered structure containing C, H and O, aligning again with the observations from XPS and FTIR.[41]

Evidence shows that SnO inhibits the formation of holes in the sp^2 SWCNT structure and the subsequent irreversible electrochemical formation of C – O bonds, through itself pseudo-reversibly reacting with the available HSO_4^-, forming Sn_3O_4 in the process. Through this, the SWCNT is protected from 'overoxidation' and thus maintains the integrity of the tube and the electrochemical performance associated.

7.5 Electrochemical Analysis

The functionalisation of pure SWCNTs in the presence of H_2SO_4 and K_2SO_4 was shown by the initial CV response at 5 mV s^{-1} from -0.4 to 1 V vs Ag/AgCl. As shown in Figure 7.7B and D, between the initial and 10th cycle drastic changes have occurred to the rectangular shape of the voltagramms of the pure SWCNTs with further changes occurring with subsequent cycles. These changes are seen by the additional wide redox

peaks on the cathodic sweep at roughly 0.25 V in H_2SO_4 and 0.1 V in K_2SO_4 and on the anodic sweep at 0.25 V, 0.5 V and 0.75 V for K_2SO_4 whilst in H_2SO_4 there is no distinctive peak, just a broad region from 0 – 1 V in which the redox processes are taking place.

Conversely, as shown in Figure 7.7C and E, a 10% mass fraction of SnO prevents this functionalisation from occurring, with subsequent cycles appearing almost identical to previous ones (the increase in the overall area is due to additional electrode wetting with subsequent cycling). The observable broad reaction peaks that deviate from the typical rectangular shape associated with EDLC are related to the redox processes due to surface oxygen groups on the terminals of the tubes.[1,15]

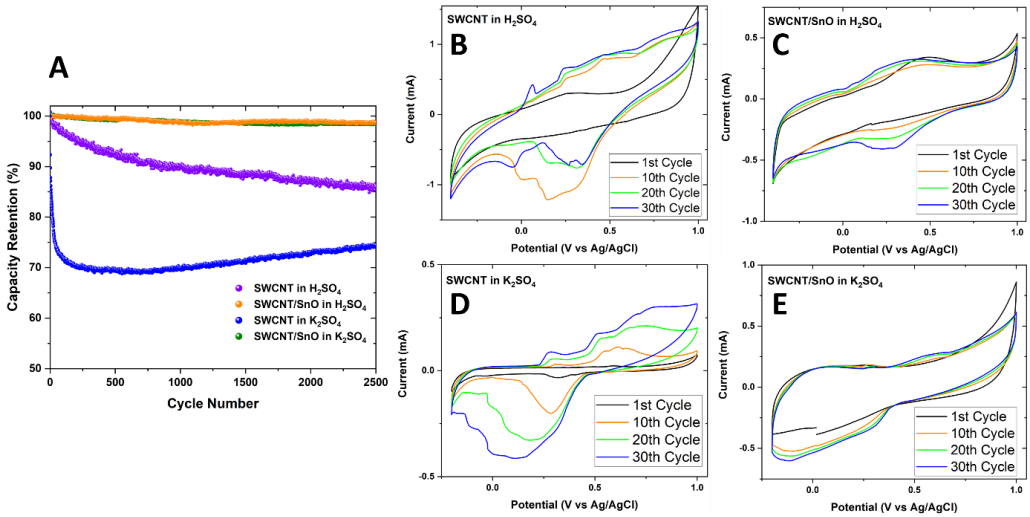

Figure 7.7: (A) Capacity retention at 10 A g^{-1} of various SC devices over 2,500 cycles. (B) CV at 5 mV s^{-1} of SWCNT H_2SO_4. (C) CV at 5 mV s^{-1} of SWCNT/SnO H_2SO_4. (D) CV at 5 mV s^{-1} of SWCNT K_2SO_4. (E) CV at 5 mV s^{-1} of SWCNT/SnO H_2SO_4.

The advantage of inhibiting the functionalisation is apparent in the cycling stability data shown in Figure 7.7A. With functionalisation, the charge capacity of the SWCNTs falls to 85% in H_2SO_4 and 74% in K_2SO_4 of its initial value after 2,500 cycles. Through the use of SnO to inhibit the functionalisation, after 2,500 cycles, capacity retention remains at 99%. To further demonstrate the effectiveness of SnO/Sn_3O_4 at preventing the functionalisation of SWCNTs, extended cycling for 15,000 and 30,000 cycles was recorded with the resulting CVs (Appendix E, Figure E.2A) displaying only minor alterations and the capacity retention remaining in excess of 95% (Appendix E, Figure E.2B) whilst both SnO/Sn_3O_4 were still present (Figure 7.3B). Herein we define capacity retention as the ratio of the capacitance at a given cycle to the value measured during the initial cycle. The over-oxidation necessary for functionalisation leads to defects and

degradation of the polymer structure of the tube, and this causes a decline in performance. EIS was carried out on both pure SWCNT and SnO/SWCNT in both electrolytes (Appendix E, Figure E.3). The EIS fitting of the equivalent circuit showed all electrodes displayed similar performances in terms of charge transfer resistance both pre/post use, with the electrodes with SnO having slightly higher resistances due to the presence of the non-conductive oxide (Figure E.3 and Table E.1).

	5 mV s^{-1}	**10 mV s^{-1}**	**20 mV s^{-1}**	**50 mV s^{-1}**	**100 mV s^{-1}**	**200 mV s^{-1}**	**500 mV s^{-1}**	**1000 mV s^{-1}**	**2000 mV s^{-1}**
CNT H_2SO_4	288 C g^{-1}	223 C g^{-1}	174 C g^{-1}	128 C g^{-1}	100 C g^{-1}	78 C g^{-1}	53 C g^{-1}	39 C g^{-1}	27 C g^{-1}
CNT K_2SO_4	387 C g^{-1}	248 C g^{-1}	154 C g^{-1}	81 C g^{-1}	50 C g^{-1}	35 C g^{-1}	27 C g^{-1}	23 C g^{-1}	20 C g^{-1}
CNT/ SnO H_2SO_4	171 F g^{-1}	128 F g^{-1}	96 F g^{-1}	73 F g^{-1}	62 F g^{-1}	55 F g^{-1}	47 F g^{-1}	39 F g^{-1}	28 F g^{-1}
	240 C g^{-1}	179 C g^{-1}	134 C g^{-1}	102 C g^{-1}	87 C g^{-1}	77 C g^{-1}	65 C g^{-1}	54 C g^{-1}	39 C g^{-1}
CNT/ SnO K_2SO_4	88 F g^{-1}	77 F g^{-1}	54 F g^{-1}	41 F g^{-1}	36 F g^{-1}	33 F g^{-1}	27 F g^{-1}	23 F g^{-1}	18 F g^{-1}
	105 C g^{-1}	92 C g^{-1}	64 C g^{-1}	50 C g^{-1}	43 C g^{-1}	39 C g^{-1}	33 C g^{-1}	28 C g^{-1}	21 C g^{-1}

Table 7.2: Capacitance in F g^{-1} and C g^{-1} of various tested electrodes at various scan rates.

Functionalisation leads to greater charge storage at low scan rates, however, as shown in Table 7.2, as the scan rate increases, the gap between the charge capacity levels off, as these surface redox reactions do not have time to take place. As the CVs of the functionalised SWCNTs differ significantly in shape from the SWCNT/SnO composite it is more correct and representative of the electrode performance to compare in terms of coulombs as the capacitance is not constant throughout the potential window, as shown in Table 7.2 (note that SWCNT/SnO are represented in Farads and Coulombs as they display rectangular CVs).[42] For real-world applications where supercapacitors are expected to act in an ultrafast fashion the SWCNT/SnO composite is favoured due to its enhanced cycling stability.

SWCNT/SnO Electrode

The electrochemistry of the SWCNT with a 10% mass fraction of SnO in H_2SO_4 was analysed using CV and GCD in Figure 7.8A and B. At 2 A g^{-1} which corresponds to a time roughly equivalent to a rate of 60 C for a battery, a capacitance of 102 F g^{-1} is delivered which would be a normal operating rate for a supercapacitor,[43] whilst at 10 A g^{-1}, 60 F g^{-1} is delivered. The specific capacitance (C_{sp}) was evaluated from CV curves using Equation 7.4 and GCD curves using Equation 7.5, where m is the mass of the electrode, υ is the scan rate, V_a and V_c are the anodic and cathodic cut-off potentials, and I is the current. As the CVs present are not perfectly rectangular, and the GCD curves are not perfectly triangular displaying a linear time-dependent change in potential at constant current,[43] the integral forms are used in Equations 7.4 and 7.5 to account for the non-ideality.[44,45]

$$C_{sp} = \frac{1}{m\upsilon(V_a - V_c)} \int_{Vc}^{Va} I\,(V)\,dV \tag{7.4}$$

$$C_{sp} = \frac{I}{m} \int \frac{1}{V(t)}\,dt \tag{7.5}$$

In CV measurements, the total current measured under a potential sweep rate may be decomposed into that related to the slow diffusion-controlled process (i_{diff}) and the current required to charge the double layer at the electrolyte interface (i_{cap}),[45,46] which is described mathematically below.

$$i(v) = i_{cap} + i_{diff} = av^b \tag{7.6}$$

$$\log i(v) = \log a + b \log v \tag{7.7}$$

Parameter b may be obtained from the slope of the linear plot of Equation 7.7 and is used to provide kinetic information about the electrochemical reactions. A b-value of 1 indicates contributions from fast surface reactions, whilst a b-value of 0.5 represents the slow semi-infinite diffusion-controlled faradaic processes that occur for battery-like materials. The b-values calculated for the SWCNT/SnO electrode were 0.85 and 0.81 for the anodic and cathodic peak currents respectively. Thus, the current primarily stems from

the capacitive contribution indicative of pseudocapacitive materials. It must be noted that if one only analyses scan rates below 50 mV s^{-1} these values increase above 0.9, suggesting the presence of a critical sweep rate below this value.[46] This occurs for many pseudocapacitive materials, indicating a slight transition from surface controlled to semi-infinite linear diffusion.[47,48] However in this situation and owing to the well-established capacitive/pseudocapacitive nature of SWCNTs, the slight deviation from unity is most likely caused by the ohmic polarization at quick scan rates.[47,49]

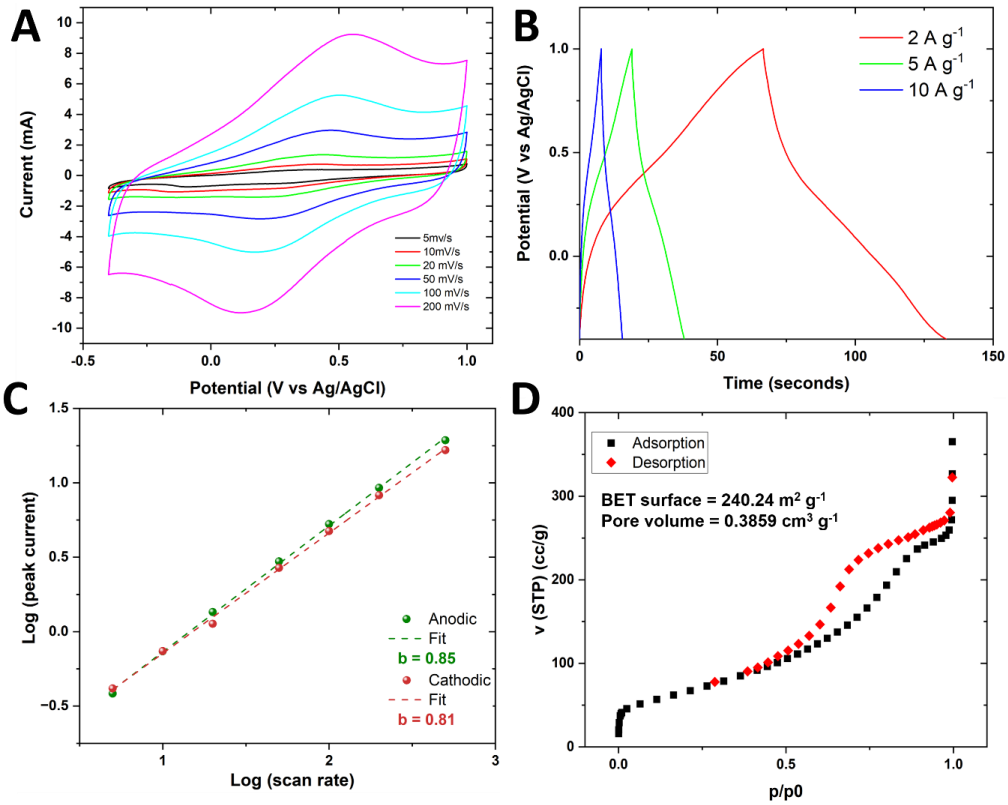

Figure 7.8: (A) CV plot for SWCNT/SnO. (B)GCD curves at various rates for SWCNT/SnO. (C) Linear plot of the log of peak current vs log of scan rate to calculate parameter *b*. (D) N_2 adsorption-desorption isotherms at 77 K for SWCNT.

In the voltage window tested the SnO has no capacitive effect except that which its surface area contributes to the EDLC, which is negligible when compared to the SWCNTs. This was demonstrated by increasing the mass content of SnO from 10 to 50, 70 and 90%, there was a fall in capacitance owing to the replacement of the SWCNT with SnO (Appendix E, Table E.2). A 10% mass fraction was the minimum amount of SnO that was required to produce the shielding effect. As you may recall, in Chapter 4 the specific surface area of SnO calculated from the N_2 isotherms (Figure 4.4) using the classic BET method ranged from 31.66 – 2.41 m^2 g^{-1} whilst the SWCNT specific area was 240.24 m^2

g^{-1}. Therefore the EDLC available is far greater through the use of the SWCNT. The role of SnO will be elaborated upon in Section 7.7.

7.6 Full-Cell Asymmetric Device

To demonstrate the advantage of extending the voltage window to real-world applications, an asymmetric device was assembled using MXene ($Ti_3C_2T_x$) as the negative electrode and 3 M H_2SO_4 in polyvinyl acetate (PVA) as the electrolyte. MXenes are a large family of 2D transition metal carbides and nitrides. They are synthesised first via the formation of ternary layered ceramics referred to as the MAX phase ($M_{n+1}AX_n$); where M is a transition metal, A is a group 13/14 element and X is carbon or nitrogen. This A group is then selectively etched off using hydrofluoric acid and the resulting MXene has the formula $M_{n+1}X_nT_x$, where T_x denotes the surface termination group of –F, –O, and –OH.[50,51] MXenes to date have shown great promise as high-rate electrodes for pseudocapacitive energy storage due to their highly reversible surface redox reactions due to their 2D structure and the large accessible surface area available.[51] Asymmetric devices increase the energy density of SC devices by combining different positive/negative electrodes to maximise the overall potential window of the device. For a SC device, the potentials of the separated electrodes extend in opposite directions during charging until each electrode reaches the same capacity.[52] Thus, the potential window of the whole cell depends on the upper limit of the positive electrode, and the lower limit of the negative electrode, as shown below:

$$E_{device} = E_{positive} - E_{negative} \quad (7.8)$$

As both electrodes present in this device display the same charge storage mechanisms (EDLC and pseudocapacitance) one may consider it an asymmetric device.[42] SEM images of the MXene sheets used are shown in Figure 7.9D. With the MXene electrodes working range between -0.8 and 0.2 V vs Ag/AgCl (Appendix E, Figure E.4A), and the SWCNT/SnO range between -0.4 and 1 V vs Ag/AgCl, the working voltage window of the device was set at 0 - 1.8 V (Figure.7C/D and Appendix E, Figure E.4B).

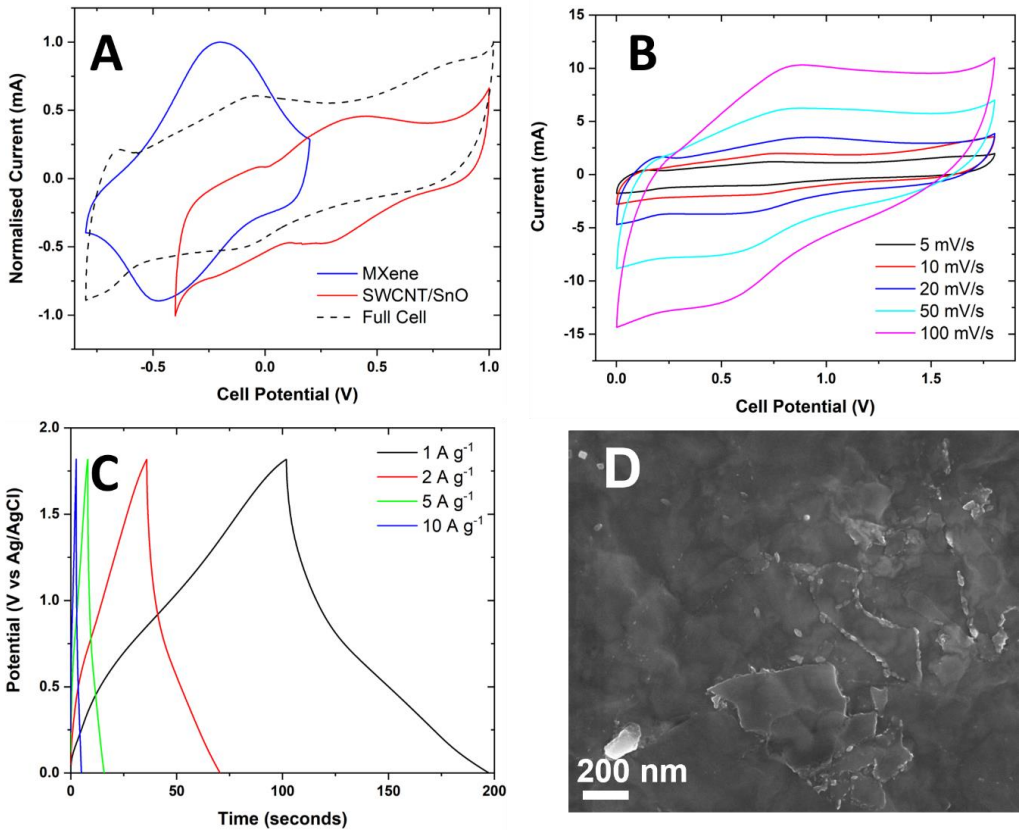

Figure 7.9: (A) CV plots of MXene, SWCNT/SnO and asymmetric full cell at 10 mV s^{-1}. (B) CV plot of the asymmetric device at various scan rates. (C) GCD curve at various rates for the asymmetric device. (D) SEM image of MXene electrode.

The energy density at 1 A g^{-1} was 24.39 Wh kg^{-1} for the SWCNT/SnO electrode in the asymmetric device dropping to 6.66 Wh kg^{-1} at 10 A g^{-1}. (Note the MXene was in excess. If accounting for the total mass of the SWCNT/SnO and MXene electrodes (not accounting for the glass slides on which they were printed upon) the results for the full asymmetric device are 9.5 Wh kg^{-1} and 2.6 Wh kg^{-1}). The energy density was calculated from the GCD curve using Equation 7.9 which considers the non-perfect triangular GCD curve of the device, where t_2 is the time the discharge finished and t_1 is the time after the initial IR drop.[52]

$$E = \int_{t1}^{t2} IV_{(t)}dt \tag{7.9}$$

The maximum power of the asymmetric device was calculated using Equation 7.10,[45,52,53] where $V_{charged}$ is the voltage of the device and ESR is the equivalent series resistance of the electrode:

$$P_{max} = \frac{V_{charged}^2}{4 \times ESR} \tag{7.10}$$

The ESR was calculated by using EIS and fitting the resulting Nyquist plot with an equivalent Randle's circuit as shown in Figure 7.10A. R_s, the point of intersection of the real axis at high frequency is the internal/series resistance and includes the intrinsic electronic resistance of the electrode material, the ohmic resistance of the electrolyte and the interfacial resistance between the electrode and current collector.[52] R_{ct} is the charge transfer resistance, C_{dl} is the double layer capacitance, and W is the Warburg element used to describe the impedance of diffusion of mobile charges in the electrode whilst C_{pseudo} is the pseudocapacitance obtainable in both the SWCNT[54,55] and MXene[56] electrodes.

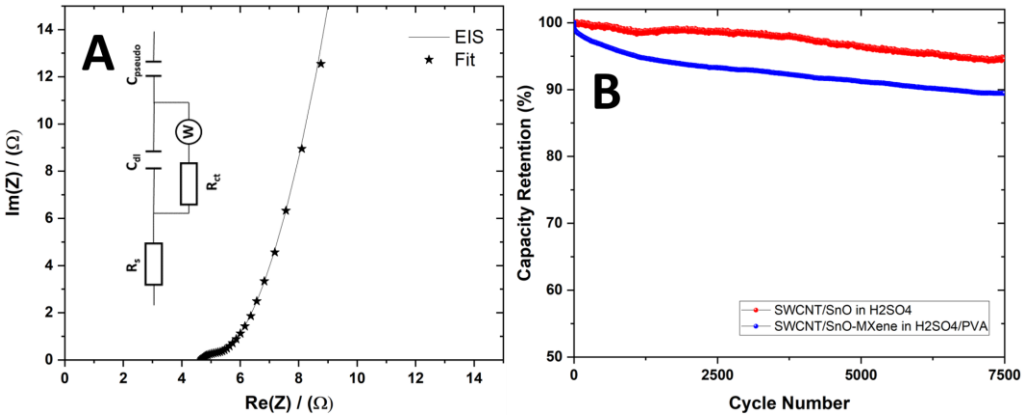

Figure 7.10: (A) EIS spectra of the asymmetric device with Z-fit approximation overlayed and equivalent circuit inset. (B) Capacity retention of SWCNT/SnO in the three-electrode configuration and in an asymmetric device over 7,500 cycles.

The ESR is a sum of the internal resistance (4.62 Ω) and the charge transfer resistance (0.99 Ω). This leads to a maximum power density of 51.5 kW kg^{-1} in terms of the SWCNT/SnO electrode in the asymmetric device (note again the MXene was in excess, the full device value is 15 kW kg^{-1}). Cycling data at 10 A g^{-1} shows the enhanced stability obtainable through the small addition of SnO to the SWCNTs with the three-electrode configuration retaining 95% of the initial capacity after 7,500 cycles whilst the asymmetric device retains 90% of its initial capacity (Figure 7.10B).

7.7 SnO as a Supercapacitor Material

As previously stated, SnO had no pseudocapacitive effect in the voltage window tested to date, and this was demonstrated as with an increased mass content of SnO, the specific capacitance of the electrode fell as the SWCNT had a much greater specific surface area

(Appendix E, Table E.2). Due to the layered structure of SnO, intercalation pseudocapacitance was investigated by exploring more negative potentials using a three-electrode setup.

Upon repeated cycling, poor CE was recorded and diminishing currents for subsequent cycles as shown in Figure 7.11A. At these negative potentials, a reduction reaction happens in place of/in parallel to ion intercalation which reduces the SnO to metallic tin. During the subsequent anodic sweep not all of the metallic tin is re-oxidised to SnO resulting in the poor CE observed. This agrees with previous work carried out on Tin(II) Oxide sensors.[57] Therefore it is of no benefit to expand the voltage window to include this reaction as it is not fully reversible and the limit of the cathodic sweep was kept at -0.4 V vs Ag/AgCl reference. Furthermore, an alternate electrolyte of LiCl was investigated. The same overall trend was observed, with diminishing currents as the number of cycles increased although the drop off was not as significant as with the H_2SO_4 electrolyte. Therefore due to the lack of reversibility, SnO is not suitable as a SC device under the conditions tested in this research. It does however, play an adequate role in shielding the SWCNTs in the voltage window tested. It must be noted that the effect the SnO had was independent of the morphology used, as all were tested and produced nearly identical electrochemical responses (Appendix E, Figure E.5).

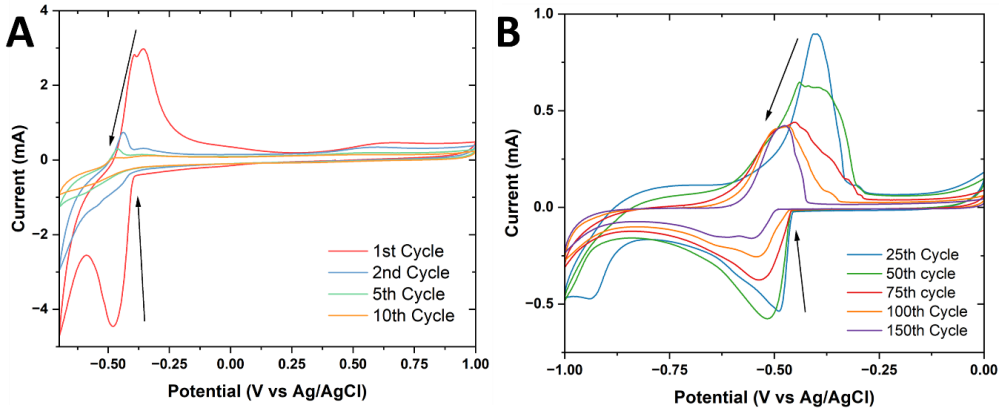

Figure 7.11: (A) CV response of SWCNT/SnO electrode from -0.7 to 1 V vs Ag/AgCl reference in H_2SO_4. (B) CV response of SWCNT/SnO electrode from -1 to 0 V vs Ag/AgCl reference in LiCl electrolyte.

7.8 Conclusion

In conclusion, pure SWCNT and SWCNT/SnO supercapacitor electrodes were successfully manufactured into functioning supercapacitor electrodes. The presence of SnO, although not adding to the capacitance of the electrode in the voltage window, importantly inhibited the oxidation and subsequent degradation of the SWCNT as confirmed by Raman spectroscopy, FTIR, and XPS. We believe that the mechanism for shielding the SWCNTs involves a pseudo-reversible reaction between the sulphate ions and SnO, which leads to the existence of both SnO and Sn_3O_4 after cycling in devices. This led to enhanced cycling stability for electrodes containing a small fraction of SnO with a capacitance of 102 F g^{-1} at 2 A g^{-1} and capacity retention in excess of 95% after 7,500 cycles at 10 A g^{-1}, thus demonstrating the advantage of inhibiting the functionalisation of SWCNTs. A 10% mass fraction was the optimum amount of SnO in the composite, which still achieved the shielding effect whilst also maximising the available capacitance from the SWCNTs. The asymmetric device assembled allowed the voltage window to be expanded to 1.8 V using MXene as the negative electrode, with an energy density of 24.39 Wh kg^{-1} at 1 A g^{-1} and capacity retention of 90% after 7,500 cycles. Through further optimisation of this device and printing more intricate geometries, we believe this figure can be improved upon.

Future work would look to further optimise the asymmetric device and explore printing more complex and intricate geometries to improve upon the power/energy density. It would also be interesting to combine the SWCNTs with another pseudocapacitive material within the voltage window to see if the capacity could be improved upon whilst also seeing if the same type of shielding occurs from the anodic oxidation of the SWCNTs.

7.9 Experimental

Printing of SWCNT and SWCNT/SnO Electrodes

SWCNT and SWCNT/SnO inks were formed using Tuball SWCNTs (0.2%) dispersed in carboxymethyl cellulose (CMC - 0.3%) and H_2O. The ratio of SWCNT to SnO was 9:1. In this work the various SnO inks were printed with a Nano3DPrint extrusion printer, without the need of additives to aid printing. For these prints, the material was extruded using a 0.26 mm internal diameter nozzle onto weighed and cleaned glass slides. The material was extruded onto a print bed set to 60 ºC to aid the drying of the printed patterns. The print speed was held at 200 mm/min to maintain consistent line and pattern formation and so adjustments could be made easily during the print process. As standard, three printed passes were deposited and allowed to dry in each print run to provide a complete homogenous film before further layers were deposited. The patterns used were designed using AutoCAD (Autodesk Inc,) and the final print path GCode was generated using the Simply3D slicing software to provide x y z pathing for the designed patterns. Successive layers were printed at 90 degrees to one another to eliminate issues that could potentially arise from print defects.

Printed devices were placed in a tube furnace and heated under vacuum with an argon air flow at a ramp of 10 ºC/min with a 2 hour hold at 400 ºC to remove H_2O and carbonise the CMC binder. Silver contacts and a protective resin layer were added subsequently.

Printing of MXene electrodes

MXenes were obtained from a Ti_3AlC_2 MAX phase powder (1 g, Carbon-Ukraine ltd.) which was delaminated using 9 M HCl (20 mL, Sigma) and LiF powder (1.6 g, Sigma) in a PTFE vessel. The solution was left stirring at 400 rpm at 35 °C for 24 h to obtain etched, multilayer $Ti_3C_2T_x$ MXene. The delaminated MXenes were obtained through washing with deionized water and centrifugation at 5000 rpm using a Thermo Scientific Heraeus Multifuge X1 for 5 min, discarding the supernatant and repeating several times until the pH of the supernatant had reached at least 6. The dispersion was then centrifuged at 1500 rpm for 30 min to sediment any multi-layer MXene or unreacted MAX phase.

Electrochemical Analysis

A three-electrode electrolytic cell was formed for electrochemical testing using a working electrode, an Ag/AgCl double junction electrode as reference electrode, and a graphite

rod as a counter electrode. Two electrode cells were formed using SWCNT/SnO as the positive electrode and MXene as the negative electrode. All electrochemical measurements: such as cyclic voltammetry (CV), galvanostatic charge-discharge (GCD) and electrochemical impedance spectroscopy (EIS) were performed using a Bio Logic VMP 300 and analysed using the EC-Lab software. CVs were recorded at scan rates of 5, 10, 20, 50, 100, 200, 500, 1000, 2000 mV s^{-1} from -0.4 to 1 V (vs Ag/AgCl) in H_2SO_4 and -0.2 to 1 V (vs Ag/AgCl) in K_2SO_4. GCD measurements were ran using the same voltage windows as for the CVs at rates of 1, 2, 5 and 10 A g^{-1}. For the asymmetric cell, 3M H_2SO_4 in PVA was used as the electrolyte and the device was formed by placing one electrode directly a top the other with the gel electrolyte acting as a separator. Note that the mass used for the calculation of the charge stored was based off the total mass of the electrode (not including the glass slide the electrodes are printed upon).

EIS was recorded at an open circuit potential from 1000 kHz to 10 mHz. The electrode was left at an open circuit voltage for 1 hour to stabilise prior to measurements and ensure no faradaic charge transfer processes were occurring. Upon commencement of the readings, the voltage remained steady throughout. The Z-fit software from EC-lab was used to fit equivalent Randle's circuits to EIS spectra and obtain values for the components.

7.10 References

1 H. Pan, J. Li and Y. Feng, *Nanoscale Res. Lett.*, 2010, **5**, 654.
2 X. Xiao, T. Li, Z. Peng, H. Jin, Q. Zhong, Q. Hu, B. Yao, Q. Luo, C. Zhang, L. Gong, J. Chen, Y. Gogotsi and J. Zhou, *Nano Energy*, 2014, **6**, 1–9.
3 B. Pal, S. Yang, S. Ramesh, V. Thangadurai and R. Jose, *Nanoscale Adv.*, 2019, **1**, 3807–3835.
4 G. U. Sumanasekera, J. L. Allen, S. L. Fang, A. L. Loper, A. M. Rao and P. C. Eklund, *J. Phys. Chem. B*, 1999, **103**, 4292–4297.
5 S. Lefrant, M. Baibarac, I. Baltog, J. Y. Mevellec, L. Mihut and O. Chauvet, *Synth. Met.*, 2004, **144**, 133–142.
6 P. Corio, P. S. Santos, V. W. Brar, G. G. Samsonidze, S. G. Chou and M. S. Dresselhaus, *Chem. Phys. Lett.*, 2003, **370**, 675–682.
7 C.-T. Hsieh, W.-Y. Lee, C.-E. Lee and H. Teng, *J. Phys. Chem. C*, 2014, **118**, 15146–15153.
8 K. K. Liu, Q. Jiang, C. Kacica, H. G. Derami, P. Biswas and S. Singamaneni, *RSC Adv.*, 2018, **8**, 31296–31302.
9 V. Velmurugan, U. Srinivasarao, R. Ramachandran, M. Saranya and A. N. Grace, *Mater. Res. Bull.*, 2016, **84**, 145–151.
10 Q. Wang, Y. Tian, S. Guan, Z. Peng and X. Fu, *ACS Appl. Energy Mater.*, 2020, **3**, 11333–11342.
11 Y. Tian, Q. Wang, Z. Peng, S. Guan and X. Fu, *Mol.* , 2021, 26.
12 A. Murugan, V. Siva, A. Shameem, S. A. Bahadur, S. Sasikumar and N. Nallamuthu, *J. Energy Storage*, 2020, **28**, 101194.
13 S. Ryan, M. P. Browne, A. Zhussupbekova, D. Spurling, L. McKeown, D. Douglas-Henry, L. Prendeville, S. Vaesen, W. Schmitt, I. Shvets and V. Nicolosi, *Electrochim. Acta*, 2023, **448**, 142168.
14 M. S. Dresselhaus, G. Dresselhaus, R. Saito and A. Jorio, *Phys. Rep.*, 2005, **409**, 47–99.
15 B. Martínez-Sánchez, J. Quílez-Bermejo, E. San-Fabián, D. Cazorla-Amorós and E. Morallón, *J. Mater. Chem. A*, 2022, **10**, 7271–7290.
16 S. Botti, ed. A. Rufoloni, IntechOpen, Rijeka, 2018, p. Ch. 10.
17 O. A. Gurova, V. E. Arhipov, V. O. Koroteev, T. Y. Guselnikova, I. P. Asanov, O. V Sedelnikova and A. V Okotrub, *Phys. status solidi*, 2019, **256**, 1800742.
18 M. P. Browne, F. Novotný, Z. Sofer and M. Pumera, *ACS Appl. Mater. Interfaces*, 2018, **10**, 40294–40301.
19 B. R. C. De Menezes, F. V Ferreira, B. C. Silva, E. A. N. Simonetti, T. M. Bastos, L. S. Cividanes and G. P. Thim, *J. Mater. Sci.*, 2018, **53**, 14311–14327.
20 S.-M. Yuen, C.-C. M. Ma, Y.-Y. Lin and H.-C. Kuan, *Compos. Sci. Technol.*, 2007, **67**, 2564–2573.
21 U. J. Kim, C. A. Furtado, X. Liu, G. Chen and P. C. Eklund, *J. Am. Chem. Soc.*, 2005, **127**, 15437–15445.
22 S. K. Mishra, S. N. Tripathi, V. Choudhary and B. D. Gupta, *Plasmonics*, 2015, **10**, 1147–1157.
23 J.-H. Choi, J. Jegal and W.-N. Kim, *J. Memb. Sci.*, 2006, **284**, 406–415.
24 L. S. Cividanes, D. D. Brunelli, E. F. Antunes, E. J. Corat, K. K. Sakane and G. P. Thim, *J. Appl. Polym. Sci*, 2012, **127**, 544–553.
25 G. Kalonga, K. Chinyama, O. Munyati and M. Maaza, *J. Chem. Eng. Mater. Sci.*, 2013, 93–102.
26 Z. Gao, T. J. Bandosz, Z. Zhao, M. Han and J. Qiu, *J. Hazard. Mater.*, 2009, **167**,

357–365.
27 P. Botschwina, *J. Chem. Phys.*, 1994, **101**, 234302.
28 C. Fang, Y. Zhang, Z. Zhang, C. Shan, W. Shen and X. Jia, *CrystEngComm*, 2018, **20**, 505–511.
29 N. M. Shaalan, D. Hamad, A. Y. Abdel-Latief and M. A. Abdel-Rahim, *Prog. Nat. Sci. Mater. Int.*, 2016, **26**, 145–151.
30 W. Zeng, Y. Liu, G. Chen, H. Zhan, J. Mei, N. Luo, Z. He and C. Tang, *RSC Adv.*, 2020, **10**, 29843–29854.
31 A. R. Babar, S. S. Shinde, A. V Moholkar and K. Y. Rajpure, *J. Alloys Compd.*, 2010, **505**, 743–749.
32 S. Jaśkaniec, S. R. Kavanagh, S. Ryan, J. Coelho, C. Hobbs, A. Walsh, D. O. Scanlon and V. Nicolosi, *npj 2D Mater. Appl.*, 2021, **5**, 27.
33 C. M. Campo, J. E. Rodríguez and A. E. Ramírez, *Heliyon*, *Heliyon*, 2016, **2**, e00112.
34 Y. He, D. Li, J. Chen, Y. Shao, J. Xian, X. Zheng and P. Wang, *RSC Adv.*, 2014, **4**, 1266–1269.
35 S. D. Balgude, Y. A. Sethi, B. B. Kale, N. R. Munirathnam, D. P. Amalnerkar and P. V Adhyapak, *RSC Adv.*, 2016, **6**, 95663–95669.
36 T. I. T. Okpalugo, P. Papakonstantinou, H. Murphy, J. McLaughlin and N. M. D. Brown, *Carbon N. Y.*, 2005, **43**, 153–161.
37 M. T. Martínez, M. A. Callejas, A. M. Benito, M. Cochet, T. Seeger, A. Ansón, J. Schreiber, C. Gordon, C. Marhic, O. Chauvet, J. L. G. Fierro and W. K. Maser, *Carbon N. Y.*, 2003, **41**, 2247–2256.
38 V. A. Davis, A. N. G. Parra-Vasquez, M. J. Green, P. K. Rai, N. Behabtu, V. Prieto, R. D. Booker, J. Schmidt, E. Kesselman, W. Zhou, H. Fan, W. W. Adams, R. H. Hauge, J. E. Fischer, Y. Cohen, Y. Talmon, R. E. Smalley and M. Pasquali, *Nat. Nanotechnol.*, 2009, **4**, 830–834.
39 P. Puech, T. Hu, A. Sapelkin, I. Gerber, V. Tishkova, E. Pavlenko, B. Levine, E. Flahaut and W. Bacsa, *Phys. Rev. B*, 2012, **85**, 205412.
40 A. Metrot and J. E. Fischer, *Synth. Met.*, 1981, **3**, 201–207.
41 J. O. Besenhard, E. Wudy, H. Möhwald, J. J. Nickl, W. Biberacher and W. Foag, *Synth. Met.*, 1983, **7**, 185–192.
42 T. Brousse, D. Bélanger and J. W. Long, *J. Electrochem. Soc.*, 2015, **162**, A5185.
43 P. Simon, Y. Gogotsi and B. Dunn, *Science.*, 2014, **343**, 1210–1211.
44 T. S. Mathis, N. Kurra, X. Wang, D. Pinto, P. Simon and Y. Gogotsi, *Adv. Energy Mater.*, 2019, **9**, 1902007.
45 A. Noori, M. F. El-Kady, M. S. Rahmanifar, R. B. Kaner and M. F. Mousavi, *Chem. Soc. Rev.*, 2019, **48**, 1272–1341.
46 J. Liu, J. Wang, C. Xu, H. Jiang, C. Li, L. Zhang, J. Lin and Z. X. Shen, , DOI:10.1002/advs.201700322.
47 V. Augustyn, P. Simon and B. Dunn, *Energy Environ. Sci.*, 2014, **7**, 1597–1614.
48 C. Chen, Y. Wen, X. Hu, X. Ji, M. Yan, L. Mai, P. Hu, B. Shan and Y. Huang, *Nat. Commun.*, 2015, **6**, 6929.
49 H. Shao, Z. Lin, K. Xu, P.-L. Taberna and P. Simon, *Energy Storage Mater.*, 2019, **18**, 456–461.
50 Y. Gogotsi and B. Anasori, *ACS Nano*, 2019, **13**, 8491–8494.
51 Q. Jiang, N. Kurra, M. Alhabeb, Y. Gogotsi and H. N. Alshareef, *Adv. Energy Mater.*, 2018, **8**, 1703043.
52 Y. Shao, M. F. El-Kady, J. Sun, Y. Li, Q. Zhang, M. Zhu, H. Wang, B. Dunn and R. B. Kaner, *Chem. Rev.*, 2018, **118**, 9233–9280.

53 L. Guan, L. Yu and G. Z. Chen, *Electrochim. Acta*, 2016, **206**, 464–478.
54 H. Pan, J. Li, • Yuan and P. Feng, , DOI:10.1007/s11671-009-9508-2.
55 T. Gu and B. Wei, *Nanoscale*, 2015, **7**, 11626–11632.
56 C. Zhan, M. Naguib, M. Lukatskaya, P. R. C. Kent, Y. Gogotsi and D. Jiang, *J. Phys. Chem. Lett.*, 2018, **9**, 1223–1228.
57 R. Díaz, I. Díez-Pérez, P. Gorostiza, F. Sanz and J. R. Morante, *J. Braz. Chem. Soc.*, 2003, **14**, 523–529

8. Conclusions and Future Work

From the outset of this PhD fellowship, the aims of the research carried out were to enhance the green energy storage technologies of LIBs, NIBs and SCs. The motivating factor for this was to improve these renewable energy storage technologies to a level in which their cost and performance could match, if not exceed the current fossil-fuel based technologies to enable an easy and fast transition to aid in the climate crisis. An additional factor is the unequal distribution of fossil fuels worldwide, therefore by enhancing renewable energy storage technology, countries and people can be self-sufficient in terms of their energy needs, and the leveraging of fossil fuels by corporations and countries should become redundant. To achieve this, SnO was investigated as a potential electrode material for LIBs, NIBs and SCs.

The initial work presented in this Thesis focused on the synthesis of SnO. A novel solvent-engineered synthesis was developed, in which through varying the alcohol/water mixture used for reflux, the morphology of the final product can be controlled and tuned. The synthesis was demonstrated to be scalable, required no expensive pre-cursors, and was carried out at ambient pressure and atmosphere; fulfilling the requirement of our material being green and cost-effective. Four unique morphologies were selected as being particularly interesting for further investigation into energy storage applications as they encompassed the unique dimensions/features obtainable through the developed synthesis; nanoflowers (SnO(EtOH), platelets (SnO(70% MeOH), perforated thick-squares (SnO(Hex)) and thick-squares (SnO(H_2O).

The unique morphologies of SnO were combined with an optimized loading of SWCNTs to form LIB anodes. To confirm that both the synthesized SnO and the SWCNTs enhanced the electrode performance, they were compared to SnO produced by Sigma Aldrich and traditional slurry-cast electrodes formed using carbon black, PVDF and NMP. The effect of morphology was investigated subsequently, with the SnO(EtOH) optimizing both the capacity and the rate performance of the electrode. In an effort to improve cyclability, whilst also reducing the cost of the electrode, alternate Tuball SWCNTs were investigated. An improvement in the cycling stability was recorded, however, it was not until an addition of 10% FEC was added to the electrolyte that stable cycling performance was achieved for the composite. Post-mortem SEM/EDX/XRD

revealed that the FEC allowed the formation of a flexible and stable SEI that could withstand the huge volumetric changes experienced during alloying, whilst also enabling the conversion reaction to continue as was also confirmed by *dQ/dV* analysis. The optimized HT SnO(EtOH) with 15% Tuball SWCNTs has an exceptional capacity of 980 mAh g^{-1} (~3 times that of graphite) at 0.1 C, an ICE of 80% and maintains a capacity of 815 mAh g^{-1} after 300 cycles at 0.5 C. Furthermore, a full-cell was developed using an NMC cathode showing how the anode could operate in this configuration, with the cathode being shown to be the limiting factor.

The synthesized SnO was investigated in NIBs following its success in LIBs, adopting the same iterative approach as carried out previously. HT SnO(EtOH) with 15% Tuball SWCNTs was once again found to optimize performance. It was deduced that the enhanced performance of the nanoflower morphology was due to its large specific surface area, whilst the thin platelets composing the nanoflower are contacted which may provide additional paths for electron flow within the material. Interestingly the composite used in the NIB underwent an activation period in which the capacity increased, and this was deduced to occur due to an electrochemical milling effect. The optimized composite had a maximum capacity of 574 mAh g^{-1} at 0.05 C, whilst in terms of cycling it had a capacity of 500 mAh g^{-1} after 60 cycles, which dropped to 405 and 261 mAh g^{-1} after 80 and 120 cycles respectively. Issues remained however around the ICE of the composite (51%) and the CE during cycling which remained under 99%. However, even with these issues, the reported work exceeds similar work carried out in the field.

Lastly, SnO in combination with SWCNTs was utilized as an SC electrode. Although the presence of SnO did not increase the capacitance through pseudocapacitance as hypothesised, it had the effect of inhibiting the functionalization and the subsequent degradation of the SWCNTs in the presence of sulphate-based electrolytes. We believe that the mechanism for shielding the SWCNTs involves a pseudo-reversible reaction between the sulphate ions and SnO, which leads to the existence of both SnO and Sn_3O_4 after cycling in devices as shown by XRD and XPS. A 10% mass fraction of SnO was the optimum addition; still enabling shielding whilst also maximising the SWCNT mass fraction which is responsible for the electrode's capacitance. The electrode obtained a capacitance of 102 F g^{-1} at 2 A g^{-1} and a capacity retention in excess of 95% after 7,500 cycles at 10 A g^{-1}. An asymmetric device was assembled with MXene with a voltage

window of 1.8 V, obtaining an energy density of 24.39 Wh kg^{-1} at 1 A g^{-1} and a capacity retention of 90% after 7,500 cycles.

Although the PhD fellowship for the most part achieved its aims, there are of course always areas for improvement and future investigations. The most pressing matter that remains is the use of SnO in the NIB. Although the results presented in this Thesis were an improvement upon previous works published in the field, for real-world applications a greater improvement is needed. This is a consequence of the limitations of the larger Na^+ ion, but as stated to reduce our dependence on Li in the battery field significant improvements must be made. To further understand the exact failing mechanism of this material, in-situ TEM and operando XRD/Raman would be beneficial to dissect the key contributors to the falling capacity (i.e. a loss of active material, a build-up of SEI, diffusion limitations of Na^+, etc.). Once this is established, a focused study could be carried out to try to inhibit the failing mechanism (such as alternate electrolytes). With the SC electrode, future work would focus on printing more intricate geometries using the ink formed, and in doing so increase the energy density of the device and develop a real-world prototype in the hopes of commercialization. The performance measured for the optimized SnO/SWCNT composite in LIBs is incredibly exciting, and to further build upon it I would like to approach other research groups who have developed optimized green cathodes, and once again develop a full-cell prototype. Furthermore, it would be interesting to advance this material into the pouch-cell configuration as this is more applicable to a real-world LIB device.

In summary, the results presented in this Thesis demonstrate the numerous applications of SnO in energy storage devices. Through the tailoring of a wet chemistry synthesis, there is no need for expensive top-down approaches or hydrothermal vessels to form nanomaterials, and this was shown. The optimized HT SnO(EtOH) with 15% Tuball SWCNTs works for both LIBs and NIBs and in this lies a huge opportunity to develop a single composite that works for both technologies. Although itself not suitable for SC use, SnO in combination with SWCNTs forms a high-capacity electrode with a large voltage window. The overall aim of this PhD fellowship was to: "*Develop a composite material that fits all technologies based on Tin(II) Oxide with the incorporation of carbon nanotubes, which can be cost effective, high in energy capacity and rate performance.*" I believe that these aims have aims have been met, with improvements on the horizon.

Appendix A

Derivation of pseudocapacitance:

Assuming the adsorbing species follow an electrochemical Langmuir isotherm of the form:

$$\frac{X}{X\text{-}1} = Ke^{\frac{VF}{RT}} \tag{A.1}$$

where K is the ratio of the forward to the reverse reaction rate constant and V is the electrode potential. Rearrangement of Equation.A.1 gives:

$$E = E^0 + \frac{RT}{F} ln\left(\frac{1}{K}\frac{X}{1-X}\right) \tag{A.2}$$

Assuming the charge required to complete a monolayer coverage is given as q, pseudocapacitance is given as:

$$C_\Phi = q\frac{dX}{dV} = \frac{qF}{RT}\cdot\frac{Ke^{\frac{VF}{RT}}}{(1+Ke^{\frac{VF}{RT}})^2} = \frac{qF}{RT}X(1\text{-}X) \tag{A.3}$$

Electric Double Layer Models

Guoy-Chapman Model:

$$C_{GC} = \left(\frac{2z^2e^2n_i^0\varepsilon_r\varepsilon_0}{kT}\right)^{\frac{1}{2}} cosh\left(\frac{ze\varphi_0}{2kT}\right) \tag{A.4}$$

Where z is the charge on the ion; e is the electron charge, n_i^0 is the concentration of the ion in the bulk solution, k is the Boltzmann constant, T is the temperature in Kelvin and φ_0 is the electric potential at the electrode.

Stern Model:

$$C_S = \frac{1}{C_{DL}} + \frac{1}{C_{GC}} \tag{A.5}$$

Appendix B

This Appendix refers to matters discussed in Chapter.4 concerning the synthesis and characterisation of SnO.

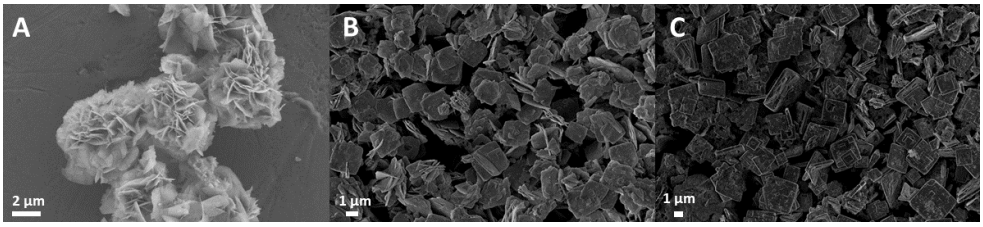

Figure B.1: (A) SnO synthesised in 1L flask demonstrating scalability without impacting result , (B) SnO synthesised in 1-propanol and (C) SnO synthesised in 1-butanol.

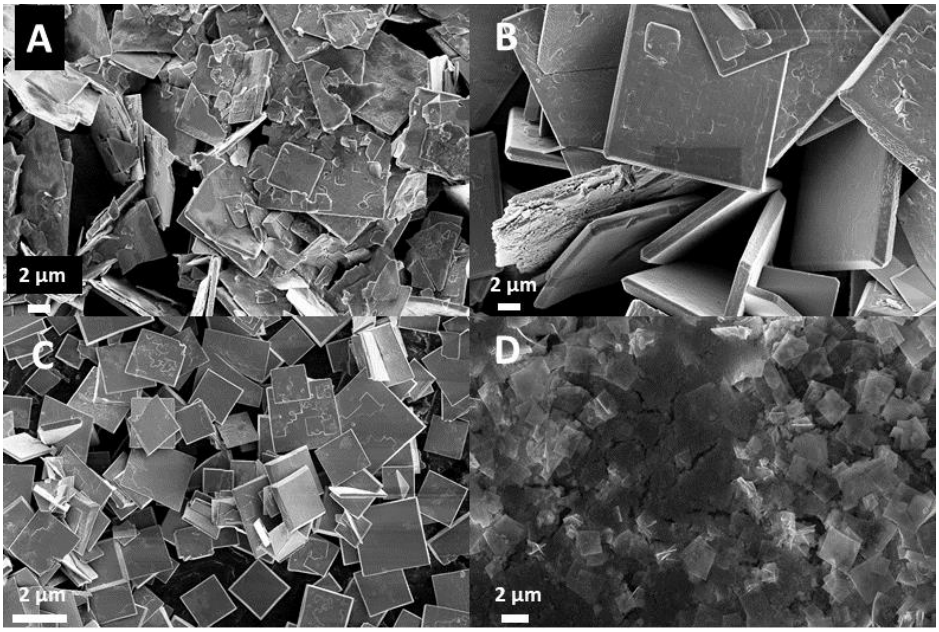

Figure B.2: SnO synthesised in methanol:water mix in ratios (A) 10:90, (B) 30:70, (C) 50:50 and (D) 90:10.

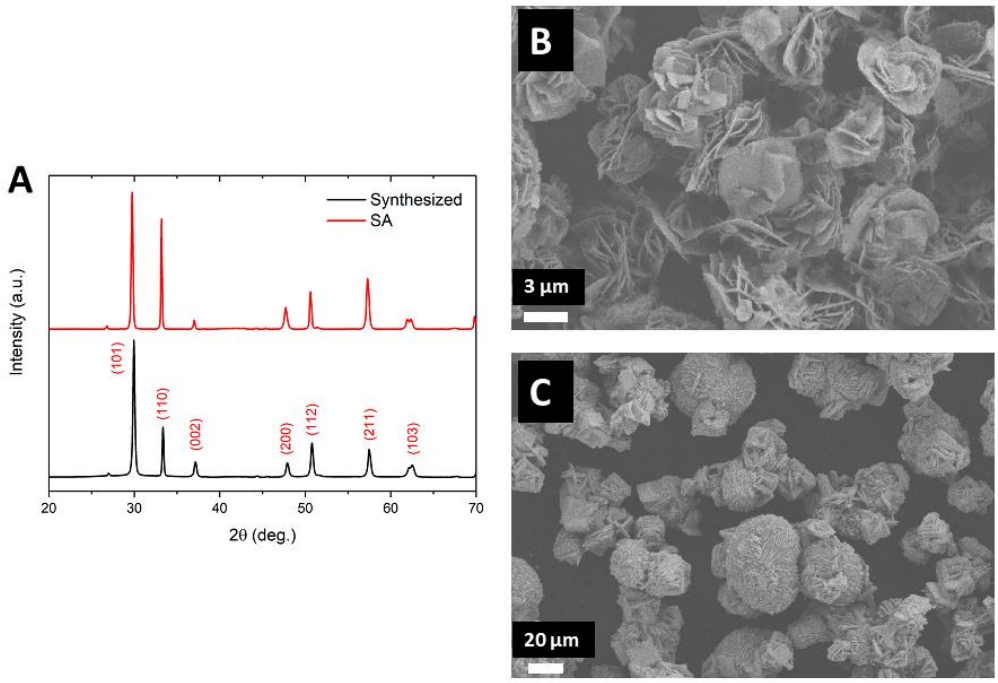

Figure B.3: (A) XRD of SA SnO and synthesised SnO, (B) SEM of synthesised SnO and (C) SEM of SA SnO.

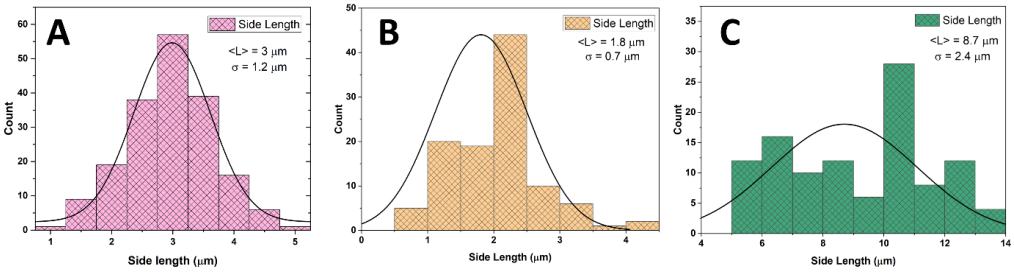

Figure B.4: Particle size distribution diagram for (A) the platelets produced in methanol:water (70:30) mixture, (B) the perforated thick squares produced in 1-hexanol and (C) the thick squares produced in water.

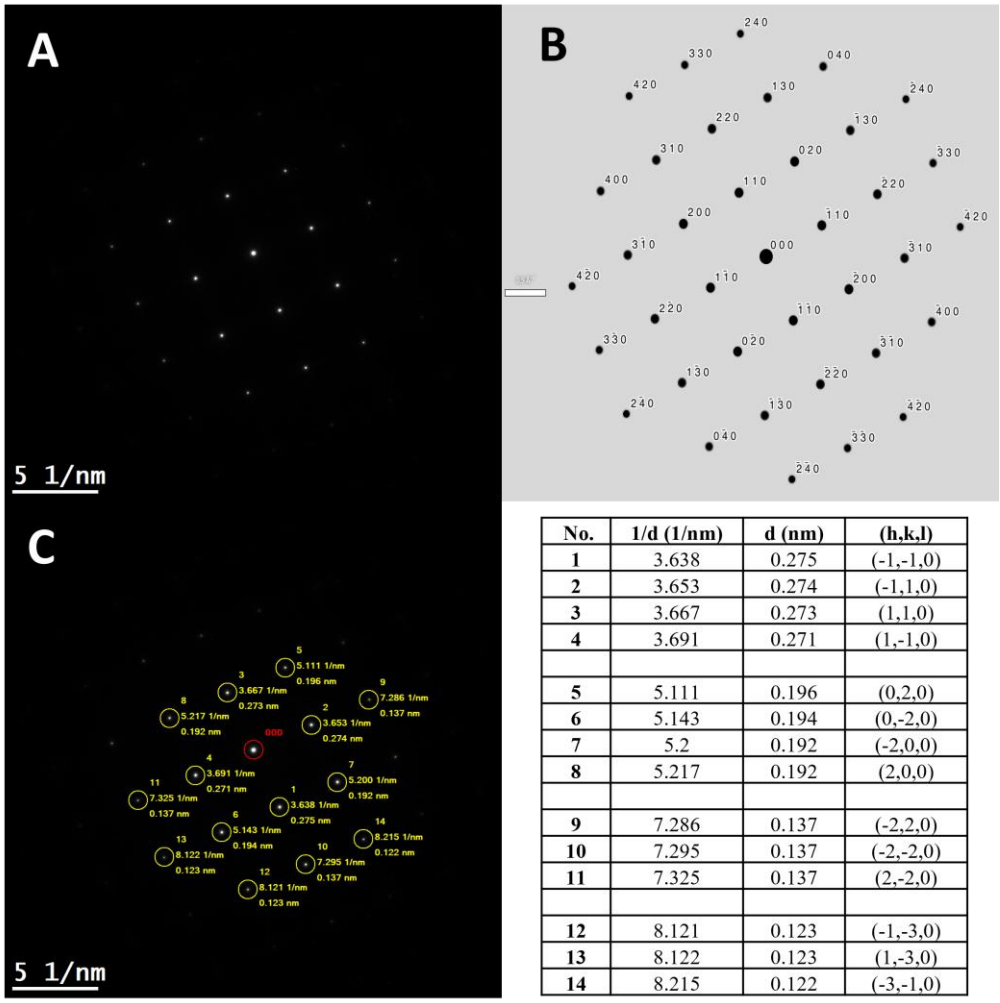

No.	1/d (1/nm)	d (nm)	(h,k,l)
1	3.638	0.275	(-1,-1,0)
2	3.653	0.274	(-1,1,0)
3	3.667	0.273	(1,1,0)
4	3.691	0.271	(1,-1,0)
5	5.111	0.196	(0,2,0)
6	5.143	0.194	(0,-2,0)
7	5.2	0.192	(-2,0,0)
8	5.217	0.192	(2,0,0)
9	7.286	0.137	(-2,2,0)
10	7.295	0.137	(-2,-2,0)
11	7.325	0.137	(2,-2,0)
12	8.121	0.123	(-1,-3,0)
13	8.122	0.123	(1,-3,0)
14	8.215	0.122	(-3,-1,0)

Figure B.5: (A) SAED of SnO platelet, (B) corresponding indexed diffraction pattern. (C) Indexed SAED with d-spacings in real/reciprocal space.

Table B:1: Tabulated results from indexed SAED.

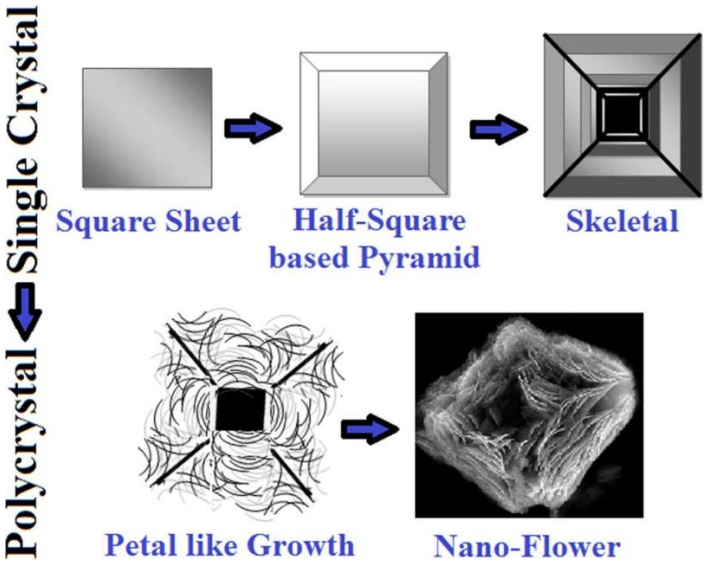

Figure B.6: Proposed steps in synthesis of nanoflowers of SnO by M.Z Iqbal et al. Adapted and reproduced with permission from Ref.[4].

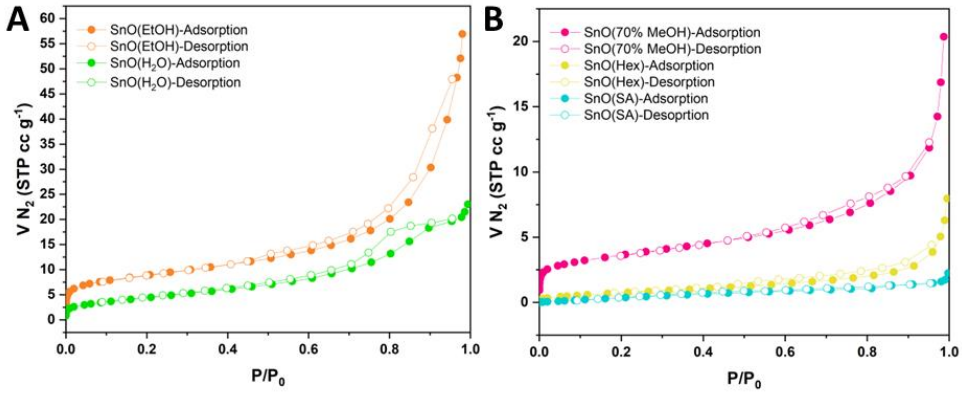

Figure B.7: (A) Adsorption/desorption isotherms of SnO synthesised in ethanol, water, (B) methanol, 1-hexanol and commercially purchased from SA.

Appendix C

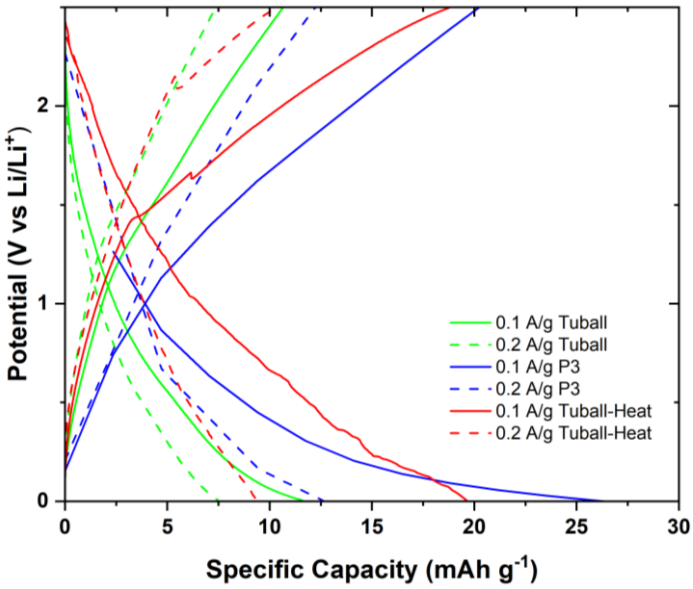

Figure C.1: GCD curves displaying the specific capacities of all SWCNTs used in Chapter 5.

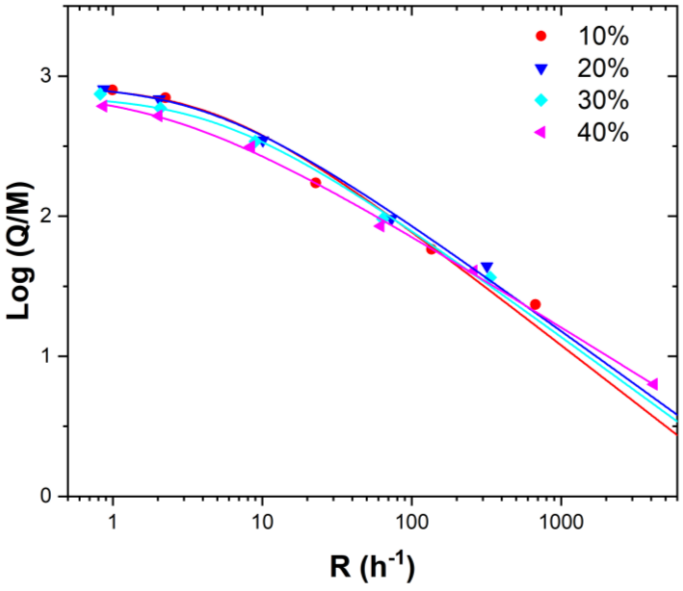

Figure C.2: Remainder of GCD experimental data fitted using Equation 5.1 for mass % of P3-SWCNT.

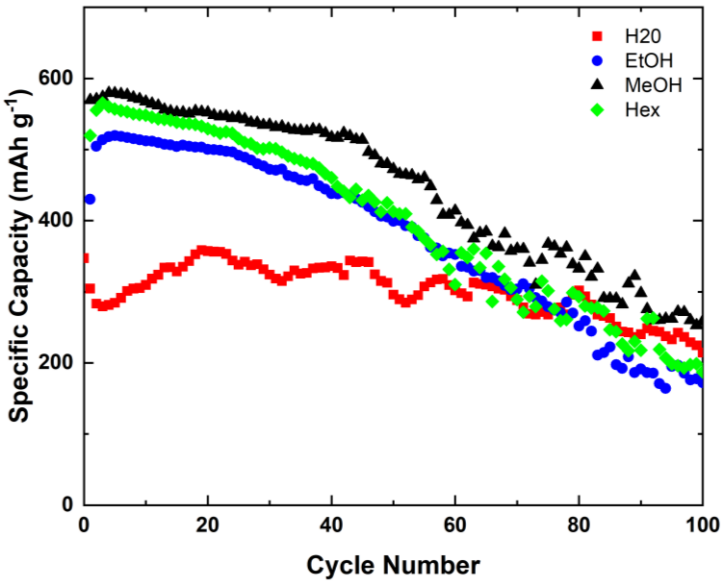

Figure C.3: GCD cycling data with a 1 V cut-off for SnO morphologies.

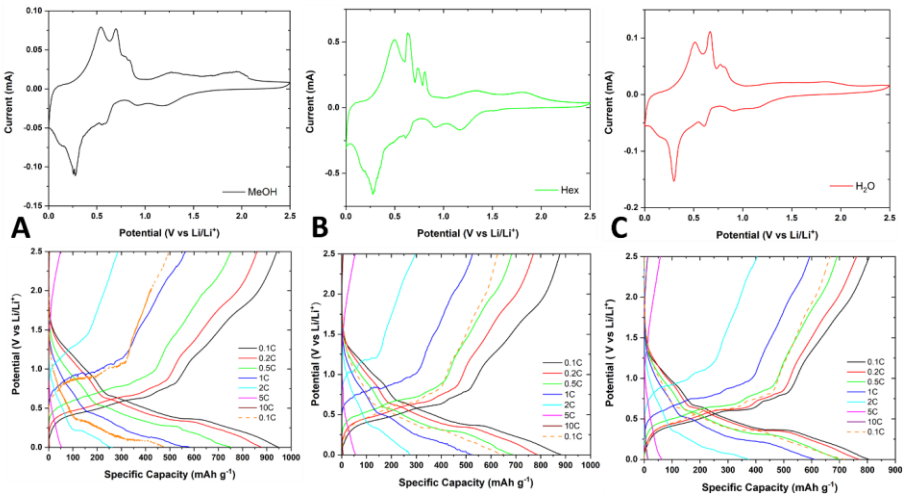

Figure C.4: CV and GCD profiles of (A) SnO (70% MeOH), (B) SnO(Hex) and (C) SnO(H_2O).

C-Rate	*Voltage of onset of conversion*	*SnO(EtOH)*	*SnO(70% MeOH)*	*SnO(Hex)*	*SnO(H_2O)*
0.1	1	60%	60%	63%	68%
0.2	1	60%	60%	63%	68%
0.5	1	60%	60%	63%	68%
1	1.2	67%	57%	70%	70%
2	1.4	67%	52%	70%	70%
0.1 (repeated)	1	70%	76%	68%	70%

Table C 1: Percentage of discharge capacity attributed to the alloying reaction for the synthesised SnO at the GCD *C-rates*.

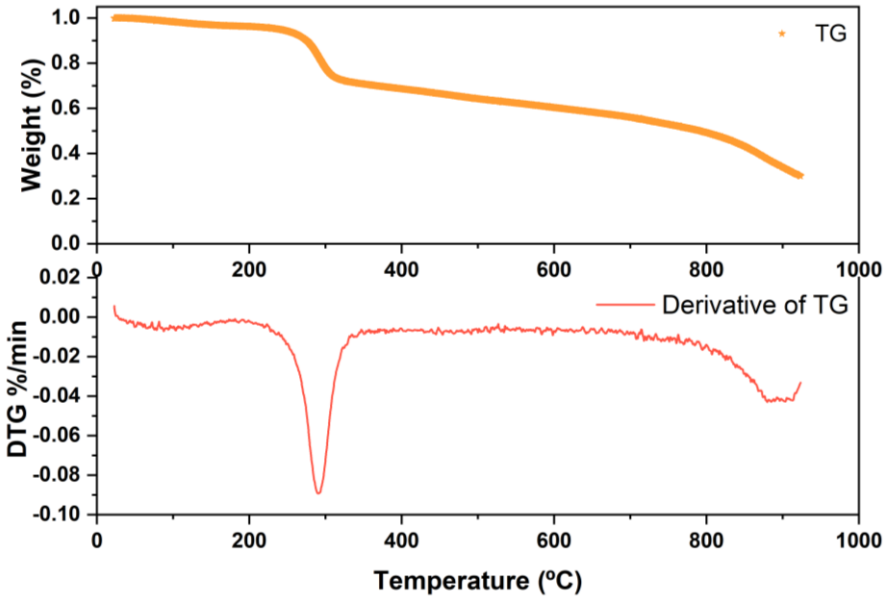

Figure C.5: TGA analysis of Tuball SWCNTs with CMC binder with the derivative of the TGA data plotted underneath to allow an accurate determination of the temperature at which the CMC is carbonised.

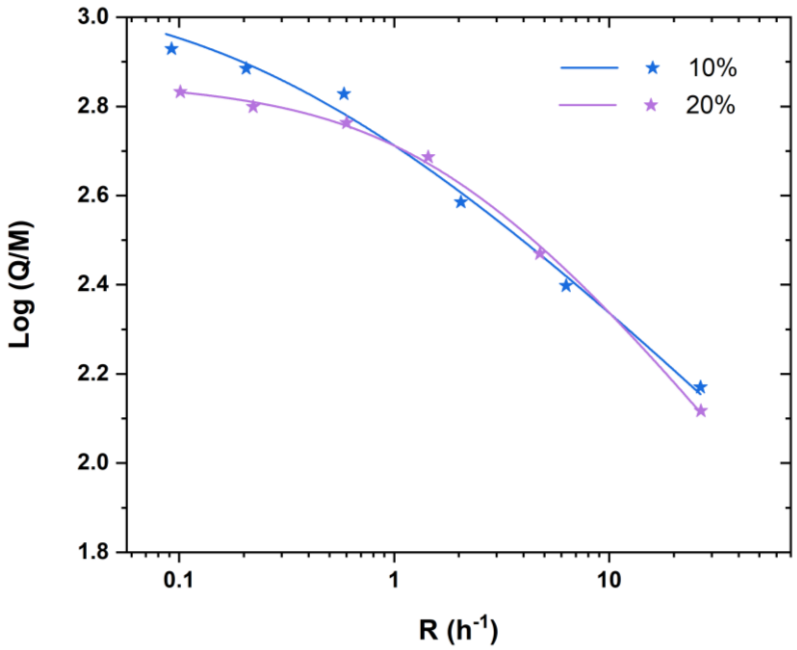

Figure C.6: 10% and 20% mass fraction Tuball SWCNTs GCD experimental data fitted using Equation 5.1.

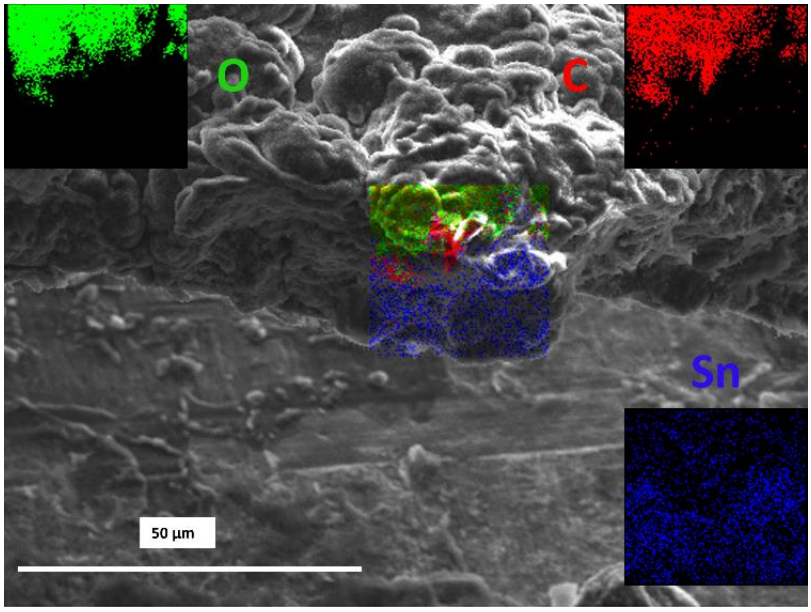

Figure C.7: EDX analysis of post-mortem SnO/SWCNT electrode with 10% FEC present in the electrolyte.

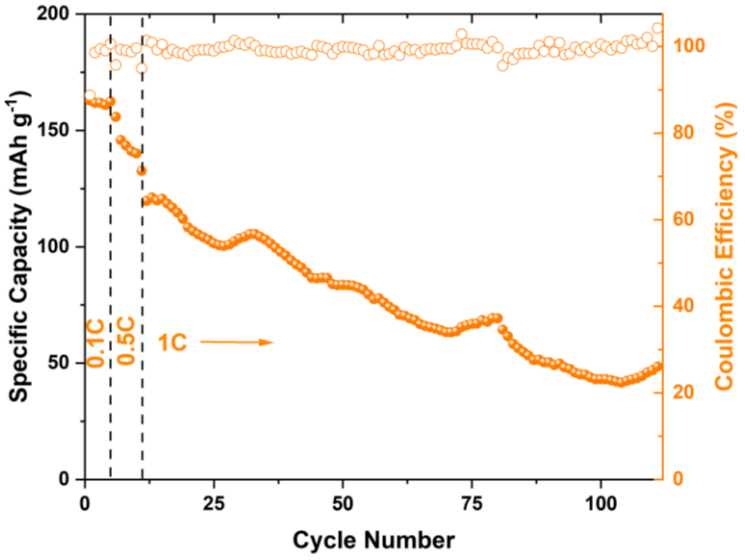

Figure C.8: NMC cathode GCD performance in terms of specific capacity.

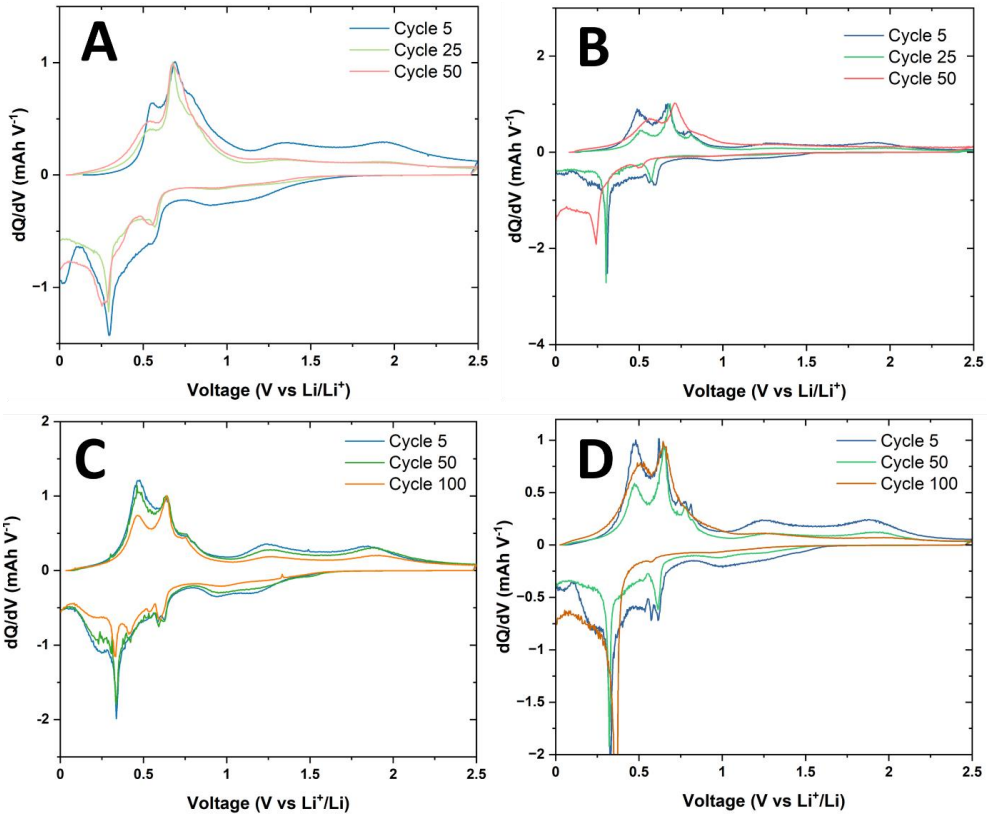

Figure C.9: Normalised differential capacity analysis of SnO with (A) 15% HT Tu-SWCNTs, (B) 15% P3-SWCNTs, (C) 15% HT Tu-SWCNTs with 10% FEC added to the cell electrolyte and (D) 15% P3-SWCNTs with 10% FEC added.

Appendix D

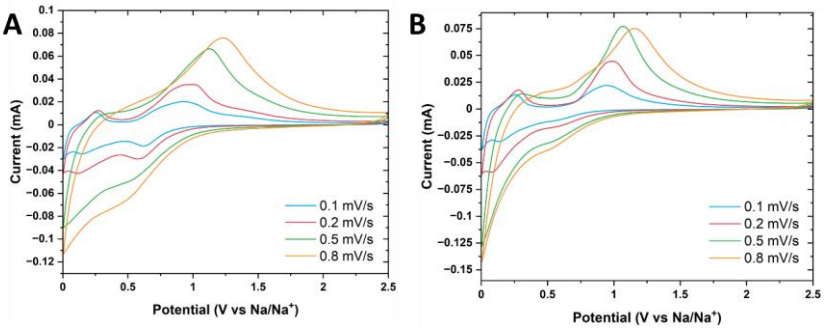

Figure D.1: CV profiles of (A) SnO(70% MeOH) and (B) SnO(Hex) at various scan rates.

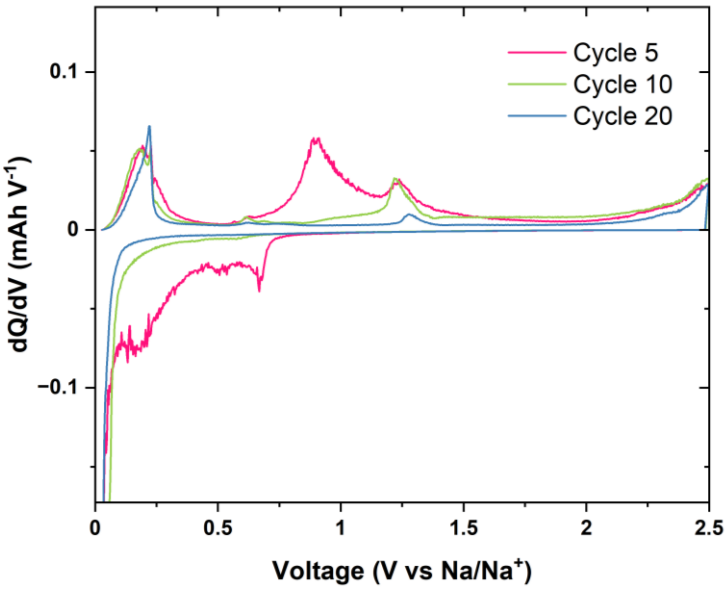

Figure D.2: *dQ/dV* analysis of diglyme electrolyte over 20 cycles at 0.1 C.

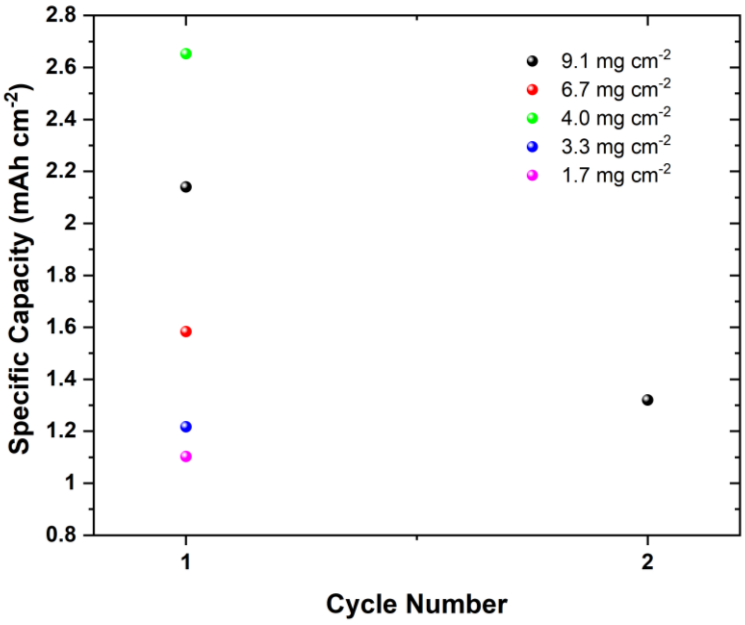

Figure D.3: Initial 2 cycles in rate test from Figure 6.10B.

Appendix E

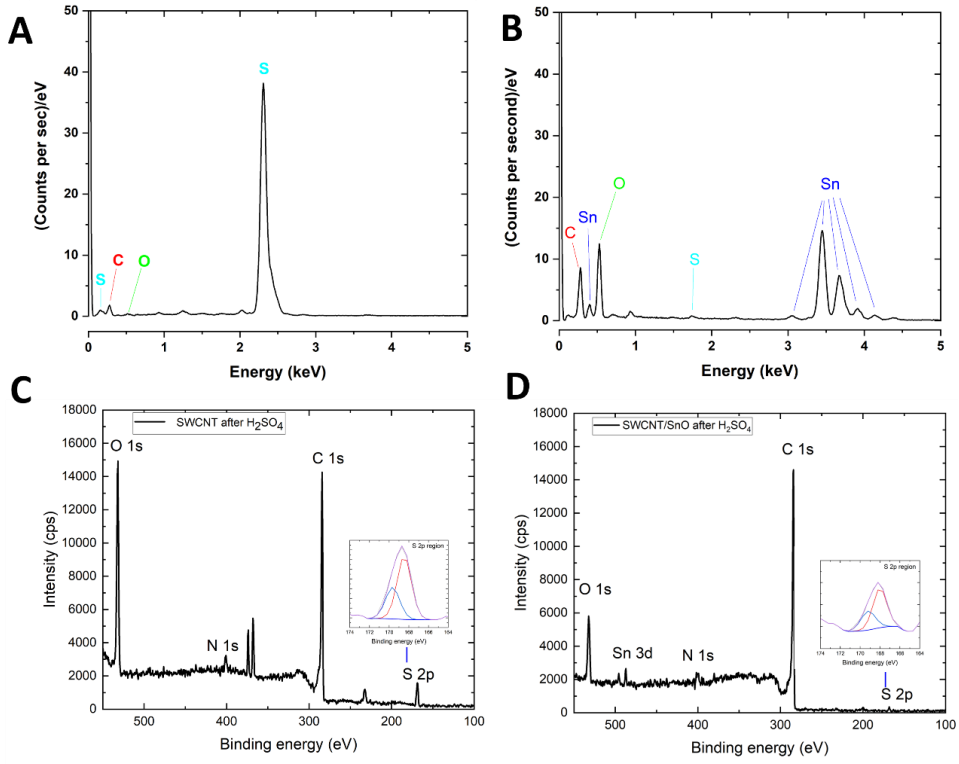

Figure E.1: EDX spectrum of (A) particles distributed on SWCNTs and (B) particles distributed on SWCNT/SnO. XPS survey scans with inserts of the S 2p region of (C) particles distributed on SWCNTs and (D) particles distributed on SWCNT/SnO.

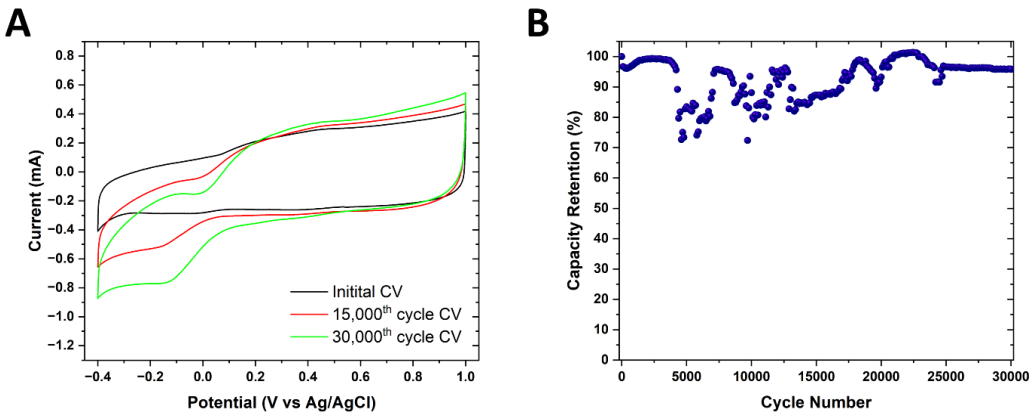

Figure E.2: (A) CVs at 10 mV s^{-1} of SWCNT/SnO electrode at initial, 15000th and 30,000th cycle and (B) corresponding capacity retention data obtained at 10 A g^{-1}.

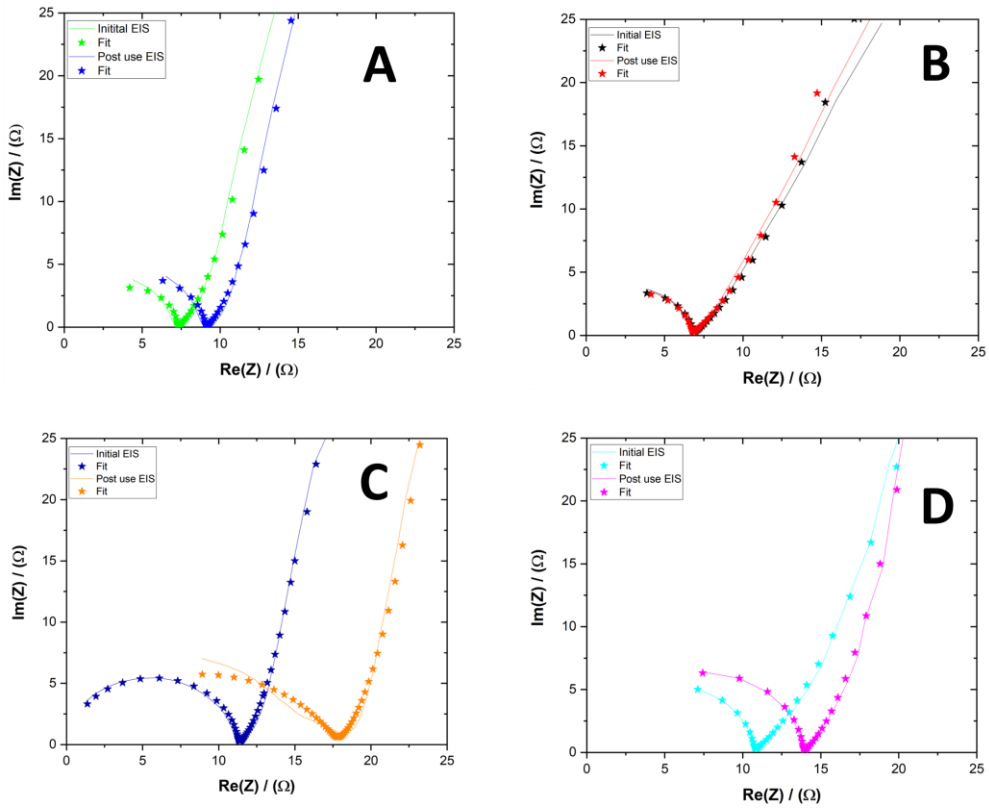

Figure E.3: EIS spectra and equivalent circuit fits of (A) SWCNT/SnO in H_2SO_4 (B) SWCNT in H_2SO_4 (C) SWCNT/SnO in K_2SO_4 (D) SWCNT in K_2SO_4.

	R_{series} (Ω)	R_{CT} (Ω)	Warburg diffusion(Ω $s^{-1/2}$)
Initial H2SO4 SWCNT	0.40	6.7	40.12
Post use H2SO4 SWCNT	0.45	6.7	38.2
Initial H2SO4 SnO-SWCNT	0.96	6.29	7.64
Post use H2SO4 SnO-SWCNT	0.53	8.53	6.43
Initial K2SO4 SWCNT	0.04	10.61	35.89
Post use K2SO4 SWCNT	1.16	12.67	19.4
Initial K2SO4 SnO-SWCNT	0.20	11.03	7.82
Post use K2SO4 SnO-SWCNT	0.02	17.66	8.08

Table E.1: EIS parameters from fitting of equivalent circuit.

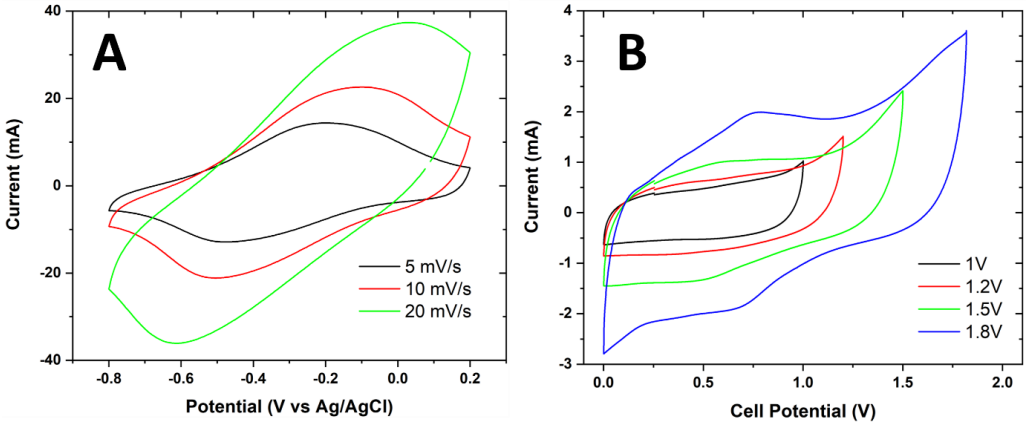

Figure E.4: (A) CV response of MXene at various scan rates. (B) CV curves of MXene and SWCNT/SnO asymmetric supercapacitor operating at voltages of 1, 1.2,1.5 and 1.8 V.

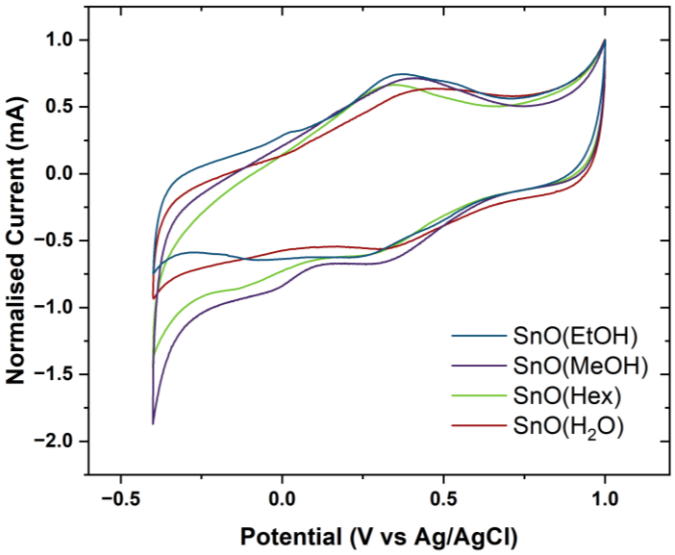

Figure E.5: CV profiles of various morphologies of SnO with SWCNT to form SC electrodes at 5 mV s^{-1}.

	5 mV s^{-1}	10 mV s^{-1}	20 mV s^{-1}	50 mV s^{-1}	100 mV s^{-1}	200 mV s^{-1}	500 mV s^{-1}	1000 mV s^{-1}	2000 mV s^{-1}
90% SnO	37.5	24.6	17.5	12.9	10.9	9.8	8.7	7.9	7.1
70% SnO	41.1	33.1	28.8	25.0	22.9	21.4	19.5	17.9	16.1
50% SnO	50.8	41.4	35.6	30.8	28.2	25.9	23.2	20.8	17.9
10% SnO	171	128	96	73	62	55	47	39	28

Table E.2: Capacitances of SWCNT/SnO electrodes at various mass loadings of SWCNTs in F g^{-1}.